INVESTIGATION OF AIR-COOLED CONDENSERS FOR WASTE HEAT DRIVEN ABSORPTION HEAT PUMPS

A Dissertation
Presented to
The Academic Faculty

by

Subhrajit Chakraborty

In Partial Fulfillment
of the Requirements for the Degree
Master of Science in Mechanical Engineering

Georgia Institute of Technology

May 2017

INVESTIGATION OF AIR-COOLED CONDENSERS FOR WASTE HEAT DRIVEN ABSORPTION HEAT PUMPS

Approved by:

Dr. Srinivas Garimella, Advisor
School of Mechanical Engineering
Georgia Institute of Technology

Dr. S. Mostafa Ghiaasiaan
School of Mechanical Engineering
Georgia Institute of Technology

Dr. Sheldon M. Jeter
School of Mechanical Engineering
Georgia Institute of Technology

Date Approved: April 25, 2017

To my mother

ACKNOWLEDGEMENTS

TABLE OF CONTENTS

LIST OF TABLES

LIST OF FIGURES

LIST OF SYMBOLS AND ABBREVIATIONS

Symbols

A	Area, m^2
A_{LD}	Dimensionless area of liquid pool
A_{VD}	Dimensionless area of vapor core
C	Constant
$\dot{C}$	Heat capacity rate, W K^{-1}
C_p	Specific heat, kJ kg^{-1} K^{-1}
D	Diameter, m; mass diffusivity, m^2 s^{-1}
Eu	Euler number
f	Friction factor
Fr	Froude number
g	Gravitational constant, 9.81 m s^{-2}
G	Mass flux, kg m^{-2} s^{-1}
Ga	Galileo number
Gz	Graetz number
h	Enthalpy, kJ kg^{-1}
H	Height, m
h_{LD}	Dimensionless height of liquid pool
j	Colburn "j" factor; Superficial velocity, m s^{-1}
Ja	Jacob number
k	Thermal conductivity, W m^{-1} K^{-1}
K_c, K_e	Contraction, expansion loss coefficient
L	Length, m
M	Molar mass, kg kmol^{-1}
$\dot{m}$	Mass flow rate, kg s^{-1}
N	Number
Nu	Nusselt number

P	Pressure, kPa
p	Pitch, m
Pr	Prandtl number
q	Quality
$\dot{Q}$	Heat duty, W
r	Radius, m
R	Thermal resistance, K W^{-1}
Re	Reynolds number
s	Spacing, m
t	Thickness, m
T	Temperature, °C
U	Overall heat transfer coefficient, W m^{-2} K^{-1}
u	Velocity, m/s
UA	Overall heat transfer conductance, W K^{-1}
v	Specific volume, m^3 kg^{-1}
$\dot{V}$	Volumetric flow rate, m^3 s^{-1}
W	Width, m
We	Weber number
x	Concentration
X	Martinelli parameter
Z	Parameter for SBG method

Abbreviations

AAD	Average absolute deviation
$AMTD$	Arithmetic mean temperature difference, K
CAT	Closest approach temperature, K
COP	Coefficient of performance
FPM	Fins per meter
$LMTD$	Log mean temperature difference, K

NTU	Number of transfer units
RH	Relative humidity
VF	Void Fraction

Greek Symbols

α	Heat transfer coefficient, W m^{-2} K^{-1}
δ	Liquid pool thickness
Δ	Differential
ε	Effectiveness
η	Efficiency
θ	Angle
μ	Dynamic viscosity, kg m^{-1} s^{-1}
ρ	Density, kg m^{-3}
σ	Surface tension, N m^{-1}
σ_c, σ_e	Area ratios for contraction and expansion
ϕ	Two-phase multiplier

Subscripts

0	Overall
accel	Acceleration
air	Air
ann	Annular
app	Apparent
avg	Average
bundle	Tube bundle/bank in multi-pass design
c	Collar, Convective, Cross-section, Contact
cond	Conduction, Condenser
crit	Critical
d	Diagonal
D	Diameter

dec	Deceleration
eff	Effective
entrance	Entrance
E	Equilibrium
exit	Exit
f	Film
fr	Frontal
fg	Vaporization
face	Face of condenser in the direction of air flow
fin	Fin
forced	Forced convection
fric	Frictional
gl	Glide
grav	Gravitational
hom	Homogenous
H_2O	Water
i	Inner, interface
in	Inlet, internal
l	Longitudinal (direction of air flow)
L	Liquid
L0	Liquid-only
m	Mixture
max	Maximum
min	Minimum
minor	Minor loss
major	Major loss
mol	Molar
NH_3	Ammonia
o	Outer
out	Outlet, external

p	Pitch
pass	Pass
r	Ratio, Reduced
rough	Roughness
row	Row
refr	Refrigerant
s	Surface
seg	Segment
staggered	Staggered row of tubes
strat	Stratified flow
t	Tube, Transverse (orthogonal to liquid and air flow)
tot	Total
TP	Two-phase
tube	Tube
unfin	Not finned
bend	Return or u-bend at the end of pass
V	Vapor
V0	Vapor-only
wall	Tube inside/outside surface
wav,d	Wave peak-to-valley depth
wav,p	Wave peak-to-valley pitch
wavy	Wavy flow

SUMMARY

Vapor absorption based heating, refrigeration, ventilation, and air-conditioning (HVAC&R) systems can utilize low-grade waste heat streams to provide heating and cooling. These thermally driven absorption systems use environmentally benign working fluids but require more heat and mass exchangers than conventional vapor compression systems. The implementation of these systems in the residential and light commercial market has not been practical for several reasons, including the lack of compact and economically viable heat and mass exchangers. Indirect coupling of the condenser in an absorption system to the ambient through an intermediate fluid loop requires additional electrical input for pumping and lowers the overall coefficient of performance (*COP*) of the system. This study considers the development of condensers directly coupled to the ambient and aims at improving the understanding of heat and mass transfer processes in heat exchangers used in absorption systems.

A detailed experimental and analytical investigation of air-coupled condensers for use in small-scale, ammonia-water absorption systems is conducted. Ammonia-water is the preferred fluid pair in small-scale absorption systems due to its high operating pressure, which allows for compact component design. Customized round-tube corrugated-fin condensers are built for an absorption chiller of 2.71 kW cooling capacity operating at severe ambient temperature conditions. Novel multi-pass tube-array design condensers are also fabricated for the same application and their performance compared with the performance of the conventional condensers. A segmented heat and mass transfer model is developed to simulate the performance of the condensers. A single-pressure ammonia-

water test facility is constructed and used in conjunction with a temperature- and humidity-controlled air-handling unit to evaluate the condensers at design and off-design operating conditions. The experimental data are used to validate and refine the design models. Performance of the condensers is recorded over a range of air temperatures, refrigerant inlet temperatures, air flow rates, and refrigerant flow rates. Several, operating variables have a large impact on round-tube corrugated-fin condenser performance, although the effect of air flow rate was lower. The novel multi-pass condensers demonstrated a steady increase in performance with increasing air flow rates. Although some fabrication issues in the present study led to the full potential of microchannel condensers not being realized, it appears that such multi-pass microchannel tube-array condensers can out-perform the conventional designs with proper manufacturing techniques. The results from this study can be applied for the development of a variety of condensers of novel configurations.

CHAPTER 1: INTRODUCTION

Space conditioning is typically provided by electrically driven vapor compression systems. In these systems, compressors are used to increase the pressure of the refrigerant, thus increasing its saturation temperature and allowing heat rejection in the condenser. The refrigerant is then expanded to a lower pressure and temperature and flows through an evaporator to draw heat from the conditioned space. The refrigerant vapor then flows into the suction side of the compressor, thus completing the cycle. Figure 1.1 Schematic of vapor compression system shows a schematic of a vapor compression system.
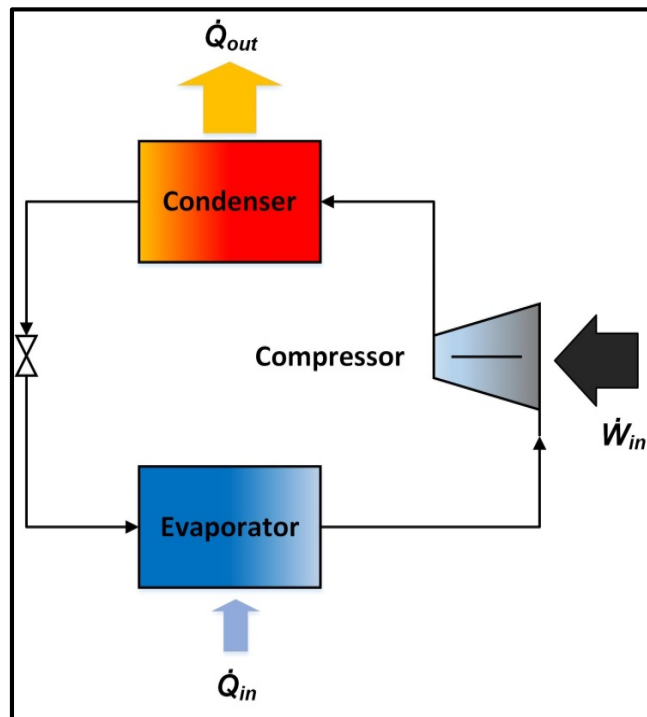
Figure 1.1 Schematic of vapor compression system

Vapor-compression cycles have several drawbacks, including the high-grade energy input required for the compression process. The large power consumption of these

systems is a significant contributor to both electricity and fuel usage, which in turn results in significant greenhouse gas emissions. The power drawn by the compressors in vapor compression chillers and air conditioners leads to high loads for electric utilities during peak periods. Additionally, these systems have relied on the use of synthetic refrigerants that contribute to global climate change.

Energy demand across the world is satisfied by chemical energy stored in fuels, and other sources such as wind, solar, nuclear, and geothermal. In the United States, even with significant advances in renewable energy generation, energy from fossil fuels still accounts for 81% of the total energy produced (EIA, 2016). Out of this energy produced from the combustion of fossil fuels, approximately two-thirds is ultimately rejected as low-grade waste heat due to conversion losses (Rattner and Garimella, 2011). Vapor absorption heat pumps can utilize this low-grade waste heat as the primary energy input to provide heating and cooling. These systems provide an alternative to conventional vapor compression systems, reducing the peak demand for electricity (Ziegler, 1999). A schematic of a single-effect absorption cycle is shown in Figure 1.2. These systems also typically use environmentally benign working pairs with no potential for global warming or ozone depletion (Lorentzen, 1995).
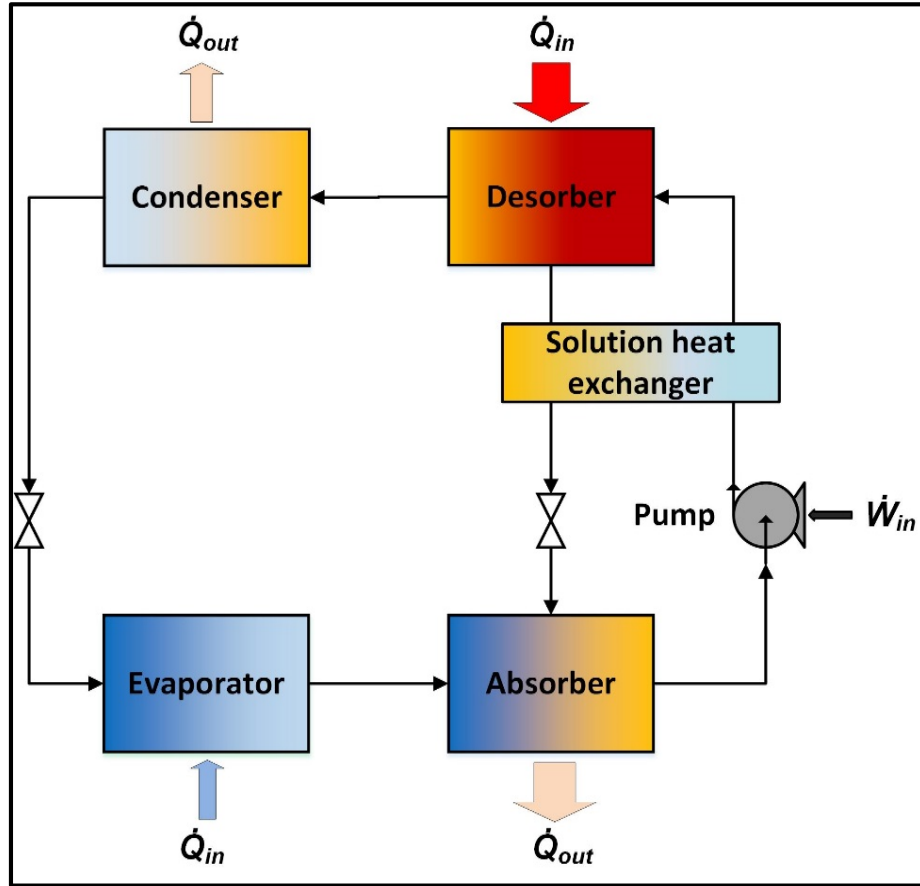
Figure 1.2 Schematic of single-effect absorption cycle

However, absorption systems require more heat and mass exchangers than vapor compression systems. The mechanical compressor in a vapor compression system is replaced by two heat and mass exchangers (the desorber and absorber) and a pump that accomplish the same task using thermal energy as the input (Herold *et al.*, 1996; Srikhirin *et al.*, 2001). As the number of components in the system increases, the system size also increases, which leads to high capital costs. Thus, absorption systems have been historically used in large-capacity industrial applications and in district heating and cooling. In such applications, these systems are either driven by waste heat from industrial processes or high-grade heat from the burning of fossil fuels.

These thermally driven absorption systems are better suited for large-scale applications with abundant thermal resources and relatively fewer constraints on component size and capital cost. Although low-grade thermal energy and waste heat are abundant, their disperse nature makes them challenging to utilize. These resources include solar thermal, geothermal, engine exhaust heat from transportation, and small-scale stationary power generation (Delahanty, 2015). Such energy sources can best be used in small-scale absorption systems for residential and light commercial applications, but small capacity absorption systems have thus far been challenging to implement.

1.1 Small Scale Absorption Heat Pump

A single-effect absorption cycle is a basic absorption cycle consisting of a minimum number of components. Advanced absorption cycles for improved efficiency with more internal heat recovery components and multiple stages of desorption have been proposed by researchers including Ziegler (1999), Kang *et al.* (2000), and Srikhirin *et al.* (2001). However, these advanced cycles need careful evaluation based on the application, and they consist of more components leading to larger systems. Thus, a single-effect absorption cycle is most suited for small-scale waste heat recovery. The single-effect absorption system considered for the present study is discussed in the next section and is shown in Figure 1.7.

An absorption heat pump requires a binary mixture as the working fluid, with one component acting as the refrigerant and the other component serving as the absorbent. The refrigerant enters the condenser usually as a saturated vapor of high purity refrigerant in a mixture with a volatile absorbent, or as a superheated refrigerant vapor in a mixture with a nonvolatile refrigerant, and undergoes condensation through heat rejection. The pressure

4

and temperature of the refrigerant are decreased by flowing it through an expansion valve, after which the refrigerant flows through the evaporator, drawing heat from the surroundings. In the absorber, refrigerant vapor from the evaporator is absorbed into the dilute solution, yielding the concentrated solution. The absorber component rejects the heat of absorption and sub-cooling of the concentrated solution. A pump is used to pressurize solution leaving the absorber and circulate solution between the absorber and desorber. The desorber receives heat from the source and desorbs the refrigerant from the concentrated solution. In addition to the main heat exchangers: condenser, evaporator, absorber, and desorber, the single-effect system under investigation also uses two recuperative heat exchangers (the solution heat exchanger and refrigerant pre-cooler) to increase the coefficient of performance of the cycle (*COP*). A rectifier component is also used downstream of the desorber to increase refrigerant purity when the working fluid has a volatile absorbent. Heat rejected in the condenser and absorber can be used to provide heat to the conditioned space in heating mode operation, while heat received by the evaporator is used to provide cooling to the conditioned space in cooling mode.

Typical working fluid pairs for absorption systems include water-lithium bromide (H_2O-LiBr) and ammonia-water (NH_3-H_2O) (Ziegler, 2002). Advantages of H_2O-LiBr systems include the non-volatility of lithium bromide, which eliminates concerns about refrigerant purity, and the high heat of vaporization of water. Disadvantages of H_2O-LiBr systems include the possibility of crystallization and increased potential for air ingress into the system (Srikhirin *et al.*, 2001). At the low temperature in the evaporator, the vapor pressure of water in water-lithium bromide cycles is well below the ambient air pressure ($P_{vap} = 0.873$ kPa at 5°C). Additionally, at such pressures, the specific volume of water

5

vapor is very large ($v_{water,vap}$ = 147 m^3 kg^{-1} at 5°C), leading to a significant increase in system size, which renders small-scale applications infeasible. Finally, H$_2$O-LiBr systems cannot be used for applications where the evaporator must operate below 0°C due to freezing concerns.

Ammonia-water has been used as the fluid pair in absorption systems since the late 1800s and is receiving renewed attention due to its environmentally benign aspects such as zero ozone depletion potential (ODP) and significantly lower global warming potential (GWP) as compared to conventional refrigerants (Herold *et al.*, 1996). The low freezing point of ammonia (−77°C) enables low system operating temperatures with applications in both heating and cooling (Srikhirin *et al.*, 2001). In addition, the high operating pressure of ammonia-water systems allows for compact component designs that enable small-capacity units. However, the use of ammonia-water also presents a variety of design challenges. Lightweight and high thermal conductivity materials such as copper and aluminum are not compatible with ammonia-water. Mini- or microchannel heat exchangers have been shown to enhance heat and mass transfer and provide high surface area-to-volume ratios. In crossflow air-coupled heat exchangers, the focus of the present study, mini- and microscale geometries are implemented using extruded rectangular tubes. These small rectangular tubes provide high tube-side heat transfer coefficients and are usually combined with louvered fins to yield compact and efficient air-coupled heat exchangers, as shown in Figure 1.3. However, materials that are compatible with ammonia, such as steel, are not conducive to extrusion. Due to these manufacturing challenges, ammonia-water systems have not benefited from the reduction in size and improvement in performance that results from the use of compact air-coupled heat exchangers.

6
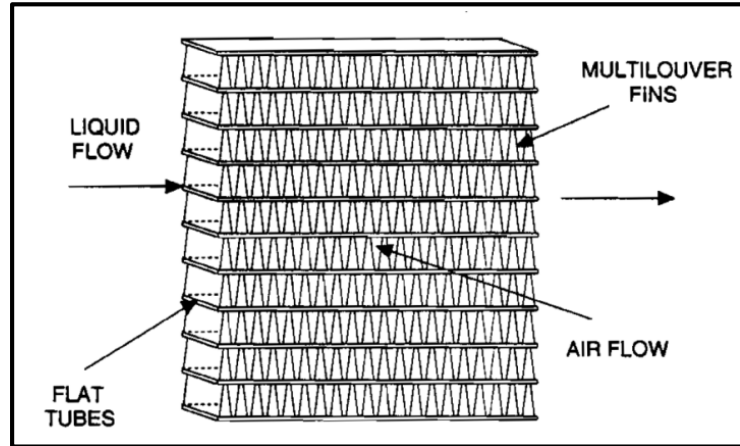
Figure 1.3 Extruded rectangular tube geometry for air-coupled heat exchangers (Garimella *et al.*, 1997)

1.2 Condenser in Compact Absorption Systems

The condenser in an absorption heat pump cycle rejects the heat of condensation to the ambient while condensing the refrigerant vapor to the liquid phase, in a manner similar to that of a condenser in vapor compression system. The absorbent (water) in an ammonia-water system is volatile and high concentrations of water (>1%) in the refrigerant stream cause a significant temperature rise in the evaporator, adversely affecting the cooling capacity of the system. Thus, for efficient operation of an ammonia-water absorption cycle, a rectifier component is required to purify the refrigerant vapor before entering the condenser (Srikhirin *et al.*, 2001). The refrigerant vapor exiting the desorber is cooled by the rectifier to condense most of the residual water vapor and increase ammonia concentration. This lowers the temperature of the refrigerant at the inlet to the condenser, posing a greater challenge for the condenser to reject heat to the ambient due to the lower temperature difference available for heat rejection.

7

In some implementations, the condenser in an absorption system is hydronically coupled with ambient air through an intermediate coupling loop, as shown in Figure 1.4. Indirect air coupling allows for the use of a non-corrosive single-phase fluid that enables the use of compact air-coupled heat exchangers made of materials with high thermal conductivity. Several researchers Ferreira *et al.* (1984); Meacham and Garimella (2004); Fernández-Seara *et al.* (2005); Garimella *et al.* (2016) have utilized efficient and compact heat exchangers in absorption systems by indirectly coupling to the ambient with an intermediate fluid loop. However, the additional electrical input for pumping of the coupling fluid and the increased temperature difference between the ambient and the refrigerant cause a decrease in system *COP*. Eliminating this coupling loop reduces packaged system size, increases *COP*, and improves the viability of implementation in mobile and small-scale systems. This requires the use of direct air-cooled condensers, which in turn also pose a number of design challenges. In comparison to large absorption cycles that use cooling towers and the resulting ambient wet bulb temperature as the heat sink, compact dry air-coupled systems require higher refrigerant temperatures because of the poor heat transfer properties of air (Herold *et al.*, 1996). A higher refrigerant temperature increases the operating pressure and water concentration, thereby affecting system performance adversely.
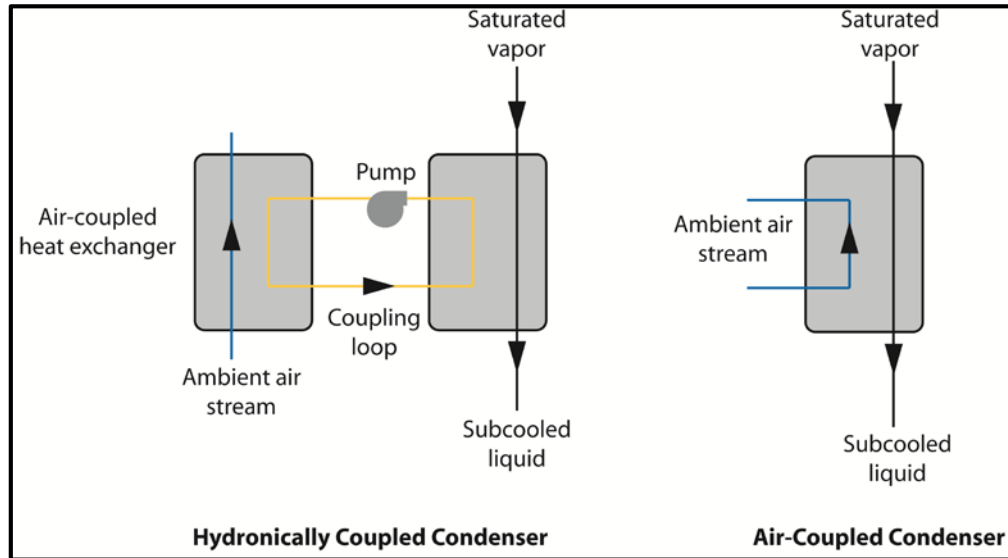
Figure 1.4 Indirect-and direct-coupled condenser systems

Because of these challenges, there is a need for the development of compact air-coupled heat exchangers compatible with ammonia-water for small-scale energy recovery. The present study investigates such condensers through analytical models validated by experiments.

1.3   Scope of Present Study

The objective of the present work is to improve the understanding of the heat and mass transfer in compact air-coupled condensers used in absorption systems. The work includes a detailed analytical and experimental study of air-cooled condensers for small-scale ammonia-water absorption heat pumps. Conventional round-tube corrugated-fin condensers used in ammonia-water systems are evaluated in this study. A novel multi-pass tube-array condenser design is also explored and its performance is compared to that of the conventional condensers.

All the condensers are built for a compact single-effect ammonia-water absorption chiller of 2.71 kW cooling capacity operating at severe ambient temperature conditions (51.7°C) representative of forward operating bases in the Middle East. A CAD model of the corresponding absorption system is shown in Figure 1.5. The CAD model is used to locate major components such as the absorber, condenser, desorber, pump assembly, and others in the system, and to determine fluid routing.
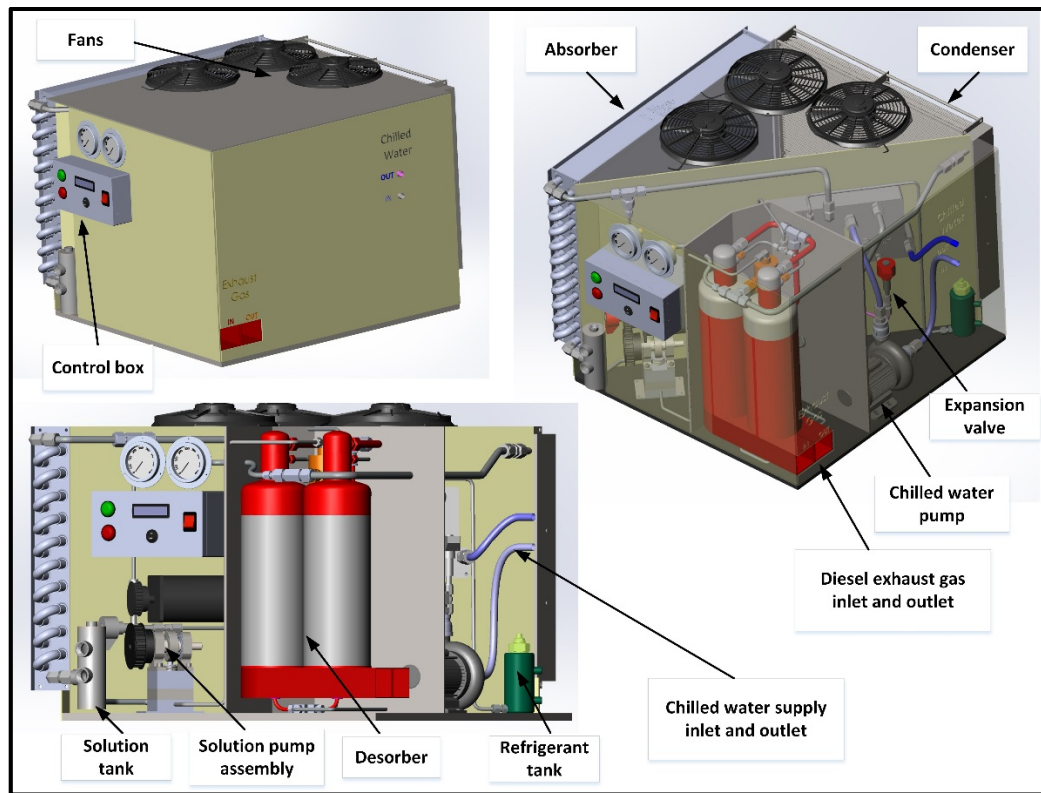
Figure 1.5 CAD model of compact absorption chiller under consideration

A prototype of the absorption chiller system is built based on the CAD model as shown in Figure 1.6. The space constraints in this compact absorption packaged system dictate the dimensions and size of the condensers and thus limit the air-flow area. The

maximum length and height of a condenser that would fit in the compact system are 0.54 m and 0.46 m, respectively.

Figure 1.6 Prototype of compact absorption chiller system under consideration

This compact absorption chiller is built for waste heat recovery from small-capacity diesel engine power generators for defense applications in severe environments. This compact ammonia-water absorption system is directly fired by exhaust gas from the diesel generator at ~400°C. The design ambient air for heat rejection by the chiller is at 51.7°C with 18% relative humidity. The cycle model for this absorption system at the design

conditions was developed by Forinash (2015), with a schematic shown in Figure 1.7. The focus of the present study is to characterize and improve the performance of the air-coupled condenser in the system (enclosed in red). Based on this cycle model, the design heat transfer rate for the condenser is 2.51 kW.
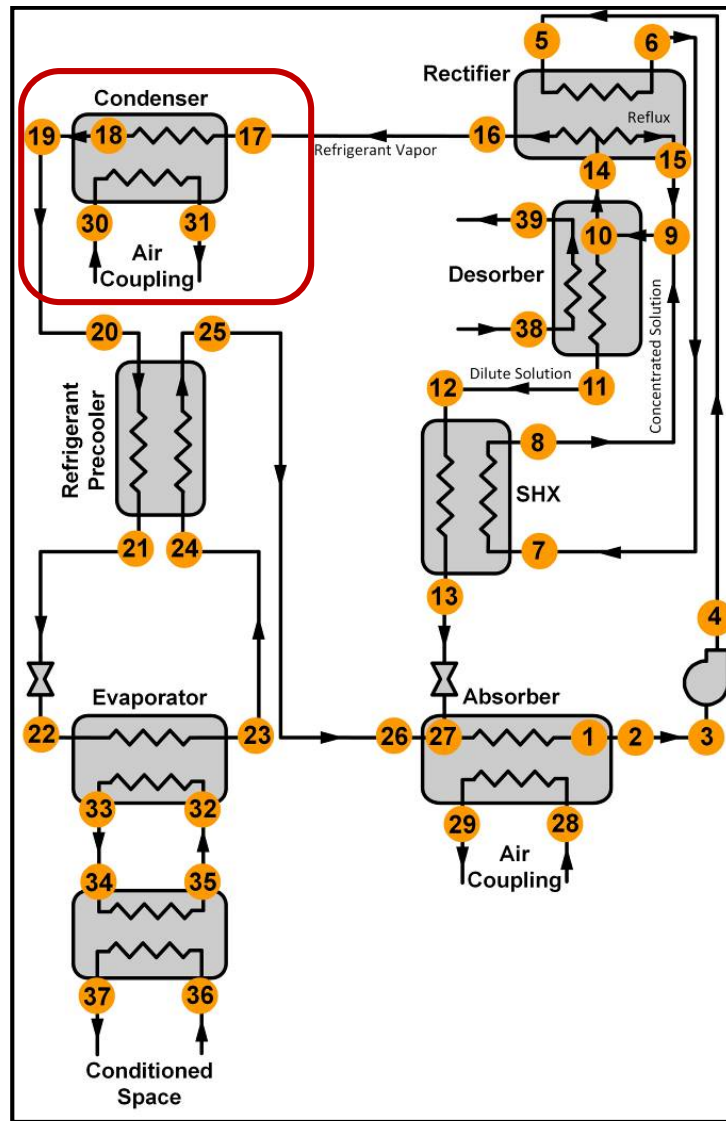
Figure 1.7 Cycle model of ammonia-water absorption system
(Forinash, 2015)

The results from this cycle model are used to determine the refrigerant inlet for the condenser at design conditions, which are shown in Table 1.1. The refrigerant is assumed to be in a saturated vapor state when entering the condenser. The cycle model predicts an ammonia mass fraction of 99.8% in the refrigerant and a temperature of 74.74°C at the inlet of the condenser. Also for the tube side, an allowable pressure drop of 13.7 kPa is budgeted in the cycle model.

Table 1.1 Condenser inlet conditions from cycle model (Forinash, 2015)

Air inlet	$\dot{V}_{air,in}$ $(\text{m}^3\text{s}^{-1})$	0.354
	$T_{air,in}$ (°C)	51.7
Refrigerant Vapor Inlet	$\dot{m}_{refr,in}$ (g s^{-1})	2.47
	$x_{refr,in}$ (-)	0.998
	$T_{refr,in}$ (°C)	74.74

The volumetric flow rate of air through the condenser is determined by the fans in the packaged system unit. A higher flow rate of air consumes more fan power leading to a decrease in the overall *COP* of the system. A design volumetric air flow rate of 0.354 m^3 s^{-1} is selected based on the optimal fan power allowance and air distribution between the air-coupled absorber and condenser. Also for the air side, an allowable pressure drop of 62 Pa is budgeted in the cycle models.

Both the conventional and novel condensers are designed and modeled using the inputs discussed above at design conditions. A segmented heat and mass transfer model is used, which divides the heat exchanger into several segments of equal length to account for variation in fluid flow and heat transfer processes due to changes in properties during the condensation process. Prototype condensers (first versions) are fabricated for both

conventional and novel multi-pass condensers. The condensers are experimentally evaluated at design and off-design operating conditions in an ammonia-water test facility coupled with an air-handling unit. The experimental results are used to fine tune the models and updates are made to the condenser designs. Prototypes of these new designs (second versions) are experimentally evaluated at design and off-design conditions. The results from the experiments are compared with model predictions, and reasons for differences between them are postulated. The present study will guide the development of designs of compact and efficient condensers of novel configurations.

1.4 Thesis Organization

The subsequent chapters of this thesis are organized as follows:

- Chapter 2 provides a review of the literature on air-coupled condenser modeling based on models for tube-side and air-side performance. Previous work on air-coupled condenser evaluation and development is also discussed in this chapter.

- Chapter 3 describes the modeling approach adopted to predict the performance of both the conventional and novel multi-pass condensers.

- Chapter 4 describes the fabrication of the condensers and the experimental setup. Details of the experimental procedure for the evaluation of the condensers are also provided in this chapter.

- Chapter 5 presents the results from the analysis and experiments of the condensers. The model predictions for both the condenser types are compared with experimental heat duties at design and off-design conditions in this chapter.

- Chapter 6 summarizes the major findings and conclusions from the present study. Recommendations for further study of air-coupled heat exchangers for compact ammonia-water absorption systems are also provided.

CHAPTER 2: LITERATURE REVIEW

A review of the literature pertinent to the present study is discussed in this chapter. For the analytical models, the reviewed literature is organized into two main sections: tube-side and air-side. Studies on air-coupled heat exchangers for ammonia-water systems are also reviewed.

2.1   Tube-Side Models

This section discusses prior work on tube-side heat transfer and pressure drop modeling of condensers. Significant research has been done to understand and model condensation in different tube geometries. Both round-tube corrugated fin condensers and the multi-pass tube-array condensers consist of horizontal tubes. Several heat transfer and pressure drop models exist for horizontal tubes, but relatively fewer models apply to the velocities and tube diameters under consideration in this study. Furthermore, ammonia-water is a zeotropic mixture, leading to a decrease in saturation temperature as condensation proceeds. Due to the high ammonia concentration (> 99%) in the vapor entering the condenser, this temperature glide occurs near the inlet of the condenser where the water fraction is relatively higher (Garimella and Coleman, 1998). Thus, mass transfer resistance is also accounted for in the tube-side of the models to predict heat transfer rates of the condensers accurately. Various condensation heat transfer and pressure drop correlations are reviewed, and their applicability to the condensers for the present application is evaluated.

2.1.1 Two–phase flow regime

Past research has shown that the heat transfer coefficient is dependent on the flow pattern during condensation in addition to its dependence on fluid properties, mass flux, vapor quality, and orientation with respect to gravity. In the shear-dominated annular flow regime, uniform heat transfer occurs approximately through the entire perimeter of the flow channel (Ghiaasiaan, 2007). In contrast, the wavy and slug flow regimes are dominated by gravity, and a pool of condensate fills the bottom, while a thin condensate film covers the top of the tube. In this case, heat transfer occurs mainly through the top part of the channel because of the high thermal resistance in the liquid pool at the bottom (Ghiaasiaan, 2007). Thus, the prevailing two-phase flow regime inside a segment is important in determining the appropriate correlation for tube-side heat transfer and pressure drop for that segment.

While there are several studies in the literature on two-phase flow regimes (Baker, 1953; Mandhane *et al.*, 1974; Taitel and Dukler, 1976), studies focusing on flow regimes during condensation in horizontal tubes are most pertinent to the present work. Soliman (1982) derived a criterion for the transition between wavy and annular flow regime using modified Froude number. The criterion is based on data collected with water, acetone, and refrigerants in 4.8 mm to 25 mm diameter horizontal tubes. The wavy flow regime defined by Soliman (1982) included both slug and stratified flow regimes, and no criterion is provided to distinguish the two. The flow regime map developed by Coleman and Garimella (2003) is based on the data obtained from R134a refrigerant flowing horizontally in circular ($D = 4.91$ mm) and rectangular ($D_H = 4.8$ mm) channels. The map defines all the condensation flow regimes inside a horizontal round tube as a function of refrigerant

mass flux and quality. Recently, Nema *et al.* (2014) used the database of Coleman and Garimella (2003) to develop a flow regime map. The map takes into account transition between macro and microscale effects and fluid property effects by utilizing dimensionless parameters. The flow regime map (Figure 2.1) by El Hajal *et al.* (2003) adapts the flow boiling pattern map of Kattan *et al.* (1998a) for condensation inside horizontal tubes. As seen from this figure, saturated vapor entering the condenser goes directly into either the annular flow regime or the stratified flow regime based on the mass flux. The study divided the gravity-controlled stratified flow regime further into fully-stratified and stratified-wavy flows and is determined by G_{strat}.
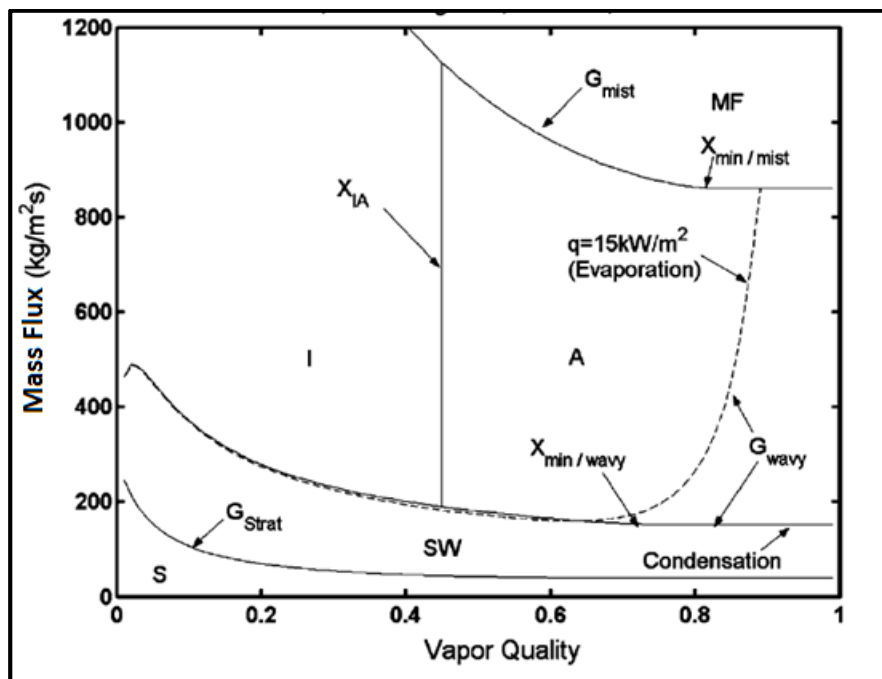
Figure 2.1 Condensation flow-regime map (El Hajal *et al.*, 2003)

The authors also propose a new correlation for two-phase flow void fraction (VF), preferable for heat transfer coefficient calculations. The VF is based on the drift flux model of Rouhani and Axelsson (1970), which was further modified by Steiner (1993) for

horizontal tubes and is shown in Equation (2.2). The void fraction suggested by El Hajal

et al. (2003) for two-phase flow pattern map and heat transfer calculations is a logarithmic

mean of the homogenous void fraction and the Steiner (1993) correlation. A comparison

of the various void fraction correlations at design conditions of the present study is

provided in Figure 2.2.

$$VF_{\text{hom}} = \left[1 + \left(\frac{\rho_V}{\rho_L}\right)\left(\frac{1 - q_{refr}}{q_{refr}}\right)\right]^{-1} \tag{2.1}$$

$$VF_{RA} = \frac{q_{refr}}{\rho_V}\left(\left[1 + 0.12\left(1 - q_{refr}\right)\right]\left[\frac{q_{refr}}{\rho_V} + \frac{1 - q_{refr}}{\rho_L}\right] + \frac{1.18\left(1 - q_{refr}\right)g\sigma(\Delta\rho)^{0.25}}{G_{refr}\rho_L^{0.5}}\right)^{-1} \tag{2.2}$$

$$VF_{hajal} = \frac{VF_{\text{hom}} - VF_{RA}}{\ln\left(\dfrac{VF_{\text{hom}}}{VF_{RA}}\right)} \tag{2.3}$$
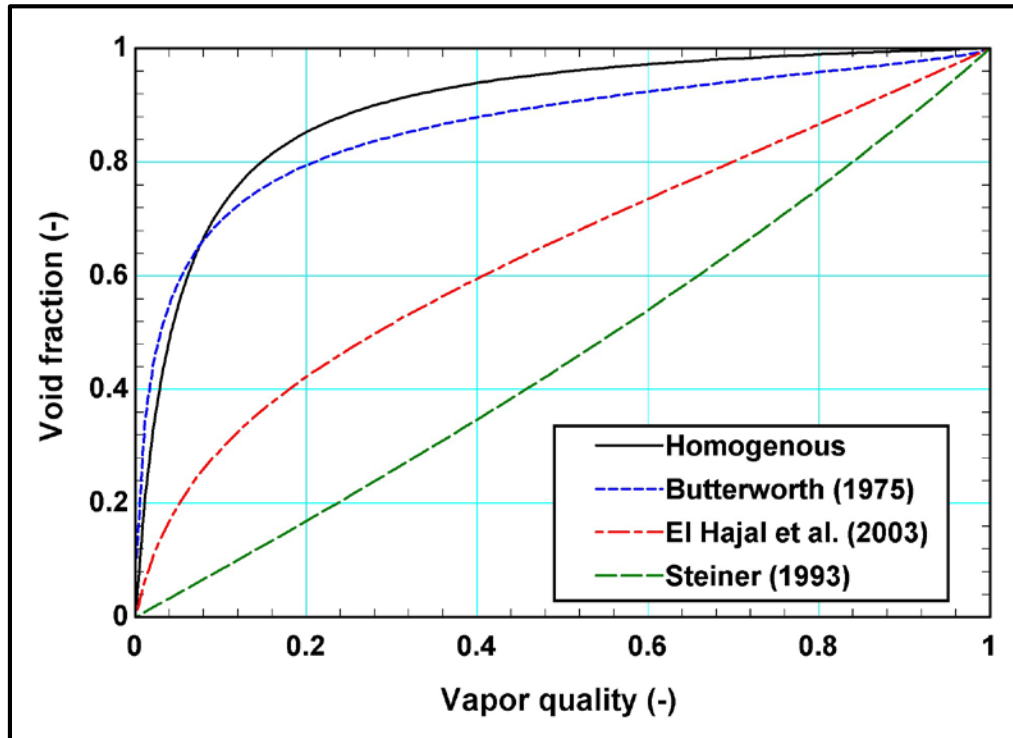
Figure 2.2 Comparison of void fraction correlations in the literature

It is noted in the study that, for condensation, the saturated vapor entering the condenser tube forms either a thin liquid film around the perimeter as an annular flow or a liquid layer at the bottom of the tube and a condensing film on the top. The latter is further subdivided and defined separately as stratified and stratified-wavy in the flow pattern map by El Hajal *et al.* (2003). This gravity-driven stratification of the vapor and liquid phases is due to the low mass flow rate of refrigerant and is typically seen in small-scale absorption systems.

2.1.2 Condensation

One of the earliest correlations for condensation in horizontal tubes was provided by Akers *et al.* (1958). They used an equivalent two-phase Reynolds number model, where

the all-liquid flow rate is used to define the Reynolds number. This equivalent two-phase Reynolds number was used in a single-phase, turbulent flow equation to predict the condensation Nusselt number. The condensation heat transfer coefficient is obtained from the Nusselt number by using the liquid thermal conductivity and the diameter of the tube. This correlation over predicts condensation heat transfer coefficients, especially at high mass fluxes (Bandhauer *et al.*, 2006).

The empirical correlation developed by Shah (1979) is widely used for predicting condensation heat transfer for a variety of refrigerants in horizontal, vertical, and inclined round tubes. The correlation was based on 474 data points from 21 experimental studies over a wide range of heat fluxes, mass fluxes, vapor velocities, and reduced pressures. Although numerous other researchers (Dobson and Chato, 1998; Moser *et al.*, 1998) compared this correlation and reported good agreement with their data, it was not suitable for very low flow rates and newer refrigerants. Later, Shah (1981) recommended conservative limits for this correlation such as all-vapor Reynolds number should be greater than 35,000 for the correlation to be applicable.

Shah (2009) updated his earlier correlation by expanding the database to include 39 sources for 22 fluids that include water, halocarbon refrigerants, hydrocarbon refrigerants, and a variety of organics condensing in horizontal, vertical, and downward-inclined tubes of diameters varying from 2 mm to 49 mm. The correlation is regime dependent. Two flow regimes are proposed for horizontal tube condensation based on dimensionless vapor velocity (J_g) and Shah's correlating parameter (Z). However, only one flow regime (regime I) is applicable for the present study because of the very low vapor Reynolds number in the

21

condensers for all test conditions. The correlation computes the heat transfer coefficient assuming all the mass is flowing as a liquid, as shown in Equation (2.4).

$$\alpha_{L0} = 0.023 \frac{k_L}{D_i} \left(\frac{G_{refr} D_i}{\mu_L} \right)^{0.8} \mathrm{Pr}_L^{0.4} \tag{2.4}$$

The heat transfer coefficient for regime I, according to Shah (2009), is calculated using Equation (2.5).

$$\alpha_I = \alpha_{L0} \left(\frac{\mu_L}{14\mu_V} \right)^n \left[\left(1 - q_{refr} \right)^{0.8} + \frac{3.8 q_{refr}^{0.76} \left(1 - q_{refr} \right)^{0.04}}{\left(P_{refr} / P_{crit} \right)^{0.38}} \right]$$

$$\tag{2.5}$$

$$n = 0.0058 + 0.557 P_r = 0.1508$$

The total refrigerant mass flux is G_{refr}, while q_{refr} refers to the average quality of the solution.

This new correlation was found to have lower mean deviation than the original Shah (1979) correlation, and was tested at reduced pressure range of 0.0008 to 0.9 and for a vast range of flow rates (4 to 820 kg m^{-2}s^{-1}) for vertical tubes. However, further research is needed to validate and extend it for horizontal and slightly inclined tubes at all-vapor Reynolds numbers less than 16,000.

The mass flow rate of the refrigerant in the condenser of an absorption system for residential and light commercial applications is typically very low, 2.47 g s^{-1} for the present study; therefore, gravity-driven condensation heat transfer correlations are the most applicable. The dominant heat transfer mode in this regime is conduction across the film at the top of the tube. Analytical studies on film condensation started with the pioneering work done by Nusselt (1916) for a pure fluid on a vertical plate. Chato (1960) developed a

similarity solution to extend the Nusselt correlation to falling-film condensation inside tubes. This is applicable only for stratified flow with low vapor velocities where condensate film covers most of the upper portion of the tubes. He also developed a separate analytical model to predict the depth of the liquid pool and compared it with experimental results using R-113 refrigerant in a tube of 27.94 mm diameter. The depth of the liquid pool at the bottom was found to be relatively constant, which allowed the heat transfer data to be predicted using a Nusselt-type correlation. A coefficient is included to account for the decrease in heat transfer due to the thickness of the liquid pool at the bottom of the tube. Jaster and Kosky (1976) added the effect of variation of liquid pool depth in a manner consistent with pressure-driven flows. However, both the correlations (Chato, 1960; Jaster and Kosky, 1976) neglect the heat transfer that occurs in the pool at the bottom of the tube. Convective heat transfer through the pool becomes significant at high mass flux and low quality situations. This effect was observed by Dobson and Chato (1998) experimentally at mass fluxes above $75 \ \mathrm{kg \, m^{-2} s^{-1}}$. A detailed experimental study on condensation in horizontal tubes over different flow regimes was conducted by Dobson and Chato (1998). They also captured the effect of interfacial-shear by the vapor on the condensate film based on their data. In contrast to ideal stratified flow, the liquid condensate film does not fall vertically due to gravity, and has both axial and circumferential components at high vapor velocities. To accommodate these effects, they developed a correlation for wavy flow, guided by a combination of experimental data analysis and analytical solutions. The correlation separately takes into account film condensation in the upper part of the horizontal tube and forced convection in the bottom pool.

23

Cavallini *et al.* (2002) compared horizontal tube condensation heat transfer coefficients from most of the past prediction methods with data obtained by independent researchers for halogenated refrigerants. This comparison showed that the available prediction methods either cannot be applied because of the cited limits of the applicable range, or significantly over predict the data, typically by 20-40%. A new heat transfer model was developed by Cavallini *et al.* (2002), which showed an improvement upon past methods. However, this model included a large number of empirical constants and showed an abrupt jump in the heat transfer coefficient across flow regime transitions. To avoid these inconsistencies and also accurately predict the hydrocarbon condensation data, Thome *et al.* (2003) proposed a heat transfer model for condensation inside horizontal, plain tubes with fewer empirical constants and exponents. Their model was based on a database consisting fifteen fluids and assumed two types of heat transfer mechanisms in the tube, convective condensation and film condensation. They defined convective condensation as the axial flow of condensate along the channel due to the imposed pressure gradient, and film condensation as the flow of condensate from the top to the bottom of the tube due to gravity. Thome *et al.* (2003) used two-phase simplified flow structures originally developed by Kattan *et al.* (1998b) for flow boiling regimes, with the only difference that the top of the tube is wetted by film condensation rather than remaining dry, as is the case during evaporation. They assumed three simplified geometries for describing annular, stratified wavy and fully stratified flow. The final model was found to predict 85% of the non-hydrocarbon database to within 20%, and 75% of the entire refrigerant database to within 20%.

2.1.3 <u>Effect of zeotropic mixture</u>

Condensation of binary or higher order zeotropic mixtures is affected by two factors that effectively reduce the heat transfer rate in condensers. Firstly, as vapor is converted to liquid, there is a nonlinear shift in the equilibrium phase concentrations. For example, in the case of condensation of ammonia-water, the ammonia concentration in the liquid phase increases along the length of the condenser. This change in equilibrium phase concentrations causes a change in the equilibrium temperature, which results in a non-constant condensation temperature (temperature glide, i.e., the difference between the bubble point and dew point temperatures.) Thus, the driving temperature ($T_{\text{interface}} - T_{\text{wall}}$) for condensation decreases throughout the condensation process, which reduces the heat transfer rate. Secondly, the condensation process is a local interfacial phenomenon with the less volatile component (water in this case) condensing more readily than the more volatile component (ammonia in this case), which results in a concentration gradient in the vapor phase. The concentration gradients in the vapor and liquid phases are referred to as a non-equilibrium condition. This mass transfer resistance limits the condensation process. Thus, the change in condensation temperature reduces the overall heat transfer rate and the mass-transfer resistance limits the rate of condensation. The condenser size is highly sensitive to both the temperature difference between the working fluid and the coolant, and the heat transfer coefficient. Thus, accounting for the temperature glide and the mass transfer resistance in the models is critical to correctly determine the required condenser surface area.

Different approaches have been used in the literature to model condensing mixtures for condenser design. Two most widely used methods to model the condensation of a

zeotropic mixture are non-equilibrium method and equilibrium method. The non-equilibrium method is more theoretically sound, but can require substantial computational resources. There is high uncertainty in mixture diffusivity properties, which makes calculation of mass transfer coefficient of vapor difficult for the non-equilibrium model (Fronk and Garimella, 2016a, b). To overcome these challenges, a simplified equilibrium model was presented in similar studies (Silver, 1947; Bell and Ghaly, 1973). According to Hewitt et al. (1994), there are two principal assumptions in this model. Firstly, both the liquid and vapor phases follow the equilibrium condensation curve and their respective enthalpies are those of the equilibrium phases at the vapor bulk temperature. Due to this assumption, the calculation method is often referred to as the equilibrium model, or the Silver-Bell-Ghaly (SBG) model, named after those who first popularized it (Silver, 1947; Bell and Ghaly, 1973). Secondly, the heat released due to condensation is assumed to pass from the interface to the coolant. In this model, sensible heat is transferred from the bulk vapor to the interface by convective heat transfer, where the heat transfer coefficient is calculated for the given geometry assuming only vapor is present, using vapor bulk properties and vapor mass flux. The argument provided by Bell and Ghaly (1973) is that calculating the sensible heat transfer coefficient in the vapor phase will result in a significant under prediction, because two-phase enhancement effects are not considered. The central idea is that the additional resistance from mass transfer, which is not calculated, will be compensated for by the underestimation of the vapor heat transfer coefficient. The decrease in condensation temperature as condensation proceeds is calculated by tracking the equilibrium temperature of the entire mixture. The SBG method can be used in conjunction with any of the pure fluid correlations, as demonstrated by Hewitt *et al.* (1994).

26

The SBG method has been used by several researchers for zeotropic mixture condensation including Del Col et al. (2005) and Cavallini et al. (2006). The study by Del Col et al. (2005) applied the SBG method based on the prevailing two-phase flow regimes inside the horizontal tube. In this study, the flow regime map of El Hajal et al. (2003) and heat transfer model of Thome et al. (2003) for pure fluid condensation were used. The heat transfer contributions of convective condensation and film condensation were used, along with their respective surface areas. To determine the respective heat transfer areas, simplified flow structures for two-phase flow patterns were used, similar to Thome et al. (2003). The SBG method was separately applied to film condensation and convective condensation to account for the effect of mass transfer resistance due to zeotropic mixture condensation. The flow regime based overall local heat transfer coefficient proposed by Del Col et al. (2005) has been validated with data for refrigerant mixtures with temperature glides of 3.5 – 22°C. The proposed method predicted 98% of refrigerant heat transfer data from Cavallini et al. within ±20%, and 70% of the data from other independent researchers within ±20%. A summary of the above heat transfer studies, along with their range of applicability is shown in Table 2.1

Table 2.1 Summary of condensation correlations for horizontal tubes

Author(s) (Year)	Approach	Working Fluids	Zeotropic Mixture Effects	D_i (mm)	Range of Applicability
Shah (1979)	Empirical	R-11, R-12, R-22, R-113, benzene, ethanol, methanol, toluene, trichloroethylene, water	Not included	7 to 40	$10.8 < G < 210.6$ kg m^{-2} s^{-1} $21 < T_{sat} < 310$°C $0.002 < P_r < 0.44$
Shah (2009)	Empirical	R-11, R-12, R-22, R-32, R-113, R-123, R-125, R-134a, R-142b, R-404A, R-502, R-507, propylene, isobutene, propane, benzene, Dowtherm 209, ethanol, toluene, methanol, water	Not included	2 to 49	$4 < G < 820$ kg m^{-2} s^{-1} $0.0008 < P_r < 0.9$
Chato (1960)	Analytical, empirical	R-113	Not included	28	Stratified flows with low vapor velocities
Dobson and Chato (1998)	Experimental, adiabatic	R-134a, R-22, 60/40 and 50/50 blends of R-32 and R-125	Not included	3.14, 4.57, 7.04	$25 < G < 800$ kg m^{-2} s^{-1} $35 < T_{sat} < 60$°C $0.21 < P_r < 0.57$
Cavallini *et al.* (2002)	Empirical	R-22, R-134a, R-125, R-32, R-236ea, R-407C, R-410A	Not included	3 to 21	$100 < G < 750$ kg m^{-2} s^{-1} $30 < T_{sat} < 50$°C $P_r < 0.75$
Thome *et al.* (2003)	Analytical, empirical	R-11, R-12, r-22, R-32, R-113, R-125, R-134a, R-236ea, a R-32/R-125 near azeotrope, R-404A, R-410A, propane, *n*-butane, iso-butane and propylene	Not included	3.1 to 21.4	$24 < G < 1022$ kg m^{-2} s^{-1} $0.02 < P_r < 0.8$
Del Col *et al.* (2005)	Analytical, empirical	R-125/236ea (46/54 – 28/72 %) R-22/124 (20/80 – 80/20%) R-290/600 (25/75 – 75/25 %)	Included	7.5, 8	$50 < G < 400$ kg m^{-2} s^{-1} $3.5 < T_{glide} < 22$°C $19 < T_{sat} < 57$°C

2.1.4 <u>Two-phase pressure drop</u>

The condenser in an absorption system works on the high saturation pressure side of the refrigerant similar to its operation in a vapor compression system. The low mass flow rate of refrigerant through the condenser usually leads to relatively small pressure drop, and is usually not a concern. However, a large pressure drop in the condenser would lead to a decrease in the saturation temperature of the refrigerant, negatively impacting heat rejection rates from the condenser. Thus, it is important to characterize and minimize the pressure drop on the tube-side of the condenser.

Pressure drop during condensation can be attributed to major, minor, gravitational, and deceleration components. The major loss component or the frictional pressure drop of the two-phase refrigerant plays a significant role in the overall pressure drop. Prior work on two-phase frictional pressure drop is discussed here.

The frictional pressure drop for two-phase flows is commonly calculated either using a homogenous mixture model or through the application of a two-phase flow multiplier to the corresponding single-phase pressure drop. In a homogenous mixture model, the two phases are assumed to be well mixed and flow with identical velocities. A simple method used by researchers for calculating two-phase flow pressure drop in homogenous flow is by analogy to single-phase flow. A single-phase correlation for friction factor such as the Blasius correlation for turbulent flow (Blasius, 1913) is used, but with the two-phase Reynolds number. The two-phase Reynolds number is similar to the single-phase Reynolds number; however, its calculation requires an appropriate estimate of viscosity of homogenous gas-liquid two-phase mixtures. A widely used correlation for

the homogenous mixture viscosity is provided by McAdams *et al.* (1942) based on liquid and vapor viscosities, and flow quality.

$$\mu_{TP} = \left(\frac{x}{\mu_V} + \frac{1-x}{\mu_L} \right)^{-1}$$

(2.6)

This simple homogenous flow idealization performs reasonably well for well-mixed two-phase flow patterns such as dispersed, bubbly or mist flow. However, its predictions deviate from most experimental data, and empirical correlations that use two-phase flow multipliers remain the most widely used method to predict pressure drop in two-phase flows (Ghiaasiaan, 2007). This concept was originally introduced by Lockhart and Martinelli (1949) and is based on a simple separated flow model. The two-phase multiplier (Φ) is used with single-phase pressure gradient to find the two-phase pressure gradient as shown in Equation (2.7).

$$\left(-\frac{dP}{dz} \right)_{fric,TP} = \Phi_{xx}^2 \left(-\frac{dP}{dz} \right)_{fric,xx}$$

(2.7)

$$xx = \text{L0, V0, L, or V}$$

Here, the right hand side pressure gradient term is single-phase, while subscript *xx* corresponds to the type of single phase. Subscripts L0 and V0 correspond to frictional pressure gradient when the entire mixture is assumed to be liquid and vapor respectively. Whereas the L and V subscripts correspond to the liquid and vapor fraction of the mixture, and the mass flux used for these two cases depends on the local quality of the mixture. Lockhart and Martinelli (1949) assumed that the two-phase multiplier is a function of the Martinelli parameter (*X*). They graphically correlated the two-phase multipliers, Φ_V^2 and

Φ_L^2, as functions of *X*. Simpler algebraic expressions have been proposed by curve-fitting the Lockhart and Martinelli (1949) multipliers while also accounting for interfacial shear forces between the phases (Chisholm and Laird, 1958; Chisholm, 1967). The expressions are shown in Equation (2.8) where the constant C depends on whether the liquid and vapor phases are in laminar or turbulent flow.

$$\Phi_V^2 = 1 + CX + X^2 \quad , \quad \Phi_L^2 = 1 + \frac{C}{X} + \frac{1}{X^2} \qquad (2.8)$$

The most widely used general-purpose correlation based on an extensive data bank for two-phase frictional pressure drop is proposed by Friedel (1979). The multipliers of this correlation are a function of the Weber number, Froude number, single-phase friction factors, and vapor and liquid phase properties. Friedel (1979) proposed separate correlations for horizontal or vertical upward flow and vertical downward flow. Müller-Steinhagen and Heck (1986) compared various empirical correlations for two-phase pressure drop with data for steam-water, R-12, and Argon. They reported that for steam–water, the Friedel (1979) correlation does better than other correlations, with about 40% of the data within a relative error of 30%. Chen *et al.* (2002) collected experimental two-phase frictional pressure drop data from the literature and found that the Friedel (1979) correlation predicted the data fairly well.

2.2   Air-Side Models

This section discusses prior work on air-side heat transfer and pressure drop for the different types of fin-tube arrangements of condensers relevant to this study. The air flows in a cross-flow orientation with respect to the refrigerant inside the tubes for the condensers considered in this work. The tubes are in a staggered arrangement, which improves air-

side heat transfer by mixing and vortex formation. Several studies on air-side heat transfer are available in the literature; however, most of them are limited in application to narrow ranges of fin-tube geometries. Recently, new fin designs have been explored, but there is an absence of studies to model the heat transfer for each fin type. Furthermore, different fin-designs have different dimensions (pitch, height, angle, thickness, etc.,) and most of the available studies are empirical. Therefore, an exhaustive empirical study covering vast ranges for all these dimensions is impractical. Aggressive fin-tube sizing of the condensers used in the present investigation falls outside the range of applicability of most of the correlations. Nevertheless, relevant air-side heat transfer and pressure drop studies are reviewed, and the most accurate correlations are used for condenser modeling.

2.2.1 <u>Round-tube corrugated-fin condenser</u>

For corrugated or herringbone wavy fins, studies have not been able to account for wide ranges of fin densities, fin thicknesses, peak-to-valley pitches, and peak-to-valley depths. The majority of studies have small variations in these dimensions.

Beecher and Fagan (1987) published heat transfer data for 20 herringbone wavy-fin configurations using a test setup that consisted of brass plates machined to the desired fin geometry along with cylindrical spacers inserted between places to simulate the tubes. All the configurations had a staggered three-row arrangement of the tubes. Webb (1990) is one of the first studies to propose a correlation for the herringbone wave fin configuration. The heat transfer correlation is based on the data of Beecher and Fagan (1987), and is limited to only three-row tube configurations. It is represented in form of Nusselt number

based on an arithmetic mean temperature difference (*AMTD*) and Graetz number (*Gz*), which makes application of the correlation difficult.

The correlation by Kim *et al.* (1997) is based on a comprehensive study on corrugated fin-and-tube heat exchangers. The study proposes both air-side heat transfer coefficient and friction factor correlations as functions of flow conditions and geometric variables of the heat exchanger. The correlation includes data from 41 herringbone wavy fin configurations from Beecher (1968), Beecher and Fagan (1987), and Wang *et al.* (1997). It predicts 92% of their heat transfer database within ±10% accuracy. They converted the AMTD based data of Beecher and Fagan (1987) to an LMTD basis for consistency. They then used the Colburn "*j*" factor to predict the heat transfer coefficient.

In a compact, stand-alone absorption system, fans are used to blow air through the condenser. Excessive pressure drop on the air-side would need increased fan power, which would decrease the overall system efficiency. Thus, pressure drop on the air-side plays an important role. The overall pressure loss can be attributed to entrance and exit loss, frictional, and acceleration components. The entrance and exit losses are calculated using appropriate loss coefficients. The acceleration pressure drop is calculated based on the contraction in flow area and increase in velocity of the air. The frictional pressure drop is the major contributor. A widely used method for frictional pressure drop is proposed by Zukauskas and Ulinskas (1983). Various methods for calculating frictional pressure drop have been analyzed by Kays and London (1984), and the difference between the methods are minor. The overall friction factor for calculating the air-side pressure drop consists of a component due to drag force on the tubes and friction from the fins (Zukauskas and Ulinskas, 1983). Kim *et al.* (1997) suggested the use of the tube bank correlation by

Zukauskas and Ulinskas (1983) for the tube drag component of friction factor. For the fin-friction factor, Kim *et al.* (1997) used a multiple regression model from their extensive database. The friction factor correlation predicts 91% of the friction data within ±15%.

2.2.2 <u>Multi-pass tube-array condenser</u>

The first version of the multi-pass tube-array condenser presented in this work does not have any fins and consists of a bank of tubes that are in cross-flow with air. One of the first correlations for a cylinder in cross-flow with air was given by Hilpert (1933). The correlation could be used to estimate air-side heat transfer coefficient for a single tube in cross-flow. In case of a tube bank, the tubes in the first row exhibit heat transfer coefficients similar to those for a single tube in cross-flow. However, the first few rows act as a turbulence generating grid, which increases the heat transfer coefficient of the tubes in the following rows. The flow conditions stabilize after the fourth or fifth row, such that little change in local heat transfer coefficient occurs after fifth row (Incropera *et al.*, 2011). Typically, the average heat transfer coefficient of the entire tube bank is used, because the total heat transfer is the main quantity of interest to heat exchanger designers. Several researchers have studied cross-flow of air in a tube bank and characterized the average heat transfer coefficient of the entire tube bundle for aligned or staggered tube banks.

Grimison (1937) introduced a correlation for average heat transfer coefficient of air in cross-flow across a tube bank. The correlations are based on the maximum velocity, or maximum Reynolds number, in the tube bank. Grimison (1937) recommends a maximum Reynolds number range of 2,000-40,000 for the average heat transfer correlation. For the

condenser under consideration here, the maximum Reynolds number at the design case is lower than the applicable range for this correlation.

A widely used correlation for tube banks has been proposed by Žukauskas (1972). As there could be a large change in air temperature because of its low specific heat, Žukauskas (1972) suggested that the arithmetic mean of inlet and outlet air temperature should be used for the correlation. This correlation for the average heat transfer is only applicable to tube banks with 20 or more rows. For tube banks with rows less than 20, the lower heat transfer coefficient of the first few tube rows need to be considered. To account for that, Žukauskas (1972) added a correction factor to be multiplied to the average Nusselt number of air.

A slightly different method for calculating the heat transfer coefficient of tube banks was proposed by Gnielinski (1978). Gnielinski (1975) proposed that the Nusselt number of single bodies of various shapes can be calculated form the same correlation as that for a flat plate if "streamed length" is used as the characteristic length everywhere. The streamed length (l) is defined by Pasternak and Gauvin (1960) as the total surface area (A) of the body divided by maximum perimeter (L) perpendicular to the flow. The stream length of a single tube in cross flow is defined by Equation (2.9).

$$l = \frac{A}{L} = \frac{\pi\left(d/2\right)L}{L} = \frac{\pi d}{2} \tag{2.9}$$

Using this stream length as the characteristic length for Reynolds and Nusselt numbers, and accounting for the spacing between two adjacent tubes, the heat transfer coefficient for a single row of tubes can be calculated. Gnielinski (1978) then extended the idea to a bank of smooth tubes in cross-flow. An arrangement factor is used for the

staggered tube bank and depends on tube outer diameter, and the longitudinal and transverse spacing between the tubes. The direction of heat flux has an effect on heat transfer coefficient for the case of temperature dependent fluid properties (Hewitt, 1990). Churchill and Brier (1953) suggested a simple ratio as shown in Equation (2.10) to account for heat flux direction in gases.

$$K_G = \left(\frac{T_{air}}{T_{tube,out}} \right)^{0.12} \tag{2.10}$$

The finned multi-pass tube-array condenser that was also investigated in the present study can be considered as a plain fin-and-tube heat exchanger. There are several studies available for plain finned-tube heat exchangers. Gray and Webb (1986) developed heat transfer and friction factor correlations for plain finned-tube heat exchangers based on six data sources (18 heat exchangers overall). The RMS error of the resulting heat transfer correlation compared to data was 7.3%. For the friction correlation, the authors used a superposition model, which assumed that the drag force on the tubes and the fins may be added together. For the friction drag from the tubes, they suggested using the correlation by Zukauskas and Ulinskas (1983). A multiple regression technique was used to match the fin friction data from 18 heat exchangers. The resulting overall friction correlation predicted the data well, with an RMS deviation of 7.8%.

Recent numerical and experimental studies have shown that increasing the diameter of tubes in a finned heat exchanger would not increase the heat transfer coefficient; instead, there would be penalty in friction factor (Torikoshi and Xi, 1995; Jang *et al.*, 1996). Thus, heat exchanger design has started shifting towards small diameter tubes. This approach is also used in the present work, where 3.175 mm tubes are used for the multi-pass tube array

condensers. The parameter transverse spacing of the tubes divided by the diameter (S_t/D) is used to determine applicability of the correlations by Gray and Webb (1986). Experiments were performed by Wang and Chi (1998) on coils with 7 mm tube diameter, which yields an S_t/D=2.88. This particular coil falls outside the range of applicability of Gray and Webb's correlation (1.97< S_t/D< 2.55).

To overcome these shortcomings in the Gray and Webb (1986) correlation, especially for small diameter tubes, Kim *et al.* (1999) proposed new heat transfer and friction factor correlations. The data set consisted of 47 heat exchangers, which included all the sources used by Gray and Webb (1986) and several other experimental studies. All these data are limited to the staggered tube layout, as the multi-row inline configuration yields lower heat transfer coefficients, and is rarely used for heat exchangers. The correlation is developed similar to Gray and Webb (1986), where it is assumed that negligible difference in heat transfer coefficients occurs when there are more than three rows in the heat exchanger. Thus, one correlation for Colburn *j* factor is proposed for all heat exchangers with three or more tube rows. They also suggested a modified correlation for heat exchangers with one or two tube rows. The overall correlation predicts 94% of the heat transfer data within ±20%.

For friction factor of plain finned-tube heat exchangers, Kim *et al.* (1999) pointed out that small diameter tubes would yield high S_t/D that would fall outside the recommended range of the Gray and Webb (1986) correlation. Using the conventional superposition model, the authors proposed correlations for both the tube and fin friction factors. Unlike the previous air-side friction correlations discussed above, for the tube friction factor, Kim *et al.* (1999) suggested use of Jacob (1938) correlation instead of

Zukauskas and Ulinskas (1983). This is because the Zukauskas and Ulinskas (1983) correlation has a higher error when data of Wang and Chi (1998) for small diameter tubes were considered. Kim *et al.* (1999) used a multiple regression technique to develop correlation for the fin friction factor. The overall friction factor correlation, when compared with the dataset of 47 sets of heat exchangers, showed an RMS error of 12.6 % and predicted 90% of the data within ±20%.

Table 2.2 Summary of Air-side Heat Transfer and Pressure Drop Correlations

Author(s) (Year)	Air side Geometry	Correlation Type	Range of Applicability
Grimison (1937)	Tube bank in cross flow	Heat transfer	$2,000 < Re_{D,max} < 40,000$ $Pr = 0.7$
Žukauskas (1972)	Tube bank in cross flow	Heat transfer	$1,000 < Re_{D,max} < 2 \times 10^6$ $0.7 < Pr < 500$
Gray and Webb (1986)	Plain fin-and-tube heat exchanger	Heat transfer, Pressure drop	$500 < \mathrm{Re}_{D,max} < 20000$ $1.82 \le (s_t/D) \le 2.60$ $1.70 \le (s_l/D) \le 2.22$ $0.08 \le (s/D) \le 0.30$ $0.011 \le (t/D) \le 0.032$
Kim et $al.$ (1999)	Plain fin-and-tube heat exchanger	Heat transfer, Pressure drop	$505 < \mathrm{Re}_{D,max} < 19766$ $0.857 \le (s_t/s_l) \le 1.654$ $1.966 \le (s_t/D) \le 2.876$ $0.081 \le (s/D) \le 0.300$
Kim et $al.$ (1997)	Wavy fin-and-tube heat exchanger	Heat transfer, Pressure drop	$500 < \mathrm{Re}_{D,max} < 6,000$ $1.16 \le (s_t/s_l) \le 1.33$ $0.15 \le (s/D_c) \le 0.33$ $3.23 \le (s_{wav,p}/s_{wav,d}) \le 5.65$ $0.29 \le (s_{wav,d}/s) \le 1$

2.3 Air-Coupled Heat Exchanger Studies

Past research efforts have investigated several air-coupled condenser designs for pure fluid applications. Material compatibility, ambient temperature, and concentration variations restrict the use of these condenser designs for the absorption system under consideration in the present study. Condensation of binary mixtures has also been studied in detail by several investigators for various geometries, mixture concentrations, flow rates and orientations, and some of the relevant work is discussed in Section 2.1. Air-side heat transfer and pressure drop in cross-flow coils with various fin geometries have been studied by some researchers, and the relevant work is discussed in section 2.2. However, there are very few studies that combine these two areas to look into air-coupled binary mixture condensation. Garimella and Wicht (1995) developed a model to analyze condensation of ammonia in flat tube, multi-louver fin heat exchangers. In addition to the performance of the air-coupled condenser, the model also calculated the required size of the heat exchanger based on the various tube, fin and louver geometries. Subsequently, Garimella *et al.* (1997) compared the performance of the flat-tube/multi louver fin heat exchanger to conventional round tube heat exchangers with various fin geometries. It was concluded that the use of flat tubes and multi-louvered fins enabled flexibility in heat exchanger design while providing a substantial reduction in size and weight for the same heat duty. However, for the present application of ammonia-water absorption systems, because of the incompatibility of ammonia-water mixtures with Aluminum, considerable manufacturing challenges must be overcome to use such geometries, such as the fabrication of flat multi-port steel tubes and the bonding of aluminum fins to steel tubes.

A study of different tube arrangements and fin types for air-cooled condensation of ammonia-water vapor for small-scale absorption systems was conducted by Garimella and Coleman (1998). The study investigated round-tube heat exchangers of tube diameter 9.525 mm with four commonly used fin-types: flat, wavy, louvered, and annular. The compatibility issue with ammonia-water was addressed by selecting carbon steel as the tube material while aluminum was specified for the fins. Variations in mixture concentration, saturation pressure, and air temperature were investigated to predict the performance of such condensers over a wide range of operating conditions. The study concluded that a round-tube wavy-fin heat exchanger provided the greatest heat transfer within the allowable pressure drop and size constraints. Forinash (2015) performed an experimental study of absorbers for ammonia-water absorption systems and verified the conclusion from Garimella and Coleman (1998), that the round tube heat exchanger with wavy aluminum fins performed best.

Thus, based on the literature, round-tube heat exchangers with aluminum wavy fins may be considered to be the state-of-the-art for ammonia-water condensers. Novel multi-pass tube-array condensers were designed in this study and their performance compared with those from the literature.

2.4   Summary

The above discussion outlines the challenges associated with the design of direct air-coupled components for compact ammonia-water absorption systems. This chapter reviews the tube-side modeling approaches in the literature, which comprises two-phase flow regime, zeotropic mixture condensation, and two-phase pressure drop models.

Correlations for air-side heat transfer and pressure drop for various finned and unfinned geometries are also discussed. Studies on ammonia-water condensers combining these two areas are very few in the literature. The available studies are mostly analytical evaluations of the condensers and require experimental validation.

The present investigation builds upon the work of previous investigators through the modeling and experimental validation of state-of-the-art and novel designs of direct air-coupled condensers for ammonia-water absorption systems. The specific modeling and experimental efforts are described in the following chapters.

CHAPTER 3: MODELING APPROACH

3.1 General Modeling Architecture

A detailed segmented numerical model is developed on the *Engineering Equation Solver* (*EES*) software platform to evaluate the performance of the air-coupled condensers. The modeling approach adopted here divides the heat exchanger into several segments of equal lengths to account for the variation in heat transfer mechanisms as condensation proceeds. The heat and mass transfer processes vary dramatically for fluid undergoing the condensation process; the decrease in void fraction affects the liquid-vapor interface available for heat transfer, and the reduction in shear between the phases increases the internal thermal resistance. In contrast, because of the preferential condensation of water, there is a high mass transfer resistance initially in the condenser. As the concentration in the two phases equalizes along the condensation process, the mass transfer resistance decreases and the overall internal heat transfer increases. Thus, it is important to model these processes accurately, and the segmented model allows this by accounting for changes in thermal resistances along the length of the condenser.

Ammonia-water is a binary mixture; therefore, three independent properties are required to determine the state point after every segment. The ammonia concentration (x_{refr}) in the mixture is constant for all segments, and is used as one of the independent properties. However, the ammonia concentration in the vapor and the liquid phases changes along the length of the condenser. The other two independent properties are the enthalpy (h_{refr}) and pressure (P_{refr}) of the solution, which are updated after every segment based on

the segment heat transfer rate and pressure drop, respectively. Depending on the conditions, subcooling of the refrigerant might occur in the last few segments in the condenser. The properties h_{refr}, P_{refr} and x_{refr} are still used to determine the state of the refrigerant after each segment. However, single phase correlations, instead of two-phase correlations, are used to determine the pressure drop and heat transfer rate in the subcooled segments.

Ammonia-water mixture properties are determined using the procedure outlined by Nagavarapu (2012). Thermodynamic properties (C_p, h, P, q, T, v) are determined using the ammonia-water mixture correlations of Ibrahim and Klein (1993). These correlations rely on the combination of independent pure component properties. Vapor transport properties (D_v, k_v, μ_v, σ_v), are determined from the Chapman-Enskog kinetic theory (Mills, 1999), and the procedure of Wilke (1950) is used to determine the vapor properties of mixture. Liquid transport properties, (k_L, σ_L) are determined from the empirical correlations of Meacham (2002) based on graphical data from Herold *et al.* (1996). For the liquid viscosity (μ_L) of ammonia-water, an empirical correlation for a wide range of temperatures (10°C- 130°C) at all concentrations is developed in the present study based on the same graphical data. Finally, the liquid diffusion coefficient (D_L) is based on an expression from Frank *et al.* (1996) using the concentration and temperature of the solution. A detailed discussion of all ammonia-water property calculations is provided in Nagavarapu (2012). For calculation of reduced pressure (P_r) of the ammonia-water mixture under consideration here, the critical pressure ($P_{crit,refr}$) is approximated as a molar average of the critical pressures of ammonia and water.

$$P_{\text{crit, refr}} = x_{\text{mol,NH}_3} P_{\text{crit,NH}_3} + x_{\text{mol,H}_2\text{O}} P_{\text{crit,H}_2\text{O}} \tag{3.1}$$

Two types of condenser designs are considered: conventional round-tube corrugated-fin air coils with carbon steel tubing, and novel multi-pass tube-array condensers consisting of a dense array of small diameter stainless steel tubes. Both the condenser designs consist of horizontal round tubes rejecting heat to the air in a cross flow configuration. Tube side heat and mass transfer modeling for the conventional and novel multi-pass condensers is similar, with adjustments made for differences in tube size and solution flow pattern. The two designs have very dissimilar air side geometries, however, and that requires different correlations for heat transfer modeling. The air-side heat transfer coefficients are typically averaged over the tube bank, and thus they stay constant for each tube except for changes in air properties due to a change in temperature.

Figure 3.1 shows a sample segment with input and output properties. Within a particular segment, the outlet properties are assumed initially for both air and refrigerant, and the average fluid properties are used in the heat transfer and pressure drop calculations. Iteration allows for the initially assumed outlet properties of the segment to be adjusted such that a solution for all parameters is reached. The calculated outlet conditions of the condensing refrigerant are set as the inlet conditions for the subsequent segment, and the process continues along the length of the heat exchanger. Well mixed solution conditions are assumed such that thermal equilibrium exists between the vapor and the liquid phases in every segment of the condenser. The model also assumes a uniform temperature profile for the inlet air across the face of the condenser. A thermal resistance network is used to calculate the heat transfer in each segment as shown in Figure 3.2.
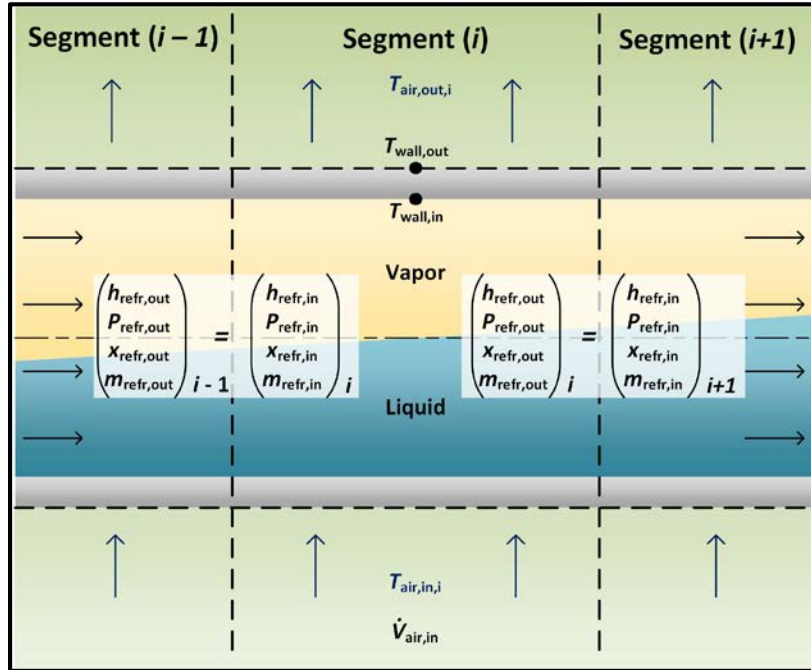
Figure 3.1 Schematic of a condenser segment used in modeling
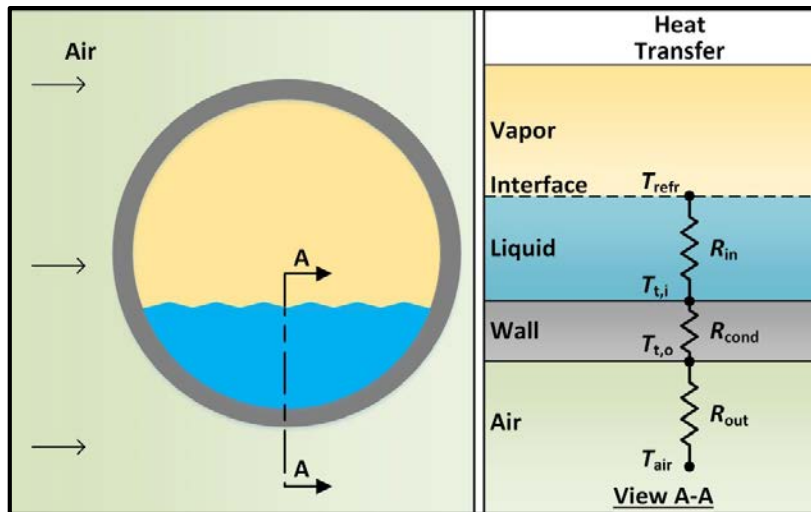
Figure 3.2 Thermal resistance network

The thermal resistance between the air and the refrigerant is composed of internal thermal resistance (with vapor and condensate film components), conductive resistance

46

(inner to outer tube wall), and external resistance (outer tube wall to bulk air). The total

thermal resistance for each segment is calculated using Equation (3.2).

$$\frac{1}{UA} = R_{total} = R_{in} + R_{cond} + R_{out} = \frac{1}{\alpha_{refr}\pi D_i L_{seg}} + \frac{\ln\left(D_o/D_i\right)}{2k_{tube}\pi L_{seg}} + \frac{1}{\eta_o \alpha_{air} A_{out,seg}} \tag{3.2}$$

Inlet refrigerant- and air- side properties are specified for the segment, and the

outlet properties are calculated using the Effectiveness-NTU method. For the corrugated

fin condenser, the effectiveness is calculated using Equation (3.3) because the air is

unmixed and the refrigerant is mixed in the heat exchanger. For the multi-pass tube array

condensers, Equation (3.4) is used because the air and refrigerant are both unmixed

(Incropera *et al.*, 2011). It is observed that the heat capacity of air is always less than the

refrigerant, suggesting Equation (3.5) for the calculation of Number of Transferred Units

(*NTU*).

$$\varepsilon = 1 - \exp\left(-C_r^{-1}\left(1 - \exp(-C_r NTU)\right)\right) \tag{3.3}$$

$$\varepsilon = 1 - \exp\left(\left(\frac{1}{C_r}\right)NTU^{0.22}\left(\exp(-C_r NTU^{0.78}) - 1\right)\right) \tag{3.4}$$

$$NTU = UA \big/ \dot{C}_{min} = UA / \dot{m}_{air,sg} C_{p,air} \tag{3.5}$$

The effectiveness is then used to calculate the heat transfer rate from the segment

using Equation (3.6). Subsequently, the outlet enthalpies of the refrigerant and air are

calculated using the heat transfer rate for the segment.

$$\dot{Q}_{seg} = \varepsilon(\dot{Q}_{max}) = \varepsilon\left(\dot{C}_{min}\left(T_{refr,in} - T_{air,in}\right)\right) \tag{3.6}$$

Unlike condensation of a pure fluid there is a drop in refrigerant temperature in the

saturated region. Due to the high ammonia concentration ($> 99\%$) in the vapor entering the

47

condenser, this temperature glide occurs near the inlet of the condenser where the water fraction is relatively higher (Garimella and Coleman, 1998). Thus, the heat capacity of the refrigerant changes along the length of the condenser and is calculated using Equation (3.7). Both the outlet temperature and the outlet enthalpy of the refrigerant are calculated in the model through iterations.

$$\dot{C}_{refr} = \dot{m}_{refr,seg} Cp_{refr} = \dot{m}_{refr,seg} \left(\frac{h_{refr,out} - h_{refr,in}}{T_{refr,out} - T_{refr,in}} \right) \tag{3.7}$$

The thermal capacity rate of the air is calculated from the mass flow rate of air around the segment ($\dot{m}_{air,seg}$) and specific heat capacity of air ($C_{p,air}$).

$$\dot{C}_{air} = \dot{m}_{air,seg} C_{p,air} \tag{3.8}$$

The $C_{p,air}$ of the air is based on the temperature and pressure conditions upstream of the segment. The $\dot{m}_{air,seg}$ is calculated by dividing the total mass flow rate of air by the number of segments in one row of tubes, as shown in Equation (3.9).

$$\dot{m}_{air,tot} = \rho_{air,in} \dot{V}_{air,in}$$
$$\dot{m}_{air,seg} = \dot{m}_{air,tot} \div \left(\frac{N_{t,row} L_{pass}}{L_{seg}} \right) \tag{3.9}$$

There is negligible change in the temperature of the refrigerant (T_{refr}) after the first few segments. The thermal capacity rate of the refrigerant approaches infinity and the heat capacity ratio (C_r) approaches zero after the initial preferential condensation of water near the inlet of the condenser. For these cases, the calculation of the ε (effectiveness) for the segment is switched to a simpler equation as shown in Equation (3.10). Use of this equation eliminates the need for calculation of Cp_{refr} which helps with the convergence of the model.

$$\varepsilon = 1 - \exp(-NTU) \qquad (3.10)$$

This modeling method is used for both condensers types. Sample calculations for the segmental analyses can be found in Appendix A. The predictions of condensation heat transfer coefficient and pressure drop needed for the model are determined using correlations in the literature. Several factors are considered to determine the appropriate correlation, such as the range of applicability, the breadth of the database, and validation by other studies. The mass flow rate of refrigerant in a small-scale absorption system is typically very low; therefore, only correlations developed for low velocity flows are considered. A detailed discussion of the correlations used for the modeling of both the condenser types is provided in the subsequent sections.

Air velocity plays a major role in the heat transfer and pressure drop correlations. The fins reduce the available air flow area and increase the air velocity at the face when the air enters the coil. The face air velocity is obtained by dividing the volumetric flow rate of air ($\dot{V}_{air}$) by the available area, as shown in Equation (3.11).

$$u_{air,face} = \frac{\dot{V}_{air}}{H_{face}(L_{pass} - N_{fin}t_{fin})} = \frac{\dot{V}_{air}}{H_{face}(L_{pass} - \dfrac{L_{pass}}{p_{fin}}t_{fin})} \qquad (3.11)$$

However, most of the correlations require the maximum velocity of air occurring within the coil. The location of this maximum velocity can either be in the transverse plane (A_t) or in the diagonal plane (A_d) for staggered arrangement of tubes as shown in Figure 3.3. Incropera *et al.* (2011) recommend a simple way to determine the location of this maximum velocity based on the geometry. Based on the tube spacing for Condenser R.1

and Condenser R.2, the maximum velocity occurs at plane A_t both the condensers, according to Equation (3.12).

$$s_d = \sqrt{s_l^2 + \left(\frac{s_t}{2}\right)^2} > \frac{s_t + D_c}{2} \qquad (3.12)$$

Knowing that maximum air velocity ($u_{air,\max}$) occurs at the plane A_t, it can be calculated using Equation (3.13). The maximum Reynolds number ($\mathrm{Re}_{D,\max}$), used in most of the air-side correlations, can now be obtained using $u_{air,\max}$ as the velocity in Equation (3.14).

$$u_{air,\max} = \frac{s_t}{s_t - D_c} u_{air,face} \qquad (3.13)$$

$$\mathrm{Re}_{D,\max} = \frac{\rho_{air} u_{air,\max} D_c}{\mu_{air}} \qquad (3.14)$$
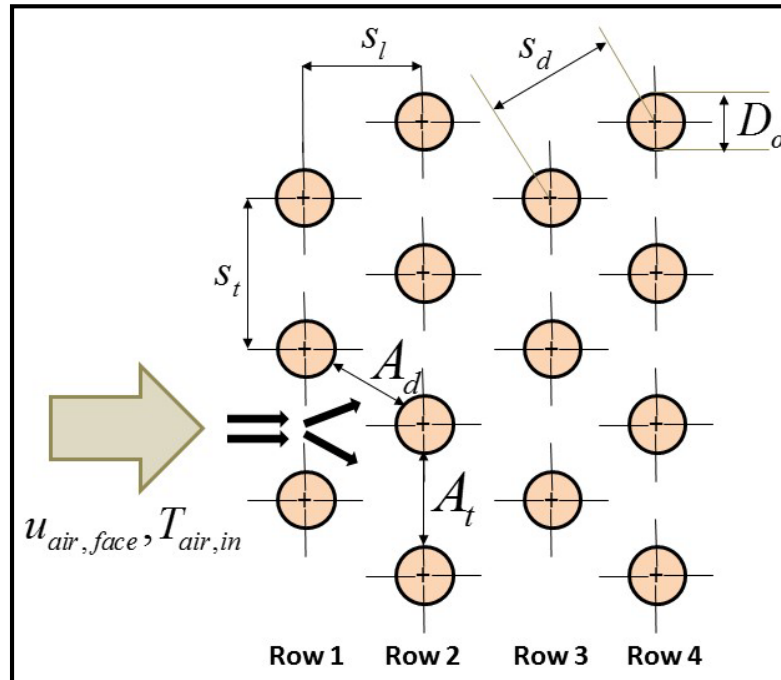
Figure 3.3 Staggered tube bank arrangement (Incropera *et al.*, 2011)

The air-side heat transfer and pressure-drop correlations used here account for the number of tube rows, lateral and transverse tube spacing, fin spacing, wavy fin pattern, and the staggered arrangement of tube rows. However, the analysis does not address the increase in inlet air temperature for the second row resulting from the heat transfer from the first tube row. The first row of tubes is exposed to unheated inlet air at 51.7°C for the design case. The outlet air from upstream tube and finned surfaces is expected to mix with fresh unheated air flowing in between the tubes of the first row (Figure 3.4). This mixing of heated and unheated air will result in higher inlet air temperatures for the second tube row.

Due to the serpentine flow of refrigerant in the round-tube corrugated fin condensers, the air temperature in the core is expected to vary laterally and vertically across

51

the face area. Thus, an accurate prediction of the inlet air temperature of a particular segment in the rear row requires an estimation of the outlet air temperatures from the upstream tube row. As an approximation, it is assumed that the inlet air temperature to a segment in the rear row is the outlet temperature from the segment in the previous (frontal) pass at the same lateral position. This assumption is explained in Figure 3.4 for four sample segments.
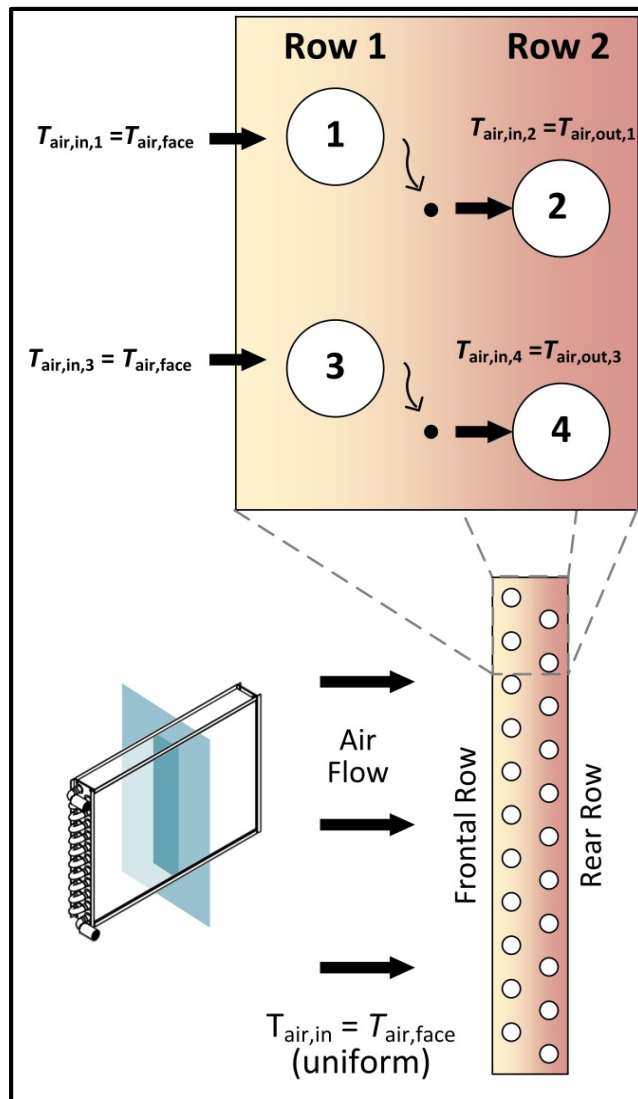
Figure 3.4 Tube arrangement schematic showing modeling approach of air temperature variation

Calculation of the heat transfer coefficient for air is not enough to determine external thermal resistance in presence of fins. Although fins increase the effective surface area, the fin itself represents a conduction resistance to the heat transfer from the surface of the tubes (Incropera *et al.*, 2011). To quantify the thermal performance of the fins, a fin efficiency (η_{fin}) is used. Fin efficiency for several finned-tube heat exchangers can be approximated using an annular fin idealization around a tube, as shown in Figure 3.5. The effective annular fin radius is determined such that the area of the fin around the tube is maintained the same as for the actual rectangular segment of the fin under consideration.
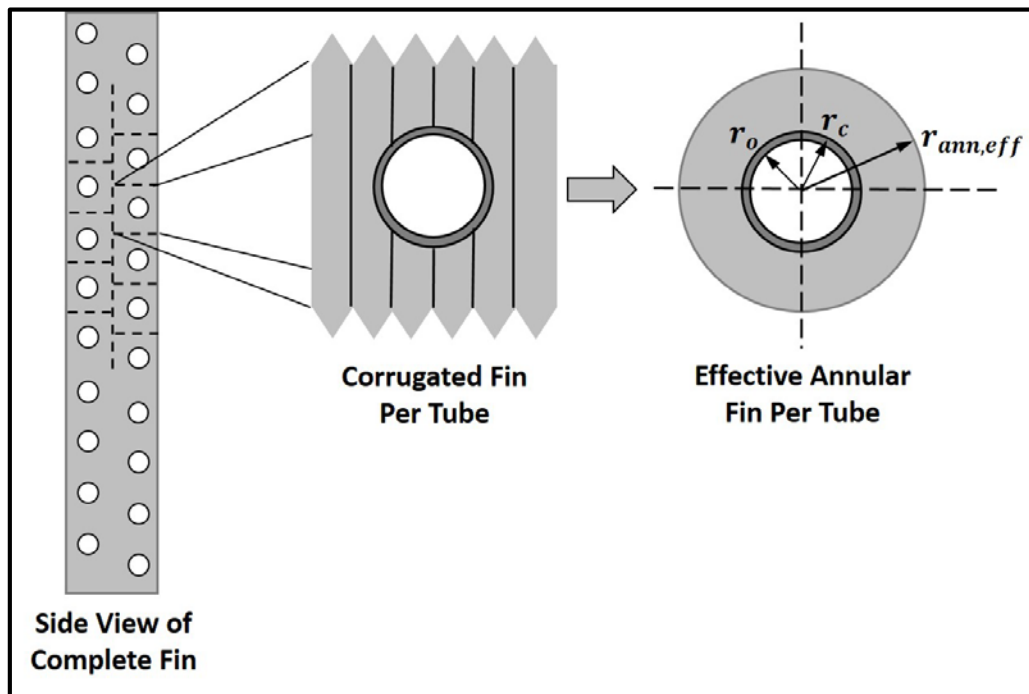
Figure 3.5 Approximation as an annular fin

For a single corrugated fin in the condenser, the fin area is calculated using Equation (3.15). This equation is derived by accounting for the surface area of the waves, subtracting the area of the holes for the tubes passing through the fin, and multiplying the

53

whole expression by two to account for both sides of the fin. For subsequent calculations, total air-side heat transfer area (A_{tot}) is calculated, which involves both total fin area ($A_{fin,tot}$) and total un-finned area ($A_{unfin,tot}$). The $A_{unfin,tot}$ represents the tube outer area exposed to the air in crossflow and is calculated as shown in Equation (3.17) . The tube outer area is covered by the collar from the fin, therefore the collar outer diameter (D_c) is used instead of tube OD (D_o) for the air-side calculations.

$$A_{fin} = 2\left(H_{fin}\left(\frac{W_{fin}}{s_{wav,p}}\right)\sqrt{s_{wav,p}^2 + s_{wav,p}^2} - N_{pass}\left(\pi\frac{D_c^2}{4}\right)\right) \tag{3.15}$$

$$A_{fin,tot} = N_{fin}A_{fin} = \frac{L_{pass}}{p_{fin}}A_{fin} \tag{3.16}$$

$$A_{unfin,tot} = \pi D_c\left(L_{tot} - N_t\left(N_{fin}t_{fin}\right)\right) = \pi D_c\left(N_t L_{pass} - N_{pass}\left(\frac{L_{pass}}{p_{fin}}t_{fin}\right)\right) \tag{3.17}$$

$$A_{tot} = A_{fin,tot} + A_{unfin,tot} \tag{3.18}$$

As the tubes in the condenser pass through all the fins, a single fin is shared by the all the tubes (N_{pass}) of the condenser. The area of the single corrugated fin per tube is equated with a single annular fin with the effective diameter ($D_{ann,eff}$) calculated as follows.

$$\frac{A_{fin}}{N_{pass}} = 2\left(\pi\frac{D_{ann,eff}^2 - D_c^2}{4}\right) \tag{3.19}$$

The fin efficiency for an annular fin is given by Incropera *et al.* (2011) and is described below. The effective outer radius ($r_{ann,eff}$) and the inner radius (r_c) of the annular

fin along with air-side heat transfer coefficient (α_{air}), fin material thermal conductivity (k_{fin}), and fin thickness (t_{fin}) are used to calculate the fin efficiency.

$$m_{fin} = \sqrt{\frac{2\alpha_{air}}{k_{fin}t_{fin}}} \tag{3.20}$$

$$C_2 = \frac{2m_{fin}r_c}{\left(m_{fin}r_{ann,eff}\right)^2 - \left(m_{fin}r_c\right)^2} \tag{3.21}$$

$$\eta_{fin} = C_2 \frac{K_1\left(m_{fin}r_c\right)I_1\left(m_{fin}r_{ann,eff}\right) - I_1\left(m_{fin}r_c\right)K_1\left(m_{fin}r_{ann,eff}\right)}{I_0\left(m_{fin}r_c\right)K_1\left(m_{fin}r_{ann,eff}\right) - K_0\left(m_{fin}r_c\right)I_1\left(m_{fin}r_{ann,eff}\right)} \tag{3.22}$$

I, K: Modified Bessel functions

As the heat transfer analysis is performed for a segment and one segment may include multiple fins, it is important to determine the overall fin efficiency for all the fins on the segment. To find the segmental area, first the total area for the condenser is calculated and divided by the total number of segments. The total number of segments is calculated as shown in Equation (3.23), where the total length of the tube in the condenser is divided by the length of one segment.

$$N_{seg,tot} = \frac{L_{tot}}{L_{seg}} = \frac{N_{pass}L_{pass}}{L_{seg}} \tag{3.23}$$

$$A_{out,seg} = \frac{A_{fin,seg} + A_{unfin,seg}}{N_{seg,tot}} \tag{3.24}$$

Overall fin efficiency for the segment is a function of the segmental areas and a single fin efficiency (Incropera *et al.*, 2011).

$$\eta_0 = 1 - \left(\frac{A_{fin,seg}}{A_{tot,seg}}\right)\left(1 - \eta_{fin}\right) \tag{3.25}$$

A grid refinement analysis is used to determine the appropriate number of segments to ensure computational efficiency without significantly reducing modeling accuracy. The segment length is increased starting at 0.025 m, and the total heat transfer rate and pressure drop are calculated. The results are compared to the value obtained from the model using the smallest segment length (0.025 m). Figure 2.3 shows the percent deviation of both the total heat transfer rate and pressure drop as a function of segment length for round-tube, corrugated-fin condensers. The error in heat transfer rate is about an order of magnitude lower than that in pressure drop. Based on this kind of grid independent study, the appropriate segment length is chosen for each condenser type to minimize model complexity without compromising on the accuracy. The segment lengths are discussed in the respective sections of the heat exchanger.
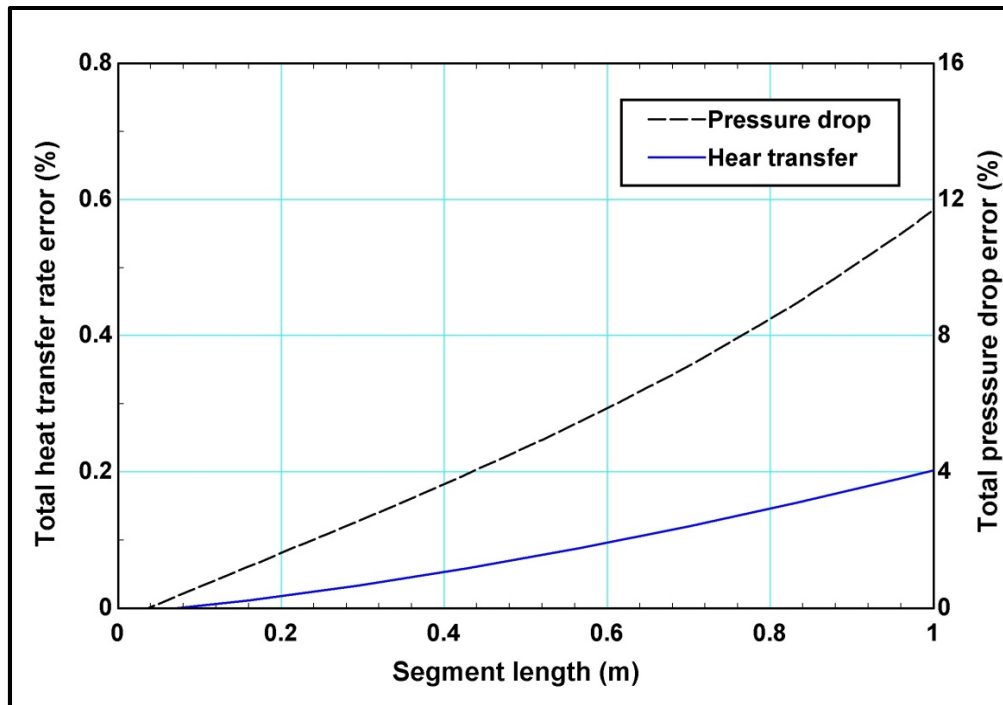
Figure 3.6 Deviation in predicted total heat transfer rate (left axis) and pressure drop (right axis)

56

3.2 Round-Tube Corrugated-Fin Condenser

Two conventional round-tube corrugated-fin air-coils (Condenser R.1 and Condenser R.2) are modeled to determine the most compact and efficient condenser design for use in the ammonia-water absorption system discussed in the Cycle Modeling section. The coils consists of a single tube that has an inlet at the top and makes staggered passes in a serpentine pattern over the air flow area to the outlet at the bottom (Figure 3.7). Thus, the refrigerant mixture is not divided into multiple paths and remains contained in a single tube. The total number of passes (N_{pass}) by this serpentine tube are distributed equally over two rows with tight U-bends at the end of each pass. The detailed design of the conventional condensers along with the variables used for modeling is illustrated in Figure 3.7. Corrugated or wavy fins with collars are press-fitted onto the tubes at a specified spacing. The round-tube corrugated-fin condensers investigated here are determined to be the most efficient and compact conventional air coils that fit within the space and weight constraints of a small-scale absorption system. Corrugated fins are selected based on the work by Garimella and Coleman (1998) in which wavy (i.e., corrugated) fins are predicted to transfer more heat than plain, lanced, and annular fins for ammonia-water applications without excessive pressure drop penalty. The segmental models are used to determine various geometric features (tube diameter, tube length, fin density). The selected dimensions of the tube-side and air-side geometry for both Condenser R.1 and Condenser R.2 are outlined in Table 3.1 and Table 3.2 respectively. A detailed discussion of the fabrication of both the condensers is provided in the next chapter.
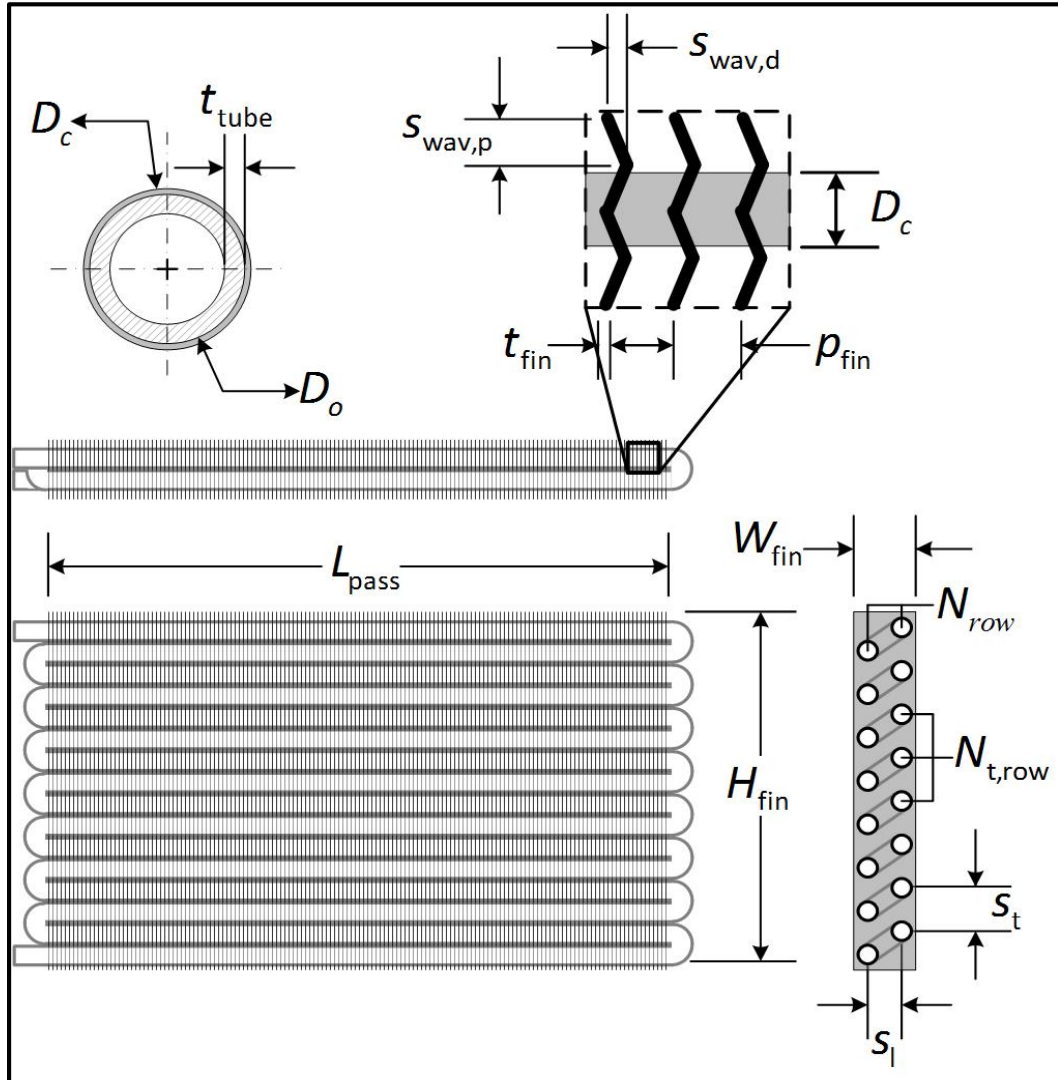
Figure 3.7 Schematic of conventional round-tube corrugated-fin condensers

Table 3.1 Round-tube corrugated-fin condenser tube-side dimensions

Tube-Side Geometry		
Dimensions	**Condenser R.1**	**Condenser R.2**
L_{seg} (m)	0.127	0.127
D_o (m)	1.59×10^{-2}	9.53×10^{-3}
t_{tube} (m)	1.25×10^{-3}	8.89×10^{-4}
L_{pass} (m)	0.508	0.508
N_{row} (-)	2	2
$N_{t,row}$ (-)	8	14
N_{pass} (-)	16	28
s_t (m)	0.038	0.025
s_l (m)	0.033	0.022
ε_{rough} (m)	1.0×10^{-5}	1.0×10^{-5}
Tube material	Carbon steel	Carbon steel

Table 3.2 Round tube corrugated fin condenser air-side dimensions

Air-Side Geometry		
Dimensions	**Condenser R.1**	**Condenser R.2**
$H_{\text{fin}}\,(\text{m})$	0.305	0.356
$W_{\text{fin}}\,(\text{m})$	0.066	0.044
$t_{\text{fin}}\,(\text{m})$	2.41×10^{-4}	1.91×10^{-4}
$p_{\text{fin}}\,(\text{m})$	2.54×10^{-3}	1.81×10^{-3}
$s_{\text{wav,d}}\,(\text{m})$	2.16×10^{-3}	1.57×10^{-3}
$s_{\text{wav,p}}\,(\text{m})$	8.20×10^{-3}	5.51×10^{-3}
$D_{c}\,(m)$	1.64×10^{-2}	9.88×10^{-3}
Arrangement	Staggered	Staggered
Fin material	Aluminum	Aluminum

3.2.1 <u>Tube side modeling</u>

3.2.1.1 Flow regime

The round tube condensers have a single tube, and thus the mass flux of refrigerant throughout the condenser remains the same. Soliman (1982) derived a criterion for the transition between wavy and annular flow regime using the modified Froude number. For liquid Reynolds number lower than 1250, the modified Froude number (Fr^{*}) is a function of the Galileo number (Ga) and Martinelli parameter (X_{tt}) as shown in Equation (3.26). The

Galileo number and the Martinelli parameter are defined by Equation (3.27) and Equation (3.28).

$$Fr^* = 0.025\,\mathrm{Re}_L^{1.59}\left(\frac{1+1.09X_{tt}^{0.039}}{X_{tt}}\right)^{1.5}\frac{1}{\sqrt{Ga}} \tag{3.26}$$

$$Ga = \frac{\rho_L(\Delta\rho)gD_i^3}{\mu_L^2} \tag{3.27}$$

$$X_{tt} = \left(\frac{\rho_V}{\rho_L}\right)^{0.5}\left(\frac{\mu_L}{\mu_V}\right)^{0.1}\left(\frac{1-q_{refr}}{q_{refr}}\right)^{0.9} \tag{3.28}$$

It was proposed by Soliman (1982) that if Fr^* of the flow is smaller than seven, a wavy flow regime exists, otherwise annular two-phase flow prevails. The test conditions for the round-tube corrugated-fin condensers result in $Fr^* < 7$, indicating the wavy flow regime. However, wavy flow defined by Soliman also includes both slug and stratified wavy flow. The flow pattern map by El Hajal *et al.* (2003) is finally used to assign a more definitive solution for flow regime. Their study divided the gravity-controlled stratified flow regime further into fully stratified and stratified wavy flows based on G_{wavy} and G_{strat}. El Hajal *et al.* (2003) introduced geometrical dimensions for stratified flow in a round tube, shown in Figure 3.8. P_L corresponds to liquid wetted perimeter and h_L corresponds to the height of the liquid pool at the bottom of the tube. A_i is the inner cross-sectional area of the tube. A_L and A_V are corresponding cross-sectional areas occupied by liquid and vapor respectively. These cross-sectional areas are based on the void fraction (*VF*) of the two-phase flow and are defined by Equation (3.29) and Equation (3.30). The void fraction

correlation suggested by El Hajal *et al.* (2003) , discussed in the literature review chapter, is used in the determination of flow regime and subsequent heat transfer calculations.

$$A_L = A_i \left(1 - VF\right) \tag{3.29}$$

$$A_V = A_i (VF) \tag{3.30}$$
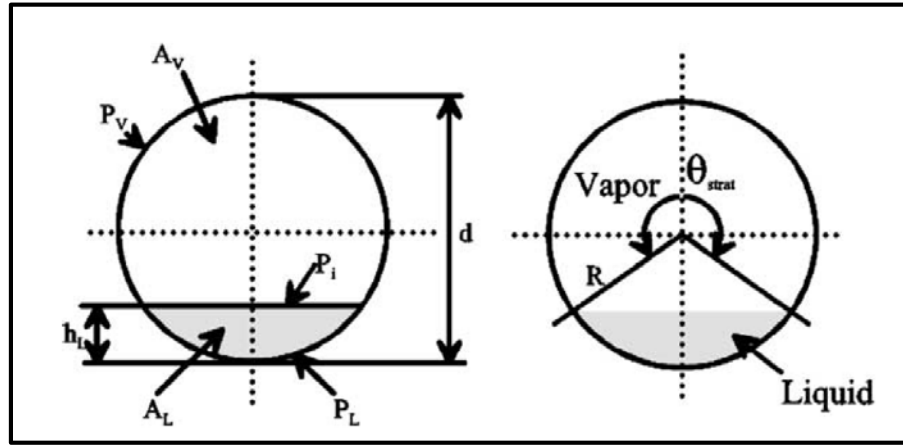
Figure 3.8 Geometrical parameters for stratified flow in a round tube
(El Hajal *et al.*, 2003)

These cross-sectional areas are further normalized using the tube internal diameter.

$$A_{LD} = \frac{A_L}{D_i^2}; \quad A_{VD} = \frac{A_V}{D_i^2} \tag{3.31}$$

The dimensionless liquid height is derived from the geometric expression in Equation (3.32). Although their study suggests calculation of the stratified angle (θ_{strat}) using iteration, an explicit correlation for this angle has been suggested by Biberg (1999) and is shown in Equation (3.33). This explicit equation is very accurate, with an error $\approx$ 0.00005 rad, and reduces iterations and complexity.

$$h_{LD} = \frac{h_L}{D_i} = 0.5 \left(1 - \cos\left(\frac{2\pi - \theta_{strat}}{2}\right)\right) \tag{3.32}$$

$$\theta_{strat} = 2\pi - 2 \left\{ \begin{array}{l} \pi(1-VF) + (1.5\pi)^{1/3} \left[1 - 2(1-VF) + (1-VF)^{1/3} - VF^{1/3} \right] \\ -0.005(1-VF)VF \left[1 - 2(1-VF) \right] \left[1 + 4 \left((1-VF)^2 + VF^2 \right) \right] \end{array} \right\} \quad (3.33)$$

The transition from annular to stratified flow-regime is governed by the plot of G_{wavy} as a function of vapor quality. The plot of G_{strat} controls the transition between fully-stratified and stratified-wavy. El Hajal *et al.* (2003) define the curves of G_{wavy} and G_{strat} as a function of the vapor quality (q_{refr}) using Equation (3.34) and Equation (3.36). The ratio of Weber number to Froude number used in the $G_{wavy,1}$ calculation is defined in Equation (3.35).

$$G_{wavy,1} = \left[\frac{16 A_{VD}^3 g D_i \rho_L \rho_V}{q_{refr}^2 \pi^2 \left(1 - (2h_{LD} - 1)^2 \right)^{0.5}} \left(\frac{\pi^2}{25 h_{LD}^2} \left(\frac{We}{Fr} \right)^{-1.023} + 1 \right) \right]^{0.5}$$

$$G_{wavy,2} = 50 - 75 \exp \left(\frac{-\left(q_{refr}^2 - 0.97 \right)^2}{q_{refr} \left(1 - q_{refr} \right)} \right) \quad (3.34)$$

$$G_{wavy} = G_{wavy,1} + G_{wavy,2}$$

$$\frac{We}{Fr} = \frac{g D_i^2 \rho_L}{\sigma_L} \quad (3.35)$$

$$G_{strat} = \left[\frac{(226.3)^2 A_{LD} A_{VD}^2 \rho_V \left(\rho_L - \rho_V \right) \mu_L g}{q_{refr}^2 \left(q_{refr} - 1 \right) \pi^3} \right] + 20 q_{refr} \quad (3.36)$$

These transition equations are used along the length of the condenser with decreasing vapor quality to determine the applicable flow regime for each segment.
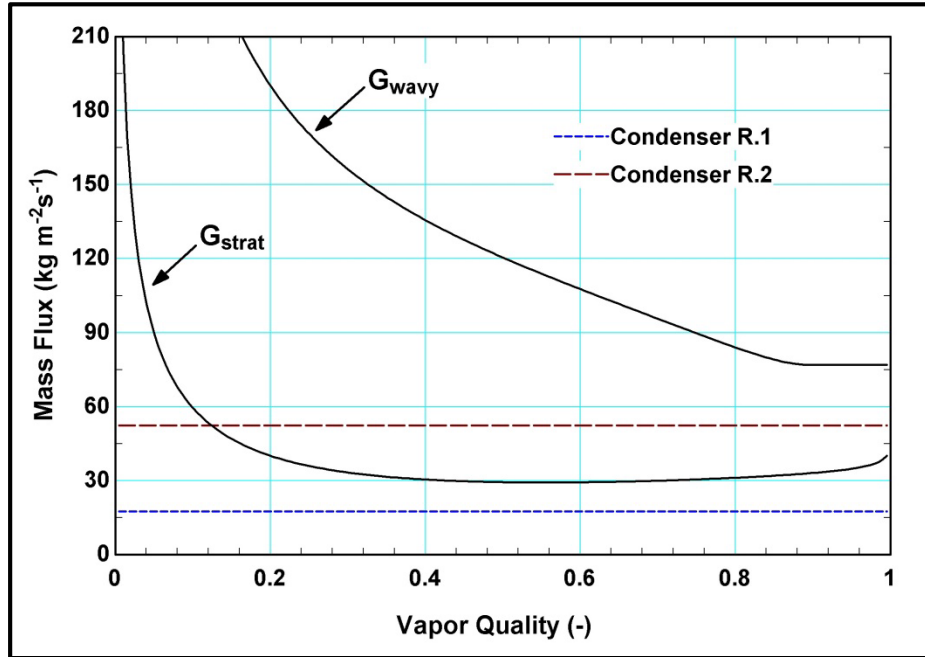
Figure 3.9 Two-phase flow regime in conventional condensers

The mass flux in these conventional condensers is constant throughout the condensation process. According to the flow regime map of El Hajal *et al.* (2003), shown in Figure 3.9, the mass flux in Condenser R.1 is always below G_{strat} at the design condition and thus a fully stratified flow exists. As seen from Figure 3.9, Condenser R.2 has stratified wavy flow in the beginning and fully stratified flow at lower qualities. Although Condenser R.2 has a higher mass flux, a stratified flow prevails at the design mass flow rate. Therefore, heat transfer correlations pertinent to stratified flow regime are applied for modeling both the conventional round-tube corrugated-fin condensers.

3.2.1.2 Heat transfer

Heat transfer is calculated in every segment of the condenser to determine the outlet state of the refrigerant. The flow regime based stratified-wavy correlation of Dobson and

Chato (1998) is applicable at very low flow rates. The correlation for Nusselt number based on the tube diameter for stratified-wavy flow is shown in Equation (3.37).

$$Nu_D = \frac{0.23 \mathrm{Re}_V^{0.12}}{1+1.11 X_{tt}^{0.58}} \left(\frac{Ga\, Pr_L}{Ja_L} \right)^{0.25} + \left(1 - \frac{\theta_L}{\pi} \right) Nu_{forced} \tag{3.37}$$

Here, Pr_L and Ja_L represent liquid Prandtl number and Jacob number, and their ratio is calculated separately in the model as shown in Equation (3.38). The fluid properties (k_L, μ_L, μ_V, Pr_L) are calculated at the average conditions across the segment, determined through iteration. This ratio requires the temperature of the inside surface of the tube ($T_{tube,in}$), which is calculated iteratively.

$$\frac{Pr_L}{Ja_L} = \frac{Cp_L \mu_L / k_L}{Cp_L (T_{refr} - T_{tube,in}) / h_{fg}} = \frac{\mu_L h_{fg}}{k_L (T_{refr} - T_{tube,in})} \tag{3.38}$$

Here θ_L is the angle subtended from the top of the tube to the liquid level at the bottom. The angle can be approximated from the void fraction by an explicit correlation suggested by Jaster and Kosky (1976), as shown in Equation (3.39).

$$\theta_L \cong \pi - \arccos(2VF - 1) \tag{3.39}$$

Heat transfer through the liquid pool at the bottom of the tube is accounted for in Equation (3.37). The forced convection Nusselt number is given by Equation (3.40).

$$Nu_{forced} = 0.0195 \mathrm{Re}_L^{0.8} Pr_L^{0.4} \sqrt{1.376 + \frac{C_1}{X_{tt}^{C_2}}} \tag{3.40}$$

The coefficients C_1 and C_2 in the equation depend on the all-liquid Froude number (Fr_{l0}).

For $0 < Fr_{L0} < 0.7$,

$$C_1 = 4.172 + 5.48 Fr_{L0} - 1.564 Fr_{L0}^2$$
$$C_2 = 1.773 - 0.169 Fr_{L0}$$
(3.41)

For $Fr_{L0} > 0.7$,

$$C_1 = 7.242$$
$$C_2 = 1.655$$
(3.42)

The above correlation matches the Dittus and Boelter (1930) single-phase correlation when the vapor quality reaches zero.

An important thing to note is both the Shah (2009) and Dobson and Chato (1998) correlations are only valid for pure fluid applications. Thus the heat transfer coefficients predicted through these correlations do not take into account the mixture mass transfer effects. The concentration of ammonia in the vapor is higher near the liquid-vapor interface than in the bulk vapor flow due to the preferential condensation of water, the less volatile component. This results in a concentration gradient in the vapor, which builds a mass transfer resistance that impedes the condensation process. The equilibrium (SBG) model is used to modify the pure fluid heat transfer coefficient to account for mixture mass transfer resistance (Silver, 1947; Bell and Ghaly, 1973). For zeotropic mixtures, there is a drop in equilibrium temperature during condensation. The heat transfer in any given segment is a combination of the sensible heat removed from the vapor and the liquid pool, and the latent heat removed because of condensation.

$$d\dot{Q}_{total} = d\dot{Q}_{liquid} + d\dot{Q}_{vapor} + d\dot{Q}_{latent}$$
(3.43)

According to Hewitt *et al.* (1994), one of the main assumptions of using the SBG method is that all the heat is transferred from the liquid-vapor interface to the coolant, which is air in this case. The total heat transfer can be written in terms of the interface

66

temperature (T_i) and air temperature (T_{air}) along with an overall heat transfer coefficient (U).

$$dQ_{total} = U\left(T_i - T_{air}\right)dA \tag{3.44}$$

Due to preferential condensation of water, there is concentration gradient near the interface, which lowers the interface temperature (T_i). As the method is an equilibrium method, the bulk vapor is assumed to be at equilibrium temperature (T_E), and sensible heat transfer from the vapor can be approximated using Equation (3.45).

$$dQ_{vapor} = \alpha_v\left(T_E - T_i\right)dA \tag{3.45}$$

$$\alpha_V = 0.023 k_V \operatorname{Re}_V^{0.8} \operatorname{Pr}_V^{0.33} D_i^{-1} \tag{3.46}$$

The Dittus and Boelter (1930) single-phase correlation is used to calculate the vapor heat transfer coefficient (α_v) and is shown in Equation (3.46). Equation (3.45) can be re-written to find the unknown interface temperature.

$$T_i = T_E - \frac{1}{\alpha_v}\frac{dQ_{vapor}}{dA} \tag{3.47}$$

Substituting Equation (3.47) into Equation (3.44)

$$dQ_{total} = U\left(T_E - \frac{1}{\alpha_v}\left(\frac{dQ_{vapor}}{dA}\right) - T_{air}\right)dA \tag{3.48}$$

The ratio of the sensible heat transfer from the vapor to the total heat transfer is termed Z and is calculated for a particular segment using Equation (3.49).

$$Z = \frac{dQ_{vapor}}{dQ_{total}} = \frac{q_{refr}\left(T_{refr,in} - T_{refr,out}\right)Cp_V}{\left(h_{refr,in} - h_{refr,out}\right)} \tag{3.49}$$

Substituting the term Z in Equation (3.48),

$$dQ_{total} = U\left(T_E - \frac{Z}{\alpha_V}\left(\frac{dQ_{total}}{dA}\right) - T_{air}\right)dA \tag{3.50}$$

Thus the total heat transfer can be expressed as shown in Equation (3.51).

$$dQ_{total} = \frac{UdA\left(T_E - T_{air}\right)}{\left(1 + U\dfrac{Z}{\alpha_V}\right)} = \frac{\left(T_E - T_{air}\right)dA}{\left(\dfrac{1}{U} + \dfrac{Z}{\alpha_V}\right)} \tag{3.51}$$

The overall heat transfer coefficient (U) is substituted from the thermal

resistance network shown in Equation (3.2).

$$dQ_{total} = \frac{\left(T_E - T_{air}\right)dA}{\left(\dfrac{1}{\alpha_{air}} + \dfrac{1}{\alpha_{cond}} + \dfrac{1}{\alpha_{refr}} + \dfrac{Z}{\alpha_V}\right)} \tag{3.52}$$

Using the SBG model, the apparent tube-side heat transfer coefficient ($\alpha_{refr,app}$) is

defined as shown in Equation (3.53).

$$dQ_{total} = \frac{\left(T_E - T_{air}\right)dA}{\left(\dfrac{1}{\alpha_{air}} + \dfrac{1}{\alpha_{cond}} + \dfrac{1}{\alpha_{refr,app}}\right)}; \quad \frac{1}{\alpha_{refr,app}} = \frac{1}{\alpha_{refr}} + \frac{Z}{\alpha_V} \tag{3.53}$$

For a particular segment, the apparent heat transfer coefficient is dependent on the

pure fluid heat transfer coefficient (α_{refr}) and the vapor phase heat transfer coefficient

(α_V). The argument provided by Bell and Ghaly (1973) is that using the single-phase vapor

heat transfer coefficient would result in a significant under prediction, which will mimic

the additional thermal resistance from mixture mass transfer effects. The study of Del Col

et al. (2005) proposed a simplified heat transfer model based on flow regime for zeotropic

mixture condensation in horizontal tubes. The equilibrium SBG approach is modified and

applied based on the prevailing two-phase flow regime. For the stratified flow condition in

the present study, the study proposed a method to apply the SBG model separately to the

pool and the film. The simplified flow structures proposed by Thome *et al.* (2003) for pure

fluid condensation were used to calculate the heat transfer and interfacial area associated

with each flow regime. For the fully stratified condition, the actual geometry and the

equivalent simplified geometry are shown in Figure 3.10.
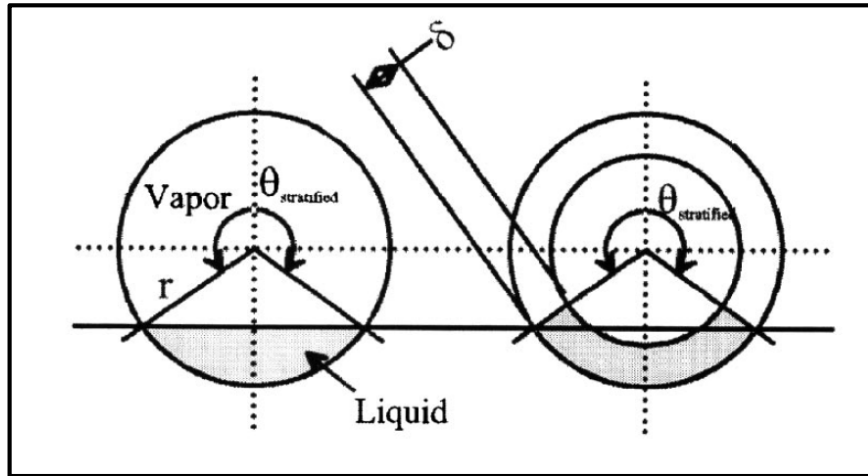
**Figure 3.10 Actual geometry (left) and simplified geometry (right) for
fully-stratified flow in horizontal tube (Thome *et al.*, 2003)**

In this simplified geometry, the liquid pool is distributed as a truncated annular ring

of uniform thickness (δ) and subtends an angle $\left(2\pi - \theta_{strat}\right)$. The top perimeter of the tube

subtending an angle $\left(\theta_{strat}\right)$ has a condensing film falling downward due to gravity. The

θ_{strat} is defined explicitly by Biberg (1999) and was shown in Equation (3.33). In the model,

two heat transfer mechanisms of convective condensation and falling-film condensation

are applied to their respective areas.
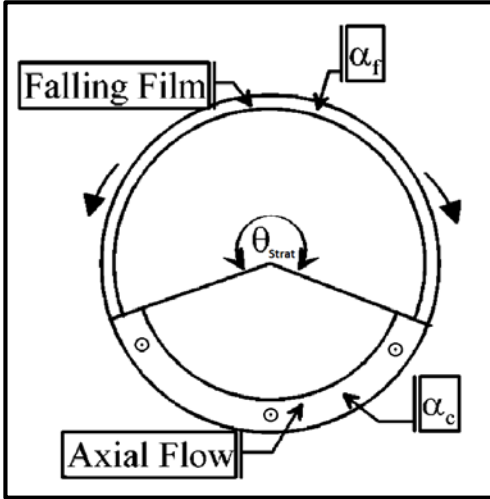
Figure 3.11 Schematic of convective axial flow and falling film in horizontal tube condensation (Thome *et al.*, 2003)

A convective heat transfer coefficient (α_c) was proposed by Thome *et al.* (2003) for the axial flow at the bottom of the tube and is shown in Equation (3.54).

$$\alpha_c = 0.003 \, \mathrm{Re}_L^{0.74} \, \mathrm{Pr}_L^{0.5} \frac{k_L}{\delta} \tag{3.54}$$

A different liquid-phase Reynolds number (Re_L) suggested by Thome et al. (2003) is used in Equation (3.54). Here the Re_L is based on mean liquid velocity of the axially flowing pool and is calculated using Equation (3.55).

$$\mathrm{Re}_L = \frac{4 G_{refr} \left(1 - q_{refr}\right) \delta}{\left(1 - VF\right) \mu_L} \tag{3.55}$$

The thickness of the liquid in axial flow (δ) is obtained by solving Equation (3.56), which is formed by geometrically analyzing the truncated annular ring. The liquid cross-sectional area (A_L) is defined in Equation (3.29).

$$A_L = \frac{2\pi - \theta_{strat}}{8} \left(D_i^2 - (D_i - 2\delta)^2 \right) \tag{3.56}$$

70

When the liquid occupies more than half of the cross-section of the tube in stratified flow, the above expression will yield a value of $\delta > D_i / 2$, which is not geometrically realistic. As suggested by the them, at low vapor qualities when $\delta > D_i / 2$, the thickness is set to $\delta = D_i / 2$.

The film condensation heat transfer coefficient $\left(\alpha_f\right)$ for the falling film at the upper perimeter of the tube used here is also suggested by Thome *et al.* (2003) as shown in Equation (3.57). Similar to the correlation of Dobson and Chato (1998), the inside surface temperature of the tube is solved iteratively for this correlation.

$$\alpha_f = 0.728\left(\frac{\rho_l(\rho_l - \rho_v)gh_{fg}k_L^{\ 3}}{\mu_L D_i (T_{refr} - T_{tube,in})}\right)^{1/4} \tag{3.57}$$

The method of Del Col *et al.* (2005) is followed, where both the convective $\left(\alpha_c\right)$ and film condensation $\left(\alpha_f\right)$ heat transfer coefficients are modified for zeotropic mixtures using the SBG method. Initially, the liquid pool has a low ammonia concentration and consists primarily of water. As the fluid moves through the heat exchanger, the ammonia condenses, thereby increasing the concentration of the liquid phase. The mixture convective heat transfer coefficient ($\alpha_{c,m}$) is defined in Equation (3.58). The term Z is the ratio of sensible heat transfer to the total heat transfer as shown in Equation (3.49).

$$\alpha_{c,m} = \left(\frac{1}{\alpha_c} + \frac{Z}{\alpha_V}\right)^{-1} \tag{3.58}$$

71

Similarly the SBG method is applied to the film-heat transfer coefficient (α_f) but without the interfacial roughness parameter. The mixture film-condensation heat transfer coefficient ($\alpha_{f,m}$) is defined in Equation (3.59)

$$\alpha_{f,m} = \left(\frac{1}{\alpha_f} + \frac{Z}{\alpha_V} \right)^{-1} \qquad (3.59)$$

Del Col *et al.* (2005) suggested a non-equilibrium mixture factor (F_m) in $\alpha_{f,m}$ to account for non-equilibrium effects in stratified flow. For the present study, negligible changes are observed with the addition of F_m because of the high concentration of ammonia (99.8%) in the refrigerant. The local overall heat transfer coefficient ($\alpha_{refr,m}$) for the zeotropic mixture is obtained from the interpolation of $\alpha_{c,m}$ and $\alpha_{f,m}$ with the respective heat transfer areas for the two mechanisms. Based on the Figure 3.11, the correlation for the apparent heat transfer coefficient on the tube-side ($\alpha_{refr,app}$) is shown in Equation (3.60).

$$\alpha_{refr,app} = \frac{\alpha_{f,m}\theta_{strat} + \left(2\pi - \theta_{strat}\right)\alpha_{c.m}}{2\pi} \qquad (3.60)$$

The internal thermal resistance is calculated using this apparent heat transfer coefficient for the thermal resistance circuit.

$$R_{in} = \frac{1}{\alpha_{refr,app}\pi D_i L_{seg}} \qquad (3.61)$$

Two methods for calculating the apparent heat transfer coefficient, applicable to the present flow conditions, are discussed here. The first method is using pure fluid heat transfer coefficient of Dobson and Chato (1998) in Equation (3.53) to include the mass transfer effects and calculate the apparent heat transfer coefficient. The second is the

72

method of Del Col *et al.* (2005), which includes mass transfer effects separately in the liquid pool at the bottom and the film at the top. Both the methods were analyzed over the whole condensation process, and significant differences are observed. Figure 3.12 shows the comparison of the apparent heat transfer coefficient for Condenser R.1 at design conditions using these two approaches.
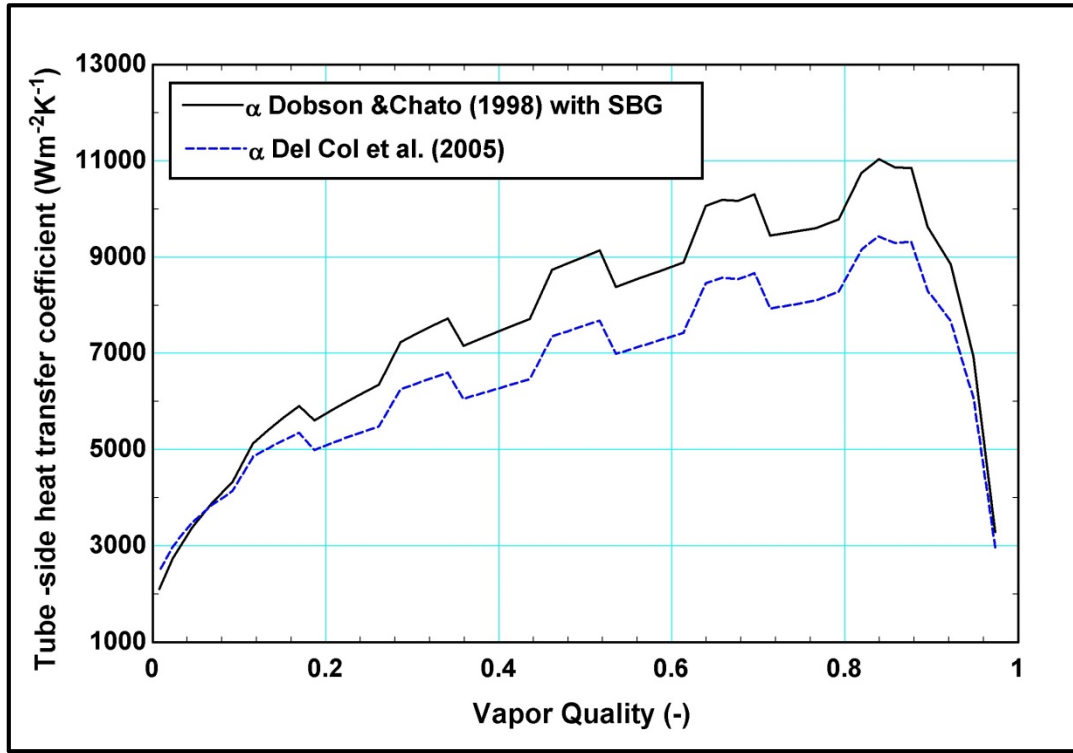
Figure 3.12 Comparison of tube-side two-phase heat transfer coefficients for Condenser R.1 at design conditions

The serrated profile of the heat transfer coefficient is due to the variation of air temperature, which is explained in section 3.2.2. There is a sudden drop in both heat transfer coefficients around vapor quality of one, which is because of the high mass transfer resistance near the inlet of the condenser. However, the method involving the correlation of Dobson and Chato (1998) seems to predict a high overall heat transfer coefficient, even

at the low refrigerant velocities investigated in this work. Upon further inspection differences in the two correlations can be attributed to the convective heat transfer coefficient in the liquid pool. The method of Del Col *et al.* (2005) is more recent, detailed, and covers a bigger database of fluids. Therefore, it is decided to apply the method of Del Col *et al.* (2005) for the conventional condensers.

Depending on the ambient conditions, the condensation process is completed and subcooling occurs near the exit of the condenser. The Churchill (1977) correlation, shown in Equation (3.62), was used to predict the heat transfer coefficient for all subcooled segments. This correlation predicts single-phase heat transfer coefficients over the full Reynolds number range encountered in this study.

$$
Nu_{D,chur} = \left[4.364^{10} + \left(\left(\frac{exp\left(\frac{2200 - Re_L}{365} \right)}{4.364^2} \right) + \frac{1}{\left(6.3 + \frac{0.079 \cdot \left(\frac{f_{chur}}{8} \right)^{0.5} Re_L Pr_L}{\left(1 + Pr_L^{0.8} \right)^{5/6}} \right)^2} \right)^{-5} \right]^{1/10}
$$

(3.62)

3.2.1.3 Pressure drop

Two-phase pressure drop during condensation can be attributed to major, minor, gravitational, and deceleration components, as shown in Equation (3.63) . Each of these components is calculated assuming a cross-section averaged steady state two-phase mixture in a one-dimensional flow system. A positive pressure drop value ($\Delta P_{\text{loss,refr}} > 0$) corresponds to a decrease in refrigerant pressure from the inlet to the outlet.

$$\Delta P_{\text{loss,refr}} = \Delta P_{\text{refr,major}} + \Delta P_{\text{refr,minor}} + \Delta P_{\text{refr,grav}} + \Delta P_{\text{refr,dec}} \tag{3.63}$$

For the horizontal tube configuration, applicable to condensers designed in this study, Friedel (1979) suggested the following equations for the two-phase liquid-only multiplier.

$$C_{Friedel,1} = \left(1 - q_{refr}\right)^2 + q_{refr}^2 \left(\frac{\rho_L}{\rho_V}\right)\left(\frac{f_{V0}}{f_{L0}}\right) \tag{3.64}$$

$$C_{Friedel,2} = 3.24 q_{refr}^{0.78}\left(1 - q_{refr}\right)^{0.224}\left(\frac{\rho_L}{\rho_V}\right)^{0.91}\left(\frac{\mu_V}{\mu_L}\right)^{0.19}\left(1 - \frac{\mu_V}{\mu_L}\right)^{0.7} Fr^{-0.045}We^{-0.035} \tag{3.65}$$

$$\phi_{L0,Friedel}^2 = C_{Friedel,1} + C_{Friedel,2} \tag{3.66}$$

The Froude (Fr) and Weber (We) numbers in Equation (3.65) are calculated using the homogenous two-phase density (ρ_{TP}).

$$\rho_{TP} = \left(\frac{q_{refr}}{\rho_V} + \frac{1 - q_{refr}}{\rho_L}\right)^{-1} \tag{3.67}$$

$$Fr = \frac{G_{refr}^2}{gD_i\rho_{TP}^2} \tag{3.68}$$

$$We = \frac{G_{refr}^2 D_i}{\rho_{TP}\sigma_L} \tag{3.69}$$

The single-phase friction factors used in Equation (3.64) are calculated based on the type of flow: laminar or turbulent. For the turbulent flow, Friedel (1979) recommends Equation (3.71) for the single phase friction factor.

$$\text{For laminar flow } (\text{Re}_{x0} \leq 1055): \qquad f_{x0} = \frac{16}{\text{Re}_{x0}} \qquad (3.70)$$

For turbulent flow $(\text{Re}_{x0} > 1055):$

$$f_{x0} = 0.25 \left[0.86859 \ln \left(\frac{\text{Re}_{x0}}{1.964 \ln(\text{Re}_{x0}) - 3.8215} \right) \right]^{-2} \qquad (3.71)$$

where $x = \text{L,V}$ for liquid or vapor

Finally, the two-phase frictional pressure gradient is calculated from the two-phase liquid-only multiplier and the single-phase pressure gradient as shown in Equation (3.72). The liquid-only single-phase pressure gradient is calculated using the Fanning friction factor, which is defined by the Blasius (1950) correlation .

$$\left(-\frac{dP}{dz} \right)_{fric,TP} = \Phi^2_{Lo,Friedel} \left(-\frac{dP}{dz} \right)_{fric,L0} = \Phi^2_{Lo,Friedel} \left(4 f_{L0} \frac{1}{D_i} \frac{G^2_{refr}}{2 \rho_L} \right) \qquad (3.72)$$

The frictional pressure gradient is calculated with the average refrigerant properties of the segment, and approximated to be constant over the segment. The major pressure loss in the segment is obtained by multiplying the length of the segment with the gradient.

$$\Delta P_{refr,major} = L_{seg} \left(-\frac{dP}{dz} \right)_{fric,TP} \qquad (3.73)$$

Although the refrigerant flow in the heat exchanger is primarily horizontal, U-bends are welded at the end of each horizontal pass curving downward and connecting to the next pass. Each U-bend leads to a minor pressure loss and a gravitational pressure rise, which are the second and third components of the overall pressure drop. To keep track of the

location of these u-bends, a counter is introduced into the model. The segment length (L_{seg}) is also chosen in such a way that it is a factor of the pass length (L_{pass}), to ensure fixed number of complete segments in each pass. The minor loss and the gravitational component are calculated at the location of the U-bends with the qualities and properties of the refrigerant at that point. The minor loss in the bend is calculated using Equation (3.74) and requires a loss coefficient for U-bend (K_{Bend}). K_{Bend} is a single-phase loss coefficient obtained from a list compiled by Ghiaasiaan (2007) from various sources.

$$\Delta P_{\text{refr,minor}} = \Phi_{L0,bend} \frac{1}{2} K_{\text{Bend}} \frac{G_{refr}^2}{\rho_L} \tag{3.74}$$

Two-phase pressure drop in a bend involves a liquid two-phase multiplier (Φ_{L0}) multiplied to the single-phase minor loss calculation. Chisholm (1967) proposed a correlation for Φ_{L0} in a bend as shown in Equation (3.75). This correlation uses a modified Martinelli's factor (X_{bend}), defined by Chisholm (1981) as the ratio of single-phase pressure drop in the liquid to pressure drop in vapor. These single-phase pressure drop calculations involve the same loss coefficient (K_{Bend}) that was used in Equation(3.74). The coefficient (C_{bend}) used in the two-phase multiplier correlation is defined by Equation (3.77).

$$\Phi_{L0} = \left(1 - q_{refr}^2\right)\left(1 + \frac{C_{bend}}{X_{bend}} + \frac{1}{X_{bend}^2}\right) \tag{3.75}$$

$$X_{Bend} = \sqrt{\frac{\Delta P_{L,bend}}{\Delta P_{V,bend}}} = \sqrt{\frac{K_{bend} G_L^2 / (2\rho_L)}{K_{bend} G_V^2 / (2\rho_V)}} \tag{3.76}$$

$$C_{bend} = \left[1 + \left(C_{2,bend} - 1\right)\left(\frac{\rho_L - \rho_V}{\rho_L}\right)^{0.5}\right]\left[\sqrt{\frac{\rho_L}{\rho_V}} + \sqrt{\frac{\rho_V}{\rho_L}}\right]$$

$$C_{2,bend} = 1 + \frac{2.2}{K_{bend}\left(2 + \frac{r_{bend}}{D_i}\right)}$$

(3.77)

Each U-bend transports the refrigerant from one pass to the next with a drop of $s_t/2$ in vertical height. The gravitational pressure rise due to this drop in height is accounted for by using Equation (3.78). The void fractions used here for pressure drop calculations are in the form presented by Butterworth (1975). Void fraction at both the inlet and the outlet of the segment are calculated from Equation (3.79) by using the pertinent vapor quality. The density and viscosity values used in this equation are averaged over the segment.

$$\Delta P_{\text{refr,grav}} = -\left[\left(1 - VF\right)\rho_L + VF \cdot \rho_V\right]g\left(\frac{s_t}{2}\right)$$

(3.78)

$$VF_{\text{in/out}} = \left[1 + 0.28\left(\frac{1 - q_{\text{refr,in/out}}}{q_{\text{refr,in/out}}}\right)^{0.64}\left(\frac{\rho_V}{\rho_L}\right)^{0.36}\left(\frac{\mu_L}{\mu_V}\right)^{0.07}\right]^{-1}$$

(3.79)

$$VF = 0.5\left(VF_{in} + VF_{out}\right)$$

The last component of the pressure drop in the refrigerant is from the deceleration of the flow due to condensation. As the condensation process continues inside the condenser, the quality of the refrigerant decreases and the density increases. As the mass flux in the refrigerant is constant, increase in density of the refrigerant leads to decrease in average velocity, decelerating the flow. The rise in pressure due to deceleration is calculated using Equation (3.80).

$$\Delta P_{\text{refr,dec}} = G_{refr}^2 \left[\frac{q_{\text{refr,out}}^2}{\rho_V VF_{\text{out}}} + \frac{(1-q_{\text{refr,out}})^2}{\rho_L (1-VF_{\text{out}})} \right] - G_{refr}^2 \left[\frac{q_{\text{refr,in}}^2}{\rho_V VF_{\text{in}}} + \frac{(1-q_{\text{refr,in}})^2}{\rho_L (1-VF_{\text{in}})} \right] \quad (3.80)$$

As described in the heat transfer section, subcooling in the last few segments of the condenser requires different correlations. For segments in the condenser where subcooling is occurring, the single phase pressure drop is calculated using the correlation developed by Churchill (1977), (Equations (3.82) and (3.82))

$$f_{\text{Chur}} = 8 \left[\left(\frac{8}{\text{Re}_L} \right)^{12} + \left(\left[2.457 \ln \left(\frac{1}{\left[\frac{7}{\text{Re}_L} \right]^{0.9} + 0.27 \frac{\varepsilon_{\text{rough}}}{D_i}} \right) \right]^{16} + \left[\frac{37530}{\text{Re}_L} \right]^{16} \right)^{-1.5} \right]^{1/12}$$

$$(3.81)$$

$$\Delta P_{\text{refr, major}} = f_{\text{Chur}} \frac{L_{seg}}{D_i} \frac{G_{refr}^2}{2\rho_{refr}} \quad (3.82)$$

During the subcooling process, there is no deceleration of the fluid.

3.2.2 Air-side modeling

The air-side geometry and dimensions are outlined in Table 3.2 for the two conventional round-tube corrugated-fin condensers. The engineering drawing for the corrugated-fin of Condenser R.1 is shown in Figure 3.13.
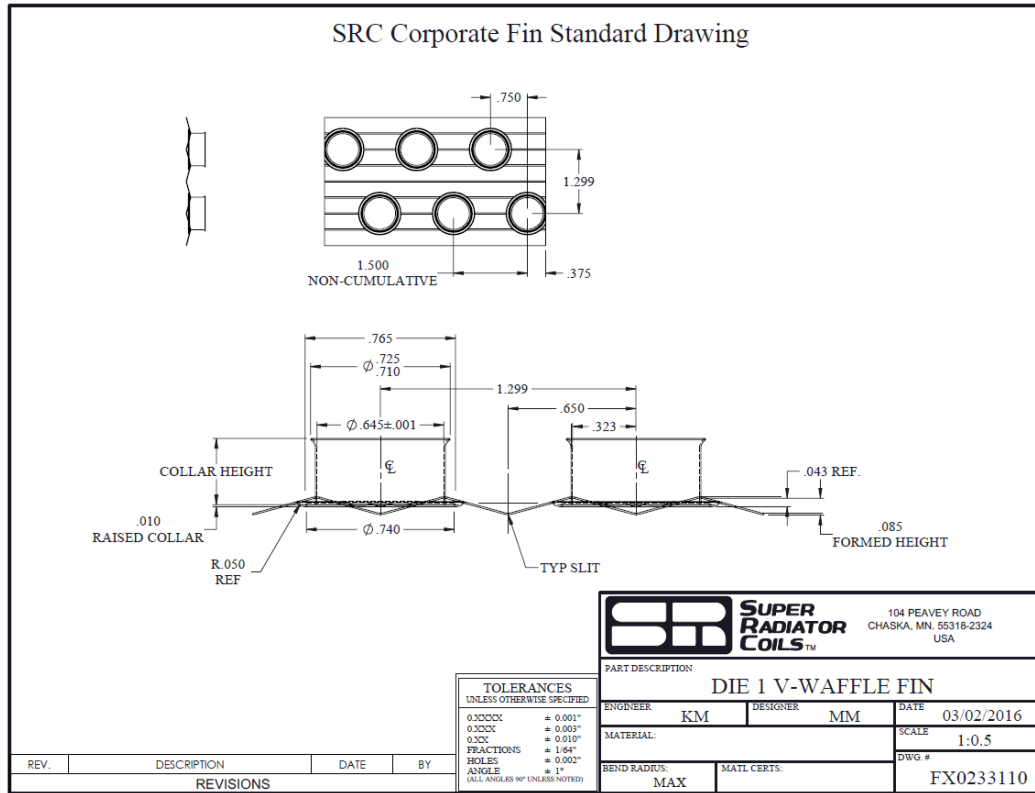
Figure 3.13 Engineering drawing of corrugated-fin with tube collars

The fins have collars in staggered locations and are press fitted onto the round tubes to ensure good heat transfer contact. Heat is transferred from the refrigerant to the tube and then to the collar and finally to the air flowing around these cylindrical collars in between the fins. For this reason, conduction resistance from the collar is added to the thermal resistance network, which is described in more detail in section 3.2.3. The fin collar diameter is used as the tube outer diameter (OD) in the subsequent air-side calculations.

The rear tube row is at downstream location of 33 mm for Condenser R.1 and 22 mm for the Condenser R.2 from the frontal row. Updating the air temperature in the model through the assumption discussed in Section 3.1 is expected to provide an accurate prediction of heat transfer rates in the conventional condensers. The inlet and outlet air

temperatures as a function of the uncoiled tube length for Condenser R.1 at design conditions are shown in Figure 3.14. The odd number passes are the frontal passes and are represented in blue color. The even number passes are the rear passes and represented in red color. The frontal passes receive a uniform face air temperature (51.7°C), while the rear passes receive heated air at the outlet temperature calculated from the segment in the previous frontal pass, located at the same lateral position along the width of the face area.
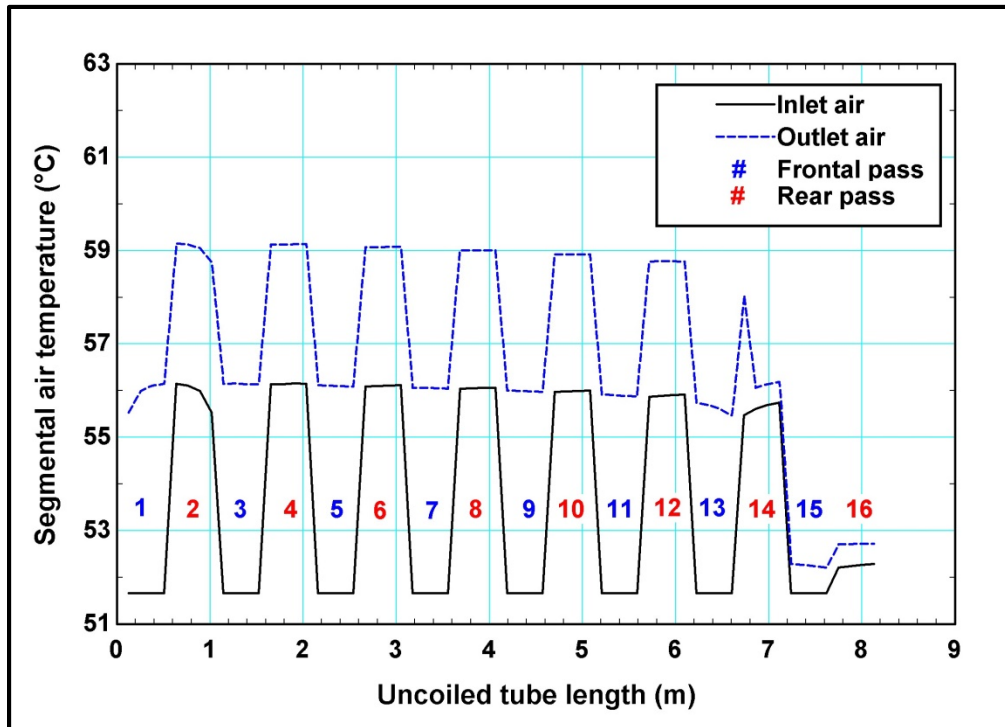
Figure 3.14 Condenser R.1 air temperatures for frontal and rear passes

This method accounts for the lateral and vertical variation in air temperature entering the rear tube row. This approach is expected to lead to better prediction of the trends in condenser performance with varying air flow rates and temperatures.

3.2.2.1 Heat transfer

The correlation of Kim *et al.* (1997) is used in the present study for predicting the heat transfer and frictional pressure drop in the conventional condensers. A database consisting of a wide range of wavy fin configurations with all the data based on the tube outer diameter is used to develop the correlations. They used the Colburn "*j*" factor to predict the heat transfer coefficient, shown in Equation (3.83). For the rows less than three, the correlation is adjusted based on the maximum Reynolds number in the core $\text{Re}_{D,\max}$.

Here, collar diameter (D_c) is used instead of tube outer diameter (D_o) to account for the larger diameter over which the air flows. The other fin dimensions are shown in Figure 3.7 and outlined in Table 3.2 except for the fin spacing ($s = p_{\text{fin}} - t_{\text{fin}}$).

$$
\begin{aligned}
&N \geq 3: \; j_N = j_3 = 0.394 \, \text{Re}_{D,\max}^{-0.357} \left(\frac{s_t}{s_1} \right)^{-0.272} \left(\frac{s}{D_c} \right)^{-0.205} \left(\frac{s_{\text{wav,p}}}{s_{\text{wav,d}}} \right)^{-0.558} \left(\frac{s_{\text{wav,d}}}{s} \right)^{-0.133} \\
&N = 1,2; \; \text{Re}_{D,\max} \geq 1000: \; j_N = j_3 \left(0.978 - 0.010N \right) \\
&N = 1,2; \; \text{Re}_{D,\max} < 1000: \; j_N = j_3 \left(1.350 - 0.162N \right)
\end{aligned}
\tag{3.83}
$$

The average air-side heat transfer coefficient is obtained from the Colburn "*j*" factor correlation Equation (3.84). Finally, the overall outside resistance for the segment is calculated as shown in Equation (3.85) using the overall fin-efficiency (η_o).

$$
j_N = \frac{\alpha_{air} \, \text{Pr}_{air}^{2/3}}{\rho_{air} u_{air,\max} C p_{air}}
\tag{3.84}
$$

$$
R_{\text{out}} = \frac{1}{\eta_0 \alpha_{air} A_{\text{out,seg}}}
\tag{3.85}
$$

82

3.2.2.2 Pressure drop

The overall pressure loss can be attributed to entrance and exit losses, frictional losses, and acceleration components.

$$\Delta P_{\text{loss,air}} = \Delta P_{\text{air,entrance}} + \Delta P_{\text{air,fric}} + \Delta P_{\text{air,accel}} + \Delta P_{\text{air,exit}} \tag{3.86}$$

The pressure decreases during contraction of the flow area and increases during expansion. In this case, due to the presence of fins and tubes, the flow area for the air decreases, which leads to contraction, and when the air leaves the condenser it experiences an expansion. Contraction and expansion loss coefficients, K_c and K_e are used to account for irreversibilities due to these sudden changes in air flow area. Values for the coefficients can be found in Kays and London (1984) as a function of Reynolds number and the contraction ratio (σ_c), i.e., the ratio of the flow area at the face of the condenser (A_{face}) to the frontal flow area (A_{fr}). A_{face} of the condenser is calculated by subtracting the area blocked by the fins from the overall frontal area.

$$\sigma_c = \frac{A_{face}}{A_{fr}} = \frac{H_{fin} L_{\text{pass}} \left(1 - t_{\text{fin}} / p_{\text{fin}}\right)}{L_{\text{pass}} H_{\text{fin}}} \tag{3.87}$$

Air-pressure changes due to contraction and expansion are approximated using Equations (3.88) and (3.89). The wind tunnel cross-sectional area is different at the inlet and the exit of the condenser suggesting use of different area ratios (σ_c, σ_e). In the present study, by convention, a rise in pressure is shown as negative. These correlations consist of both reversible and irreversible parts.

$$\Delta P_{\text{air,entrance}} = \frac{G_{air}^2}{2\rho_{\text{air,in}}} \left(1 - \sigma_c^2 + K_c\right) \tag{3.88}$$

83

$$\Delta P_{air,exit} = -\frac{G_{air}^2}{2\rho_{air,out}}\left(1 - \sigma_e^2 - K_e\right) \qquad (3.89)$$

The frictional losses usually account for the major portion of the pressure losses. The study of Kim *et al.* (1997) on corrugated wavy-fins, which was used for the heat transfer correlation, provides an appropriate friction factor correlation. The air-side overall friction factor for finned-tube geometries is usually calculated using a superposition model that combines the friction factors from the tube and the fin. Kim *et al.* (1997) suggested Equation (3.90) for the overall friction factor, which requires the fin total area ($A_{fin,tot}$) and the total air-side area including both fins and tubes (A_{tot}).

$$f_{air} = f_{f,air}\left(\frac{A_{fin,tot}}{A_{tot}}\right) + f_{t,air}\left(1 - \frac{A_{fin,tot}}{A_{tot}}\right)\left(1 - \frac{t_{fin}}{p_{fin}}\right) \qquad (3.90)$$

Kim *et al.* (1997) suggested the use of a tube bank correlation by Zukauskas and Ulinskas (1983) for the tube-friction factor ($f_{t,air}$), which is detailed in Section 3.3.2.2. For the fin-friction factor ($f_{f,air}$), they performed a multiple regression analysis on the experimental data and proposed Equation (3.91).

$$f_{f,air} = 4.467\,\text{Re}_{D,max}^{-0.423}\left(\frac{s_t}{s_l}\right)^{-1.08}\left(\frac{s}{D_c}\right)^{-0.0339}\left(\frac{s_{wav,p}}{s_{wav,d}}\right)^{-0.672} \qquad (3.91)$$

Finally, the frictional pressure drop is calculated from the overall friction factor using Equation (3.92). Here, A_c corresponds to the cross-sectional flow area available for air flow at the plane of first tube row, as shown in Equation (3.93)

$$\Delta P_{air,fric} = f_{air}\frac{A_{tot}}{A_c}\frac{G_{air}^2}{2\rho_{air}} \qquad (3.92)$$

$$A_c = (H_{fin} - N_{t,row}D_c)L_{\text{pass}}\left(1 - t_{\text{fin}}/p_{\text{fin}}\right) \tag{3.93}$$

Kim *et al.* (1997) suggested limits in dimensionless parameters for their heat transfer and pressure drop correlations based on comparisons with their data. These applicability limits, along with the values of the dimensionless parameters, for both condensers at design conditions are outlined in Table 3.3. It can be seen that the values for both the condensers under consideration here are mostly within the range of applicability of the correlations suggested by Kim *et al.* (1997).

Table 3.3 Range of applicability for Kim *et al.* (1997) wavy-fin correlation

Limitations Heat transfer	Limitations Friction factor	Design Conditions Condenser R.1	Design Conditions Condenser R.2
$500 \leq Re_D \leq 6000$	$500 \leq Re_D \leq 9000$	2162	1124
$1.16 \leq \dfrac{S_t}{S_l} \leq 1.33$	$1.16 \leq \dfrac{S_t}{S_l} \leq 1.33$	1.16	1.16
$0.15 \leq \dfrac{s}{D_c} \leq 0.33$	$0.11 \leq \dfrac{s}{D_c} \leq 0.33$	0.14	0.16
$1.44 \leq \dfrac{S_{wav,p}}{S_{wav,d}} \leq 10$	$3.23 \leq \dfrac{S_{wav,p}}{S_{wav,d}} \leq 5.65$	3.8	3.1
$0.23 \leq \dfrac{S_{wav,d}}{s} \leq 1.21$	$0.29 \leq \dfrac{S_{wav,d}}{s} \leq 1$	0.94	0.63

The final portion of the pressure drop accounts for the acceleration or deceleration of the flow with heating or cooling.

$$\Delta P_{\text{air,accel}} = \frac{G_{\text{air}}^2}{2\rho_{\text{air,in}}}\left(\frac{\rho_{\text{air,in}}}{\rho_{\text{air,out}}} - 1\right) \tag{3.94}$$

3.2.3 Thermal resistance

Calculation of the internal and external thermal resistances is described in Sections 3.2.1 and 3.2.2 respectively. The conduction resistance is the only part left to be determined. For the conventional condensers, the collars from the corrugated fins are press-fitted onto outer surfaces of the tubes. Therefore, the collars present an additional conduction resistance to heat transfer. The overall conduction resistance (R_{cond}) is the sum of the resistances from the fin-collar and tube as shown in Equation (3.95). The collar material is aluminum, the same as the fins, while the tube material is carbon steel. Respective conductivities k_{fin} and k_{tube} are used for the calculation of the conduction thermal resistance. The contact resistance (R_c) between the press-fitted collar and the tube is calculated from the interface conductance (α_c) using Equation (3.96). Here, A_s is the surface area of the tube in contact with the collar, and a typical α_c value ($6000 \text{ W m}^{-2}\text{K}^{-1}$) for contact between steel and aluminum is used. The contact resistance calculated for a segment in Condenser R.1 is 0.008 K W^{-1}, whereas the internal, external and conduction resistances are $0.065 \text{ K W}^{-1}, 0.163 \text{ K W}^{-1}$, and 0.014 K W^{-1}, respectively. This analysis shows that contact resistance between the collar and the tube in the conventional round-tube corrugated-fin condensers has an insignificant effect on the heat transfer in the condenser.

$$R_{cond} = R_{collar} + R_{tube} = \frac{\ln\left(D_o/D_i\right)}{2k_{tube}\pi L_{seg}} + \frac{\ln\left(D_c/D_o\right)}{2k_{fin}\pi L_{seg}} \qquad (3.95)$$

$$R_c = \frac{1}{\alpha_c A_s} \qquad (3.96)$$

The total thermal resistance of a segment is determined by combining all the resistances in series using Equation (3.2). The thermal resistances for Condenser R.1 and Condenser R.2 at design conditions are plotted in Figure 3.15 and Figure 3.16 respectively. The sudden jump in the internal thermal resistance for both the condensers is due to transition to the subcooled region of the refrigerant. In the two-phase region, the outer thermal resistance from the air is dominant. The conduction resistance from the tube and the collar is negligible compared to the other resistances.
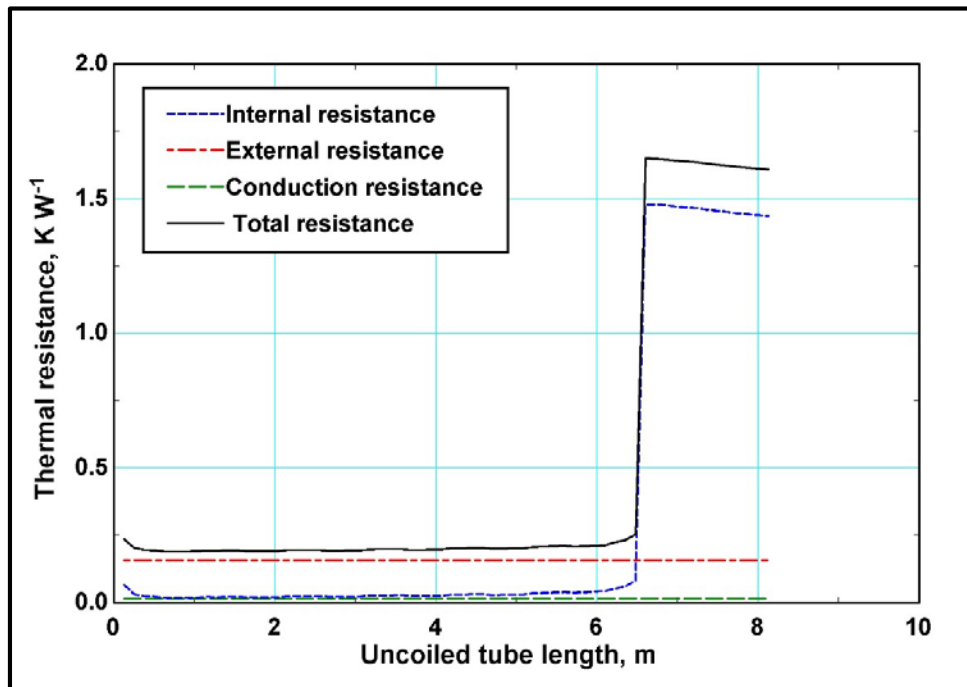
Figure 3.15: Thermal resistances Condenser R.1 at design conditions
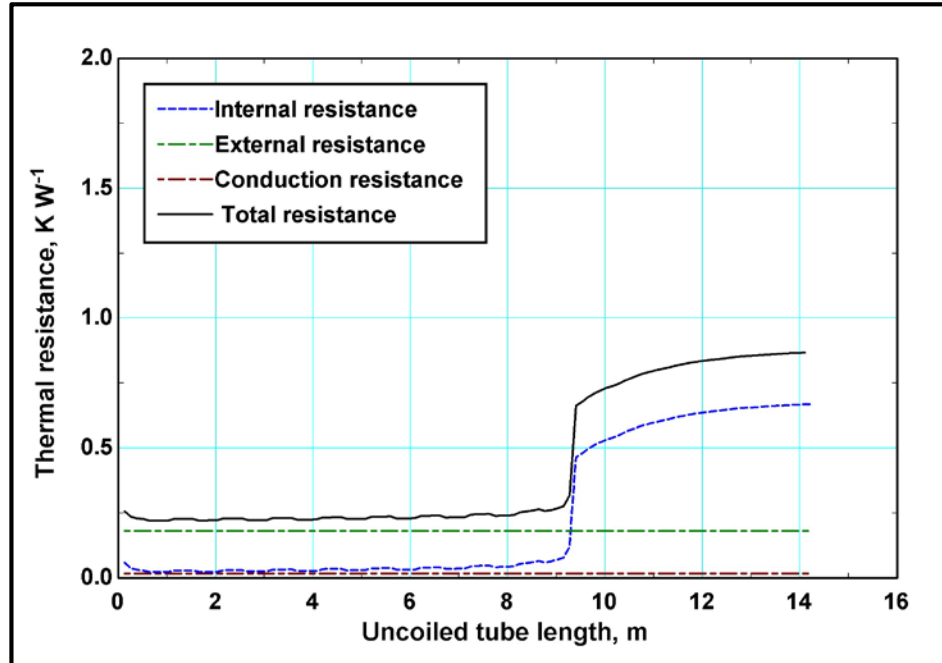
Figure 3.16: Thermal resistances Condenser R.2 at design conditions

3.3 Multi-Pass Tube-Array Condenser

Two novel multi-pass tube-array condensers (Condenser M.1 and Condenser M.2) are designed and modeled. Condenser M.1 consists of a dense array of tubes. Condenser M.2 is a version with plain fins fitted to the tube-array for increased air-side area. Both condensers have bundles of parallel tubes joined in a single header. As shown in Figure 3.17, the header is split into two halves, with each tube making four passes before returning at the other end of the header. The tube bundles in the condensers are in series with respect to the flow of refrigerant and consist of a decreasing number of parallel tubes to account for the decrease in specific volume as the refrigerant condenses. The number of parallel tubes in each tube bundle ($N_{t,bundle}$) for both the condensers is shown in Table 3.4. Although Condenser M.1 consists of four tube bundles and Condenser M.2 consists of 6 tube bundles, both condensers have 120 tubes. These condensers are experimentally

88

evaluated in the wind tunnel, and the results are used to validate and refine the models. The mass flux of refrigerant flowing through a segment depends on the number of parallel tubes, which varies from one tube bank to another. Similar to the case for conventional round tube coils, segmented models are developed for both multi-pass condensers. These models divide the condenser into small segments of equal lengths along the path of the refrigerant to track the variation of properties and heat transfer processes during condensation.
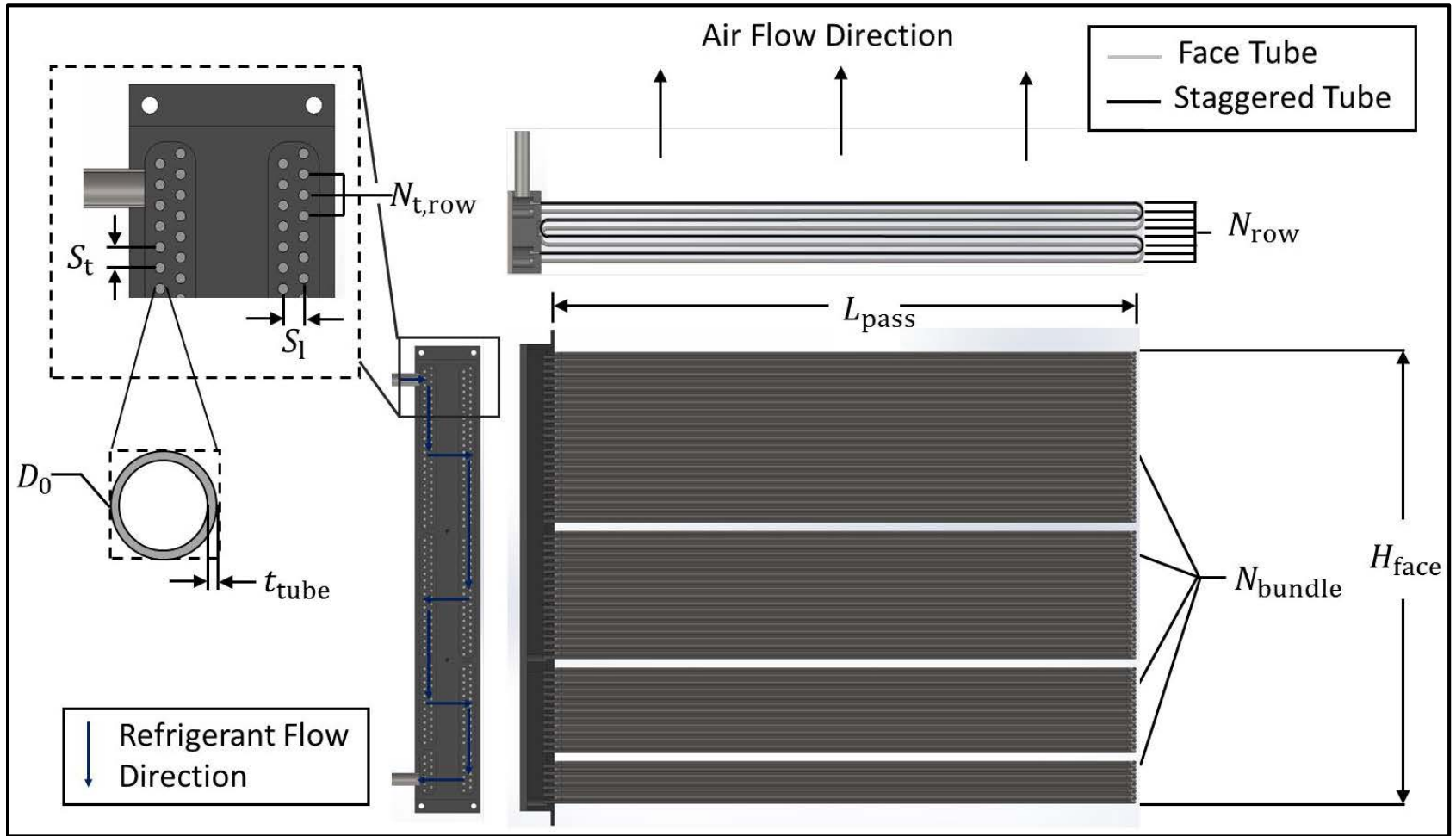
Figure 3.17 Schematic of multi-pass tube-array condensers

Table 3.4 Multi-pass tube-array condensers tube-side dimensions

Tube-Side Geometry		
Dimensions	**Condenser R.1**	**Condenser R.2**
$L_{\text{seg}}\ (\text{m})$	0.508	0.508
$D_{\text{o}}\ (\text{m})$	3.175×10^{-3}	3.175×10^{-3}
$t_{\text{tube}}\ (\text{m})$	5.08×10^{-4}	5.08×10^{-4}
$L_{\text{pass}}\ (\text{m})$	0.508	0.508
$N_{bundles}\ (\text{-})$	4	6
$N_{t,total}\ (\text{-})$	120	120
$N_{t,bundle}\ (\text{-})$	$N_{t,bundle1} = 48$ $N_{t,bundle2} = 36$ $N_{t,bundle3} = 24$ $N_{t,bundle4} = 12$	$N_{t,bundle1} = 48$ $N_{t,bundle2} = 32$ $N_{t,bundle3} = 18$ $N_{t,bundle4} = 12$ $N_{t,bundle5} = 6$ $N_{t,bundle6} = 4$
$s_{\text{t}}\ (\text{m})$	6.35×10^{-3}	6.35×10^{-3}
$s_{\text{l}}\ (\text{m})$	6.35×10^{-3}	6.35×10^{-3}
$\varepsilon_{\text{rough}}\ (\text{m})$	1.0×10^{-5}	1.0×10^{-5}
Tube material	Stainless steel	Stainless steel

Table 3.5 Multi-pass tube-array condensers air-side dimensions

Air-Side Geometry		
Dimensions	**Condenser M.1**	**Condenser R.2**
$N_{row}\,(-)$	8	8
$N_{t,row}\,(-)$	60	60
$H_{\text{face}}\,(\text{m})$	0.381	0.381
$W_{\text{fin}}\,(\text{m})$	N/A	2×0.019
$t_{\text{fin}}\,(\text{m})$	N/A	2.54×10^{-4}
$p_{\text{fin}}\,(\text{m})$	N/A	2.54×10^{-3}
Arrangement	Staggered	Staggered
Fin material	Stainless steel	Stainless steel

3.3.1 Tube-side modeling

3.3.1.1 Flow regime

The novel multi-pass tube-array condensers have tubes with very small diameter (3.175 mm) but the refrigerant flow is split into multiple tubes, which decreases the mass flux in each tube. Among the two-phase flow regime studies in the literature, the flow pattern map of El Hajal *et al.* (2003) includes low mass flux regions. Furthermore, the study also divides the stratified flow regime into stratified-wavy and fully-stratified flow regimes. The mass fluxes in both the multi-pass condensers are plotted on their flow regime map and are shown in Figure 3.18. In contrast to the case for conventional condensers, the

mass flux is not constant in the multi-pass condensers, and increases after each tube bundle as condensation proceeds. The refrigerant mass flow rate for a segment in a particular tube bundle is determined using Equation (3.97) from the total mass of vapor entering the condenser. This calculated mass flow rate is assumed to be constant for all the tubes in that bundle or block.

$$\dot{m}_{refr,seg} = \frac{\dot{m}_{cond,in}}{N_{t,bundle}} \tag{3.97}$$

Despite this design effort of increasing the mass flux with decreasing vapor quality, the flow in both the condensers is stratified. As seen from Figure 3.18 the two-phase refrigerant flow is fully-stratified in Condenser M.1 at design conditions. For Condenser M.2, however, the flow is fully-stratified in the first two tube bundles and stratified-wavy in the rest of the condenser. From this exercise, it is established that heat transfer correlations for stratified flows are appropriate for modeling these multi-pass condensers.
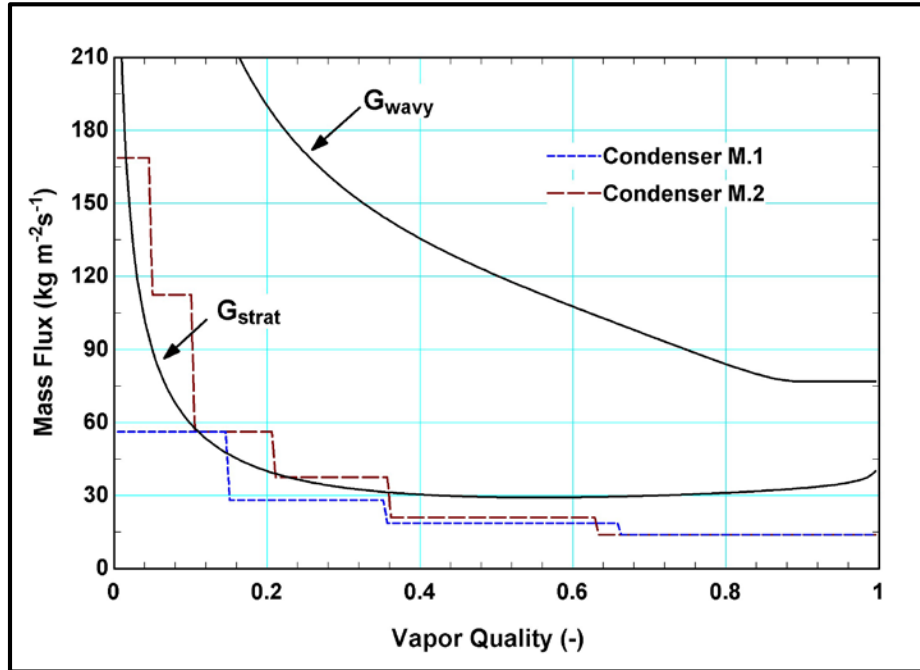
Figure 3.18: Two-phase flow-regime in multi-pass condensers

3.3.1.2 Heat transfer

The models of the multi-pass condensers use segmental analysis to predict the heat transfer and pressure drop inside the tubes. It is assumed that the refrigerant is uniformly distributed into all the parallel tubes of that bundle. A face tube and a staggered tube are modeled separately in every tube bundle as shown on the top view in Figure 3.17. This is because the air inlet temperature to the staggered tube is different from the corresponding temperature for the face tube (Section 3.1). The Dobson and Chato (1998) heat transfer coefficient correlation with SBG framework accounts for mass transfer effects. Del Col *et al.* (2005) includes mass transfer effects separately in the liquid pool at the bottom and the film at the top. In contrast to the conventional condenser models, the first method is used for the multi-pass condenser models. This is because the method of Del Col *et al.* (2005)

uses simplified geometries inside the tube, which requires the calculation of the geometric parameters shown in Figure 3.8. The inner diameter of the tubes in the multi-pass condensers is very small (2.16 mm) compared to the tubes in the conventional condensers, which may not justify the precise calculation of the geometric parameters of the film and the pool for this design. The two-phase heat transfer coefficient in Condenser M.1 at design conditions is shown in Figure 3.19 as a function of vapor quality. The sharp changes in slope of the curve are because of the sudden change in air inlet temperature from one tube bundle to the next. The film heat transfer coefficient calculation requires the temperature difference between the refrigerant and the inner tube as shown in Equation (3.38). A decrease in the temperature difference $(T_{refr} - T_{tube,in})$ increases the film heat transfer coefficient, which is the reason for the sudden jump around 0.2 vapor quality in Figure 3.19. The drop in heat transfer coefficient at qualities above 0.9 is because of the high mass transfer resistance near the entrance of the condenser.
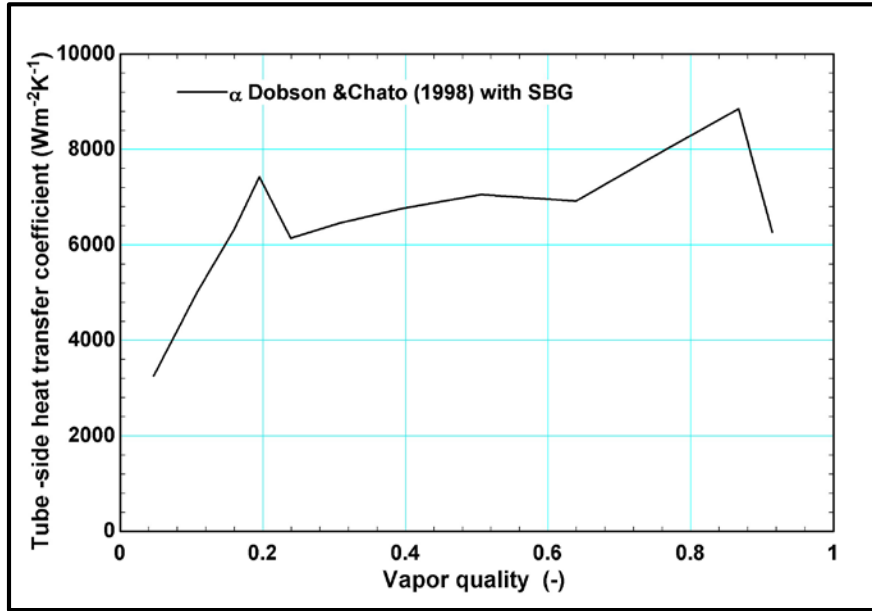
**Figure 3.19 Tube-side apparent heat transfer coefficient for
Condenser M.1 at design conditions**

At the design conditions, the model predicts that subcooling occurs in Condenser M.1 in the fourth or the last tube bundle. Similar to the case for the conventional condensers, the single-phase heat transfer correlation of Churchill (1977) is used to model the tube-side heat transfer coefficient. A significant difference in the heat transfer coefficients between the two-phase and single-phase is observed, and its effect on the thermal resistance is discussed in section 3.3.3.

3.3.1.3 Pressure drop

The tube-side pressure drop components for the multi-pass condensers are calculated using the methods described in Section 3.2.1.3, except for the gravitational component of pressure drop. The refrigerant trickles down with due to gravity inside the header and the gravitational pressure rise is based on the difference in height of the tube outlet and height of the tube inlet for the next tube bundle. To make the model simpler and

minimize instabilities in computation, the gravitational head of the entire condenser is assumed to be distributed equally among all the segment of the condenser as shown in Equation (3.98).

$$\Delta P_{\text{refr,grav}} = -\left[\left(1 - VF\right)\rho_L + VF \cdot \rho_V\right] g \frac{H_{face}}{L_{total}} L_{seg} \qquad (3.98)$$

3.3.2 <u>Air-side modeling</u>

The air-side geometries of Condenser M.1 and Condenser M.2 are different. Condenser M.1 consists of a dense array of plain tubes without fins. The second version, Condenser M.2, consists of plain fins fitted on to this dense array of tubes. This difference in geometries necessitates different heat transfer correlations and methods for their respective models. The air-side geometries and dimensions are shown in Table 3.5. These dimensions are also seen in the schematic of a staggered tube bank arrangement shown in Figure 3.3. Some common variables frequently used in correlations are derived from these dimensions, as shown in Equation (3.99).

$$a = \frac{s_t}{D_o}; \; b = \frac{s_l}{D_o}; \; c = \sqrt{\left(\frac{a}{2}\right)^2 + b^2} \qquad (3.99)$$

Due to the absence of fins in Condenser M.1, the $u_{air,face}$ is approximated as shown in Equation (3.100). The maximum velocity and maximum Reynolds number can now be calculated using Equations (3.13) and (3.14), by replacing D_c with D_o of the tube. The air flow area at the plane of a tube row (A_c) is calculated using Equation (3.101)

$$u_{air,face} = \frac{\dot{V}_{air,in}}{H_{face} L_{pass}} \tag{3.100}$$

$$A_c = \left(H_{face} - N_{t,row} D_o \right) L_{pass} \tag{3.101}$$

Air temperature is also updated after each tube row for all the eight rows. The analysis is similar to the discussion on conventional condensers in Section 3.2.2. For this multi-pass condenser design, refrigerant flows back and forth with respect to the air flow direction. The refrigerant flow direction is shown with arrows in Figure 3.17. The horizontal arrows represent refrigerant flow through a tube bundle rejecting heat to the air, while the vertical arrows represent the downward flow of refrigerant inside the header to the next tube bundle. As the air-flow direction in the condenser stays constant, the refrigerant and the air are in cross-counter flow in one tube bundle and cross-parallel flow in the next tube bundle (shown in Figure 3.20). Thus, in the model, the air temperature is updated accordingly with respect to the flow of refrigerant in the model. The cross-counter flow in a tube bank requires iterations to calculate the air temperature from one side and the refrigerant temperature from the other side. This increased the complexity of the model, and segment length is increased to the length of one pass (0.508 m) to avoid computational instabilities. With this larger segment length, the numerical error, compared to the calculations using smallest segment length (0.025 m), is still less than 1% for heat transfer rate and less than 6% for tube-side pressure drop.
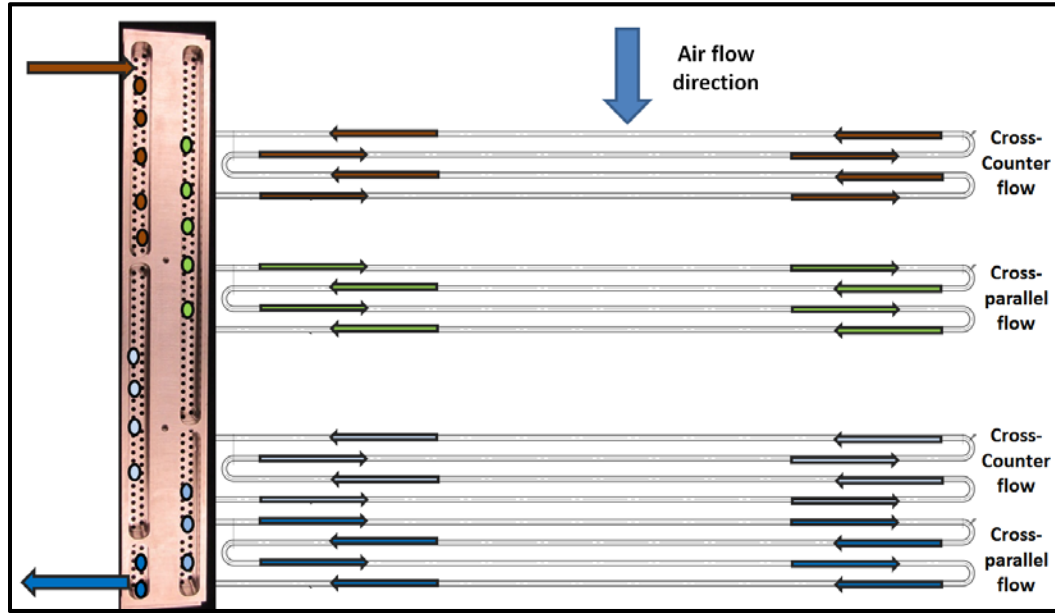
Figure 3.20 Flow of refrigerant with respect to air in Condenser M.1

3.3.2.1 Heat transfer

The heat transfer correlation for tube banks suggested by Žukauskas (1972) is shown in Equation (3.102). The variables *C* and *m*, used in the calculation of the Nusselt number, are a function of the maximum Reynolds number in the coil, which is defined in Equation (3.14). The Prandtl number of air at the surface temperature (Pr_s) is calculated at the tube outer surface temperature for the particular segment. All the other properties used in the correlation are evaluated at the arithmetic mean of the air inlet and outlet temperature of the segment.

$$\overline{Nu}_{D(Rows>20)} = C \, Re_{D,\max}^{m} \, Pr^{0.36} \left(\frac{Pr}{Pr_s} \right)^{0.25} \tag{3.102}$$

In cases where the tube bank has less than 20 rows, the lower heat transfer coefficient from the first few rows of tubes plays a role in the average heat transfer coefficient (Žukauskas, 1972). For the present study, the multi-pass tube-array condensers

99

have eight rows of tubes, and this is accounted for by adding a coefficient (C_2) to the average Nusselt number. The air-side heat transfer coefficient is then calculated from the Nusselt number for that segment.

$$\overline{\text{Nu}}_{D(Rows=8)} = C_2 \overline{\text{Nu}}_{D(Rows>20)} \qquad (3.103)$$

It is observed that the air-side heat transfer coefficient proposed by Žukauskas (1972) has a discontinuity at $\text{Re}_{D,\max}$ of 1000. This is because of the sudden change in parameters C and m used in Equation (3.102), which are both functions of the maximum Reynolds number of air.

The Martin (2002) approach for calculation of heat and mass transfer rates from pressure drop correlations uses the pressure drop correlation of Gaddis and Gnielinski (1985) to calculate the heat transfer coefficient in bundles of tubes in crossflow of air. The average Nusselt number for a tube bank, according to Martin (2002), is given by Equation (3.104). Here the temperature ratio at the end of the equation was suggested by Churchill and Brier (1953) and accounts for the rise in air temperature near the outer surface of the tubes.

$$\overline{Nu}_{air,martin} = 0.404 Lq^{1/3} \left(\frac{T_{air,avg}}{T_{tube,o}} \right)^{0.12} \qquad (3.104)$$

$$Lq = 0.92 Hg_s \frac{\text{Pr}}{c} \left(\frac{4a}{\pi} - 1 \right) \qquad (3.105)$$

The term Hg_s in Equation (3.105) corresponds to the Hagen number for staggered arrangement of tubes. The term is divided into laminar and turbulent components as shown in Equation (3.106). These components are defined in Equations (3.107) and (3.108). The

100

term $f_{t,n}$, defined in Equation (3.109), is used to account for the influence of inlet and

outlet pressure losses, and should be set to zero for $N_{t,row} > 10$.

$$Hg_s = Hg_{lam} + Hg_{turb,s}\left(1 - \exp\left(-\frac{\mathrm{Re}_{D,\max} + 200}{1000}\right)\right) \tag{3.106}$$

$$Hg_{lam} = 140\,\mathrm{Re}_{D,\max}\frac{\left(b^{0.5} - 0.6\right)^2 + 0.75}{a^{1.6}\left(\dfrac{4ab}{\pi} - 1\right)} \quad \text{for } b > 0.5\sqrt{2a+1} \tag{3.107}$$

$$Hg_{turb,s} = f_{t,s}\,\mathrm{Re}_{D,\max}^{1.75} + f_{t,n}\,\mathrm{Re}_{D,\max}^{2} \tag{3.108}$$

$$f_{t,n} = \frac{1}{2a^2}\left(\frac{1}{N_{t,row}} - \frac{1}{10}\right) \quad \text{for } b > 0.5\sqrt{2a+1} \tag{3.109}$$

$$f_{t,s} = 1.25 + \frac{0.6}{\left(a - 0.85\right)^{1.08}} + 0.2(b/a - 1)^3 - 0.005(a/b - 1)^3 \tag{3.110}$$

Both the Žukauskas (1972) and Martin (2002) correlations are applied to Condenser

M.1 and plotted with increasing Reynolds number of air (shown in Figure 3.21). The

discontinuity in the Žukauskas (1972) correlation is evident at $\mathrm{Re}_{D,\max} = 1000$. However, at

the maximum flow rate of air for the present study, $\mathrm{Re}_{D,\max}$ is 834, which is below the

region with the discontinuity.
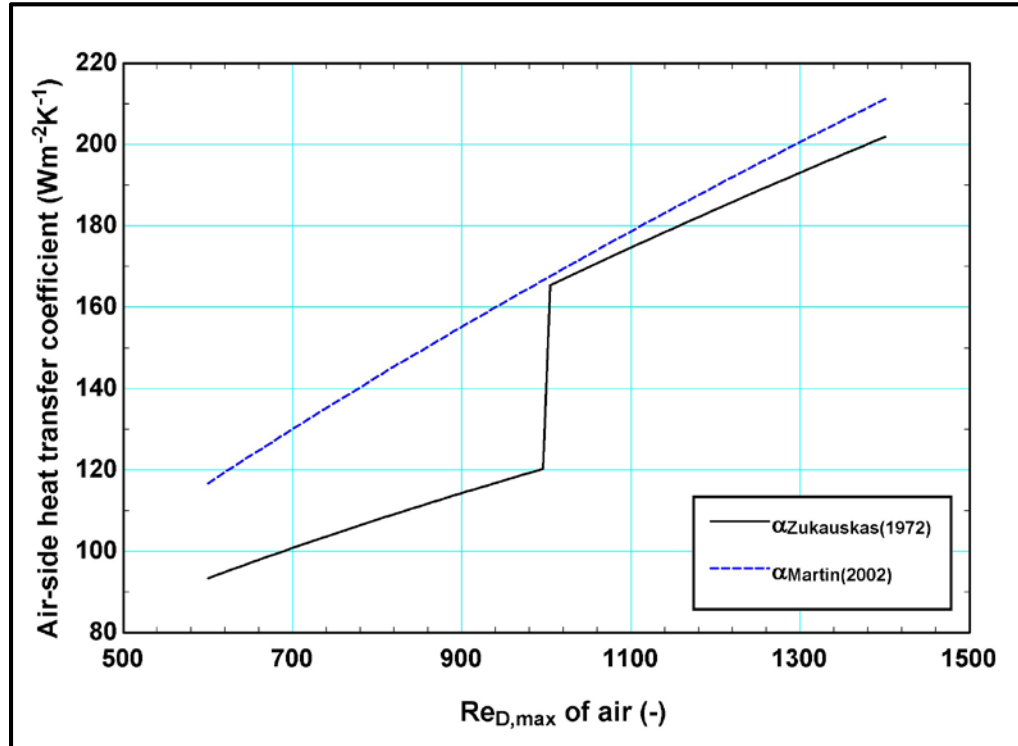
Figure 3.21 Air-side heat transfer correlations for Condenser M.1

Condenser M.2, a finned multi-pass condenser, consists of plain fins fitted on a staggered tube bank. In contrast to Gray and Webb (1986), the Kim *et al.* (1999) correlation also incorporates heat exchangers with small diameter tubes, very relevant to the present design. Therefore, the Kim *et al.* (1999) correlation is used for modeling the air-side heat transfer coefficient of Condenser M.2. Their j-factor correlation is shown in Equation (3.111), and is valid for plain fin staggered tube heat exchangers with more than three rows. As Condenser M.2 consists of eight staggered tube rows (N_{row}), the correlation is applied without any modification. Finally, the air-side heat transfer coefficient from the Colburn "*j*" factor is obtained from Equation (3.84).

$$j_{air(Rows>3)} = 0.163 \text{Re}^{-0.369} \left(\frac{s_t}{s_l} \right)^{0.106} \left(\frac{s}{D_o} \right)^{0.0138} \left(\frac{s_t}{D_o} \right)^{0.13} \tag{3.111}$$

The engineering drawing of the plain fin used in Condenser M.2 is shown in Figure 3.22. As the tubes of the condenser are fabricated and bent separately, these plain fins are designed to fit on the tubes just before brazing. Each of the tubes in the condenser makes four passes in the air, and it is only possible to have the first pass and last pass of the tube in contact with the fin. Furthermore, there is cut out at the center of the fin for the middle two passes, resulting in a decrease in the heat transfer area of the fin. These aspects of the fin are accounted for in the model of Condenser M.2 by locally switching to a tube bank correlation for the heat transfer coefficient. The air velocity and Reynolds number are also modified for the middle passes because of the absence of fins.
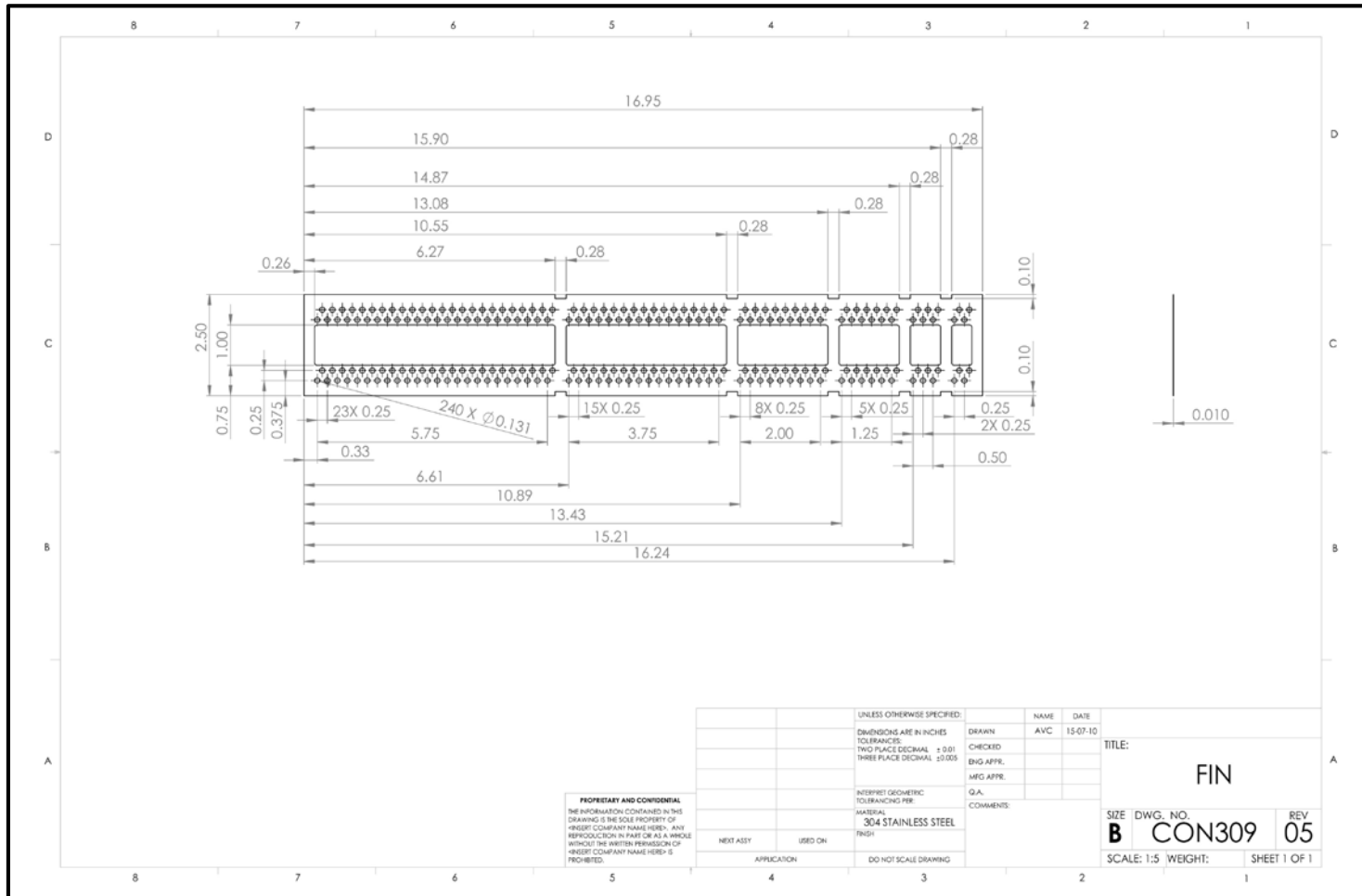
Figure 3.22 Engineering drawing of Condenser M.2 fin

3.3.2.2 Pressure drop

For an un-finned bank of tubes in crossflow, the entrance and exit effects of contraction and expansion are typically already accounted for in the frictional pressure drop correlations (Kays and London, 1984). The air-side pressure drop then consists only of frictional and acceleration components. The frictional pressure drop from the tubes in Condenser M.1 is modeled by determining the tube-friction factor ($f_{t,air}$). Zukauskas and Ulinskas (1983) provide a correlation for the Euler number for the first N tube rows (Eu_N) in Equation (3.112). This correlation is based on the Euler number for many rows of tubes (Eu). Coefficients used in determining Euler number (A_{Eu}, B_{Eu}, C_{Eu}, D_{Eu}, E_{Eu}, and k_1) and the correction factor for fewer tube rows (C_z) may be found in the book by Hewitt (1990).

$$Eu_N = C_z Eu; \quad Eu = k_1 \left(A_{Eu} + \frac{B_{Eu}}{Re_{D,Z}} + \frac{C_{Eu}}{Re_{D,Z}^2} + \frac{D_{Eu}}{Re_{D,Z}^3} + \frac{E_{Eu}}{Re_{D,Z}^4} \right) \tag{3.112}$$

Eu_N corresponds to the average friction factor and is related to $f_{t,air}$ using Equation (3.113) (Kim *et al.*, 1997). Here, $A_{t,out}$ corresponds to the outside area of the tubes exposed to the air, while $A_{c,t}$ corresponds to the flow area available for air in the first row in the absence of fins. In the case of Condenser M.1, these areas are defined in Equations (3.114) and (3.115).

$$Eu_N = f_{t,air} \frac{A_{t,out}}{A_{c,t}} N_{t,row} \tag{3.113}$$

$$A_{t,out} = N_{t,total} \left(4\pi D_o L_{pass} \right) \tag{3.114}$$

$$A_{c,t} = \left(H_{face} - N_{t,row} D_o \right) L_{pass} \tag{3.115}$$

105

Finally, the frictional pressure drop from the tubes is calculated using Equation (3.116)

$$\Delta P_{\text{air,t}} = \frac{1}{2} f_{t,air} \rho_{\text{air}} u_{\text{max}}^2 \left(\frac{A_{\text{t,out}}}{A_{\text{c,t}}} \right)$$

(3.116)

Similar to the heat transfer correlation for plain fins, the Kim *et al.* (1999) correlation is used for fin frictional pressure drop in Condenser M.2. Their fin-friction factor ($f_{f,air}$) correlations for plain fins is shown in Equation (3.117)

$$f_{f,air} = 1.455 \, \text{Re}_{D,\text{max}}^{-0.656} \left(\frac{s_t}{s_l} \right)^{-0.347} \left(\frac{s}{D_o} \right)^{-0.134} \left(\frac{S_t}{D_o} \right)^{1.23}$$

(3.117)

Limits on dimensionless parameters for the heat transfer and pressure drop correlation for the Kim *et al.* (1997) correlation along with the values of these parameters for Condenser M.2 at design conditions are shown in Table 3.6. It can be seen that the values for both condensers are mostly within the range of applicability of the correlations of Kim *et al.* (1997).

Table 3.6 Range of applicability for Kim *et al.* (1999) plain-fin correlations

Limitations Heat transfer	Limitations Friction factor	Design Conditions Condenser R.1
$505 \leq Re_D \leq 24707$	$505 \leq Re_D \leq 19766$	663.4
$0.857 \leq \dfrac{S_t}{S_l} \leq 1.654$	$0.857 \leq \dfrac{S_t}{S_l} \leq 1.654$	1
$1.996 \leq \dfrac{S_t}{D_o} \leq 2.881$	$1.996 \leq \dfrac{S_t}{D_o} \leq 2.876$	2
$0.081 \leq \dfrac{s}{D_o} \leq 0.641$	$0.081 \leq \dfrac{s}{D_o} \leq 0.641$	0.72

The fin-friction factor $f_{f,air}$ is used in conjunction with the tube-friction factor $f_{t,air}$ to find overall friction factor as shown in Equation (3.90). The rest of the air-side pressure drop components for the multi-pass tube-array condensers are obtained using the equations described in Section 3.2.2.2 for conventional condensers.

3.3.3 Thermal resistance

The thermal resistances of the multi-pass condensers are calculated similar to the conventional condensers using the correlations discussed in Sections 3.3.1 and 3.3.2. The thermal resistances for Condenser M.1 are plotted along the length of the condenser and shown in Figure 3.23. The external air-side resistance is the dominant resistance throughout the condenser. It is quite evident that Condenser M.1 is air-side limited, and fins must be added to increase air-side area and decrease the external resistance. This is accomplished in Condenser M.2 with the addition of plain fins, and the thermal resistance is decreased in the tube passes where the fins are attached. This can be observed in Figure 3.24, where the

middle passes without fins have higher external resistance. The first and the last passes in a tube bundle have lower resistance: about one-fourth the value of the resistance of the middle passes. As the external resistance is the dominant resistance, the fins increase the heat transfer rate by about four times for the first and last passes in a tube bundle.
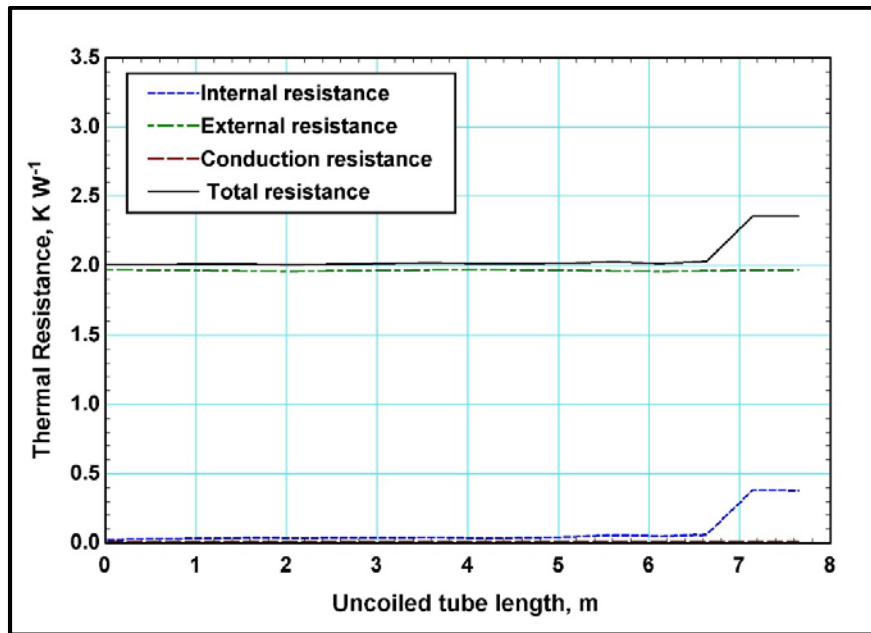
Figure 3.23: Thermal resistances of Condenser M.1 at design conditions
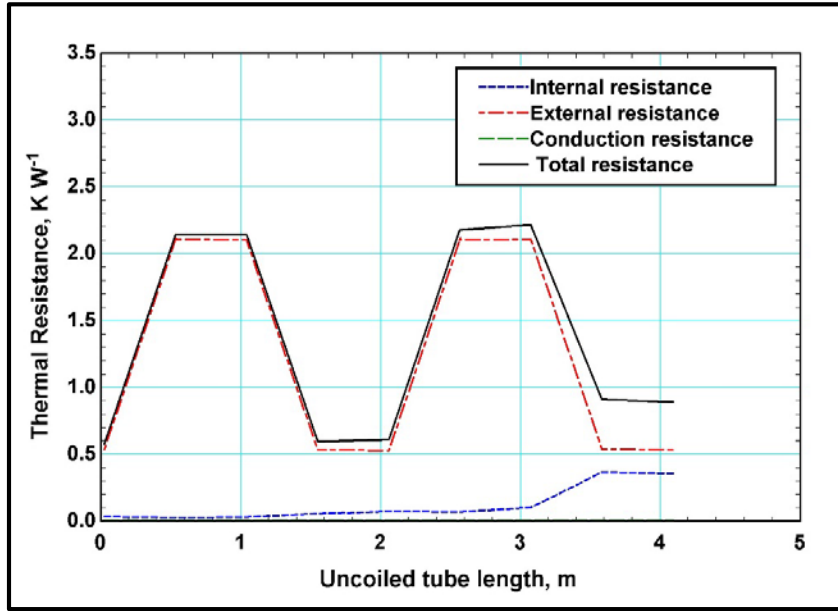
Figure 3.24 Thermal resistances of Condenser M.2 at design conditions

The $\varepsilon - NTU$ method described in Section 3.1 is also used here to determine the heat rejection rate. The outlet conditions of refrigerant and air for the segment are calculated from this heat transfer rate.

An important thing to note is that the refrigerant is assumed to be distributed uniformly among all the tubes in a bundle. Based on this assumption, a face tube and a staggered tube, each with four passes, are modeled for each tube bundle. The heat rejection rate for the tube ($\dot{Q}_{tube}$) is the sum of the heat transfer rates from all segments ($\dot{Q}_{seg}$). The total heat transfer rate for that tube bundle and the whole condenser are calculated using Equations (3.118) and (3.119). The predictions from the modeling method described above are compared with data and presented in the Chapter 5.

$$\dot{Q}_{t,bundle} = \frac{N_{t,bundle}}{2} \dot{Q}_{tube,face} + \frac{N_{t,bundle}}{2} \dot{Q}_{tube,staggered} \tag{3.118}$$

$$\dot{Q}_{tot} = \sum_{1}^{N_{bundles}} \dot{Q}_{t,bundle} \tag{3.119}$$

CHAPTER 4: EXPERIMENTAL APPROACH

The design and fabrication of two types of air-coupled condensers, the layout and construction of the test facility, and a description of the experimental procedure are presented in this chapter.

4.1 Air-Coupled Condenser Fabrication

The design and fabrication of the air-coupled condensers are guided by the cost of machining and assembly, materials compatibility, internal pressure, total mass, and anticipated heat transfer rate. Two versions of condensers are fabricated for both round-tube and tube-array designs. The second versions of the condensers are fabricated after experimental evaluation of the first versions and are intended to improve the performance. All four of the condensers are designed to fit in a compact, small-capacity absorption heat pump operating at extreme ambient conditions, as discussed in the introduction.

4.1.1 Round-tube corrugated-fin condenser

Two conventional round-tube condenser coils are fabricated and evaluated. These condensers are custom designed for the absorption system with a design condenser heat rejection rate of 2.51 kW into the ambient air. For compatibility with ammonia-water, carbon steel tubes are used for both the condensers. Corrugated fin geometry is used for the fins as they were shown to perform better than other fin types as discussed in the literature review chapter. Furthermore, aluminum is used as the fin material because of the high thermal conductivity of Aluminum and its low density. These corrugated aluminum fins have collars press-fitted onto the tubes carrying the refrigerant, which provides good contact between the fin and the tube, thereby limiting the contact resistance. The first

version of the round tube corrugated-fin air coil (Condenser R.1) is fabricated with a fin density of 394 FPM. The tube outer diameter (OD) of the coil is selected as 0.016 m with a wall thickness of 1.245×10^{-3} m. The overall heat exchanger has a length of 0.508 m and height of 0.305 m. Condenser R.1 has 16 passes distributed equally over two tube rows ($N_{t,row}$=8) as shown in Figure 4.2. A staggered tube arrangement is selected for better mixing of air. Experimental evaluation of Condenser R.1 at design conditions showed that the overall heat transfer rate is about 2.34 kW (96% of design heat duty). It is also observed that the pressure drop on both the solution side and air-side were lower than the budgeted values for the system. Thus, a higher pressure drop could be accommodated in the condenser to increase the heat transfer rate. This led to the fabrication of Condenser R.2 with a smaller tube OD of 9.525×10^{-3} m and increased fin density of 551 FPM. Smaller tube diameter also enables a smaller wall thickness, 0.889×10^{-3} m, which leads to a decrease in weight of the condenser. The smaller tube diameter yields higher tube-side heat transfer coefficients, but the tube-side heat transfer area also decreases for the same number of passes. Thus, to keep the tube-side heat transfer area similar to that of Condenser R.1, the total number of passes for Condenser R.2 is increased to 28 passes distributed over two tube rows as shown in Figure 4.3. However, this results in an increase in height of Condenser R.2 by 0.05 m compared to that of Condenser R.1. The length of the coil is kept constant at 0.508 m to conform to the space constraints of the compact heat pump. A photograph of the round-tube corrugated-fin design with two fin densities is shown in Figure 4.1. The temperature of a fin drops with increasing distance from the tube, which decreases the heat transfer from the fin to air. This implies that increasing the size of the

fins has diminishing returns. Thus, a smaller fin width (0.044 m) is chosen for Condenser R.2 because of its smaller tube OD compared to the 0.066 m used for Condenser R.1.

These round-tube corrugated-fin condensers were fabricated by Super Radiator Coils, a manufacturer of custom-made air coupled heat exchangers. Design parameters such as fin types, fin and tube materials, fin densities possible for a tube size, and tube spacing (based on minimum bending radius) were discussed with the manufacturer. Based on the predictions from an initial model for round-tube corrugated-fin condensers, Condenser R.1 is designed and fabricated. After the experimental evaluation of Condenser R.1, the assumptions in the model are modified to predict heat transfer rates better. This refined model, discussed in detail in Chapter 3, is run with different combinations of the design variables as inputs to yield a configuration for the second version with better heat transfer while staying within the design constraints of pressure drop, space, and weight. The resulting optimum design for Condenser R.2 was fabricated, and experiments show an increase in heat transfer rate to about 2.55 kW. (Upon receipt, each coil was pressure tested to 3500 kPa, beyond the operating pressure (2930 kPa), to ensure the absence of leaks upon charging.)
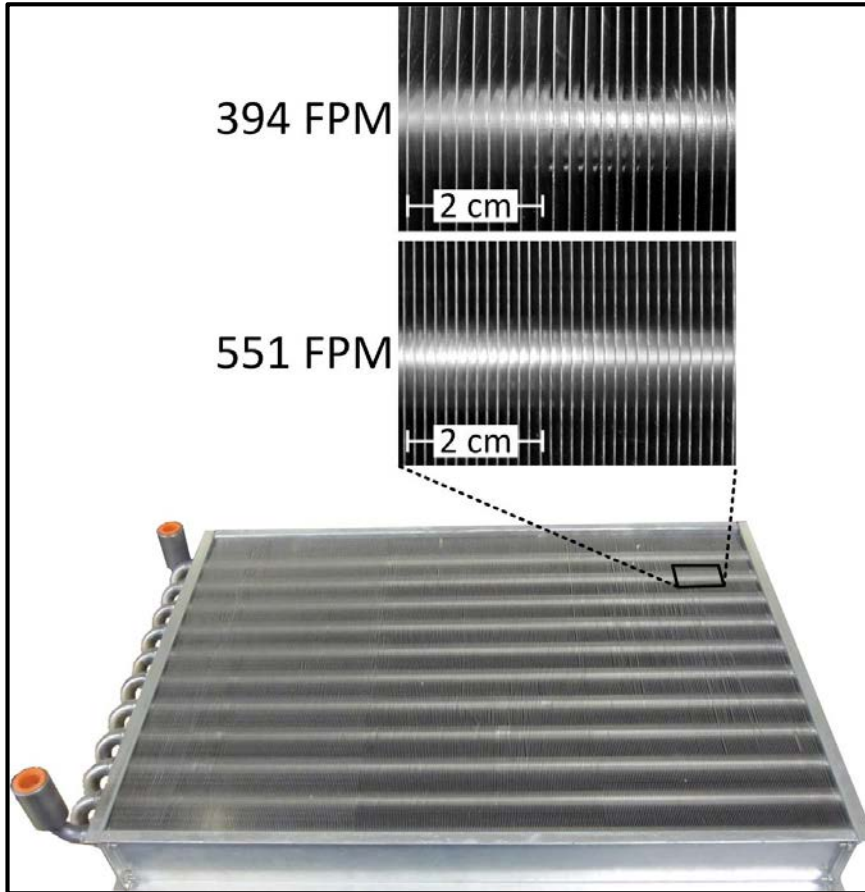
**Figure 4.1 Photograph of round-tube corrugated-fin condenser
with 394-FPM and 551-FPM fin densities**
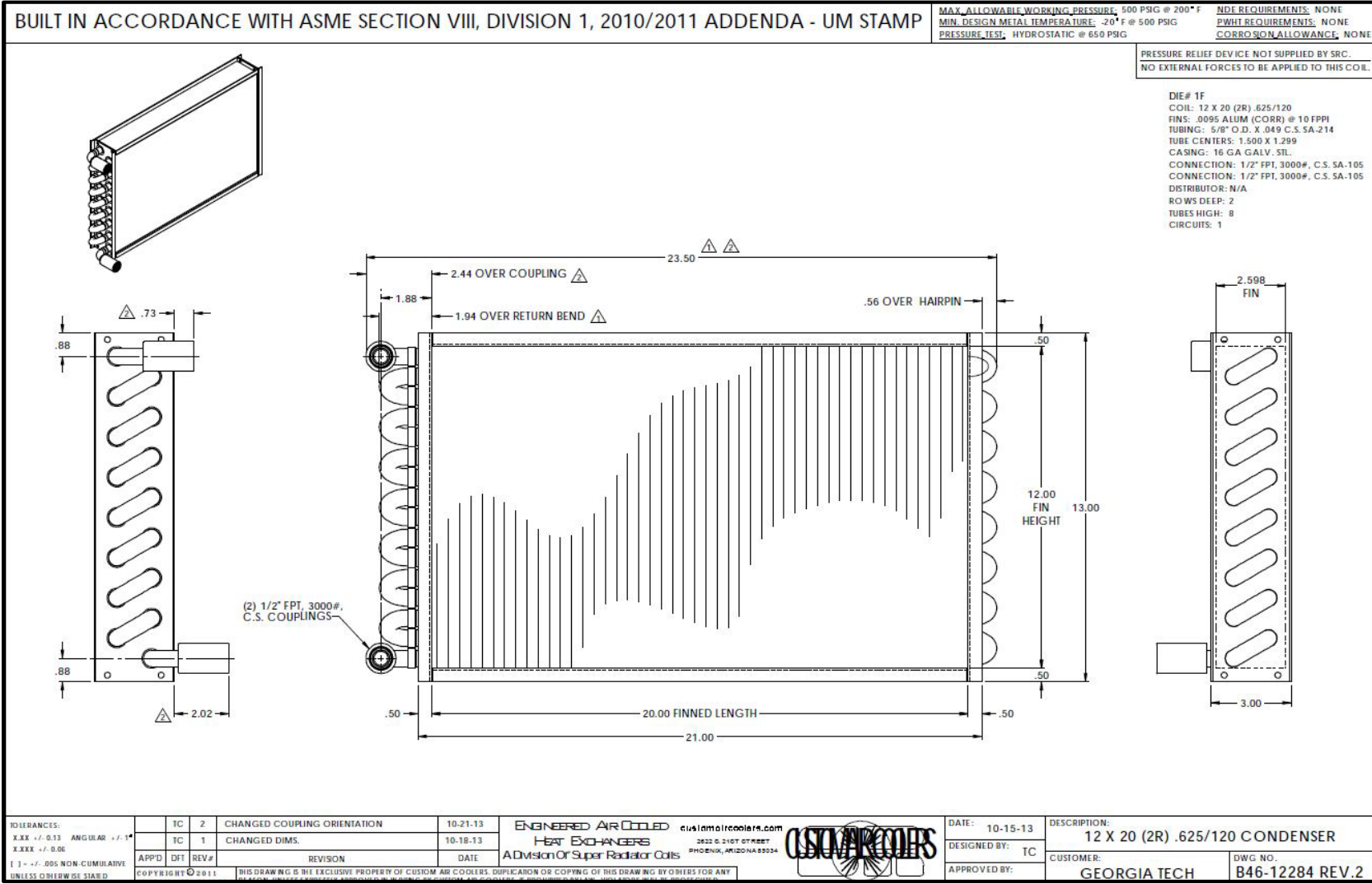
Figure 4.2 Drawing of 394-FPM round-tube corrugated-fin condenser
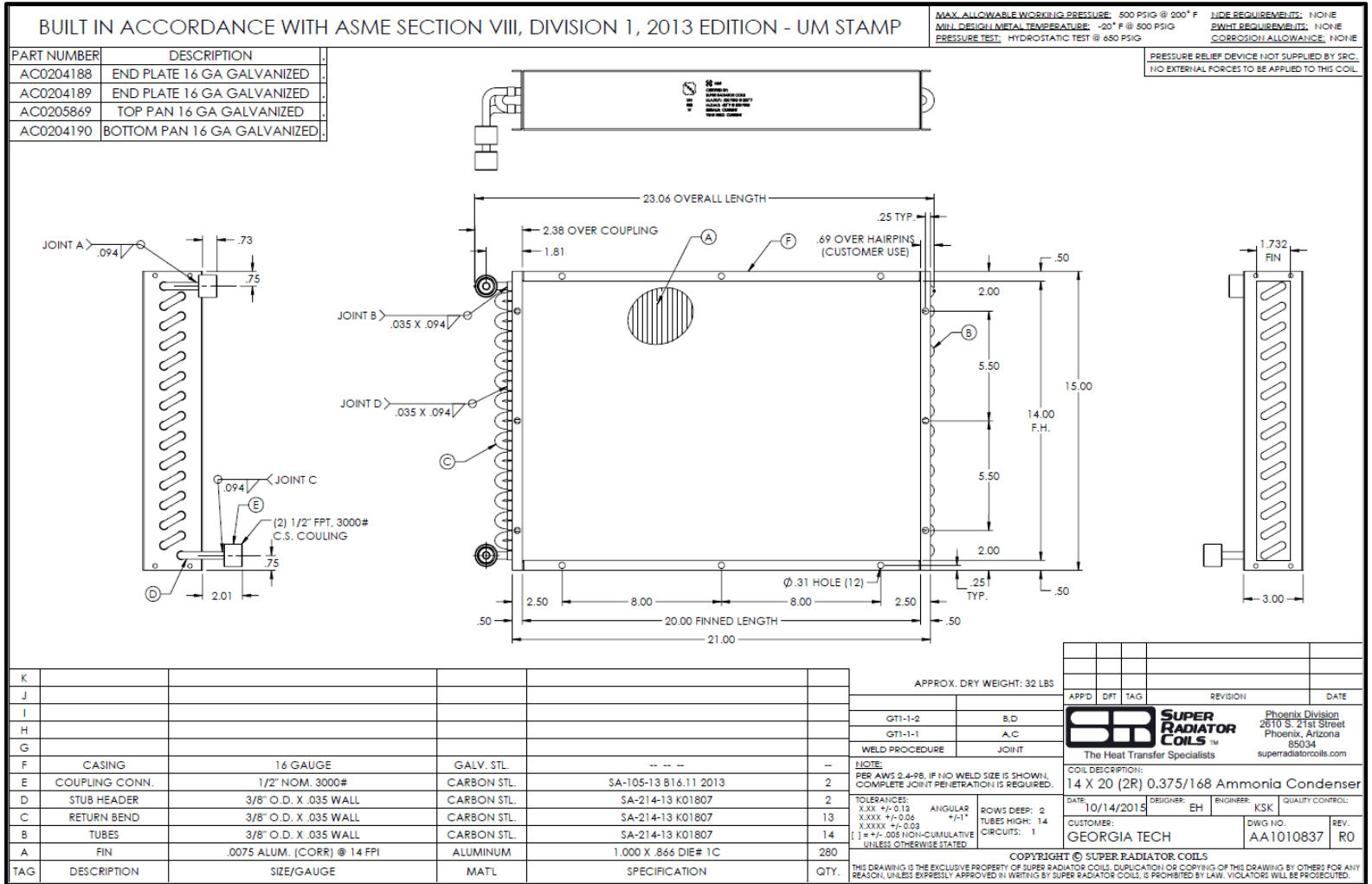
Figure 4.3 Drawing of 551-FPM round-tube corrugated-fin condenser

115

4.1.2 Multi-pass tube-array condensers

Two novel air-coupled condensers (Condenser M.1 and Condenser M.2) are designed in the present study to address the manufacturing challenges associated with carbon and stainless steel heat exchangers and potentially yield better heat transfer performance over conventional designs. The condensers are designed to work in the same compact absorption heat pump system with a design heat rejection rate of 2.51 kW into the ambient air. A multi-pass horizontal tube-array design is adopted for the condensers, which consists of multiple tube banks joined in a single header. Both the condensers have overall dimensions of 0.381 m height by 0.508 m width, and consist of a total of 120 tubes with an outer diameter of $3.175{\times}10^{-3}$ m and a wall thickness of $5.080{\times}10^{-4}$ m. The first version of the multi-pass condenser (Condenser M.1) and the path of the refrigerant inside the condenser are shown in Figure 4.4. The refrigerant vapor enters at the top of the condenser, splits into the first bundle of 48 staggered parallel tubes, and makes four passes in cross counter-flow through the air. The partially condensed refrigerant then recombines in the header before splitting into the second tube bundle of 36 parallel tubes and makes another four passes in cross co-flow through the air. As shown in the modeling chapter, the refrigerant switches between cross-counter and cross co-flow with respected to air while flowing from one tube bundle to the next. This pattern continues through the following two tube bundles before the refrigerant exits as a subcooled liquid at the bottom of the condenser. The large number of small diameter tubes results in high heat transfer coefficients and relatively high surface area on the air side. The number of parallel tubes in each subsequent tube bundle decreases to account for the decrease in specific volume

during condensation. Both the multi-pass tube-array condensers are designed in this manner to yield a relatively constant homogeneous velocity of the refrigerant throughout the condenser, which results in flow regimes that are optimal for heat transfer. The two-phase flow regimes prevalent in both the condensers are discussed in Chapter 3.

Test results for Condenser M.1 show a heat transfer rate at design conditions of about 2.35 kW. The second version of the Multi-pass tube-array design (Condenser M.2), similar to the conventional condensers, is made to improve performance and is shown in Figure 4.5 Multi-pass tube array condenser models were refined based on the experimental results. Thermal resistance plots from the refined model, shown in Chapter 3, clearly indicated that the heat transfer in Condenser M.1 is air-side limited. Hence, plain fins are designed to be installed in Condenser M.2 taking into consideration possible ways to braze them on the tubes while maximizing contact area.

The tubes in this multi-pass design consist of multiple bends, and they are fabricated and bent independently from other parts of the condenser. These tubes along with the fins are then sent to be brazed together into the header. The fabrication process for the multi-pass condensers involves the fins to be affixed on the tubes at the last step before brazing. Thus, the fins are designed to accommodate this fabrication process, and it is only possible to have the first pass and final pass of the tube to be in contact with the fin, although each tube makes four passes in the air. Various fabrication techniques such as stamping, water jetting, and laser cutting are explored for manufacturing the fins for this condenser. Due to tight tolerances of the size and position of the holes, a laser cutter is selected for fabricating the fins. The laser cut fins have the mid-section cut out for the two intermediate passes of each tube and are shown in Figure 4.6. The fins are installed at a

density of 394 fins per meter and held in place by custom made spacers as shown in the zoomed view in Figure 4.5. The header for Condenser M.2 is also redesigned, as shown in Figure 4.7, to increase the number of tube bundle from four to six while still maintaining the total number of tubes at 120. This decreases the number of parallel tubes per tube bank and therefore increases the tube-side refrigerant mass flux. Higher mass flux yields better heat transfer coefficients and also typically reduces maldistribution of liquid and vapor in the headers.
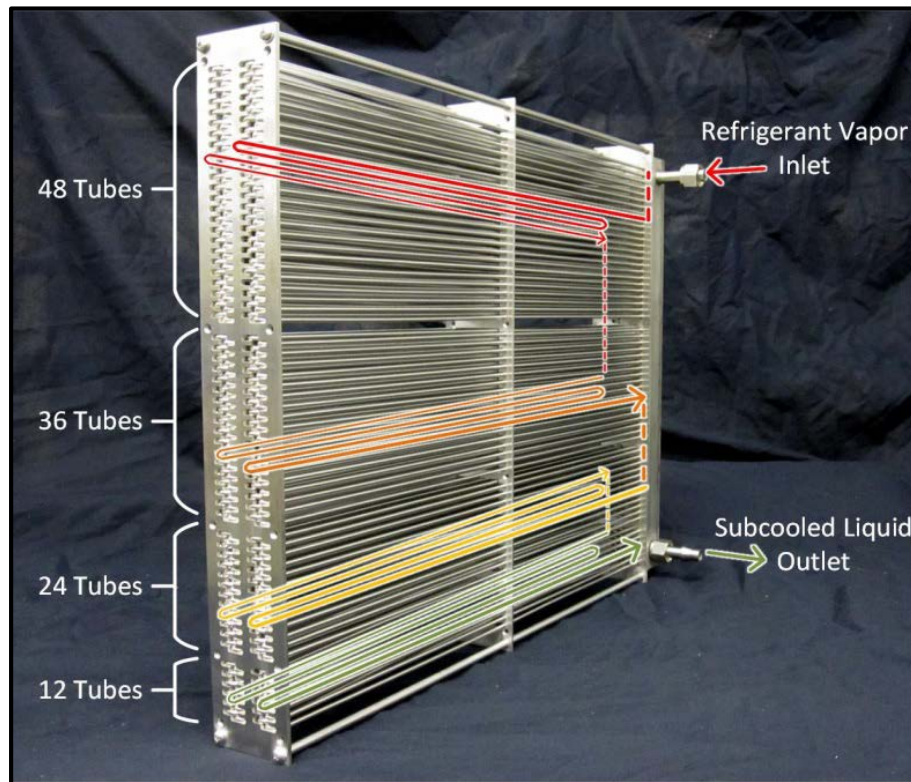
Figure 4.4 Schematic of refrigerant flow in the first version of multi-pass tube-array condenser (Condenser M.1)
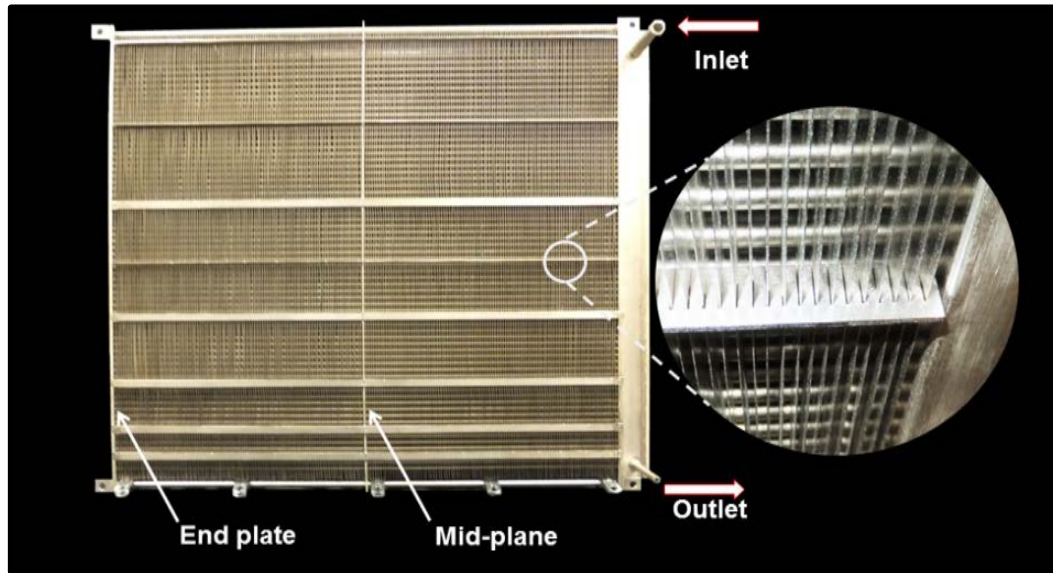
Figure 4.5 Second version of multi-pass tube-array condenser (Condenser M.2) with plain fins and spacer (zoomed)
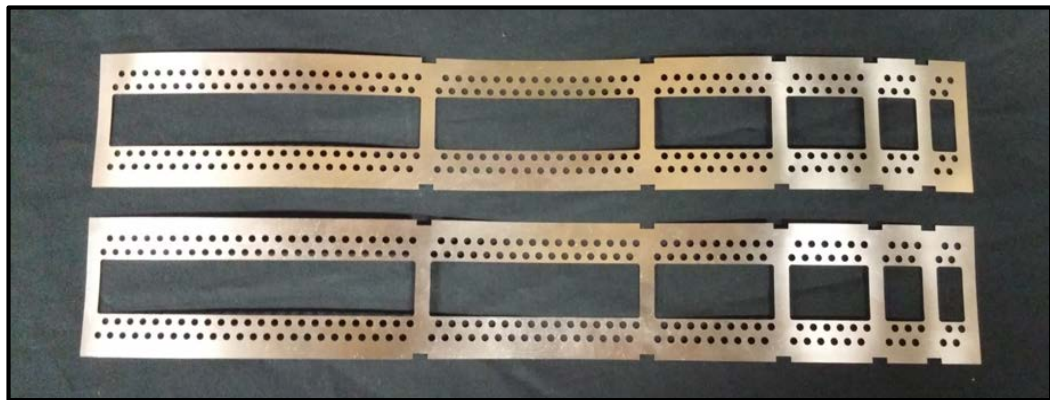
Figure 4.6 Laser cut fins for Condenser M.2
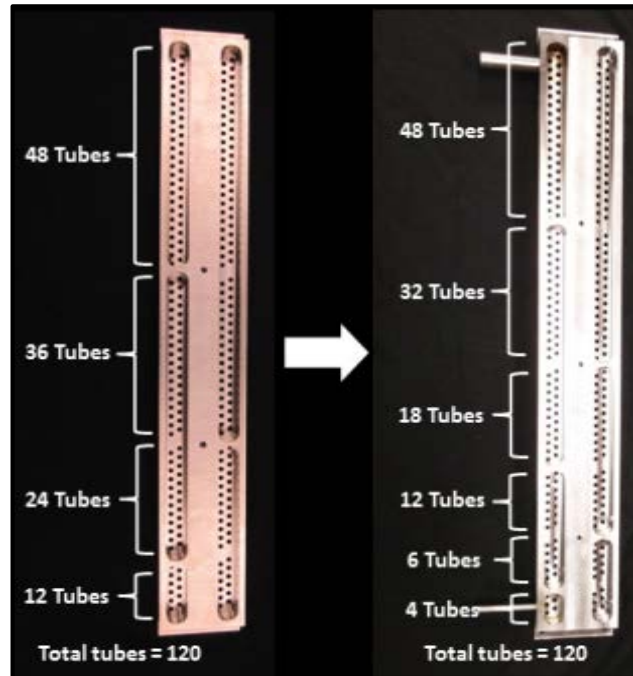
Figure 4.7 Modification of header design from Condenser M.1 (left)

4.2 Air-Cooled Condenser Experimental Test Setup

All the above-mentioned condensers, after fabrication, are tested in an air-handling unit in conjunction with a single-pressure ammonia-water test facility. The test setup is designed to simulate a range of ambient and solution inlet conditions for the condenser in the absorption system during normal operation.

4.2.1 Ammonia-water test facility

The ammonia-water test facility is constructed to treat the refrigerant to desired condenser inlet conditions in the system. A two-pressure test facility, replicating an entire absorption system, is usually required to reach specific condenser refrigerant inlet conditions expected in a heat pump. But a two-pressure system introduces significant complexity and requires all the components of a single-effect cycle including the

recuperative heat exchangers for operation at the desired conditions. Moreover, it is not possible to directly control and vary the condenser refrigerant inlet properties in such a setup. Thus, a single pressure test facility is constructed, and a schematic of the test loop with state points is shown in Figure 4.8. A separate pressurized hot water loop, parallel to the main loop, is used to boil the refrigerant in the boiler. The water is heated in the water loop using an electric circulation heater (Watlow CBDNF29R3S). The hot water transfers heat to ammonia-water in the counter-flow boiler (Exergy 00677-3 RW). The two-phase solution flows from the boiler [4] into the separator, where a tall sight glass mounted in parallel is used to observe the liquid level in the separator. Saturated vapor separates from the liquid due to buoyancy and exits at the top of the separator [5]. The liquid exits at the bottom of the separator [6] and flows through a regulating valve [8] (Swagelok SS-43GS8), which enables control of the liquid level in the separator. The saturated vapor flows into the condenser [11] in which heat is rejected in cross-flow to air. A bulls-eye sight glass [9] is used to verify that no liquid is flowing into the condenser. Depending on the operating conditions and performance of the condenser, the exiting solution [12] can be in a two-phase or subcooled state. This solution from the condenser combines with the liquid from the separator [13] and enters the subcooler. The subcooler (FlatPlate FPN3X8-14) cools the liquid mixture further to avoid cavitation in the gear pump. A solution tank upstream of the gear pump is used to maintain a solution inventory for the loop. The gear pump pumps the solution into the boiler at state point 3, completing the loop. Mass flow rates are measured using flow meters (MicroMotion CMF025M319NU) for the combined solution entering the boiler [3] and for the liquid exiting the separator [7]. Hence, the vapor mass flow rate through the condenser is the difference between the total and liquid mass flow

rates. Pressure transducers are located at the separator liquid outlet (Omega PX409-500AI) and condenser inlet (Omega PX409-750AI). Type-T thermocouples (Omega TMQSS-125G-6) are located upstream and downstream of all heat exchangers in the system. A differential pressure transducer is used to measure the tube-side pressure drop across the condenser (Omega PX409-015DWUI). Accuracy specifications and operating ranges for instrumentation used in this loop are detailed in Table 4.1.
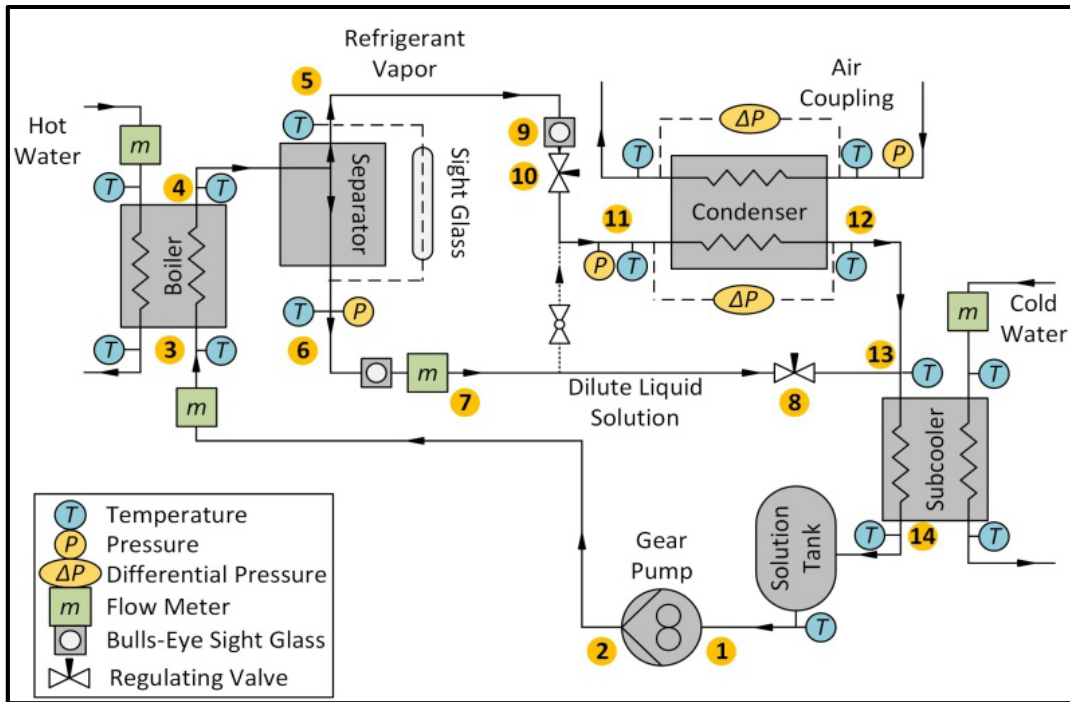
Figure 4.8 Ammonia-water test facility schematic

4.2.2 Air-handling unit

The air-handling unit preconditions the temperature and flow rate of the air entering the condenser. The condenser is mounted such that the air flows in cross flow to the solution, which flows inside the tubes of the condenser, as shown in Figure 4.9. A variable-speed fan is used to draw air across a series of measurement and flow conditioning devices.

122

The air first encounters a round-tube finned coil that circulates chilled water for any necessary pre-cooling. The air can then be heated by flowing over a steam-carrying air coil. Additionally, a series of ports along the face of the flow area permit the adjustment of humidity through the addition of steam. A flow straightener with an extruded honeycomb-like structure helps promote unidirectional flow. The air then flows over an array of thermal dispersion flow meters (Ebtron GP1 Type B) and a relative humidity sensor (Johnson Controls HE-67P2-0N00P). The flow area is then reduced to match the face area of the air-coupled heat exchanger being tested. The air flows through a second flow straightener before reaching the inlet face of the absorber. Thermocouple arrays upstream and downstream of the condenser are used to record approximate temperature profiles. The upstream and downstream arrays include 16 type-T thermocouple wires (Omega TT-T-30) in a 4×4 grid. A differential pressure transducer (Dwyer 607-3) is mounted with ports just upstream and downstream of the condenser. Automated vents in the ducting can be controlled to permit recirculation of air to be drawn from and rejected to the atmosphere.
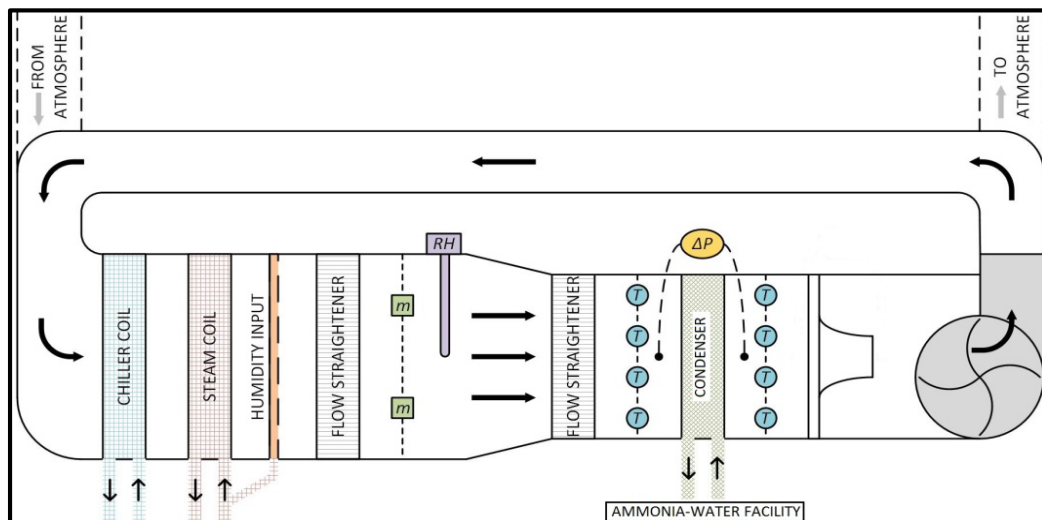
Figure 4.9 Air-handling unit schematic for air-coupled condenser testing

4.2.3 <u>Equipment and instrumentation</u>

A number of sensors and instruments are installed to determine the fluid states upstream and downstream of all equipment. A list of hardware and instrumentation used in the ammonia-water loop, air-handling loop, and the hot water loop is shown in Table 4.1. A temperature controlled oil bath is used for calibrating all the T-type thermocouples for accurate measurements. A National Instruments data acquisition system along with LabVIEW VI software is used to measure and record the data from these instruments. The data acquisition system uses temperature, voltage and current cards to detect signals from various sensors.

The ammonia-water test facility built for conditioning the refrigerant to desired condenser inlet conditions is shown in Figure 4.10. Flexible stainless steel hoses lined with PTFE are used to transport the refrigerant vapor and liquid streams to and from the condenser, which is mounted in the air-handling unit. The condenser inlet vapor hose has a diameter of 1.27×10^{-3} m, whereas the outlet liquid hose has a diameter 6.35×10^{-3} m. The larger diameter of the condenser inlet vapor hose addresses the high specific volume of vapor, and limits pressure drop. The smaller diameter tube at the condenser outlet results in a higher mass flux and helps in the mixing of liquid and vapor during extreme conditions when full condensation does not occur in the condenser. For accurate mixture temperature measurement at such conditions, a serpentine tube section is connected to the condenser outlet for better mixing with the thermocouple located downstream. A picture of the serpentine tube section is shown in Figure 4.10. All tubes and hoses in the ammonia-water facility and connections to the condenser are insulated with fiberglass or foam to minimize heat loss. The position of the tube-side differential pressure transducer is crucial to measure

the pressure drop across the condenser accurately. The setup of the differential pressure

transducer is illustrated in Figure 4.12. The bulls-eye sight glass is used to verify the liquid

level of the column visually, and the tube-side frictional pressure drop in the condenser is

calculated by subtracting the hydrostatic pressure of the liquid column (ρgh) from the

differential pressure transducer reading.
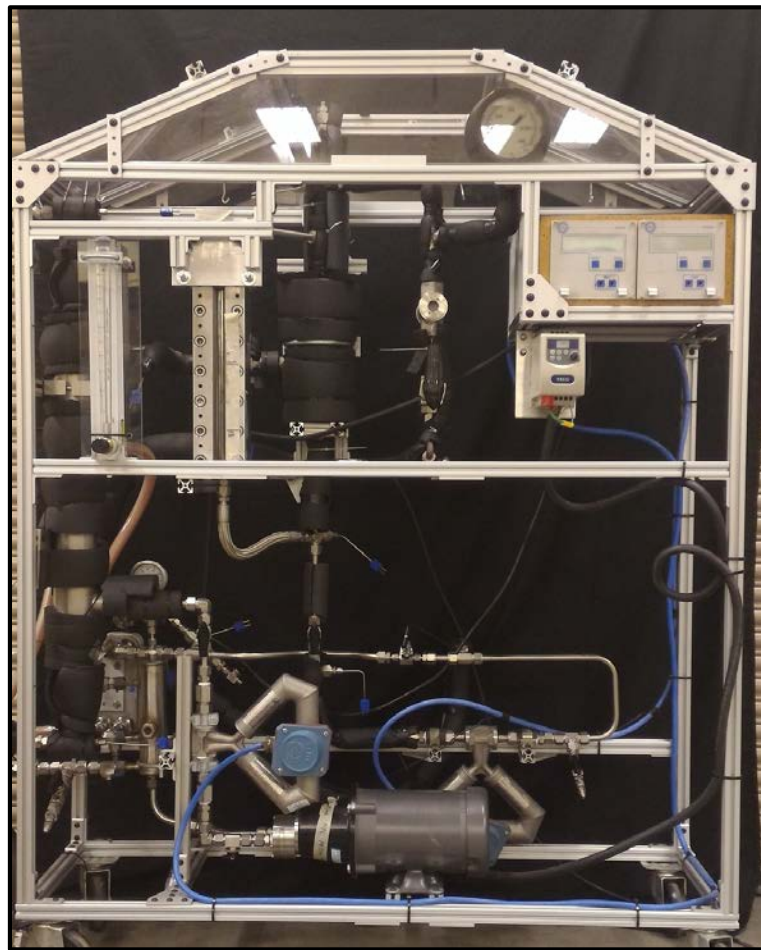
Figure 4.10 Picture of ammonia-water test facility
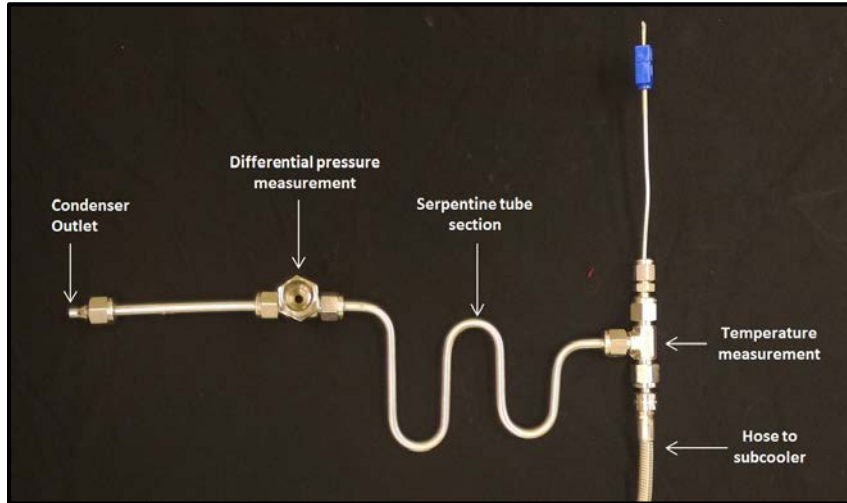
Figure 4.11 Picture of serpentine tube section for mixing
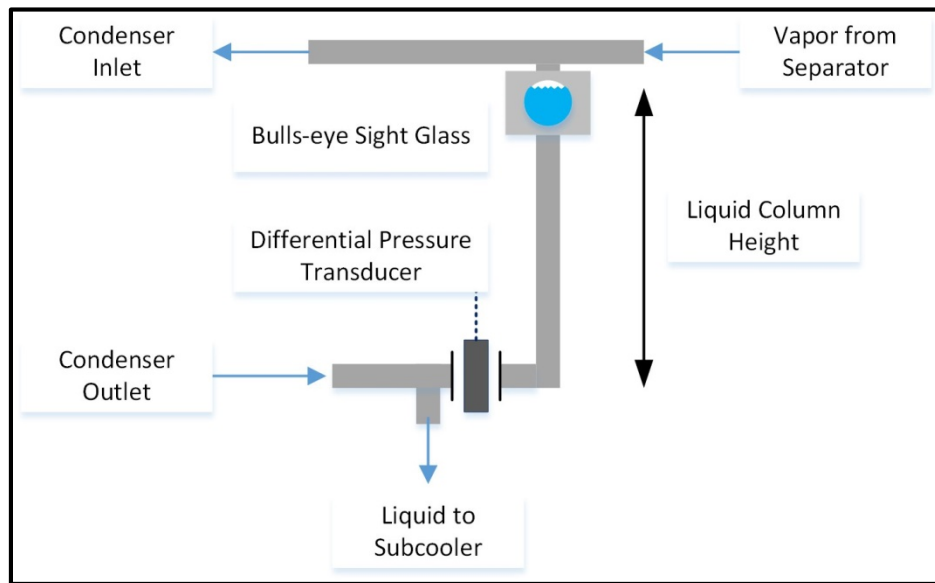
Figure 4.12 Tube-side differential pressure transducer position and measurement technique

Table 4.1 Equipment and instrumentation used for condenser testing

Fluid Loop	Name	Vendor	Model	Range	Accuracy
Ammonia-Water	Solution Gear Pump	Tuthill	TXS2.6EEET3W NB3OCO	-	-
	Combined Solution Flow Meter	MicroMotion	CMF025M319NU	0.60 kg s^{-1}	0.1% Reading
	Boiler Shell-and-Tube	Exergy	00677-3 RW	5.171 MPa	-
	Separator	In-House	Custom	600 psi	-
	Separator Sight Glass	PresSure Products	Seven LL Reflex	650 psi	-
	Vapor Sight Glass	PresSure Products	-	600 psi	-
	Liquid Flow Meter	MicroMotion	CMF025M319NU	0.60 kg s^{-1}	0.1% Reading
	Liquid Regulating Valve	Swagelok	SS-43GS8	-	-
	Vapor Regulating Valve	Swagelok	SS-6NRS8	-	-
	Subcooler	FlatPlate	FPN3X8-14	300 psi	-
	Solution Tank	In-house	Custom	-	-
	Fume Hood	Vent-A-Kiln	1332-500	0.19 m^3 s^{-1}	-
	Tube-Side Differential Pressure Transducer	Omega	PX409-015DWUI	103.4 kPa	1% FS
	Separator Absolute Pressure Transducer	Omega	PX409-500AI	3.447 MPa	0.5% FS
	Condenser Absolute Pressure Transducer	Omega	PX409-750AI	5.171 MPa	0.5% FS
	Type-T Thermocouple Probes	Omega	TMQSS-125G-6	−270-400°C	1°C or 0.75%
Air	Air-Side Differential Pressure Transducer	Dwyer	607-3	249 Pa	1% FS
	Absolute Air Pressure Transducer	Omegadyne	PX02K1-26A5T	88.04-108.4 kPa	0.1% FS
	Humidity Sensor	Johnson Controls	HE-67P2-0N00P	0-100%	2% FS
	Air Thermal Dispersion Flow Meter	Ebtron	GP1 Type B	25.4 m s^{-1}	2% Reading
	Inlet and Outlet (4x4 grid) Thermocouple Arrays	Omega	TT-T-30	0-150°C	1°C or 0.75%
	Flow Straighteners	Air Monitor	1.22×0.76 m, 0.61×0.61 m	-	-
Water	Water Absolute Pressure Transducer	Rosemount	2088: A3S2BA1M7	5.516 MPa	0.075% FS
	Water Flow Meter	Rosemount	8711: ASA30FR1E5G1	12 m s^{-1}	0.25% Reading
	Water Heater	Watlow	CBDNF29R3S	10.5 kW	-
	Water Gear Pump	Concentric Rockford	1070089	-	-
All	Data Acquisition System	National Instruments	cDAQ-9178	-	-

The inlet and outlet air temperatures of the condensers are also measured to calculate air-side heat duty and compare with the solution side. For accurate air temperature measurements, 4×4 thermocouple arrays are installed immediately upstream and downstream of the condenser. The disruption of air flow by the temperature measurements is prevented by using 0.254-mm thermocouple wire in the thermocouple arrays. These soldered thermocouple beads are held in place by four structural 0.51-mm stainless steel cables, stretched vertically across the face of the condenser. The thermocouple arrays are offset by 0.0254 m from the face of the condensers. A picture of the air-outlet thermocouple array arrangement is shown in Figure 4.13. Air pressure transducers are mounted to measure absolute and differential pressures and are perpendicular to the air flow at the middle of the condenser. Acrylic sheets, insulation, and tape are used to seal the condenser and prevent any air flow around the condenser.

Figure 4.13 Photograph of Condenser M.1 with the outlet thermocouple array

4.3 Experimental Procedure

4.3.1 <u>Charging and discharging procedure</u>

After the construction of the ammonia-water facility, leak testing is performed. The design pressure of the condenser in the absorption system is about 2900 kPa. The first pressure test is done with compressed air at 480 kPa. Significant leaks such as inlet/outlet valve partially open can be detected at this time as they usually make an audible noise. The second pressure test is performed with nitrogen at 3500 kPa along with a soap solution that detects small leaks by forming bubbles. These small leaks usually occur at fittings, which are tightened or changed to stop the leak. The facility is left pressurized at 3500 kPa over a period of 24 hours and the drop in absolute pressure is recorded. The pressure drop through leaks from the facility is calculated after adjusting for absolute pressure changes

due to change in temperature. If the resultant pressure drop from small leaks over a period of 24 hours is more than 15 kPa, a refrigerant leak testing is performed. For refrigerant leak testing, the facility is first filled with R134a, boosted with nitrogen to 3500 kPa, and a refrigerant leak detector is used to find tiny leaks. After all the non-negligible leaks are eliminated, the facility is ready for charging.

The heat pump cycle model predicts 99.79% ammonia mass fraction entering the condenser at a temperature of 74.74°C at design conditions. As it is quite difficult to attain such purity in a single pressure test facility, ammonia directly from industrial grade cylinders (99.99% pure) is used as the refrigerant for testing. Higher purity of ammonia leads to smaller temperature glide; therefore, the condenser inlet solution temperature must be lowered to keep the saturated liquid temperature in the condenser same as that in the overall cycle model. Thus, at design conditions, the inlet temperature of the refrigerant vapor is adjusted to 65.15°C to account for higher purity of refrigerant during component level testing. The temperature profiles of the refrigerant in the condenser for both the concentrations are shown in Figure 4.14. Having an adjusted refrigerant inlet temperature of 65.15°C matches the temperature profiles better and simulates system-level performance better.
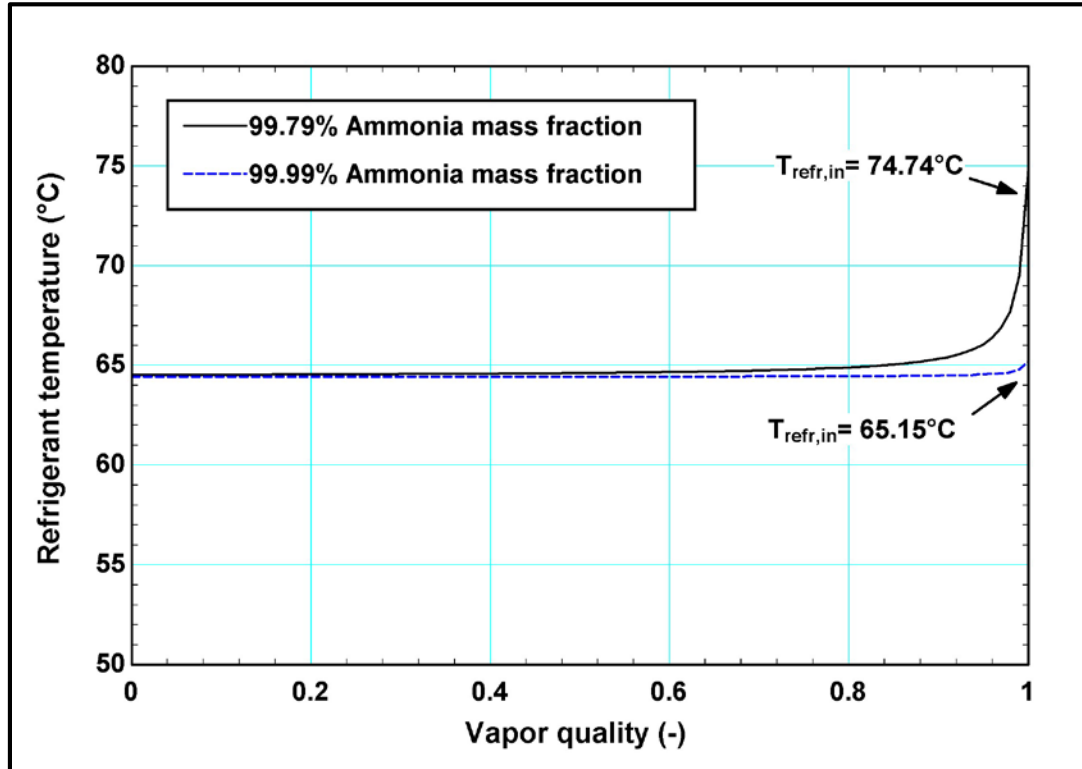
Figure 4.14 Temperature profile for adjusted condenser inlet conditions

The charging and discharging processes were conducted using a 115-liter tank, shown in Figure 4.15. This tank allows the operator to discharge any residual ammonia in the lines safely. Hoses connect the tank to the facility, ammonia cylinder, and vacuum pump. The presence of non-condensable gases in the system can have a significant effect on performance. The vacuum pump is used to evacuate the ammonia-water loop and the connected hoses. The valve to the vacuum pump is closed after the hoses and the system reach an absolute pressure less than 7 kPa. The ammonia cylinder is loaded on a weighing scale to measure the mass of ammonia leaving the tank. The tank is opened slowly, with the operator carefully checking for any signs of leakage. The ammonia is allowed to fill the connecting hose, and after that, the scale is zeroed. The valve between the facility and

131

the hose is slowly opened to allow the ammonia to flow into the facility. Due to the large drop in pressure between the ammonia tank and the facility, frost may form on the valve and the charging lines. Once the desired mass of ammonia has been added to the system (~2.4 kg for the present facility), the valve between the ammonia tank and facility is closed, along with the ammonia tank. As seen in Figure 4.15, the lines filled with ammonia are connected to the water in the tank through a valve. The valve is slowly opened for the absorption of ammonia from the lines into the water. Once all the ammonia from hoses is absorbed in the water, the tank is carefully disconnected.

Discharging of the system uses the same setup with the vacuum pump connection and the ammonia cylinder connection shut off. The discharge process involves the slow release of ammonia from the system into the large volume of water in the tank for proper disposal. The tank has a tapered outlet port with a ball valve at the bottom. This port allows for the discharge of water absorbed with ammonia while pouring fresh water into to the tank at the top. The pressure gauge on the water tank is monitored during the charging and discharging process for any sudden spike in pressure in the lines. The system is flushed with water and air to through all flow paths to remove any traces of ammonia.

Due to the toxicity and slight flammability of ammonia, care must be taken to minimize the risk of injury during testing and especially during charging/discharging. The ammonia-water test facility is surrounded by a curtain, and a fume hood is mounted on top of it. If a leak were to occur, the ammonia would be primarily contained within the curtained facility and funneled into the fume hood for safe venting. The laboratory is equipped with ammonia sensors (Honeywell MDA Scientific Midas, P/N: Midas-E-NH3) and gas masks (Sperian, NIOSH 100400) are kept on-hand in the event of a rapid leak.

After charging and discharging, all hoses exposed to ammonia are dipped in a tank of water or under a fume hood until no traces of ammonia are detectable. Protective eyewear is used throughout test facility construction and condenser testing. Care must be taken to prevent rises in pressure that approach working pressure limits of the hoses and other equipment in the facility.
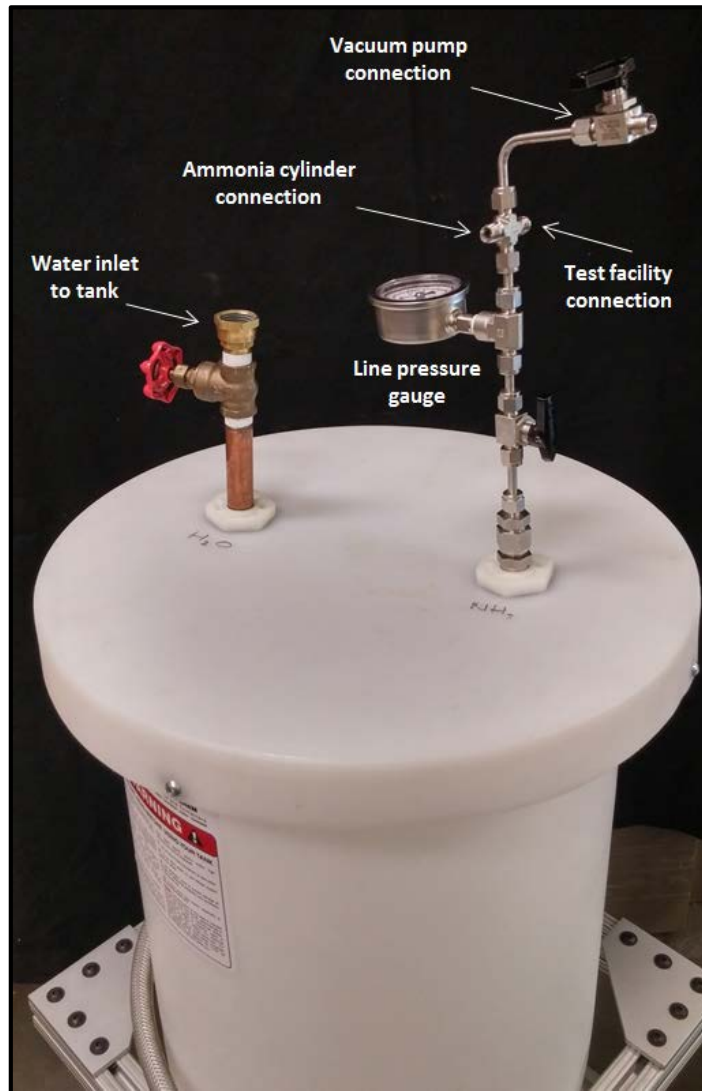
Figure 4.15 Ammonia charging and discharging tank

4.3.2 <u>Startup and testing procedure</u>

Prior to startup, initial checks are performed on the air-handling unit and the ammonia-water facility. Power to the sensors and instruments is switched on, and the outputs are checked on LabVIEW VI. In cases of erroneous values from sensors, troubleshooting is performed to fix the I/O instrumentation before the facility is started. After these initials checks and fixes, all fluids are circulated before addition of any heat. The water pump, ammonia solution pump, and the wind-tunnel fan are switched on. Once flow meters verify a steady flow of these fluids, heat is introduced. The steam line to the heating coil in the air-handling unit is slowly opened, and the electric heater on the water loop is set to higher temperatures. The set point temperature of the heater is raised gradually, with the operator keeping careful track of the water and ammonia-water pressures. Hoses in the water loop limit the water pressure to 415 kPa. Therefore the water loop is charged accordingly with water to keep the pressure below 415 kPa at the highest temperature point during testing (90°C). Once vapor starts flowing through the condenser, cooling water flows through the subcooler to prevent pump dry-out in case two-phase solution exiting the condenser. The temperature of the air is simultaneously raised through the flow of steam in the heating coil in the air-handling unit until the condenser inlet temperature is reached. The pump speed is gradually increased through the pump frequency controller to increase flow rates. Charge adjustment is usually performed at this point. If the liquid level is very high in the separator at the desired vapor flow rate, ammonia is bled out of the system to avoid spilling of liquid into the vapor line. If the solution tank before the gear pump has a very low level of liquid, ammonia is added to the system to avoid pump running dry. The addition of more ammonia requires the facility to be cooled to low

facility pressures. Sometimes when both the pressures in the facility and the cylinder reach saturation, the cylinder needs to be located on an elevated platform to add more ammonia to the system. Increasing the height of the cylinder creates a gravitation head for the liquid in the cylinder to flow into the system.

As the vapor flow rate increases through the condenser, the pressure drop across the condenser also increases inhibiting a further increase in vapor flow rate. Regulating valves on the vapor and liquid lines are used to adjust the vapor flow rate into the condenser as well as the height of the liquid level in the separator. The regulating valve on the liquid side is slowly closed to increase the pressure head of the pump and force more vapor to enter the condenser. Visual confirmation of single-phase flow in the vapor and liquid streams is possible through the Bulls-eye sight glasses.

Air inlet temperature to the condenser is indirectly controlled by the flow rate of steam through the heating coil in the air-handling unit. At start-up, a high steam flow rate is set to raise the temperature of the air because of the large thermal mass of the wind-tunnel. As the temperature of the air approaches the desired air inlet temperature, the steam flow rate is decreased. Running the air-handling unit while it is open to the atmosphere gives the operator better control over the condenser air inlet temperature. In recirculation mode, the air temperature starts rising due to the addition of heat from testing the condenser, and cold water needs to be pumped through the coils to keep the temperature steady. Controlling the cold water flow rate adds one more level of complexity for the operator. However, if the air-handling unit is open to the atmosphere, it is susceptible to outside ambient temperature fluctuations due to weather and time of the day. Also, at very low ambient temperatures, the steam coil is unable to raise the air temperature to 52°C.

Thus, most of the tests are performed in recirculation mode, and the operator very cautiously adjusts the steam flow rate to supply the difference between heat loss from the wind tunnel to the heat added by the condenser.

Data are collected upon achievement of steady state, when no upward or downward trend is observed in temperature and pressure readings. The refrigerant pressure transducer reading usually shows small spikes (~2% - 8% of the absolute pressure) due to operation of the gear pump in the facility. Oscillations in refrigerant and air mass flow rates within a small range ($\pm$ 2% of the average) are also acceptable. Readings are taken over a three-minute timeframe at a frequency of three measurements per second and averaged to account for any oscillatory behavior.

CHAPTER 5: RESULTS AND DISCUSSION

The conventional and novel multi-pass condensers are evaluated in the air-handling unit along with the single-pressure ammonia-water facility as discussed in the experimental approach section. Tests are conducted at design and off-design operating conditions. This chapter discusses and compares the predictions of the models with results from the tests on the condensers.

The test matrix used to evaluate these condensers is shown in Table 5.1. Test number [1] in the matrix represents the design conditions for the condenser in the heat pump system with only the modification of the refrigerant inlet temperature to 65.13°C. Test numbers [2] and [3] represent the upper and lower bounds of air inlet temperature variation, which replicates changes in ambient temperature for the system. In an actual system, a change in ambient temperature will also cause a change in refrigerant inlet temperature to the condenser. Thus, the refrigerant inlet temperature of the condenser is also changed with the ambient air temperature based on the modeling of the heat pump cycle. The corresponding cycle model values of the refrigerant inlet temperature are further modified for the present test conditions because of the higher ammonia concentration (99.99%) used in the test facility. This is done to correlate component level testing with actual operating conditions of the heat pump. Test numbers [4] and [5] represent the lower and upper limits of volumetric flow rate of air. The condensers are also evaluated by changing the refrigerant flow rate as shown in test numbers [6] to [7]. The shaded fields in Table 5.1 represent values that are different from design conditions.

Table 5.1 Test matrix for evaluation of condensers

Variable	Unit	Test Number						
		1	**2**	**3**	**4**	**5**	**6**	**7**
$T_{air,in}$	°C	**51.7**	**35**	**52**	51.7	51.7	51.7	51.7
$T_{ref,in}$	°C	**65.13**	**56.98**	**65.15**	65.13	65.13	65.13	65.13
$\dot{V}_{air,in}$	m³ s⁻¹	**0.35**	0.35	0.35	**0.33**	**0.46**	0.35	0.35
$\dot{m}_{ref}$	g s⁻¹	**2.47**	2.47	2.47	2.47	2.47	**1.90**	**2.50**

Analysis of the data is conducted on the Engineering Equation Solver (EES) (Klein, 2014) platform. Time-averaged values of different measured variables from the DAQ are used to calculate fluid properties and heat transfer rates. Vapor is assumed to be saturated at the refrigerant vapor outlet of the separator. This phase-quality assumption is required to determine the concentration of refrigerant vapor entering the condenser and hence set the third required state property along with the measured pressure and temperature. Air-side temperatures are calculated by averaging the 16 thermocouple measurements upstream and downstream of the condenser. Heat transfer rates are calculated on both the refrigerant- and the air- sides using inlet and outlet temperatures along with flow rates. At steady state operation, the heat transfer rates on both sides are compared and verified to be within 10%. The measured heat transfer rate from the solution side is used for further analysis due to non-uniformities in air temperature and velocity, and the difficulty in obtaining a well-mixed temperature representative of the entire air stream. The solution-side thermocouples provide a localized and well-mixed temperature measurement.

An uncertainty propagation analysis is conducted on the data from the present study. The calculation of the experimental heat transfer rate of the condenser is influenced by uncertainties in instrumentation, including thermocouples, pressure transducers, and flow meters. The method of uncertainty propagation proposed by Taylor and Kuyatt (1994) is used here. The uncertainty (U) in a calculated or dependent variable (y) is given by Equation (5.1). Here y is a function of several measured and independent variables $(x_1, x_2, x_3, \text{ etc.})$, and $(U_{x_1}, U_{x_2}, U_{x_3}, \text{etc.})$ are the respective uncertainties in the measurement of these independent variables. The uncertainty from random variation of the measurements is very low as numerous readings of the data points are collected and time averaged during steady state operation.

$$U_y^2 = \left(\frac{\partial y}{\partial x_1} U_{x_1} \right)^2 + \left(\frac{\partial y}{\partial x_2} U_{x_2} \right)^2 + \left(\frac{\partial y}{\partial x_3} U_{x_3} \right)^2 + ... \tag{5.1}$$

The uncertainties of all measurement devices are listed in Chapter 4. The estimation of a representative uncertainty in the tube-side heat transfer rate for one data point from its constituent measurement uncertainties is shown in Table 5.2.

Table 5.2 Uncertainty propagation used in heat transfer rate calculation

Partial Derivative	Uncertainty in measurement	% Uncertainty (of total)
$\dot{Q}_{\text{sol,HX}} = 2.368 \pm 0.0463 \, \text{kW} \, (\pm 1.9\%)$		
$\left(\partial \dot{Q}_{\text{sol,HX}} \big/ \partial \Delta P_{\text{sol,HX}} \right) = -0.00002$	$\pm 1.03 \, \text{kPa}$	0.00%
$\left(\partial \dot{Q}_{\text{sol,HX}} \big/ \partial \dot{m}_{\text{conc}} \right) = 7.301$	$\pm 0.015 \, \text{g s}^{-1}$	2.46%
$\left(\partial \dot{Q}_{\text{sol,HX}} \big/ \partial \dot{m}_{\text{dil}} \right) = -7.301$	$\pm 0.015 \, \text{g s}^{-1}$	2.46%
$\left(\partial \dot{Q}_{\text{sol,HX}} \big/ \partial P_{\text{sol,HX}} \right) = -0.00724$	$\pm 25.85 \, \text{kPa}$	34.36%
$\left(\partial \dot{Q}_{\text{sol,HX}} \big/ \partial T_{\text{sep,vap,out}} \right) = -0.06064$	$\pm 0.25 \text{°C}$	10.71%
$\left(\partial \dot{Q}_{\text{sol,HX}} \big/ \partial T_{\text{sol,hx,in}} \right) = 0.1304$	$\pm 0.25 \text{°C}$	49.51%
$\left(\partial \dot{Q}_{\text{sol,HX}} \big/ \partial T_{\text{sol,HX,out}} \right) = -0.01305$	$\pm 0.25 \text{°C}$	0.5%

5.1 Round-Tube Corrugated-Fin Condenser

The results from conventional round-tube corrugated-fin condensers (Condenser R.1 and Condenser R.2) are discussed in this section.

5.1.1 <u>Heat transfer</u>

The total heat transfer rate ($\dot{Q}_{total}$) is given by Equation (5.2) and is subdivided into two parts: heat transfer from condensation ($\dot{Q}_{cond}$) and heat transfer from subcooling of the refrigerant ($\dot{Q}_{subcool}$). These duties can be written in terms of the respective overall heat transfer coefficient (*U*), the heat transfer area (*A*), and logarithmic mean temperature difference (*LMTD*).

$$\dot{Q}_{total} = \dot{Q}_{cond} + \dot{Q}_{subcool} = U_{cond} \cdot A_{cond} \cdot LMTD_{cond} + U_{subcool} \cdot A_{subcool} \cdot LMTD_{subcool} \quad (5.2)$$

Air-side temperature plays a major role and determines the driving temperature difference for heat rejection from the condenser. Experimental results at various air and refrigerant inlet temperatures are shown for both conventional condensers in Figure 5.1. The air flow rate and other parameters are kept constant at design values during this variation of air inlet temperature to the condenser. The rate of heat rejection from the condensers gradually decreases as the air temperature increases. This is due to a decrease in the temperature difference between the two fluid streams (air and the refrigerant), reducing the *LMTD* of the heat exchanger. As shown in Figure 5.1, at the design temperature of 51.7°C, the heat transfer rate is about 2.34 kW (93% of design heat duty). The heat transfer rate for Condenser R.1 drops below design (2.51 kW) at about 48°C. Therefore, the condenser would perform well in a packaged system heat pump unit operating at ambient temperatures at or below 48°C. However, Condenser R.2 performs well above the design heat duty requirement for the full range of temperatures (37°C - 52°C). Model predictions for both conventional condensers are shown with solid lines in Figure 5.1. The model predicted heat transfer rates follow the trend of the experimental results and decrease with increasing air inlet temperatures. The Average Absolute Deviation (AAD) between predicted and measured values is calculated using Equation (5.3).

$$AAD = \frac{1}{N}\sum_{1}^{N}\frac{abs\left(\text{Measured-Predicted}\right)}{\text{Measured}}\times100\% \tag{5.3}$$

The AAD for Condenser R.1 is 2.10%, while for Condenser R.2, it is 1.47%. Overall, the models underpredict the measured data. The reason for this discrepancy is the method applied in the model to predict the progression of temperature within the

141

component. It is assumed that the air inlet temperature to the second row of tubes is at the outlet temperature of the first tube. This assumption increases the air temperature for the second row of tubes in the heat exchanger and leads to under predicting of the model heat transfer rate. As seen from Figure 5.1, the discrepancy between the model predictions and experimental results is pronounced at low temperatures, especially for Condenser R.1. This can be explained by the 50% larger transverse spacing between the tubes of Condenser R.1 than that of Condenser R.2. Larger spacing between front row tubes increases exposure of the second row to colder air, which enhances the experimental heat transfer rate at low air temperatures for Condenser R.1.
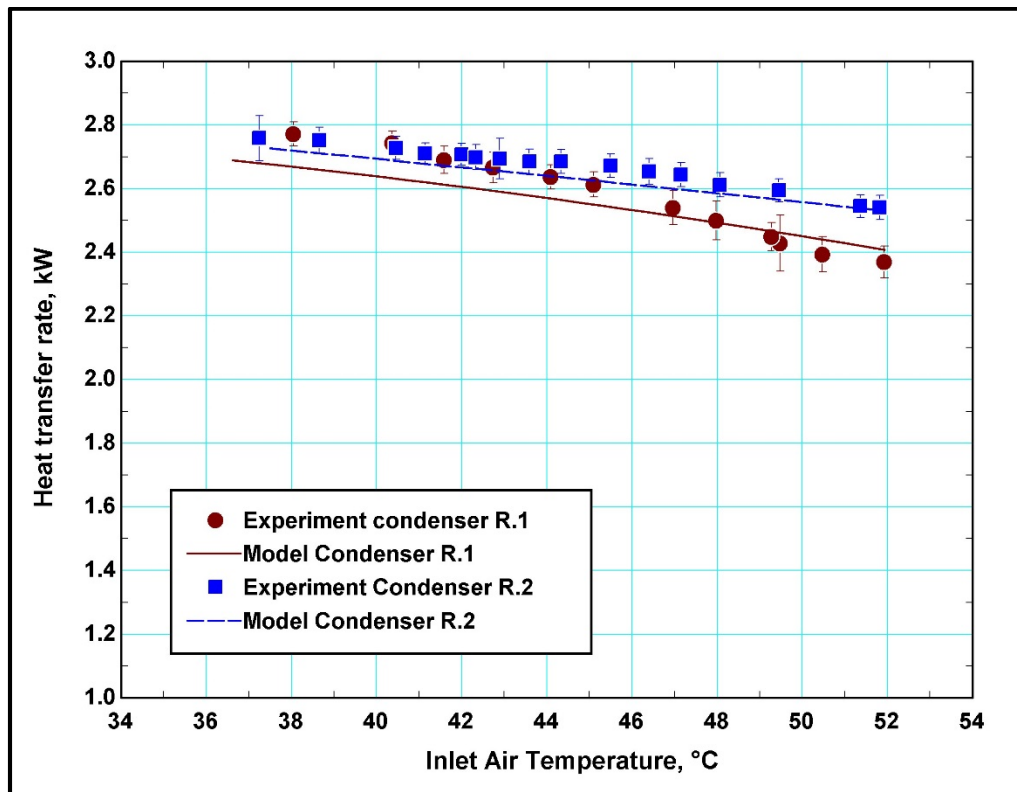
Figure 5.1 Heat duty of conventional corrugated-fin condensers with variation in ambient air temperature

Experimental results for both conventional condensers at various volumetric air flow rates are shown in Figure 5.2. Inlet air temperature, as well as refrigerant flow rate and temperature, are kept constant at design values. As the air flow rate is increased, the heat transfer rate increases for both condensers due to two factors. First, higher air velocities increase the air-side heat transfer coefficient. Second, higher mass flow rates of air increase the thermal capacity rates, leading to a smaller increase in air temperature and larger *LMTD* values for the heat exchanger. Model predictions of total heat transfer rate for both the condensers are also shown in Figure 5.2. The models closely predict the heat transfer rate with 1.51% AAD for Condenser R.1 and 0.89% AAD for Condenser R.2.
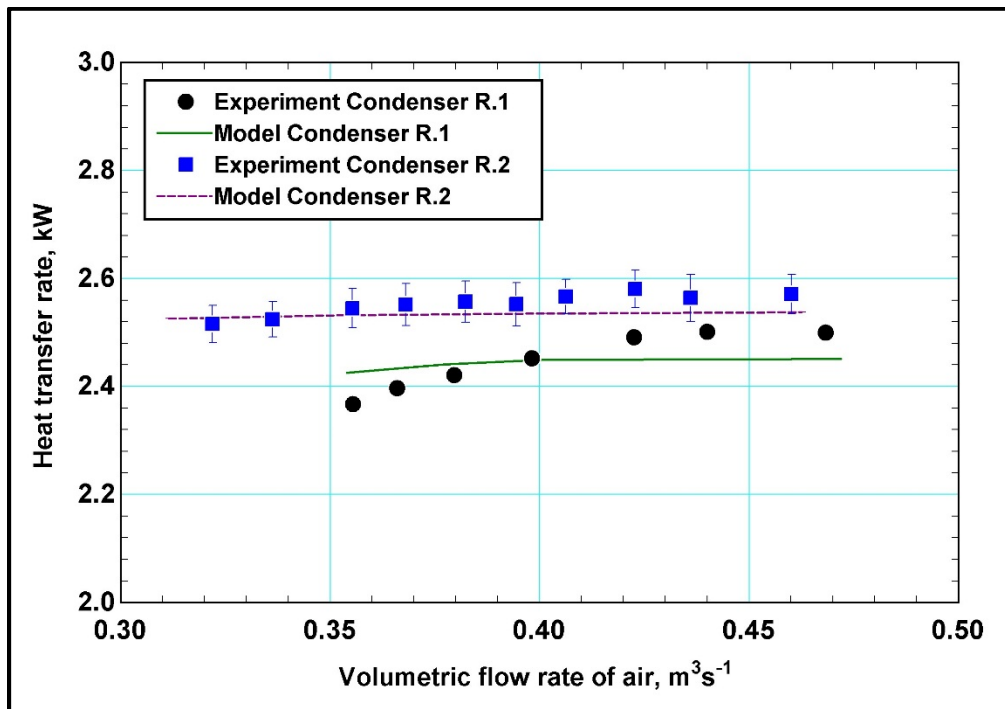
Figure 5.2 Heat duty of conventional corrugated-fin condensers with variation in air flow rate

The degree of refrigerant subcooling ($T_{subcool}$) as a function of air flow rate is shown in

Figure 5.3 for both conventional condensers. As the refrigerant flow rate and inlet conditions are the same for all the data points, $\dot{Q}_{cond}$ from Equation (5.2) is also almost constant for all points, except for minor differences due to slightly different two-phase/single-phase pressure drops and the corresponding saturation temperature changes. An increase in air flow rate increases both U_{cond} and $LMTD_{cond}$ but decreases A_{cond}, for constant $\dot{Q}_{cond}$, leaving more area for subcooling. Thus, changes in $\dot{Q}_{total}$ are due to changes in $\dot{Q}_{subcool}$ when air flow rate is varied. This can be confirmed by the fact that the trends of $\dot{Q}_{total}$ in Figure 5.2 and $T_{subcool}$ in

Figure 5.3 are the same for both the condensers.
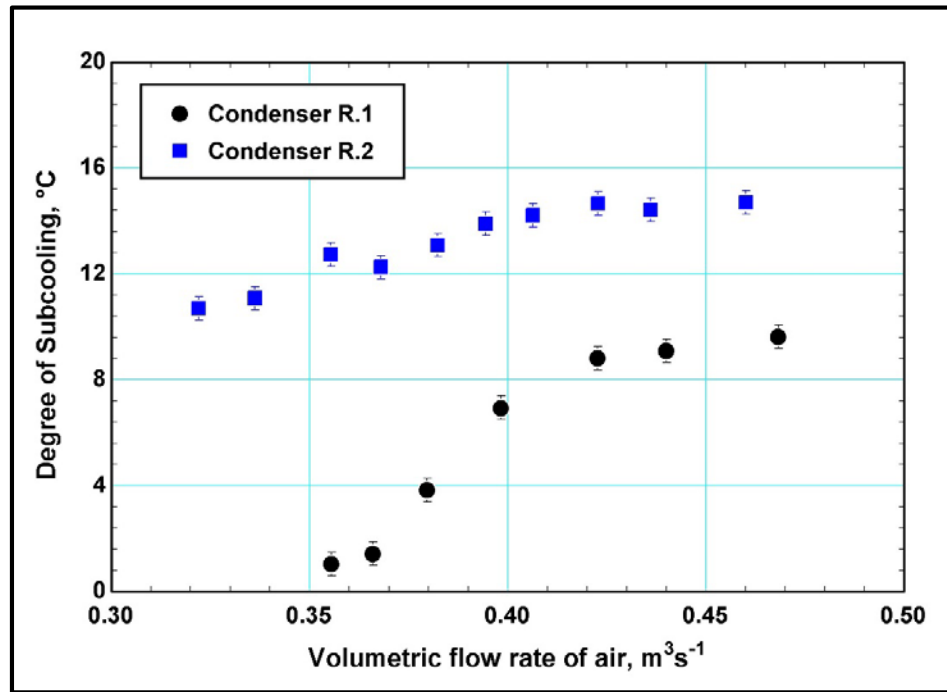
Figure 5.3 Refrigerant subcooling as a function of air flow rate for round-tube corrugated-fin condensers

As shown in Figure 5.2, the heat transfer rate for Condenser R.2 increases very slightly with about a 33% increase in air volumetric flow rate. This is due to a high degree of subcooling in the condenser. As the refrigerant heat capacity is low in the subcooling section, the refrigerant outlet temperature approaches the air inlet temperature, creating a pinch point. The same effect can be observed for Condenser R.1 for air flow rates greater than $0.42 \text{ m}^3\text{s}^{-1}$, where the heat transfer rate reaches a plateau. Another important observation is that Condenser R.1 plateaus at about 10°C of subcooling, whereas Condenser R.2 plateaus at about 15°C of subcooling. This can be explained from the thermal resistance plots predicted in Chapter 3. At the subcooled state, the internal resistance is higher than the external thermal resistance suggesting that the condensers are tube-side limited in that area. The internal thermal resistance of Condenser R.2 is lower than that of Condenser R.1 due to the smaller tube OD. The lower tube-side thermal resistance in the subcooled region leads to a high degree of subcooling for Condenser R.2.

5.1.2 Pressure drop

The tube-side pressure drop is measured between the condenser inlet and outlet, and corrected using the procedure discussed in Chapter 4. The tube-side pressure drop for the conventional condensers with varying solution flow rates is shown in Figure 5.4. Pressure drop increases for both condensers with increasing refrigerant flow rate and mass flux. The measured tube-side pressure drop for Condenser R.1 varies from -1 kPa to -0.2 kPa over the range of the refrigerant flow rates considered. The measured total pressure drop is higher for Condenser R.2 and ranges from 0.1 kPa to 2.7 kPa. This is because the Condenser R.2 has a smaller tube diameter than Condenser R.1. So, for the same mass flow

of refrigerant, the refrigerant mass flux and velocity is higher in Condenser R.2, leading to larger tube-side pressure drop. The uncertainty in the differential pressure transducer is 1% of the full-scale and the average uncertainty for the condensers is ±1.034 kPa. The model predictions for both Condenser R.1 and Condenser R.2 are also shown in Figure 5.4. The measured values follow the model predictions well and the differences are within the experimental uncertainty bars.
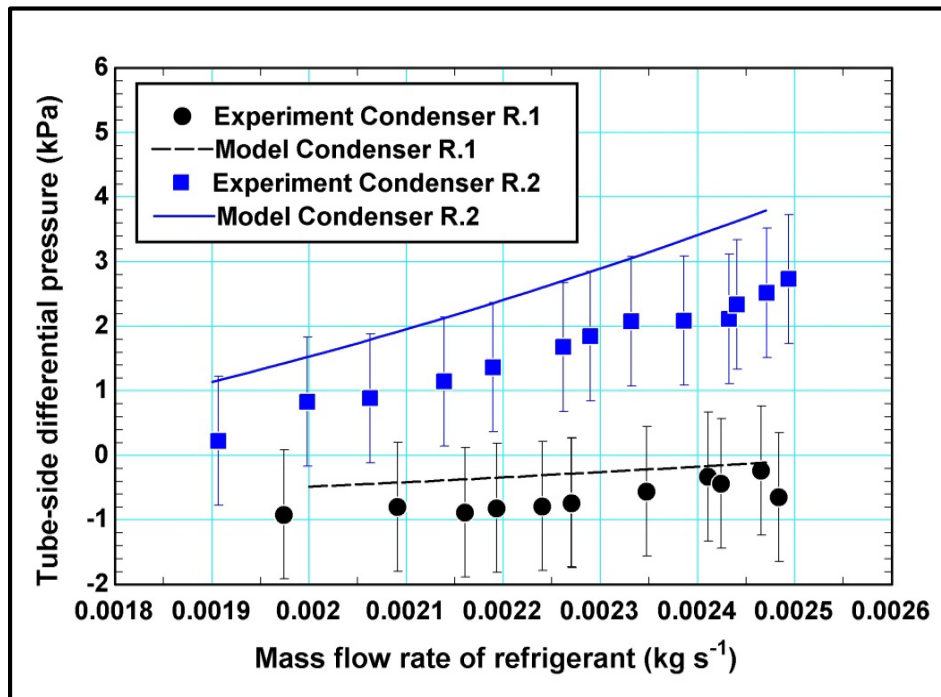
Figure 5.4 Tube-side pressure drop with variation in refrigerant flow for round-tube corrugated-fin condensers

Figure 5.4 shows that the tube-side pressure drop is negative for Condenser R.1, i.e., the refrigerant is at a higher pressure at the condenser outlet than at the condenser inlet. This is because of the high gravitational head and low frictional pressure drop, as the refrigerant flows in the direction of gravity. A representative plot of total pressure drop

146

predicted by the model along the length of Condenser R.1 is shown in Figure 5.5. The discontinuities in the slope of the pressure drop plot are due to increases in hydrostatic pressure between horizontal passes. The magnitude of these pressure drops can be seen to increase along the length of the condenser. This can be explained with the increase in refrigerant density due to decreasing vapor quality. Near the inlet of the condenser, frictional pressure drop dominates and the total pressure drop is positive. Near the end of the condenser, the gravitational pressure rise dominates and leads to negative total pressure drop in the condenser.
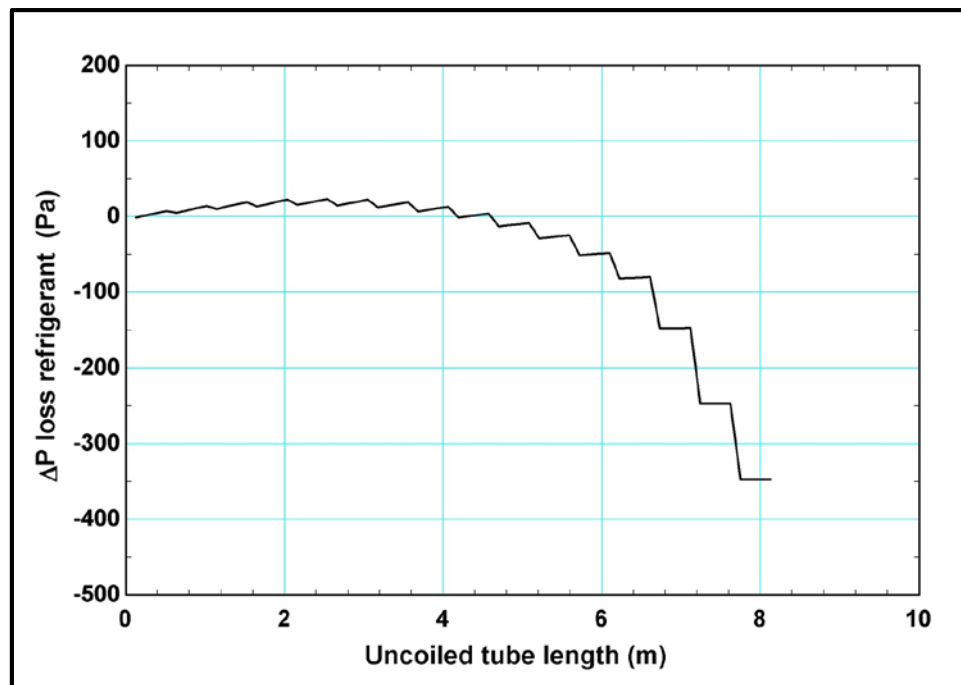
Figure 5.5 Total pressure drop in Condenser R.1 along the length of condenser

The air-side pressure drop is measured for both conventional condensers for the same range of volumetric air flow rates. However, the air free flow area (A_c) in the core of the two condensers is different: for Condenser R.1 it is 0.08 m^2, whereas for Condenser

R.2 the area is 0.10 m². Therefore, Reynolds number in the core ($\text{Re}_{D,\max}$) for the two condensers is different for the same volumetric flow rate. Thus, for proper comparison of the condensers, the air-side pressure drop is plotted with respect to the core velocity $(u_{\max})$ of air as shown in Figure 5.6. The air-side pressure drop increases with increasing volumetric flow rate of air for both condensers. While Condenser R.1 has a lower fin density, its smaller A_c results in higher velocity and higher pressure drops. The experimentally measured air-side pressure drop for Condenser R.1 ranges from 30.4 Pa to 48.9 Pa for the volumetric flow rate range from $0.35 \text{ m}^3\text{s}^{-1}$ to $0.46 \text{ m}^3\text{s}^{-1}$. Condenser R.2 has a larger A_c resulting in lower velocity and lower air-side pressure drop even with higher fin density. The experimentally measured air-side pressure drop for Condenser R.2 ranges from 21.6 Pa to 35.1 Pa for the volumetric flow rate range from $0.33 \text{ m}^3\text{s}^{-1}$ to $0.46 \text{ m}^3\text{s}^{-1}$.

A well-established correlation for air-side pressure drop for plain fins by Gray and Webb (1986) is also used and compared with the data, as shown in Figure 5.6. The wavy-fin correlation by Kim *et al.* (1997) is also plotted in the same figure for Condenser R.2. It is observed that the experimental data fall between the values predicted by the two correlations. The air flow in Condenser R.2 is at low velocities and reaches fully developed conditions because of the high fin-density and low Reynolds number in the core of the coil. At such high fin densities, the wavy fin is not particularly effective at providing additional mixing mechanisms. This may explain the air-side pressure drop in Condenser R.2 being similar to that seen in plain-finned heat exchangers.

Figure 5.6 shows the air-side pressure drop being significantly over predicted by the wavy fin models for both the condensers throughout the range of test data. The AAD between the model and the experimental results is 15.8% and 52.7% for Condenser R.1 and Condenser R.2, respectively. For Condenser R.1 at design conditions, major frictional losses dominate the air-side pressure drop (98.4%), while minor losses account for 1.3%, and acceleration in the core for 0.3% of the total air-side pressure drop. Of the total air-side frictional pressure drop, friction from the fins accounts for 96%, with the remainder from the tubes. The overall friction factor from experimental data, plain fin model, and wavy fin model, calculated from the superposition of the fin and tube friction factor, is plotted in Figure 5.7. The wavy fin model predicts significantly higher values of friction factors for Condenser R.2 because of the low Reynolds number of the flow. Also, Condenser R.2 has a larger contact area with air due to the higher fin density. It can be also observed from Figure 5.7 that the friction-factor values for Condenser R.1, deduced from the experimental data, are closely predicted by the wav-fin correlation. However, experimental friction factor values for Condenser R.2 are better predicted by the plain-fin correlation due to the low Reynolds number of the flow and the much higher fin density. Due to these reasons, wavy-fin pressure drop predictions for Condenser R.2 are significantly higher and do not follow the trend observed in the experiments. The authors (Kim *et al.*, 1997) in comparing their correlation with the data have noted that the error increases for configurations with a small number of rows at low Reynolds number. This over-prediction of pressure-drop in wavy-fin and tube heat exchangers has also been observed by past researchers (Forinash, 2015), especially for coils with high fin density.

Additional investigations on air-side pressure drop covering a large range of wave depth

and pitch of wavy fins are necessary to achieve better predictions.
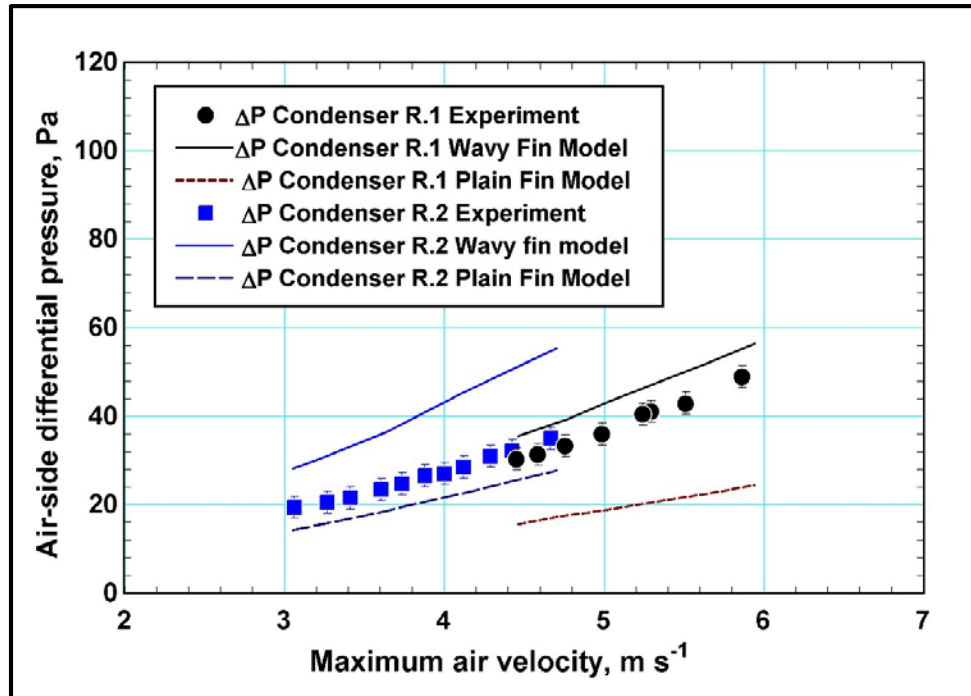
Figure 5.6 Air-side pressure drop for round-tube corrugated-fin condensers
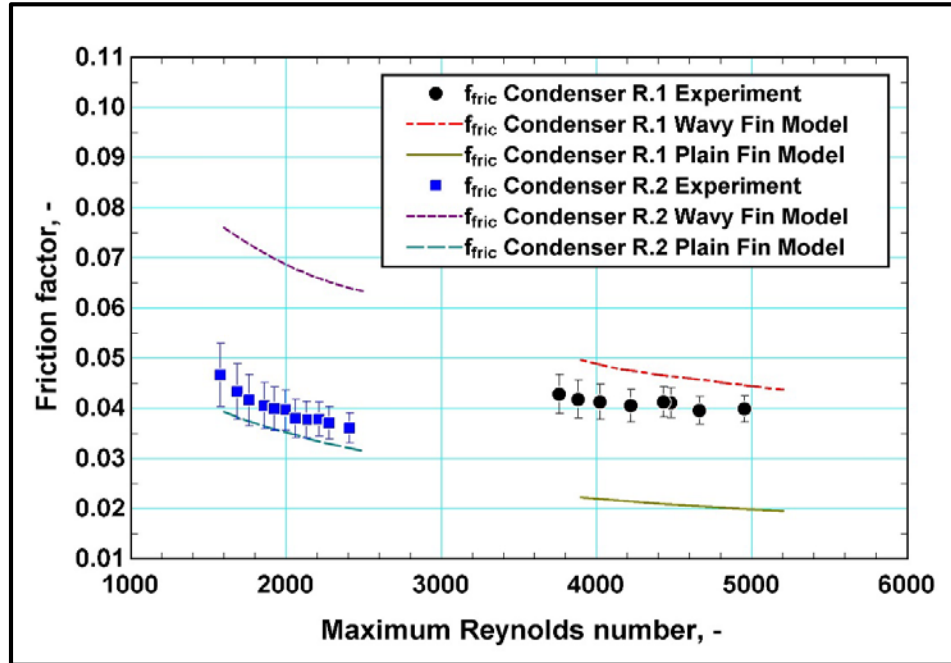
Figure 5.7 Air-side friction factor for round-tube corrugated-fin

5.2 Multi-Pass Tube-Array Condenser

The results from the novel multi-pass tube-array condensers (Condenser M.1 and Condenser M.2) are discussed in this section.

5.2.1 <u>Heat transfer</u>

The multi-pass tube array condensers have a complex geometry compared to the conventional condensers. The tube bundles in the multi-pass tube-array design consist of several parallel tubes and are in series arrangement with each other. As described in Chapter 3, alternate tube bundles have the refrigerant flowing in cross-parallel and cross-counterflow orientation with respect to the air. The heat rejected per pass for Condenser M.1 by all parallel tubes in a tube bundle is shown in Figure 5.8. The tube bundles and

their respective flow arrangement are labeled in the figure. Each tube consists of four passes that represent the four data points per tube bundle. The sum of the heat transfer rates for all the data points in the plot provides the total heat rejected by the condenser at steady state. Heat transfer increases with subsequent passes for the cross-counter flow arrangement and decreases with subsequent passes for the cross-parallel flow arrangement. This is because the refrigerant experiences lower inlet air temperature with every pass in a cross-counter flow arrangement and the opposite in a cross-parallel arrangement. As the refrigerant temperature is relatively constant after the initial glide, the air temperature is the key driver for heat transfer. Thus a lower inlet air temperature increases heat transfer and vice-versa. It can be also seen from Figure 5.8 that the overall heat transfer rate decreases with tube bundle number. This is mainly because the number of parallel tubes per tube bundle decreases, reducing the total heat transfer rate. This effect is also enhanced by the decrease in tube-side heat transfer coefficient as condensation proceeds.
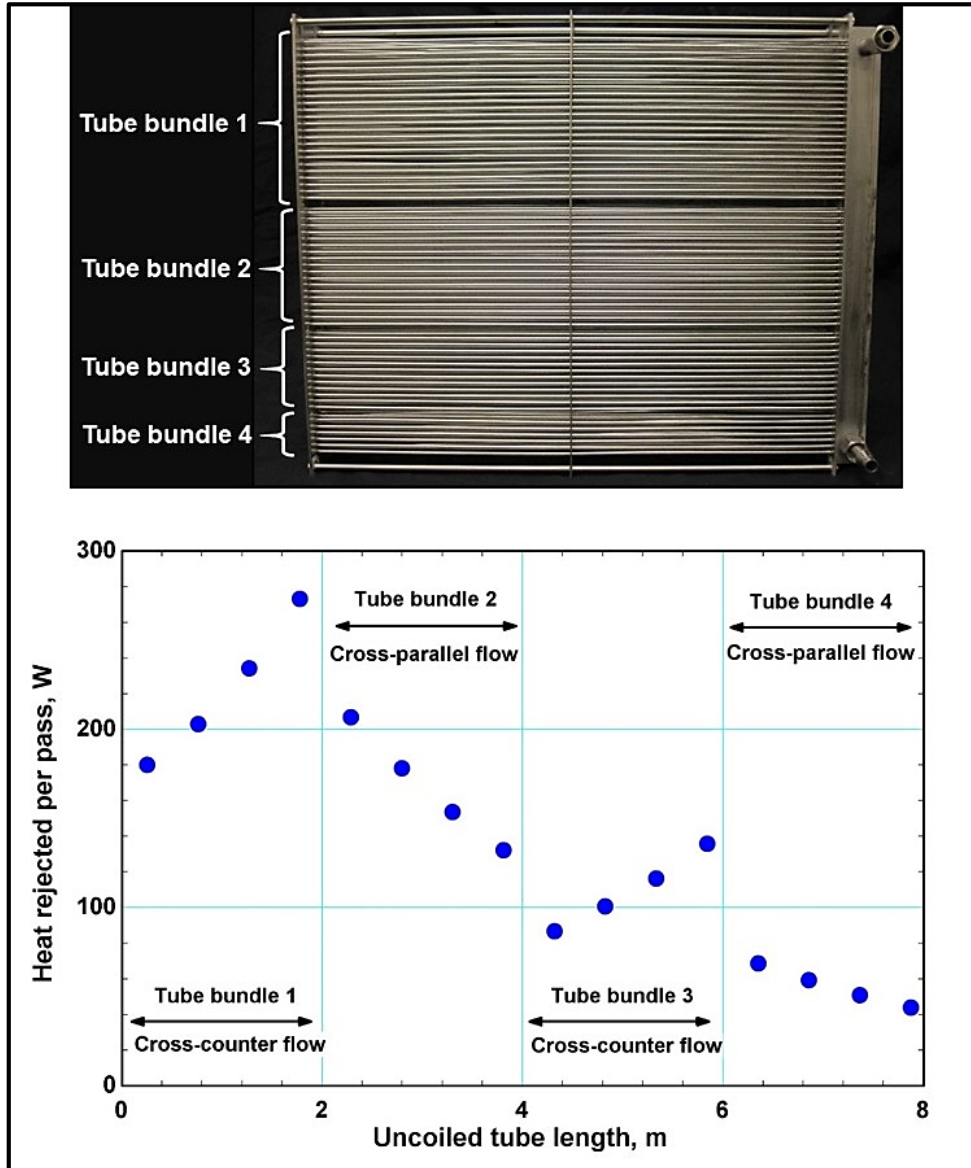
Figure 5.8 Heat rejection per pass in multi-pass tube-array Condenser M.1 at design conditions

The modeling strategy described in Chapter 3 is used for both multi-pass

condensers and the predicted total heat transfer rate is plotted with respect to the fraction

of the total tube-side area in Figure 5.9. It should be noted that the tube-side area for

Condenser M.1 and Condenser M.2 is the same. Thus, the fraction of the tube-side area

required to accomplish condensation is a good measure of comparison between the two

versions of the multi-pass condensers. The model predicts that Condenser M.2 performs

significantly better than Condenser M.1 with the addition of fins and approaches the

maximum heat rejection rate (2.6 kW) with about two-thirds of the total tube-side area.

However, the experimental heat transfer rate for Condenser M.2 is about 2.45 kW while

utilizing the entire tube-side area. This discrepancy between the predicted and measured

results is explored further. It is found that the fins in Condenser M.2 have poor contact with

the tubes.
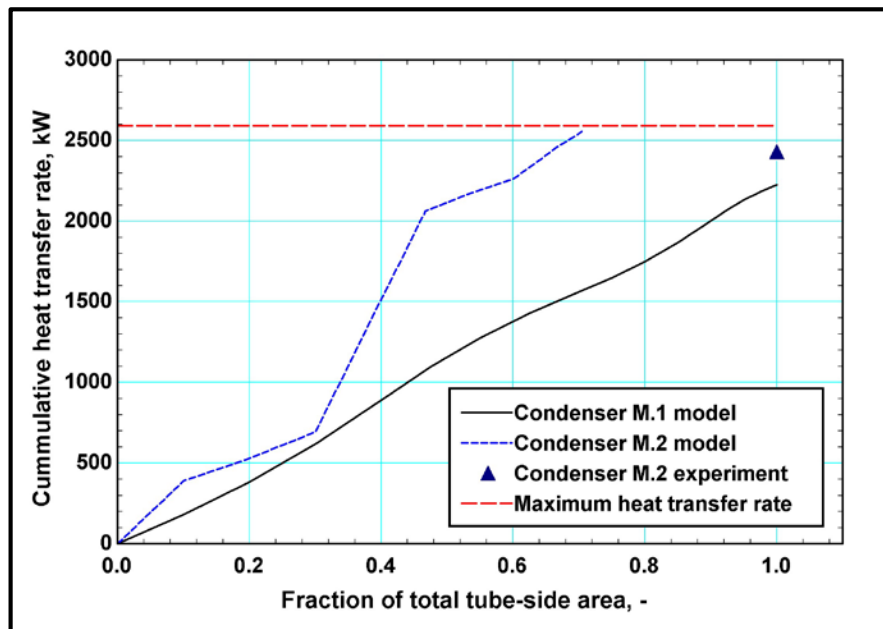
Figure 5.9 Predicted total heat transfer rate for multi-pass tube-array condensers at design conditions

The plain fins are fabricated using a laser cutter to increase the air-side area for

Condenser M.2. Unlike commercially available finned tube coils, these custom made fins

do not have a collar for fin-tube contact. The outer diameter of the tubes is 3.175 mm and the fins are fabricated with 3.328 mm openings. The hole size is kept slightly larger than the tube OD to allow for manufacturing tolerances and ease of assembly of 200 fins on 120 tubes. A brazing alloy was used to fill the gap between the hole and the tube OD. However, careful inspection revealed poor fin-tube contact. The brazing alloy, due to its high viscosity, seems to have not crept into the small gap between the tube and the fin in most places. Moreover, the brazing process requires the coil assembly to be kept in the oven for an extended period of time, which further increases the challenge. Due to the poor wetting of liquid metals, the brazing alloy does not stay in the gaps, but accumulates at the bottom due to gravity. Figure 5.10 shows the accumulation of brazing alloy at the bottom of the tube leading to partial contact between the fin and the tube. There are 12000 contact spots and it is difficult to quantify and model each one of them. An average contact angle (θ_c) subtended by the brazing alloy at the center of the tube is assumed for modeling purposes. The model for Condenser M.2 is accordingly modified to simulate heat transfer accurately.
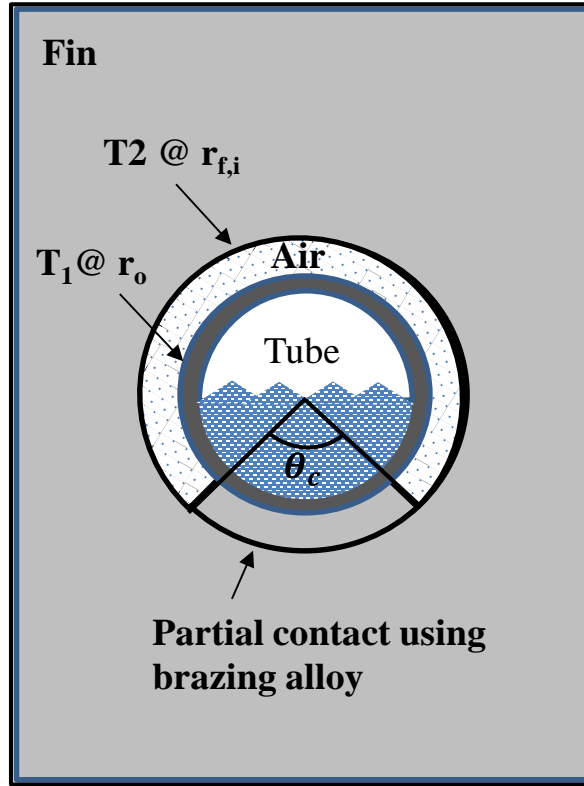
Figure 5.10 Schematic showing modeling of partial contact of tubes with plane fins in Condenser M.2

The contact angle (θ_c), shown in Figure 5.10, is used to calculate the contact resistance. The heat transfer through the fin (q_{fin}) can be written with an appropriate form of Fourier's law in radial coordinates, as shown in Equation (5.4). Acknowledging the fact that q_{fin} is independent of the radius and integrating in the radial direction, the contact resistance (R_c) is calculated, as shown in Equation (5.6).

$$q_{fin} = -k_{fin}(r\theta_c t_{fin})\frac{dT}{dr} \tag{5.4}$$

$$\frac{q_{fin}}{\theta_c t_{fin}} \int_{r_o}^{r_{f,i}} \frac{dr}{r} = -\int_{T_1}^{T_2} k_{fin} dT \tag{5.5}$$

$$R_c = \frac{(T_1 - T_2)}{q_{fin}} = \frac{\ln(\frac{r_{f,i}}{r_o})}{k_{fin}\theta_c t_{fin}} \tag{5.6}$$

The thermal resistance network for Condenser M.2 is modified to include this contact resistance as shown in Figure 5.11. Two parallel thermal resistances between tube wall and air can be identified: direct air contact or heat transfer through the fins. The conductive resistance through the tube $(R_{t,cond})$, the convective resistance from tube to air $(R_{t,air})$, the fin resistance $(R_{f,air})$, and the contact resistance (R_c), as shown in Figure 5.11, are defined for a single segment in Equations (5.7) to (5.10). The air gap between the tube and the fin can be assumed to be an insulator due to its low thermal conductivity and thus the resistance (R_{air}) is assumed to be infinite.

$$R_{t,cond} = \frac{\ln(r_o/r_i)}{2\pi k_{tube} L_{seg}} \tag{5.7}$$

$$R_{t,air} = \frac{1}{\alpha_{air} A_{unfin,seg}} \tag{5.8}$$

$$R_{f,air} = \frac{1}{\eta_{fin}\alpha_{air} A_{fin,seg}} \tag{5.9}$$

$$R_c = \frac{\ln(r_{f,i}/r_o)}{k_{fin}\theta_c(t_{fin} \times N_{fin,seg})} \tag{5.10}$$
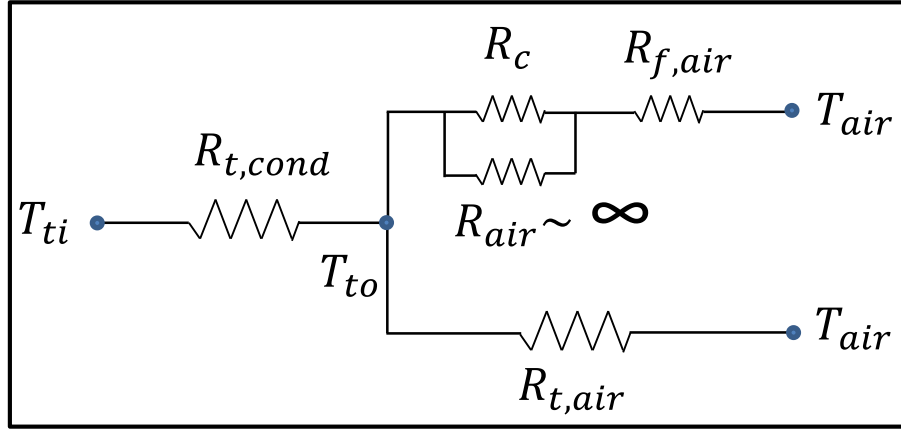
Figure 5.11 Modified thermal resistance network for Condenser M.2

The total thermal resistance of the network for Condenser M.2 is calculated using Equation (5.11).

$$R_{tot} = R_{in} + R_{t,cond} + \left(\frac{1}{(R_c + R_{f,air})} + \frac{1}{R_{t,air}} \right)^{-1} \tag{5.11}$$

However, the value of the average contact angle (θ_c) is required for calculation of R_c. The value of θ_c is determined to be $2°$ to achieve agreement between model predictions and experimental results at design conditions. It is expected that the actual contact angle will vary over a wide range of values. Although a $2°$ average contact is very small, representing failed brazing of the fins on the tubes, it introduces substantial sensitivity on the heat transfer rate of the condenser due to the huge number of contact points (12,000). The modified thermal resistances for Condenser M.2 are plotted along the length of the condenser as shown in Figure 5.13. The serrations in the outside resistance are caused by the absence of fins in the middle passes two of the tube. Similar to other resistance plots, the internal resistance suddenly increases with the transition to subcooled region at the end of the condenser.

158
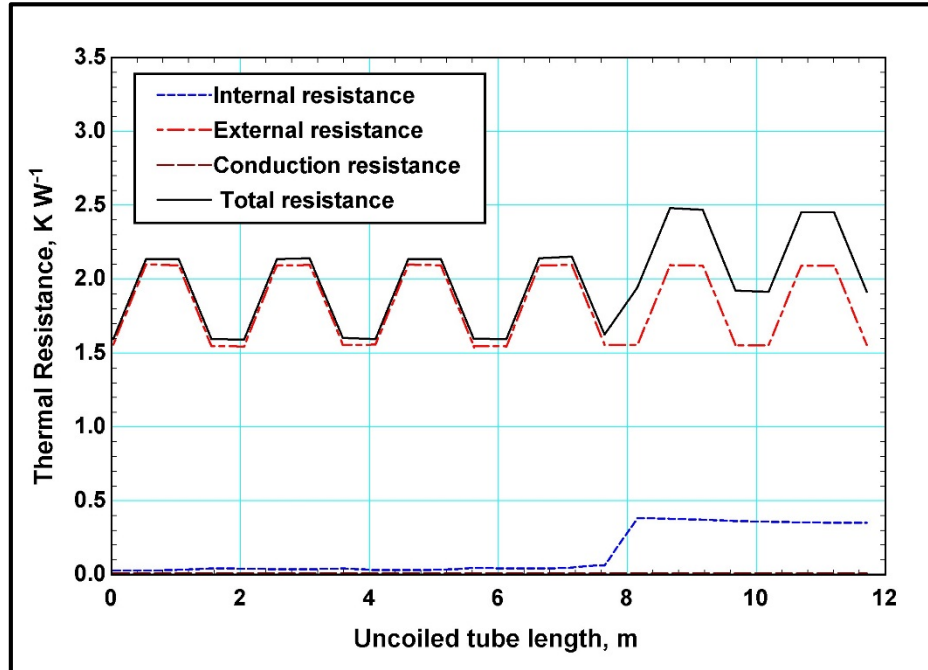
**Figure 5.12 Thermal resistances of Condenser M.2 modeled with
partial contact of fins**

Heat transfer in Condenser M.2 is predicted subsequently using the modified model which takes into account the partial contact of fins. The performance of both the multi-pass condensers is compared at design conditions and shown in Figure 5.13. Condenser M.2 shows about 4% increase in heat duty in comparison to Condenser M.1 at design conditions.

159
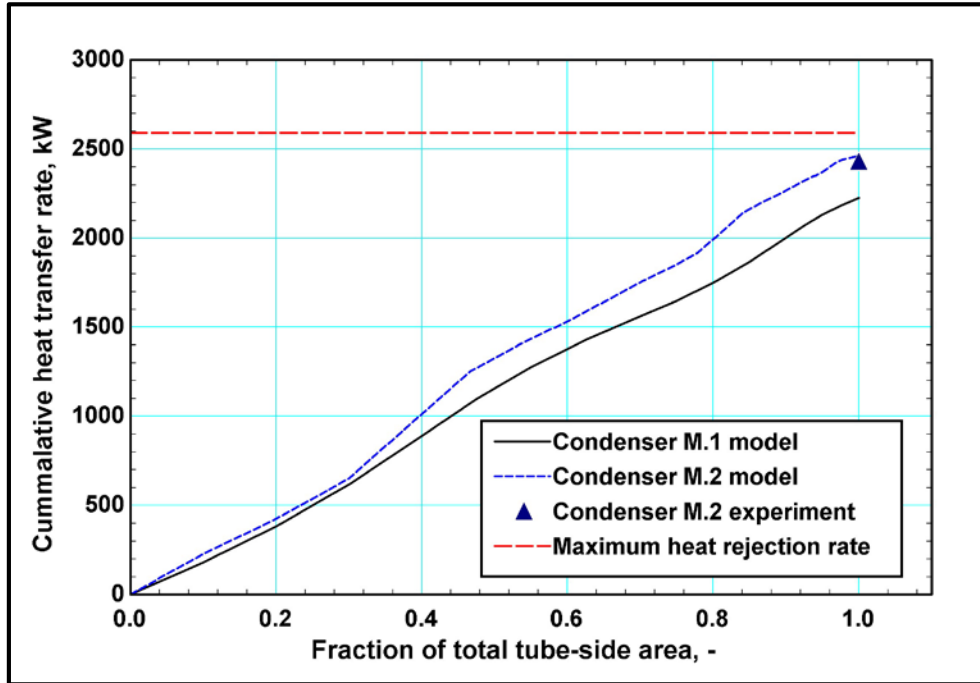
Figure 5.13 Predicted total heat transfer rate for multi-pass tube-array condensers at design conditions

Similar to the conventional condensers, the multi-pass condensers are evaluated over a range of air inlet temperatures. The refrigerant inlet temperature is also varied along with the ambient air temperature, as shown in the test matrix in Table 5.1, to simulate actual system operation. The rest of the variables are kept constant at design values. Experimental and model predictions of the heat rejection rates for both the multi-pass condensers are shown in Figure 5.14. As expected, the heat transfer rate for both condensers is higher at lower ambient temperatures. This is because as the air inlet temperature decreases, the *LMTD* of the heat exchanger increases, increasing the heat duty. As seen from the plot, the heat transfer rates drop below design (2.51 kW) at about 48°C for Condenser M.1 and at about 50.5°C for Condenser M.2. The model predictions for both condensers follow the trend well and are shown with solid lines in the same plot. The AAD between predictions

and measured values is 2.82% and 2.14% for Condenser M.1 model and Condenser M.2 model, respectively. Similar to the case for the conventional condensers, deviation from the data occurs mostly at lower air inlet temperatures, in part due to the assumption that inlet air temperature to the staggered tube row is the outlet temperature of the first row. However, at lower air inlet temperature, air received by the staggered tube row is likely to be at a lower temperature. Furthermore, heat loss from the header is not accounted for in the model.
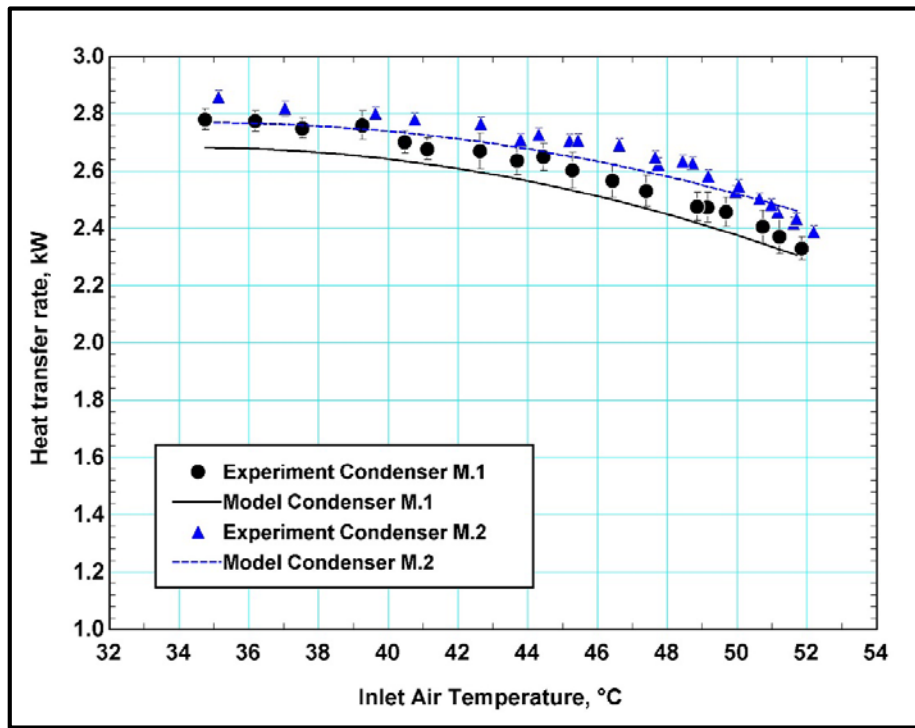
Figure 5.14 Heat-duty of multi-pass tube-array condensers with variation in ambient temperature

Air flow rates for both multi-pass condensers are varied independently and the heat duties for both multi-pass condensers are shown in Figure 5.15. There is a steady increase in heat transfer rate for both condensers with increasing air-flow rate. As explained for the conventional condensers, this increase in performance is attributed to two factors: increase

in heat transfer coefficient (*U*) and increase in heat capacity leading to higher *LMTD* between the two fluids. The models also predict this steady increase in heat duty with air flow rate as shown in Figure 5.15. The AAD between predictions and measured values is 3.18% and 1.64% for Condenser M.1 model and Condenser M.2, respectively. In general, the data for Condenser M.1 have higher uncertainties than those for Condenser M.2. This is due to minor improvements to the facility after Condenser M.1 testing to better control the inlet conditions and also decrease experimental uncertainties.
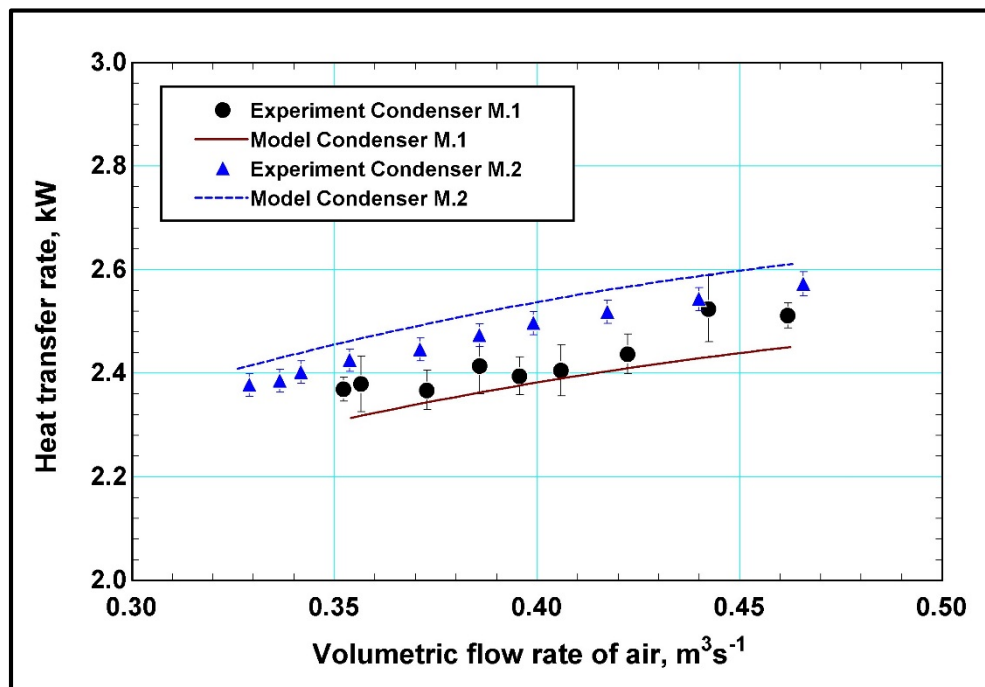
Figure 5.15 Heat-duty of multi-pass tube-array condensers with variation in air-flow rate

The multi-pass tube-array condenser models provide further insight into the total heat transfer rate described in Equation (5.2). The predicted increase in overall heat transfer for Condenser M.1 when the air-flow rate is increased by 31% is ~26%. The air-side heat transfer coefficient increases by about 14% for a 31% increase in air flow rate. The

162

remainder of the increase is due to the increase in overall *LMTD* between the air and the refrigerant sides. Another important observation to make here is that unlike the round-tube corrugated-fin condensers, the heat transfer rates do not plateau out in the case of the multi-pass condensers. This is mainly because the *LMTD* continues to increase for the multi-pass condensers up to an air flow rate of $0.47 \text{ m}^3\text{s}^{-1}$. In the multi-pass tube-array design, air passes through eight rows of tubes as compared to two tube rows in the conventional condenser design, thereby offering a closer approximation to an overall counterflow configuration. The temperature of the air rises sharply through the initial tube rows due to the low specific heat capacity of air. Figure 5.16 shows the experimental temperature profile at the inlet and outlet of Condenser M.1 at the design conditions. Some tube surface temperature measurements were also conducted on the condensers to approximate the refrigerant temperature inside the tubes. These tube surface temperatures are plotted as a line in Figure 5.16, where the peaks represent the tubes with vapor and the troughs represent the tubes filled with subcooled liquid. The outlet air temperature can be seen to reach to values above 62°C whereas the vapor temperature is about 64°C. The last few tube rows seem to receive air at high temperatures and are not able to reject heat. An increase in air flow rate increases the thermal capacity rate of air, lowers the inlet air temperature for the last tube rows increasing the performance of the condensers. Moreover, the multi-pass tube-array design allows use of tubes with very small OD, leading to very low internal thermal resistance. As seen from Figure 5.12, the multi-pass condensers are air-side limited in the sub-cooled region in contrast to the conventional condensers. Thus, multi-pass tube-array design benefits from the steady increase in heat transfer rate for a large range of airflow rates, unlike the conventional condensers.
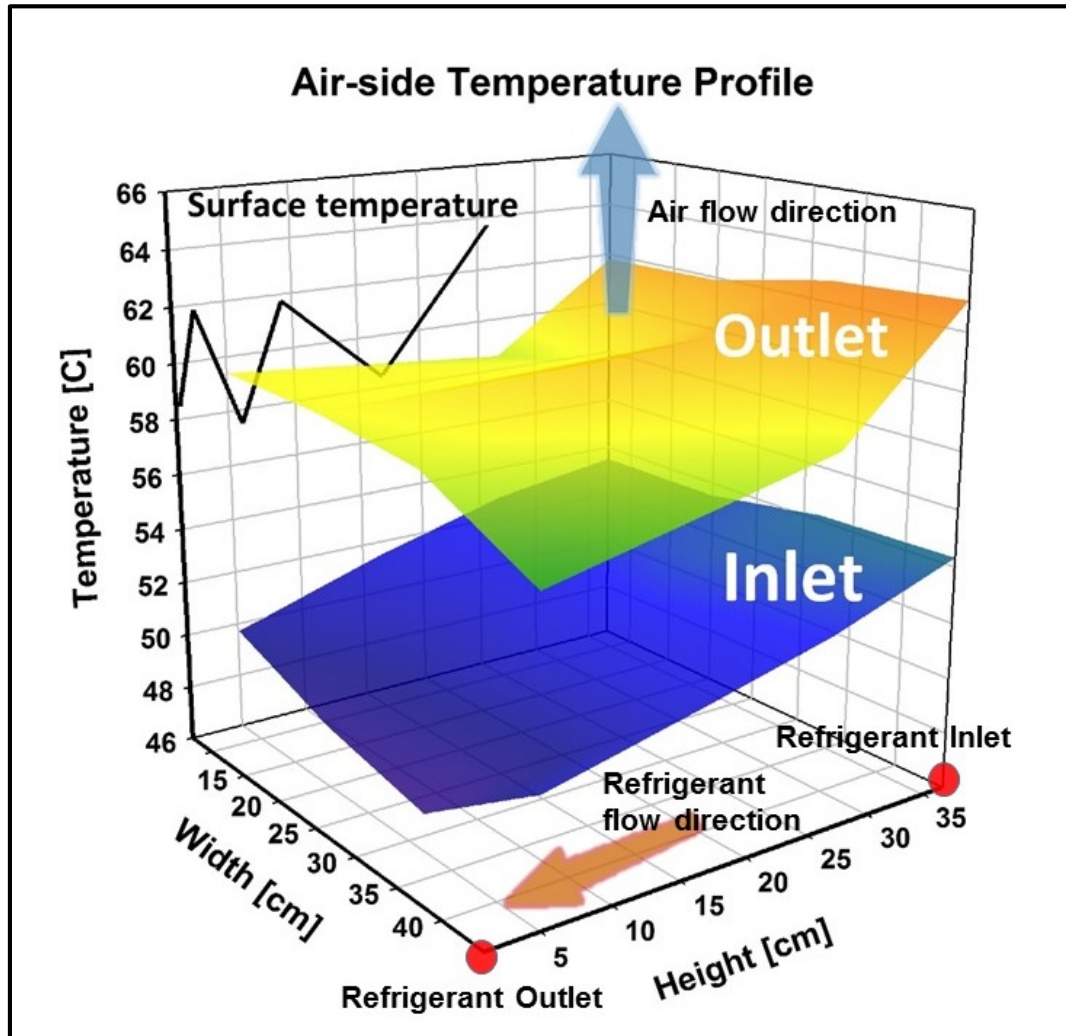
Figure 5.16 Air-temperature profile at the inlet and outlet of Condenser M.1

5.2.2 Pressure drop

The tube-side pressure drop for the multi-pass tube-array condensers with increasing refrigerant flow rates is shown in Figure 5.17. Overall refrigerant pressure drop magnitudes are very small for both condensers, and increase with increasing refrigerant flow rate. The measured tube-side pressure drop in Condenser M.1 and Condenser M.2 ranges from -0.91 kPa to -0.11 kPa, and from 1.72 kPa to 6.53 kPa, respectively, over the

range of the refrigerant flow rates considered. Refrigerant experiences larger pressure drop in Condenser M.2 than in Condenser M.1 because of the increased number of passes and tube bundles. In addition, the refrigerant mass flux and velocity is higher in Condenser M.2 due to fewer parallel tubes per tube bundle, leading to larger tube-side pressure drop. The model predictions for both Condenser M.1 and Condenser M.2 are also shown in Figure 5.17 as lines. The model predictions follow the trend of the measured pressure drop values. The predicted pressure drops for Condenser M.2 are lower than the data throughout the range of mass flow rates. One possible reason for this discrepancy is that the models do not account for pressure drop in the header. The last two tube bundles in Condenser M.2 consist of very few tubes and could lead to a noticeable pressure drop in the header.
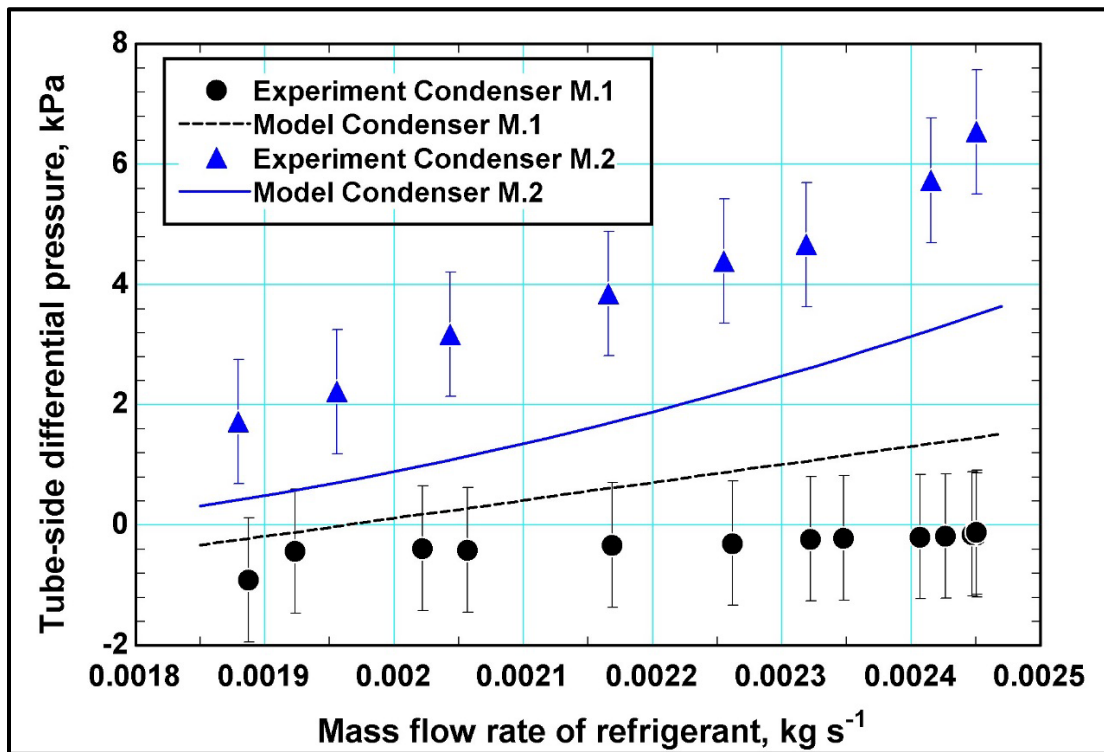
Figure 5.17 Tube-side pressure drop with variation in refrigerant flow rate for multi-pass tube-array condensers

The refrigerant pressure drop per pass in each tube bundle, predicted by the model for Condenser M.2, is shown in Figure 5.18. The figure provides an insight into the various phenomena occurring inside the condenser that affect refrigerant pressure drop. There are six tube bundles, each consisting of parallel tubes making four passes in the air. In each tube bundle, the pressure drop decreases due to the increase in gravitational component ($\Delta P_{refr,grav}$). Also, the slope of this decrease in pressure drop per pass increases in subsequent tube bundles. This is due to the increase in refrigerant density and decrease in vapor quality along the length of the condenser. The number of parallel tubes per tube bundle is labeled in Figure 5.18 and can be seen to decrease as the refrigerant condenses. This leads to a rise in pressure drop when refrigerant flows from one tube bundle to another. Also, there is a sudden drop in the last pass of the fourth tube bundle. This is because condensation is complete and the model switches to a friction factor correlation for subcooled state. The pressure drop is very high for all the passes in the last tube bundle due to very few parallel tubes. Although the last tube bundle (tube bundle 6) consists of single-phase fluid, it contributes to about 27% of the total pressure drop due the much smaller flow area for the refrigerant.
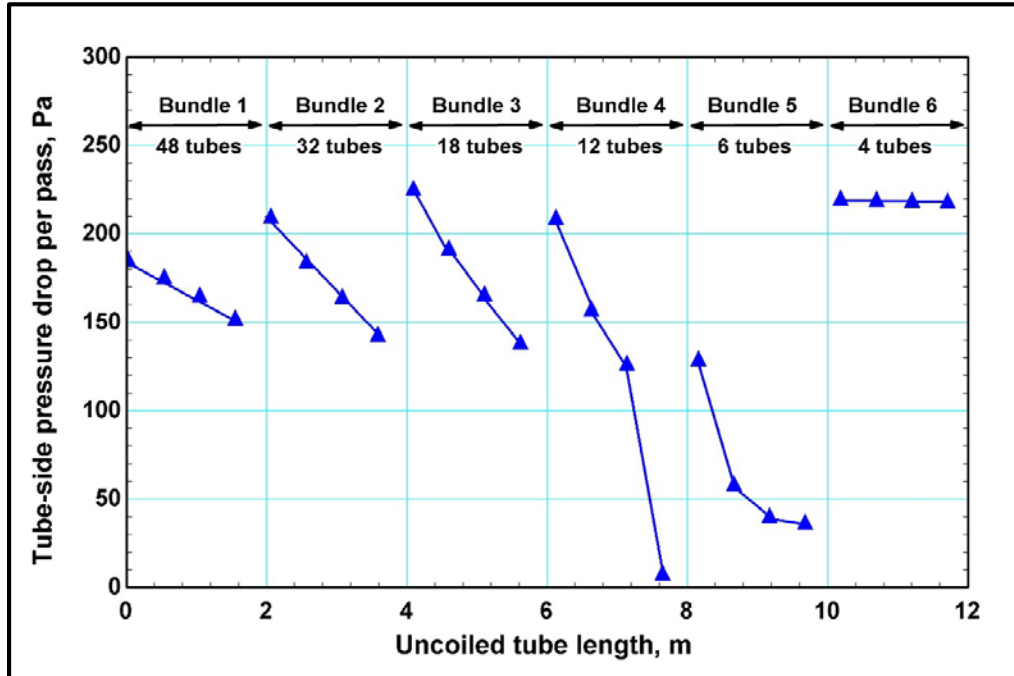
Figure 5.18 Pressure drop per pass along the length of Condenser M.2

The air-side pressure drop is measured for both multi-pass tube-array condensers at various air-flow rates and is shown in Figure 5.19. The magnitude of pressure drop increases for both condensers with an increase in volumetric flow rate of air. The experimentally measured air-side pressure drop for Condenser M.1 ranges from 21.74 Pa to 33.17 Pa for the volumetric flow rate range from $0.35 \text{ m}^3\text{s}^{-1}$ to $0.44 \text{ m}^3\text{s}^{-1}$. The measured air-side pressure drop for Condenser M.2 ranges from 24.81 Pa to 42.42 Pa for the volumetric flow range from $0.34 \text{ m}^3\text{s}^{-1}$ to $0.46 \text{ m}^3\text{s}^{-1}$. The reason for the higher air-side pressure drop in Condenser M.2 is due to the presence of fins, which leads to higher air velocity and more surface area for frictional pressure drop. However, the increase in air-side pressure drop is not very significant because the middle-sections of the fins are cut away in this particular design. The model predictions of pressure drop are shown for both

multi-pass condensers in Figure 5.19. The models over-predict the pressure drop, with an

AAD of 19.81% for Condenser M.1 and an AAD of 20.42% for Condenser M.2.
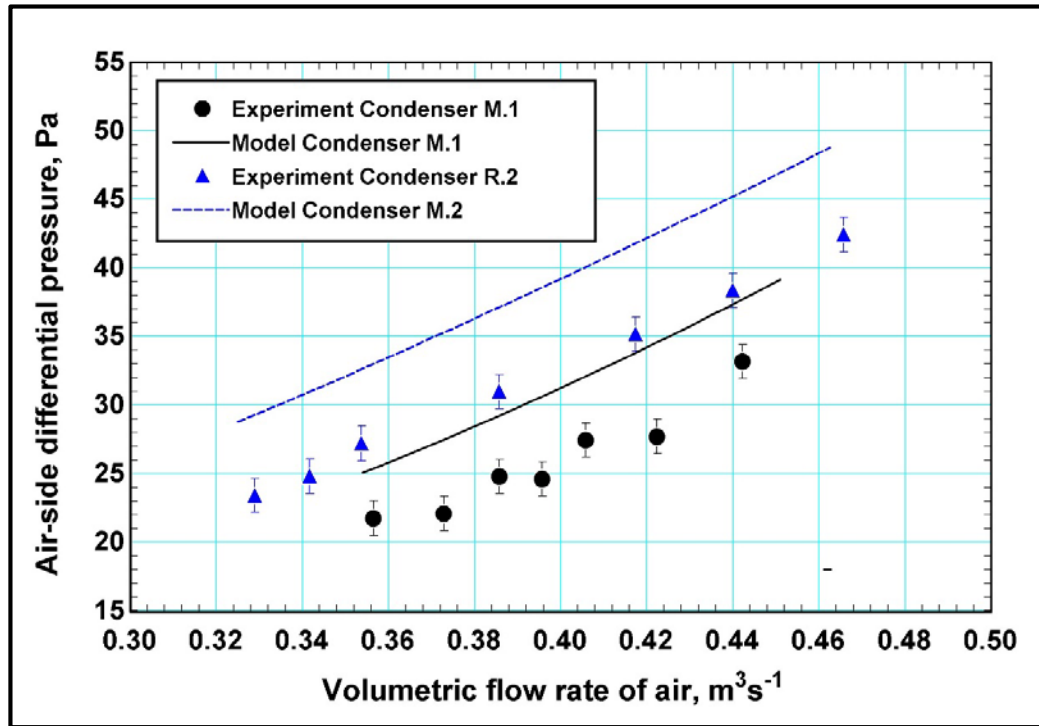
Figure 5.19 Air-side pressure drop for multi-pass tube-array condensers

CHAPTER 6: CONCLUSIONS AND RECOMMENDATIONS

6.1 Conclusions

A detailed analytical and experimental investigation of air-cooled condensers for small-scale ammonia-water absorption heat pumps was conducted. Custom-made round-tube corrugated-fin condensers were investigated. A novel multi-pass tube-array condenser design was also developed and its performance was investigated. Two versions of the condensers were fabricated and tested for the both the conventional and multi-pass designs. The condensers were designed to meet the requirements of a compact 2.71 kW cooling capacity absorption chiller operating at extreme ambient temperatures. The design heat duty for the condenser in this system was 2.51 kW at an ambient air temperature of 51.7°C.

A segmented heat and mass transfer model was developed to simulate the performance of the condensers. The segmented model allowed accurate characterization of the pressure drop and heat and mass transfer processes as they varied during condensation. The conventional coils consist of a single tube with larger tube ODs and have corrugated fins on the air-side. The multi-pass tube-array coils consist of a dense array of small diameter tubes attached to a single header. Thus, the models for the two designs differ in both architecture and heat transfer correlations. After evaluation of the first versions of the condensers, the models were refined to predict the experimental heat transfer rates better. The refined models were used to design improved versions of the condensers to meet the design heat duty requirements at the extreme ambient conditions.

A single-pressure ammonia-water test facility was constructed and used in conjunction with a temperature- and humidity-controlled air handling unit to test the

condensers at design- and off-design operating conditions. The test facility preconditioned the refrigerant, and the air-handling unit preconditioned the air to the desired inlet conditions. The models for the all the condensers were able to predict the heat transfer rate at design conditions with less than 3% AAD, except for the second version of the multi-pass tube-array condenser. The initial model over-predicts the heat rejection rate for this finned multi-pass tube-array condenser. This discrepancy between the model and the experiment for this condenser is traced back to poor contact between the fins and the tubes due to issues in the manufacturing process. The model for this second version was modified to account for this additional contact resistance between the fin and the tube. The resulting AAD between the modified model and the data is 1.2%.

The condensers were tested over a range of air inlet temperatures (35-52°C), ammonia-water inlet temperatures (56.98-65.15°C), air flow rates (0.33-0.46 m^3 s^{-1}), and ammonia-water flow rates (1.9-2.5 g s^{-1}). At the design conditions of 51.7°C air temperature and 0.35 m^3 s^{-1} air flow rate, the first and second versions of the round-tube corrugated-fin condensers demonstrated heat duties of 2.364±0.037 kW and 2.545±0.033 kW, respectively. At the same design conditions, the first and second versions of the multi-pass tube-array condensers demonstrated heat duties of 2.330±0.041 kW and 2.434±0.013 kW, respectively. The first versions of the condensers exhibited comparable performance, with each falling within the margin of error of the other. The second version of both configurations showed improvement, with the round-tube corrugated-fin condensers showing a more significant improvement (+7.66%) than the multi-pass condenser (+4.46%). The second version of the round-tube corrugated-fin condensers, with 551 FPM and 9.53 mm tube OD, is able to meet the design heat duty requirement (2.51 kW) staying

170

within the budgeted values for air-side and tube-side pressure drop. The condenser is able to reject 2.545 kW of heat with a tube-side differential pressure drop of 2.517±1.03 kPa and an air-side differential pressure drop of 26.54±2.5 Pa.

Air and refrigerant inlet temperatures, and refrigerant flow rate were shown to have a large impact on corrugated-fin condenser performance, but air-side flow rate had a marginal effect. However, the novel multi-pass condensers demonstrated a steady increase in performance with increasing air flow rates. Thus, at higher air-flow rates, it was shown that the multi-pass tube-array condensers perform similar to the conventional corrugated-fin condensers.

6.2 Recommendations

The present study investigates several configurations of air-coupled heat exchangers and increases the understanding of heat and mass transfer analysis in compact condensers for ammonia-water heat pumps. Based on the challenges faced during the study and the performance results, several avenues are described in this section for the continued development of compact air-coupled heat exchangers for use in low-grade waste heat-driven systems.

6.2.1 Experimental and analytical investigation

The air-coupled component evaluation in the present investigation was intended to take place at near-uniform air inlet velocity and temperature profiles. However, with the available equipment and test facilities, there is a gradient in the air temperature profile entering the condenser. The steam coil heating the air has an inlet at the top, loops through the entire cross-section of the wind-tunnel unit and has an outlet at the bottom. The steam

entering the coil transfers heat to the air and condenses at the bottom of the coil, leading to a decreasing temperature of the air exiting the steam coil from the top to the bottom of the wind tunnel. This temperature gradient is increased as the hot air separates to the top of the wind-tunnel and the cold air remains at the bottom due to the difference in densities. One potential idea is to reverse the direction of the steam to allow density gradients to cause mixing. However, having the condensing steam flowing opposite to gravity will lead to undesirbale vapor blocks and liquid pools. Thus, for uniform heating of the air the best solution would be the use of electric heaters instead of a steam coil. Also, in this study, the heat input to the air is controlled by manually varying the flow rate and pressure of the steam to reach a steady state inlet temperature. Electric heaters in combination with a PID controller would make it easier to control the heat input, and in turn, the inlet air temperature to the condenser.

While the standardized wind tunnel testing procedure allows direct comparison with other air-coupled heat exchangers, it is likely to deviate from the conditions expected in a packaged system. The air-coupled heat exchangers in a compact absorption system would likely be located on the sides of a rectangular cuboid, and the fans would be placed on top to conserve volume and minimize plumbing. The performance of the heat exchangers in such a configuration will be impacted by this non-uniform and multi-directional airflow profile. Experimental investigations of the air-coupled heat exchangers in the configuration expected in a packaged system are necessary to validate performance. Furthermore, an actual two-pressure absorption system would be able to condition the refrigerant to the required inlet pressure, temperature, and concentration, which is not possible in a single pressure facility.

172

Analytical investigations in this study included heat and mass transfer analysis along with simple structural calculations to ensure the integrity of the air-coupled heat exchangers. Computational Fluid Dynamics (CFD) analyses could be used in the future to better understand airflow patterns across the heat exchanger. For the novel multi-pass tube-array condensers, maldistribution in the headers was confirmed during testing from the surface temperature measurements. In the present study, it is predicted that maldistribution had a negligible effect on the performance because the condensers were limited by air-side heat transfer resistance. However, an in-depth study of maldistribution in the headers would be useful to simulate of heat transfer rates accurately, especially in situations where the air-side resistance is comparable to the tube-side resistance.

6.2.2 <u>Improvement in heat exchanger design</u>

Conventional round-tube corrugated-fin heat exchangers have been mass produced for decades and they provide reasonable performance at a low cost. However, these coils could be improved further for widespread use in waste heat recovery systems in the future. Insertion of wire coils, twisted tape, or conductive packing could be used to potentially enhance mixing for enhanced mass transfer during zeotropic mixture condensation. Figure 6.1 shows twisted tape being inserted into the tubes of the corrugated-fin condenser coil.

**Figure 6.1 Twisted tape (top) and twisted tape being inserted into
round-tube corrugated-fin condenser (bottom)**

Surface enhancements are also a possibility to increase the heat transfer coefficients

on both the tube side and the air-side. For the air-side, a variety of fin patterns and spacings

could be investigated and would result in broadening of knowledge for air coil designers.

However, these modifications to decrease heat transfer resistance will lead to an increase

in pressure drop and could be implemented in scenarios where there is room for additional

pressure drop.

The multi-pass tube-array is a novel design, and continued development is required

to allow mass production. The addition of fins to decrease the air-side thermal resistance

was warranted in the present study. However, the manufacturing process should be

improved to avoid the thermal contact issues seen in the present study with the addition of

fins. These problems prevented a representative assessment of the true potential of microchannel tube, finned array heat exchangers in the present study. A stamped fin with collars (shown in Figure 6.2) would lead to better contact with tubes and will be more effective than a laser cut fin. Also, the cost of each stamped fin would decrease with increase in quantity. Close attention to tolerances is also required during the stamping process for such small OD tubes. Furthermore, the fins could be made of aluminum instead of stainless steel to increase the thermal conductivity by over an order of magnitude. Different fin geometries could also be explored to increase the air-side heat transfer coefficient. With such modifications on the air-side, the multi-pass condensers are expected to show significant improvement in performance, thereby out-performing the conventional condensers. Also, based on the results from the present study, it was shown that multi-pass tube-array condensers will perform even better at higher air and refrigerant flow rates.

Figure 6.2 Sample corrugated-fin with collars

175

The methods and results from this study can be applied to the development of a variety of air-coupled heat exchangers of novel configurations. In combination with the findings from previous and future studies, this effort could increase the viability of small-scale waste heat recovery through the use of absorption cooling and heating systems.

APPENDIX
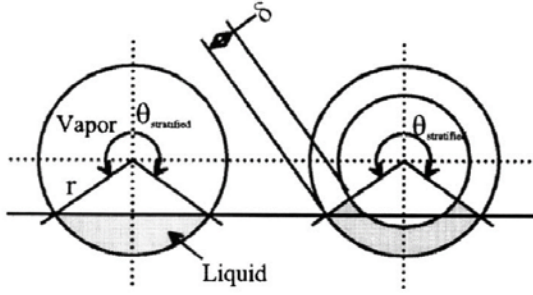
A.1 Heat and Mass Transfer Sample Calculations
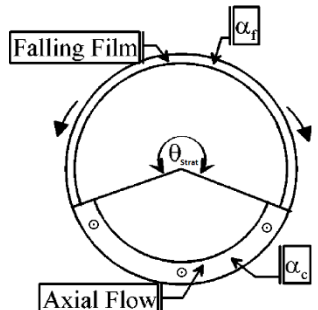
Segmental round-tube, corrugated-fin condenser: sample calculations		
Inputs	Equations	Results
Tube-Side Geometry Intermediate Calculations:		
$D_o = 0.016$ m	$D_i = D_o - 2t_{tube}$	$D_i = 0.013$ m
$t_{tube} = 1.25 \times 10^{-3}$ m	$A_i = \dfrac{\pi}{4} D_i^2$	$A_i = 1.41 \times 10^{-4}$ m^2
$N_{t,row} = 8$		
$N_{row} = 2$	$L_{tot} = L_{pass} N_{pass}$	$L_{tot} = 8.128$ m
$L_{pass} = 0.508$ m	$N_{seg,tot} = L_{total} / L_{seg}$	$N_{seg,tot} = 64$
$L_{seg} = 0.127$ m		
Two-Phase Flow Regime:		
	$VF = \left[1 + 0.28 \left(\dfrac{1 - q_{refr,avg}}{q_{refr,avg}} \right)^{0.64} \left(\dfrac{\rho_V}{\rho_L} \right)^{0.36} \left(\dfrac{\mu_L}{\mu_V} \right)^{0.07} \right]^{-1}$ (Butterworth, 1975)	$VF = 0.968$
	$A_{LD} = \dfrac{A_i (1 - VF)}{D_i^2}$	$A_{LD} = 0.025$
	$A_{VD} = \dfrac{A_i (VF)}{D_i^2}$	$A_{VD} = 0.025$

Segmental round-tube, corrugated-fin condenser: sample calculations		
Inputs	Equations	Results
$q_{refr,avg} = 0.86$ $\rho_L = 537.70$ kg m^{-3} $\rho_V = 23.16$ kg m^{-3} $\mu_L = 1.24 \times 10^{-4}$ kg m^{-1}s^{-1} $\mu_V = 1.19 \times 10^{-5}$ kg m^{-1}s^{-1} $D_i = 0.0134$ m $A_i = 1.41 \times 10^{-4}$ m^2 $g = 9.81$ m s^{-2} $\sigma_L = 0.0128$ N m^{-1} $\dot{m}_{refr} = 2.47 \times 10^{-3}$ kg s^{-1}	$$\theta_{strat} = 2\pi - 2\left\{ \begin{array}{l} \pi(1-VF) + (1.5\pi)^{1/3} \\ \times\left[1 - 2(1-VF) + (1-VF)^{1/3} - VF^{1/3}\right] \\ -0.005(1-VF)VF\left[1-2(1-VF)\right] \\ \times\left[1 + 4\left((1-VF)^2 + VF^2\right)\right] \end{array} \right\}$$ (Biberg, 1999)	$\theta_{strat} = 5.203$ rad
	$h_{LD} = \dfrac{h_L}{D_i} = 0.5\left(1 - \cos\left(\dfrac{2\pi - \theta_{strat}}{2}\right)\right)$	$h_{LD} = 0.071$
	$\dfrac{We}{Fr} = \dfrac{gD_i^2 \rho_L}{\sigma_L}$	$\dfrac{We}{Fr} = 73.78$
	El Hajal $et\ al.$ (2003) method for determining flow regime $$G_{wavy,1} = \left[\dfrac{16 A_{VD}^3 g D_i \rho_L \rho_V}{q_{refr}^2 \pi^2 \left(1 - (2h_{LD} - 1)^2\right)^{0.5}} \left(\dfrac{\pi^2}{25 h_{LD}^2} \left(\dfrac{We}{Fr}\right)^{-1.023} + 1 \right) \right]^{0.5}$$	$G_{wavy,1} = 77.13$ kg m^{-2}s^{-1}
	$G_{wavy,2} = 50 - 75\exp\left(\dfrac{-\left(q_{refr}^2 - 0.97\right)^2}{q_{refr}\left(1 - q_{refr}\right)}\right)$	$G_{wavy,2} = 0.9113$ kg m^{-2}s^{-1}
	$G_{strat} = \left[\dfrac{(226.3)^2 A_{LD} A_{VD}^2 \rho_V \left(\rho_L - \rho_V\right)\mu_L g}{q_{refr}^2 \left(q_{refr} - 1\right)\pi^3}\right] + 20 q_{refr}$	$G_{strat} = 32.3$ kg m^{-2}s^{-1}
	$G_{refr} = \dfrac{\dot{m}_{refr}}{A_i}$	$G_{refr} = 17.55$ kg m^{-2}s^{-1} $G_{refr} < G_{strat} \Rightarrow$ Stratified flow

Fluid Properties for Initial Segment:

$P_{refr,in} = 2950$ kPa $\quad$ $T_{refr,in} = 65.2°C$	$G_{refr} = \dfrac{\dot{m}_{refr,seg}}{A_i}$	$G_{refr} = 17.55$ kg m^{-2}s^{-1}
$x_{refr,in} = 99.99\%$ NH$_3$ $h_{refr,in} = 1278$ kJ K^{-1} $q_{refr,in} = 0.995$	$x_{molar,refr} = \dfrac{\dfrac{x_{refr}}{M(NH_3)}}{\dfrac{x_{refr}}{M(NH_3)} + \dfrac{1-x_{refr}}{M(H_2O)}}$	$x_{molar,refr} = 99.99\%$
$D_i = 0.013$ m $\dot{m}_{refr,seg} = 2.47 \times 10^{-3}$ kg s^{-1} $A_i = 1.41 \times 10^{-4}$ m^2	$P_{crit,refr} = x_{molar,refr}P_{crit,NH_3} + \left(1 - x_{molar,refr}\right)P_{crit,H_2O}$	$P_{crit,refr} = 11334$ kPa
	$P_{r,refr} = \dfrac{P_{refr}}{P_{crit,refr}}$	$P_{r,refr} = 0.261$
$h_L = f(T_{refr}, P_{refr}, q_{refr} = 0)$ $\quad = 315.9$ kJ kg^{-1}	$\text{Pr}_L = \dfrac{Cp_L \mu_L}{k_L}$	$\text{Pr}_L = 1.695$
$x_L = f(T_{refr}, P_{refr}, q_{refr} = 0)$ $\quad = 0.9947$	$\text{Re}_L = \dfrac{G_{refr}(1 - q_{refr})D_i}{\mu_L}$	$\text{Re}_L = 22.32$
$\rho_L = f(T_{refr}, P_{refr}, q_{refr} = 0)$ $\quad = 537.2$ kg m^{-3}	$\text{Re}_{L0} = \dfrac{G_{refr}D_i}{\mu_L}$	$\text{Re}_{L0} = 1895$
$\sigma_L = f(T_{refr}, x_L) = 0.032$ N m^{-1} ** $\mu_L = f(T_{refr}, x_L)$	$\text{Pr}_V = \dfrac{Cp_V \mu_V}{k_V}$	$\text{Pr}_V = 1.214$
$\quad = 1.24 \times 10^{-4}$ kg m^{-1}s^{-1} ** $k_L = f(T_{refr}, x_L)$	$\text{Re}_V = \dfrac{G_{refr}q_{refr}D_i}{\mu_V}$	$\text{Re}_V = 19484$
$\quad = 0.387$ W m^{-1}K^{-1} **	$\text{Re}_{V0} = \dfrac{G_{refr}D_i}{\mu_V}$	$\text{Re}_{V0} = 19716$
$Cp_L = f(T_{refr}, x_L) = 5293$ J kg^{-1}K^{-1}	$h_{fg} = h_V - h_L$	$h_{fg} = 9.67 \times 10^5$ J kg^{-1}

$h_V = f(T_{refr}, P_{refr}, q_{refr} = 1)$ $\quad = 1283 \text{ kJ kg}^{-1}$ $x_V = f(T_{refr}, P_{refr}, q_{refr} = 1)$ $\quad = 0.9999$ **Correlations developed are provided in Appendix A.3 $\rho_V = f(T_{refr}, P_{refr}, q_{refr} = 1)$ $\quad = 23.25 \text{ kg m}^{-3}$ $\mu_V = f(T_{refr}, P_{refr}, x_V) = 1.19 \times 10^{-5} \text{ kg m}^{-1}\text{s}^{-1}$ $k_V = f(T_{refr}, P_{refr}, x_V) = 0.033 \text{ W m}^{-1}\text{K}^{-1}$ $Cp_V = f(T_{refr}, P_{refr}, x_V) = 3394 \text{ J kg}^{-1}\text{K}^{-1}$	$\Delta\rho = \rho_L - \rho_V$	$\Delta\rho = 514 \text{ kg m}^{-3}$
	$Ga = \dfrac{\rho_L (\Delta\rho) g D_i^3}{\mu_L^{\,2}}$	$Ga = 4.2 \times 10^8$
	$X_{tt} = \left(\dfrac{\rho_V}{\rho_L}\right)^{0.5} \left(\dfrac{\mu_L}{\mu_V}\right)^{0.1} \left(\dfrac{1 - q_{refr}}{q_{refr}}\right)^{0.9}$	$X_{tt} = 4.88 \times 10^{-3}$
	$VF_{\text{hom}} = \left[1 + \left(\dfrac{\rho_V}{\rho_L}\right)\left(\dfrac{1 - q_{refr}}{q_{refr}}\right)\right]^{-1}$	$VF_{\text{hom}} = 0.9994$
$P_{\text{crit,NH}_3} = 11333 \text{ kPa}$ $P_{\text{crit,H}_2\text{O}} = 22064 \text{ kPa}$	$VF_{RA} = \dfrac{q_{refr}}{\rho_V} \left(\dfrac{\left[1 + 0.12\left(1 - q_{refr}\right)\right]\left[\dfrac{q_{refr}}{\rho_V} + \dfrac{1 - q_{refr}}{\rho_L}\right]}{+ \dfrac{1.18\left(1 - q_{refr}\right) g\sigma(\Delta\rho)^{0.25}}{G_{refr}\rho_L^{0.5}}} \right)^{-1}$ (Rouhani and Axelsson, 1970)	$VF_{RA} = 0.9841$
	$VF_{hajal} = \dfrac{VF_{\text{hom}} - VF_{RA}}{\ln\left(\dfrac{VF_{\text{hom}}}{VF_{RA}}\right)}$ (El Hajal *et al.*, 2003)	$VF_{hajal} = 0.9917$

Tube-Side Heat Transfer Coefficient:		
$A_i = 1.41 \times 10^{-4}$ m^2	$A_L = A_i (1 - VF)$	$A_L = 1.17 \times 10^{-6}$ m^2
$D_i = 0.013$ m	(Biberg, 1999)	$\theta_{strat} = 5.67$ rad $= 324.3°$
$VF = 0.9917$	$$\theta_{strat} = 2\pi - 2\left\{ \begin{array}{l} \pi(1-VF) + (1.5\pi)^{1/3} \\ \times \left[1 - 2(1-VF) + (1-VF)^{1/3} - VF^{1/3} \right] \\ -0.005(1-VF)VF\left[1 - 2(1-VF) \right] \\ \times \left[1 + 4\left((1-VF)^2 + VF^2 \right) \right] \end{array} \right\}$$	
$\sigma_L = 0.032$ N m^{-1}		
$\mu_L = 1.24 \times 10^{-4}$ kg m^{-1}s^{-1}		
$k_L = 0.387$ W m^{-1}K^{-1}		
$Cp_L = 5293$ J kg^{-1}K^{-1}		
$g = 9.81$ m s^{-2}	$A_L = \dfrac{2\pi - \theta_{strat}}{8}\left(D_i^2 - (D_i - 2\delta)^2 \right)$	$\delta = 2.59 \times 10^{-4}$ m
$h_{fg} = 9.67 \times 10^5$ J kg^{-1}		
$\Delta\rho = 514$ kg m^{-3}		
$T_{refr} - T_{tube,in} = 3.06$ K *		
$q_{refr} = 0.985$ *		
$Cp_V = 3.39$ kJ kg^{-1}K^{-1}		
$\Delta T_{gl,seg} = 0.196$ K*		
$\Delta h_{refr,seg} = 19.03$ kJ kg^{-1} *	(Thome *et al.*, 2003)	
	Del Col *et al.* (2005) method for heat transfer and mass transfer in zeotropic mixture $$\alpha_f = 0.728\left(\frac{\rho_L (\Delta\rho) g h_{fg} k_L^3}{\mu_L D_i (T_{refr} - T_{tube,in})} \right)^{1/4}$$	$\alpha_f = 9573$ W m^{-2}K^{-1}

$Re_{L,th} = \dfrac{4G_{refr}\left(1-q_{refr}\right)\delta}{\left(1-VF\right)\mu_L}$	$Re_{L,th} = 260.9$
$\alpha_c = 0.003\,Re_{L,th}^{0.74}\,Pr_L^{0.5}\,\dfrac{k_L}{\delta}$	$\alpha_c = 357.6\ \mathrm{Wm^{-2}K^{-1}}$
Bell and Ghaly (1973) method for mass transfer resistance $Z = q_{refr}Cp_V\,\dfrac{\Delta T_{gl,seg}}{\Delta h_{refr,seg}}$	$Z = 0.03445$
$\alpha_V = 0.023k_V\,Re_V^{0.8}\,Pr_V^{0.33}\,D_i^{-1}$	$\alpha_V = 164.5\ \mathrm{W\,m^{-2}K^{-1}}$
$\alpha_{c,m} = \left(\dfrac{1}{\alpha_c}+\dfrac{Z}{\alpha_V}\right)^{-1}$	$\alpha_{c.m} = 332.7\ \mathrm{W\,m^{-2}\ K^{-1}}$
$\alpha_{f,m} = \left(\dfrac{1}{\alpha_f}+\dfrac{Z}{\alpha_V}\right)^{-1}$	$\alpha_{film} = 3186\ \mathrm{Wm^{-2}K^{-1}}$
$\alpha_{refr,app} = \dfrac{\alpha_{f,m}\theta_{strat}+\left(2\pi-\theta_{strat}\right)\alpha_{c.m}}{2\pi}$ 	$\alpha_{refr,app} = 2876\ \mathrm{Wm^{-2}K^{-1}}$

Air-side Geometry Intermediate Calculations:

$D_o = 0.0159$ m	$D_c = D_o + 2t_{fin}$	$D_c = 0.0164$ m
$H_{fin} = 0.305$ m	$s = p_{fin} - t_{fin}$	$s = 2.299 \times 10^{-3}$ m
$W_{fin} = 0.066$ m	$s_d = \sqrt{s_l^2 + \left(\dfrac{s_t}{2}\right)^2}$	$s_d = 0.038$ m
$N_{t,row} = 8$		
$N_{pass} = 16$	$A_{face} = H_{fin} L_{pass} \left(1 - t_{fin}/p_{fin}\right)$	$A_{face} = 0.14$ m^2
$L_{seg} = 0.127$ m	$A_{fr} = L_{pass} H_{fin}$	$A_{fr} = 0.155$ m^2
$L_{pass} = 0.508$ m	$A_c = (H_{fin} - N_{t,row} D_c) L_{pass} \left(1 - t_{fin}/p_{fin}\right)$	$A_c = 0.079$ m^2
$L_{tot} = 8.128$ m	$A_{c,t} = \left(H_{face} - N_{t,row} D_o\right) L_{pass}$	$A_{c,t} = 0.088$ m^2
$N_{seg,tot} = 64$	$A_{fin} = 2\left(H_{fin}\left(\dfrac{W_{fin}}{s_{wav,p}}\right)\sqrt{s_{wav,p}^2 + s_{wav,p}^2} - N_{pass}\left(\pi \dfrac{D_c^2}{4}\right)\right)$	$A_{fin} = 0.025$ m^2
$t_{fin} = 2.41 \times 10^{-4}$ m		
$p_{fin} = 2.54 \times 10^{-3}$ m		
$s_t = 0.038$ m	$A_{fin,tot} = N_{fin} A_{fin} = \dfrac{L_{pass}}{p_{fin}} A_{fin}$	$A_{fin,tot} = 5.055$ m^2
$s_l = 0.033$ m		
$s_{wav,d} = 2.16 \times 10^{-3}$ m	$A_{unfin,tot} = \pi D_c \left(L_{tot} - N_t \left(N_{fin} t_{fin}\right)\right)$	$A_{unfin,tot} = 0.379$ m^2
$s_{wav,p} = 8.20 \times 10^{-3}$ m	$A_{tot} = A_{fin,tot} + A_{unfin,tot}$	$A_{tot} = 5.434$ m^2
	Area of fin per tube, treated as an annular fin of an effective diameter, $D_{ann,eff}$ $$A_{ann,fin} = \dfrac{A_{fin}}{N_{pass}} = 2\left(\pi \dfrac{D_{ann,eff}^2 - D_c^2}{4}\right)$$	$D_{fin,eff} = 0.035$ m
	$r_{ann,eff} = \dfrac{D_{ann,eff}}{2}$	$r_{ann,eff} = 0.018$ m

	Finned area per segment, along single serpentine tube $A_{\text{fin,seg}} = \dfrac{A_{fin,tot}}{N_{seg,tot}}$	$A_{\text{fin,seg}} = 0.078 \text{ m}^2$
	Unfinned area per segment (exposed tube) $A_{\text{unfin,sg}} = \dfrac{A_{unfin,tot}}{N_{seg,tot}}$	$A_{\text{unfin,seg}} = 5.92 \times 10^{-3} \text{ m}^2$
	Total, finned and unfinned, area per segment $A_{out,seg} = A_{\text{fin,seg}} + A_{\text{unfin,seg}}$	$A_{\text{out,seg}} = 0.085 \text{ m}^2$

Air-Side Heat Transfer Coefficient:

$A_{fr} = 0.155 \text{ m}^2$ $A_{face} = 0.14 \text{ m}^2$ $D_c = 0.0164 \text{ m}$ $r_c = 0.0082 \text{ m}$ $r_{ann,fin} = 0.0178$ $T_{air} = 0.5\left(T_{air,in} + T_{air,out} *\right)$ $\quad = 53.6\,^{\circ}\text{C}$ $k_{air} = f(\bar{T}_{air}) = 2.78 \times 10^{-2} \text{ W m}^{-1}\text{K}^{-1}$ $C_{p,air} = f(\bar{T}_{air}) = 1.04 \text{ kJ kg}^{-1}\text{K}^{-1}$ $\mu_{air} = f(\bar{T}_{air}) = 1.98 \times 10^{-5} \text{ kg m}^{-1}\text{s}^{-1}$ $\rho_{air} = 0.5\left(\rho_{air,in} + \rho_{air,out} *\right)$ $\quad = 1.05 \text{ kg m}^{-3}$ $\dot{V}_{air} = 0.354 \text{ m}^3\text{ s}^{-1}$	$u_{air,fr} = \dfrac{\dot{V}_{air}}{A_{fr}}$	$u_{air,fr} = 2.284 \text{ m s}^{-1}$
	$u_{air,face} = \dfrac{\dot{V}_{air}}{A_{face}}$	$u_{air,face} = 2.529 \text{ m s}^{-1}$
	$u_{air,max} = \dfrac{s_t}{s_t - D_c} u_{air,face}$	$u_{air,max} = 4.459 \text{ m s}^{-1}$
	$\text{Re}_{D,max} = \dfrac{\rho_{air} u_{air,max} D_c}{\mu_{air}}$	$\text{Re}_{D,max} = 3897$
	$\text{Pr}_{air} = \dfrac{c_{p,air}\mu_{air}}{k_{air}}$	$\text{Pr}_{air} = 0.741$
	Colburn "j" factor based on number of tube rows (Kim *et al.*, 1997) $N \geq 3: \; j_N = j_3 = 0.394\,\text{Re}_{D,max}^{-0.357}\left(\dfrac{s_t}{s_l}\right)^{-0.272}\left(\dfrac{s}{D_c}\right)^{-0.205}\left(\dfrac{s_{wav,p}}{s_{wav,d}}\right)^{-0.558}\left(\dfrac{s_{wav,d}}{s}\right)^{-0.133}$ $N = 1, 2;\; \text{Re}_{D,max} \geq 1000:\; j_N = j_3\left(0.978 - 0.010N\right)$ $N = 1, 2;\; \text{Re}_{D,max} < 1000:\; j_N = j_3\left(1.350 - 0.162N\right)$	$j_N = 0.0177$

$s_t = 0.038$ m	$j_N = \dfrac{\alpha_{kim}\, \mathrm{Pr}_{air}^{2/3}}{\rho_{air} u_{air,max} Cp_{air}}$	$\alpha_{kim} = 80.87$ W m^{-2}K^{-1}
$s_l = 0.033$ m	$\alpha_{air} = \alpha_{Kim}$	$\alpha_{air} = 80.87$ W m^{-2}K^{-1}
$s_{wav,d} = 2.16 \times 10^{-3}$ m	$m_{fin} = \sqrt{\dfrac{2\alpha_{air}}{k_{fin} t_{fin}}}$	$m_{fin} = 52.98$ m^{-1}
$s_{wav,p} = 8.20 \times 10^{-3}$ m		
$s = 2.29 \times 10^{-3}$ m	$C_2 = \dfrac{2 r_c}{m_{fin}\left(\left(r_{ann,eff}\right)^2 - \left(r_c\right)^2\right)}$	$C_2 = 1.209$
$A_{fin,seg} = 0.078$ m^2		
$A_{tot,seg} = 0.085$ m^2	$\eta_{fin} = C_2 \dfrac{K_1\left(m_{fin} r_c\right) I_1\left(m_{fin} r_{ann,eff}\right) - I_1\left(m_{fin} r_c\right) K_1\left(m_{fin} r_{ann,eff}\right)}{I_0\left(m_{fin} r_c\right) K_1\left(m_{fin} r_{ann,eff}\right) - K_0\left(m_{fin} r_c\right) I_1\left(m_{fin} r_{ann,eff}\right)}$ I, K : Modified Bessel functions	$\eta_{fin} = 0.884$
	$\eta_0 = 1 - \left(\dfrac{A_{fin,seg}}{A_{tot,seg}}\right)\left(1 - \eta_{fin}\right)$	$\eta_o = 0.892$
Thermal Resistance and Heat Transfer Rate:		
$D_c = 0.0164$ m	$R_{cond} = R_{collar} + R_{tube} = \dfrac{\ln\left(D_o/D_i\right)}{2 k_{tube} \pi L_{seg}} + \dfrac{\ln\left(D_c/D_o\right)}{2 k_{fin} \pi L_{seg}}$	$R_{cond} = 0.014$ K W^{-1}
$D_o = 0.0159$ m		
$D_i = 0.013$ m	$R_{in} = \dfrac{1}{\alpha_{refr,app} \pi D_i L_{seg}}$	$R_{in} = 0.065$ K W^{-1}
$k_{tube} = 15.44$ W m^{-1}K^{-1}		
$k_{fin} = 238.2$ W m^{-1}K^{-1}	$R_{out} = \dfrac{1}{\eta_0 \alpha_{air} A_{out,sg}}$	$R_{out} = 0.163$ K W^{-1}
$L_{seg} = 0.127$ m	$R_{total} = R_{in} + R_{cond} + R_{out}$	$R_{total} = 0.242$ KW^{-1}
$\alpha_{refr,app} = 2876$ Wm^{-2}K^{-1}	$UA = 1/R_{total}$	$UA = 4.126$ W K^{-1}

$\rho_{air} = 1.05 \text{ kg m}^{-3}$ $\dot{V}_{air} = 0.354 \text{ m}^3 \text{ s}^{-1}$	$\dot{m}_{air,tot} = \rho_{air,in} \dot{V}_{air,in}$	$\dot{m}_{air,tot} = 0.376 \text{ kg s}^{-1}$
$C_{p,air} = 1.04 \text{ kJ kg}^{-1} \text{ K}^{-1}$ $\Delta T_{gl,seg} = 0.196 \text{ K*}$	$\dot{m}_{air,seg} = \dot{m}_{air,tot} \div \left(\dfrac{N_{t,row} L_{pass}}{L_{seg}} \right)$	$\dot{m}_{air,seg} = 0.012 \text{ kg s}^{-1}$
$\Delta h_{refr,seg} = 19.03 \text{ kJ kg}^{-1} \text{*}$	$\dot{C}_{air} = \dot{m}_{air,seg} C_{p,air}$	$\dot{C}_{air} = 12.14 \text{ WK}^{-1}$
$h_{refr,in} = 1278 \text{ kJ kg}^{-1}$ $T_{refr,in} = 65.2°C$	$\dot{C}_{refr} = \dfrac{\Delta h_{refr,seg}}{\Delta T_{gl,seg}}$	$\dot{C}_{refr} = 239.7 \text{ WK}^{-1}$
$T_{air,in} = 51.7°C$	$NTU = UA/\dot{C}_{min} = UA/\dot{C}_{air}$	$NTU = 0.339$
$N_{t,row} = 8$	$\dot{Q}_{max} = \dot{C}_{min} \left(T_{refr,in} - T_{air,in} \right)$	$\dot{Q}_{seg} = 164.3 \text{ W}$
$L_{seg} = 0.127 \text{ m}$	$\varepsilon = 1 - \exp\left(-C_r^{-1}(1 - \exp(-C_r NTU)) \right)$	$\varepsilon = 0.286$
$L_{pass} = 0.508 \text{ m}$	$\dot{Q}_{seg} = \varepsilon(\dot{Q}_{max})$	$\dot{Q}_{seg} = 47 \text{ W}$
*Determined through iterations	$\dot{Q}_{seg} = \dot{m}_{air,seg} C_{p,air} \left(T_{air,out} - T_{air,in} \right)$	$T_{air,out} = 55.54°C$
	$\dot{Q}_{seg} = \dot{m}_{air,seg} \left(h_{refr,in} - h_{refr,out} \right)$	$h_{refr,out} = 1259 \text{ kJ kg}^{-1}$

A.2 Pressure Drop Sample Calculations

Tube-Side Pressure Drop:		
Two-phase Frictional Pressure Drop Friedel (1979)		
$Re_{L0} = 1895$ $Re_{V0} = 19716$ $q_{refr} = 0.995$	$Re_{L0} > 1055 \Rightarrow$ Turbulent flow correlation $f_{L0} = 0.25 \left[0.86859 \ln\left(\dfrac{Re_{L0}}{1.964 \ln(Re_{L0}) - 3.8215} \right) \right]^{-2}$	$f_{L0} = 0.0125$
$\rho_L = 537.2 \text{ kg m}^{-3}$	$Re_{V0} > 1055 \Rightarrow$ Turbulent flow correlation $f_{V0} = 0.25 \left[0.86859 \ln\left(\dfrac{Re_{V0}}{1.964 \ln(Re_{V0}) - 3.8215} \right) \right]^{-2}$	$f_{V0} = 0.0065$
$\rho_V = 23.25 \text{ kg m}^{-3}$ $\mu_L = 1.24 \times 10^{-4} \text{ kg m}^{-1}\text{s}^{-1}$ $\mu_V = 1.19 \times 10^{-5} \text{ kg m}^{-1}\text{s}^{-1}$ $D_i = 0.0134 \text{ m}$	$\rho_{TP} = \left(\dfrac{q_{refr}}{\rho_V} + \dfrac{1 - q_{refr}}{\rho_L} \right)^{-1}$	$\rho_{TP} = 23.58$
$\sigma_L = 0.032 \text{ N m}^{-1}$ $L_{seg} = 0.127 \text{ m}$	$Fr = \dfrac{G_{refr}^2}{g D_i \rho_{TP}^2}$	$Fr = 4.22$
$G_{refr} = 17.55 \text{ kg m}^{-2} \text{ s}^{-1}$	$We = \dfrac{G_{refr}^2 D_i}{\rho_{TP} \sigma_L}$	$We = 13.66$
	$C_{Friedel,1} = \left(1 - q_{refr}\right)^2 + q_{refr}^2 \left(\dfrac{\rho_L}{\rho_V} \right)\left(\dfrac{f_{V0}}{f_{L0}} \right)$	$C_{Friedel,1} = 11.66$
	$C_{Friedel,2} = 3.24 q_{refr}^{0.78} \begin{pmatrix} \left(1 - q_{refr}\right)^{0.224} \left(\dfrac{\rho_L}{\rho_V} \right)^{0.91} \left(\dfrac{\mu_V}{\mu_L} \right)^{0.19} \\ \left(1 - \dfrac{\mu_V}{\mu_L}\right)^{0.7} Fr^{-0.045} We^{-0.035} \end{pmatrix}$	$C_{Friedel,2} = 3.99$
	$\phi_{L0,Friedel}^2 = C_{Friedel,1} + C_{Friedel,2}$	$\phi_{L0,Friedel} = 4.77$

	$\left(-\dfrac{dP}{dz}\right)_{fric,TP} = \Phi^2_{Lo,Friedel}\left(4f_{L0}\dfrac{1}{D_i}\dfrac{G^2_{refr}}{2\rho_l}\right)$	$\left(-\dfrac{dP}{dz}\right)_{fric,TP} = 24.34\ \text{Pa m}^{-1}$
	$\Delta P_{refr,major} = L_{seg}\left(-\dfrac{dP}{dz}\right)_{fric,TP}$	$\Delta P_{refr,major} = 3.091\ \text{Pa}$

Tube-Side Pressure Drop Due to Deceleration

$q_{refr,in} = 0.994$ $q_{refr,out} = 0.976$ $G_{refr} = 17.55\ \text{kg m}^{-2}\ \text{s}^{-1}$ $\rho_L = 537.2\ \text{kg m}^{-3}$ $\rho_V = 23.25\ \text{kg m}^{-3}$ $\mu_L = 1.24\times10^{-4}\ \text{kg m}^{-1}\text{s}^{-1}$ $\mu_V = 1.19\times10^{-5}\ \text{kg m}^{-1}\text{s}^{-1}$	$VF_{in} = \left[1+0.28\left(\dfrac{1-q_{refr,in}}{q_{refr,in}}\right)^{0.64}\left(\dfrac{\rho_V}{\rho_L}\right)^{0.36}\left(\dfrac{\mu_L}{\mu_V}\right)^{0.07}\right]^{-1}$	$VF_{in} = 0.996$
	$VF_{out} = \left[1+0.28\left(\dfrac{1-q_{refr,out}}{q_{refr,out}}\right)^{0.64}\left(\dfrac{\rho_V}{\rho_L}\right)^{0.36}\left(\dfrac{\mu_L}{\mu_V}\right)^{0.07}\right]^{-1}$	$VF_{out} = 0.990$
	$\Delta P_{refr,dec} = G^2_{refr}\left[\dfrac{q^2_{refr,out}}{\rho_V VF_{out}}+\dfrac{\left(1-q_{refr,out}\right)^2}{\rho_L\left(1-VF_{out}\right)}\right]$ $-\,G^2_{refr}\left[\dfrac{q^2_{refr,in}}{\rho_V VF_{in}}+\dfrac{\left(1-q_{refr,in}\right)^2}{\rho_L\left(1-VF_{in}\right)}\right]$	$\Delta P_{refr,dec} = -0.385\ \text{Pa}$ Negative pressure loss corresponds to pressure rise due to deceleration

Tube-Side Pressure Drop Due to Gravity

$VF = 0.992$ $s_t = 0.038\ \text{m}$ $\rho_L = 537.2\ \text{kg m}^{-3}$ $\rho_V = 23.25\ \text{kg m}^{-3}$	Gravitational pressure rise $\Delta P_{refr,grav} = -\left[\left(1-VF\right)\rho_L+VF\cdot\rho_V\right]g\left(\dfrac{s_t}{2}\right)$	$\Delta P_{refr,grav} = -4.99\ \text{Pa}$

Tube-Side Pressure Drop Due to Minor Losses

	$G_L = G_{refr}\left(1-q_{refr}\right)$	$G_L = 0.258\ \text{kg m}^{-2}\ \text{s}^{-1}$

$q_{refr} = 0.995$ $G_{refr} = 17.55 \text{ kg m}^{-2} \text{ s}^{-1}$ $\rho_L = 537.2 \text{ kg m}^{-3}$ $\rho_V = 23.25 \text{ kg m}^{-3}$ $s_d = 0.038$ $D_i = 0.0134 \text{ m}$	$G_V = G_{refr} \left(q_{refr} \right)$	$G_V = 17.29 \text{ kg m}^{-2} \text{ s}^{-1}$
	$X_{Bend} = \sqrt{\dfrac{\Delta P_{L,bend}}{\Delta P_{V,bend}}} = \sqrt{\dfrac{K_{bend} G_L^2 / \left(2\rho_L \right)}{K_{bend} G_V^2 / \left(2\rho_V \right)}}$	$X_{bend} = 3.1 \times 10^{-3}$
	$r_{bend} = \dfrac{s_d}{2}$	$r_{bend} = 0.019$
$K_{L,UBend} = 0.2$, from Cengel and Cimbala (2006)	$C_{bend} = \left[\sqrt{\dfrac{\rho_L}{\rho_V}} + \sqrt{\dfrac{\rho_V}{\rho_L}} \right] \left[1 + \left(1 + \dfrac{2.2}{K_{bend} \left(2 + \dfrac{r_{bend}}{D_i} \right)} - 1 \right) \left(\dfrac{\rho_L - \rho_V}{\rho_L} \right)^{0.5} \right]$	$C_{bend} = 20.77$
	$\Phi_{L0} = \left(1 - q_{refr}^2 \right) \left(1 + \dfrac{C_{bend}}{X_{bend}} + \dfrac{1}{X_{bend}^2} \right)$	$\Phi_{L0} = 3227$
	$\Delta P_{\text{refr,minor}} = \Phi_{L0,bend} \dfrac{1}{2} K_{\text{Bend}} \dfrac{G_{refr}^2}{\rho_L}$	$\Delta P_{\text{refr,minor}} = 185.1 \text{ Pa}$
Total Tube-Side Pressure Drop		
	Total tube-side pressure drop in segment $\Delta P_{\text{loss,refr}} = \Delta P_{\text{refr,major}} + \Delta P_{\text{refr,minor}} + \Delta P_{\text{refr,grav}} + \Delta P_{\text{refr,dec}}$	$\Delta P_{loss,refr} = 182.8 \text{ Pa}$

$P_{refr,in} = 2950$ kPa	$P_{refr,out} = P_{refr,in} - \Delta P_{loss,refr}$	$P_{refr,out} = 2949.82$ kPa
$\Delta P_{refr,major} = 3.091$ Pa		
$\Delta P_{refr,minor} = 185.1$ Pa		
$\Delta P_{refr,grav} = -4.99$ Pa		
$\Delta P_{refr,dec} = -0.385$ Pa		

Air-Side Pressure Drop:

Pressure Drop Due to Frictional Losses		
$s_t = 0.038$ m $s_l = 0.033$ m $D_c = 0.0164$ m	Ratio of transverse tube spacing to tube outer diameter $a = s_t/D_c$	$a = 2.33$
	Ratio of longitudinal tube spacing to outer diameter $b = s_l/D_c$	$b = 2.01$
$\mathrm{Re}_{D,max} = 3897$ $A_{Eu}{}^* = 0.33$ $B_{Eu}{}^* = 98.9$	Constant used in air-side pressure drop calculation (Zukauskas *et al.*, 1968) $k_1 = \left(a_t/b_t \right)^{-0.048}$	$k_1 = 0.993$
$C_{Eu}{}^* = -1.48 \times 10^4$ $D_{Eu}{}^* = 1.92 \times 10^6$ $E_{Eu}{}^* = -8.62 \times 10^7$	Euler number for air flow over tube bank $Eu = k_1 \left(A_{Eu} + \dfrac{B_{Eu}}{\mathrm{Re}_{D,max}} + \dfrac{C_{Eu}}{\mathrm{Re}_{D,max}^2} + \dfrac{D_{Eu}}{\mathrm{Re}_{D,max}^3} + \dfrac{E_{Eu}}{\mathrm{Re}_{D,max}^4} \right)$ (Zukauskas *et al.*, 1968)	$Eu = 0.352$
$C_z{}^* = 0.81$ *Determined from Hewitt (1990).	Euler number, corrected for fewer than 10 tubes $Eu_N = C_z Eu$	$Eu_z = 0.285$
$A_{c,t} = 0.088$ m^2 $N_{t,row} = 8$ $L_{pass} = 0.508$ m	$Eu_N = f_{t,air} \dfrac{N_{pass} \left(4\pi D_c L_{pass} \right)}{A_{c,t}} N_{t,row}$	$f_{t,air} = 0.033$
	$f_{f,air} = 4.467 \, \mathrm{Re}_{D,max}^{-0.423} \left(\dfrac{s_t}{s_l} \right)^{-1.08} \left(\dfrac{s}{D_c} \right)^{-0.0339} \left(\dfrac{s_{wav,p}}{s_{wav,d}} \right)^{-0.672}$ (Kim *et al.*, 1997)	$f_{f,air} = 0.051$

$s_{\text{wav,d}} = 2.16 \times 10^{-3}$ m $s_{\text{wav,p}} = 8.20 \times 10^{-3}$ m $s = 2.29 \times 10^{-3}$ m $t_{fin} = 2.41 \times 10^{-4}$ m $p_{fin} = 2.54 \times 10^{-3}$ m $A_{fin,tot} = 5.055$ m^2 $A_{tot} = 5.434$ m^2 $A_{unfin,tot} = 0.378$ m^2 $G_{air} = 4.71$ kg m^{-2}s^{-1} $\rho_{air} = 1.05$ kg m^{-3}	$f_{air} = f_{f,air}\left(\dfrac{A_{fin,tot}}{A_{tot}}\right) + f_{t,air}\left(1 - \dfrac{A_{fin,tot}}{A_{tot}}\right)\left(1 - \dfrac{t_{fin}}{p_{fin}}\right)$	$f_{air} = 0.049$
	$\Delta P_{air,fric} = f_{air}\dfrac{A_{tot}}{A_c}\dfrac{G_{air}^2}{2\rho_{air}}$	$\Delta P_{air,fric} = 34.97$ Pa
	$\Delta P_{air,fin} = f_{f,air}\dfrac{G_{air}}{2\rho_{air}}\left(\dfrac{A_{fin,tot}}{A_c}\right)$	$\Delta P_{air,fin} = 33.47$ Pa
	$\Delta P_{air,t} = \dfrac{1}{2}f_{t,air}\dfrac{G_{air}}{\rho_{air}}\left(\dfrac{A_{unfin,tot}}{A_{c,t}}\right)$	$\Delta P_{air,t} = 1.49$ Pa
Pressure Drop Due To Expansion, Contraction, and Acceleration		
$A_{face} = 0.14$ m^2 $A_{WT} = 1.032$ m^2 $A_{fr} = 0.155$ m^2 $G_{air} = 4.71$ kg m^{-2}s^{-1} $\rho_{air,in} = 1.061$ kg m^{-3} $\rho_{air,out} = 1.048$ kg m^{-3}	$\sigma_c = \dfrac{A_{face}}{A_{fr}}$ [Contraction ratio at the entrance of condenser]	$\sigma_c = 0.905$
	$\sigma_e = \dfrac{A_{face}}{A_{WT}}$ [Contraction ratio at the exit of condenser]	$\sigma_e = 0.136$
	$C_c = 1 - \dfrac{1 - \sigma_c}{2.08(1 - \sigma_c) + 0.5371}$	$C_c = 0.871$
	$K_c = \left(\dfrac{1}{C_c} - 1\right)^2$	$K_c = 0.022$
	$K_e = (1 - \sigma_e)^2$	$K_e = 0.747$
	$\Delta P_{air,entrance} = \dfrac{G_{air}^2}{2\rho_{air,in}}\left(1 - \sigma_c^2 + K_c\right)$	$\Delta P_{air,entrance} = 2.115$ Pa

	$\Delta P_{air,exit} = -\dfrac{G_{air}^2}{2\rho_{air,out}}\left(1-\sigma_e^2-K_e\right)$	$\Delta P_{air,exit} = -2.47$ Pa
	Pressure drop due to acceleration of flow due to heating $\Delta P_{air,accel} = \dfrac{G_{air}^2}{2\rho_{air,in}}\left(\dfrac{\rho_{air,in}}{\rho_{air,out}}-1\right)$	$\Delta P_{air,accel} = 0.13$ Pa
Total Air-Side Pressure Drop		
$\Delta P_{air,entrance} = 2.12$ Pa $\Delta P_{air,fric} = 33.47$ Pa $\Delta P_{air,accel} = 0.13$ Pa $\Delta P_{air,exit} = -2.47$ Pa	$\Delta P_{loss,air} = \Delta P_{air,entrance} + \Delta P_{air,fric} + \Delta P_{air,accel} + \Delta P_{air,exit}$	$\Delta P_{loss,air} = 34.74$ Pa

A.3 Ammonia-water Liquid Property Correlations

Ammonia-water Liquid Properties	
Liquid Viscosity Correlation	
Developed in this work for ammonia-water liquid viscosity $\left(\mu_L,\ \text{kg m}^{-1}\text{s}^{-1} \right)$ Applicability: $10°C \le T_{refr} \le 130°C$ $0 \le x_{refr} \le 1$	$\mu_L = 1.461 \times 10^{-3} - 3.160 \times 10^{-5} T_{refr} + 3.289 \times 10^{-7} T_{refr}^2 - 1.237 \times 10^{-9} T_{refr}^3 + 5.698 \times 10^{-3} x_{refr}$ $\quad - 1.431 \times 10^{-2} x_{refr}^2 + 5.353 \times 10^{-3} x_{refr}^3 + 1.977 \times 10^{-3} x_{refr}^4 - 1.463 \times 10^{-4} T_{refr} x_{refr}$ $\quad + 3.815 \times 10^{-4} T_{refr} x_{refr}^2 - 2.027 \times 10^{-4} T_{refr} x_{refr}^3 + 1.238 \times 10^{-6} T_{refr}^2 x_{refr} - 3.231 \times 10^{-6} T_{refr}^2 x_{refr}^2$ $\quad + 1.627 \times 10^{-6} T_{refr}^2 x_{refr}^3 - 3.553 \times 10^{-9} T_{refr}^3 x_{refr} + 9.471 \times 10^{-9} T_{refr}^3 x_{refr}^2 - 4.505 \times 10^{-9} T_{refr}^3 x_{refr}^3$
Developed by Nagavarapu (2012) for ammonia-water liquid thermal conductivity $\left(k_L,\ \text{W m}^{-1}\text{K}^{-1} \right)$	$k_L = 0.5727 + 1.702 \times 10^{-3} T_{refr} - 0.054 x_{refr} - 5.835 \times 10^{-6} T_{refr}^2 + 8.49 \times 10^{-9} x_{refr}^2$ $\quad - 3.341 \times 10^{-3} T_{refr} x_{refr}$
Developed by Nagavarapu (2012) for ammonia-water liquid surface tension $\left(\sigma_L,\ \text{N m}^{-1} \right)$	$\sigma_L = 39.922 + 1.211 \times 10^{-6} T_{refr}^3 - 1.195 \times 10^{-3} T_{refr}^2 + 0.2970 T_{refr} - 6.204 x_{refr}^3$ $\quad + 103.357 x_{refr}^2 - 4.857 x_{refr} 1.945 \times 10^{-4} x_{refr}^2 T_{refr}^2 + 0.1851 x_{refr}^2 T_{refr}$ $\quad + 1.405 \times 10^{-3} x_{refr} T_{refr}^2 - 0.7007 x_{refr} T_{refr}$

A.4 Experimental Data Reduction and Uncertainty Calculations

Experimental Data Reduction: sample calculations		
Inputs	Equations	Results
Air side measurements and calculations		
$T_{air,in,avg} = 51.93 \pm 0.75°C$	$P_{air,out,HX} = P_{air,in,HX} - \Delta P_{air,HX}$	$P_{air,out} = 97069.9$ Pa
$T_{air,out,avg} = 58.54 \pm 0.75°C$	$\dot{V}_{air} = u_{air,ebtron} \times A_{air,ebtron}$	$\dot{V}_{air} = 0.353$ m^{3}s^{-1}
$P_{air,in,HX} = 97100 \pm 108.4$ Pa	$\dot{m}_{air} = \rho_{air,in} \times \dot{V}_{air}$	$\dot{m}_{air} = 0.368$ kg s^{-1}
$\Delta P_{air,HX} = 30.1 \pm 2.5$ Pa	$\rho_{air,in} = f(T_{air,in}, RH_{air,in}, P_{air,in,HX})$	$\rho_{air,in} = 1.043$ kg m^{-3}
$RH_{in} = 4.65 \pm 2\%$	$\omega_{air} = f(T_{air,in}, RH_{air,in}, P_{air,in,HX})$	$\omega_{air} = 3.73 \times 10^{-3}$
$A_{air,ebtron} = 0.929$ m^2	$h_{air,in,avg} = f(T_{air,in,avg}, \omega_{air}, P_{air,in,HX})$	$h_{air,in,avg} = 61.68$ kJ kg^{-1}
$u_{air,ebtron} = 0.380$ m s^{-1}	$h_{air,out,avg} = f(T_{air,out,avg}, \omega_{air}, P_{air,out,HX})$	$h_{air,out,avg} = 68.56$ kJ kg^{-1}
	$\dot{Q}_{air} = \dot{m}_{air}\left(h_{air,out,avg} - h_{air,in,avg}\right)$	$\dot{Q}_{air} = 2.471$ kW
Air side heat transfer rate uncertainty		
$\dfrac{\partial \dot{Q}_{air}}{\partial \dot{m}_{air}} = h_{air,out} - h_{air,in} = 6.88$ kJ kg^{-1} $U_{\dot{m}_{air}} = 7.382 \times 10^{-3}$ kg s^{-1} $\dfrac{\partial \dot{Q}_{air}}{\partial h_{air,in,avg}} = -\dot{m}_{air} = -0.368$ kg s^{-1} $U_{h_{air,in,avg}} = 0.1903$ kJ kg^{-1} $\dfrac{\partial \dot{Q}_{air}}{\partial h_{air,out,avg}} = \dot{m}_{air} = 0.368$ kg s^{-1} $U_{h_{air,out,avg}} = 0.1903$ kJ kg^{-1}	$U_{\dot{Q}_{air}}^2 = \left(\dfrac{\partial \dot{Q}_{air}}{\partial \dot{m}_{air}} U_{\dot{m}_{air}}\right)^2 + \left(\dfrac{\partial \dot{Q}_{air}}{\partial h_{air,in,avg}} U_{h_{air,in,avg}}\right)^2 + \left(\dfrac{\partial \dot{Q}_{air}}{\partial h_{air,out,avg}} U_{h_{air,out,avg}}\right)^2$	$U_{\dot{Q}_{air}} = 0.111$ kW

Experimental Data Reduction: sample calculations		
Inputs	Equations	Results
Refrigerant side measurements and calculations		
$\dot{m}_{sol,dil} = 8.31\times10^{-3} \pm 1.51\times10^{-5}$ kg s^{-1}	$\dot{m}_{refr} = \dot{m}_{sol,conc} - \dot{m}_{sol,dil}$	$\dot{m}_{refr} = 2.46\times10^{-3}$ kg s^{-1}
$\dot{m}_{sol,conc} = 1.07\times10^{-2} \pm 1.51\times10^{-5}$ kg s^{-1}	$x_{dil} = f(T_{sep,liq,out}, P_{refr,in}, q=0)$ Saturated liquid condition is assumed at the bottom of the separator	$x_{dil} = 0.992$
$T_{sep,liq,out} = 65.21 \pm 0.25°C$	$x_{refr} = f(T_{sep,vap,out}, P_{refr,in}, q=1)$ Saturated vapor condition is assumed at the top of the separator	$x_{refr} = 0.999$
$T_{sep,vap,out} = 65.41 \pm 0.25°C$	$h_{refr,in} = f(T_{refr,in}, P_{refr,in}, x_{refr})$	$h_{refr,in} = 1277$ KJ kg^{-1}
$P_{refr,in} = 2947 \pm 25.85$ kPa	$\rho_{refr,out} = f(T_{refr,out}, P_{refr,out}, x_{refr})$	$\rho_{refr,out} = 536.8$ kg m^{-3}
$T_{refr,in} = 65.17 \pm 0.25°C$	$\Delta P_{refr,HX,act} = \Delta P_{refr,HX,meas} - (\rho_{refr} g H_{column})$ Actual refrigerant pressure drop is calculated from measured value by subtracting the hydrostatic pressure head of the column	$\Delta P_{refr,HX,act} = -0.329$ Pa
$\Delta P_{refr,HX,meas} = 1.709 \pm 1.03$ kPa		
$T_{refr,out} = 64.17 \pm 0.25°C$		
$g = 9.81$ m s^{-2}	$P_{refr,out} = P_{refr,in} - \Delta P_{refr,HX,act}$	$P_{refr,out} = 2948$ kPa
$H_{column} = 0.387$ m	$h_{refr,out} = f(T_{refr,out}, P_{refr,out}, x_{refr})$	$h_{refr,out} = 314.9$ kJ kg^{-1}
	$T_{refr,satliq} = f(P_{refr,out}, x_{refr}, q=0)$	$T_{refr,satliq} = 64.82°C$
	$T_{deg,subcool} = T_{refr,satliq} - T_{refr,out}$	$T_{deg,subcool} = 0.652°C$
	$\dot{Q}_{refr} = \dot{m}_{refr}(h_{refr,in} - h_{refr,out})$	$\dot{Q}_{refr} = 2.37$ kW
	$EB_{air/refr} = \left\| \dfrac{\dot{Q}_{refr} - \dot{Q}_{air}}{\dot{Q}_{refr}} \right\| \times 100$ Energy balance between air and refrigerant heat transfer rate	$EB_{air/refr} = 4.28\%$

Experimental Data Reduction: sample calculations		
Inputs	Equations	Results
	Tube-side heat transfer rate uncertainty	
$\dfrac{\partial \dot{Q}_{refr}}{\partial \dot{m}_{refr}} = h_{refr,in} - h_{refr,out} = 962.1 \text{ kJ kg}^{-1}$ $U_{\dot{m}_{refr}} = 2.14 \times 10^{-5} \text{ kg s}^{-1}$ $\dfrac{\partial \dot{Q}_{refr}}{\partial h_{refr,in}} = \dot{m}_{refr} = 2.46 \times 10^{-3} \text{ kg s}^{-1}$ $U_{h_{refr,in}} = 18.28 \text{ kJ kg}^{-1}$ $\dfrac{\partial \dot{Q}_{refr}}{\partial h_{refr,out}} = -\dot{m}_{refr} = -2.46 \times 10^{-3} \text{ kg s}^{-1}$ $U_{h_{refr,out}} = 1.33 \text{ kJ kg}^{-1}$	$U_{\dot{Q}_{refr}}^2 = \left(\dfrac{\partial \dot{Q}_{refr}}{\partial \dot{m}_{refr}} U_{\dot{m}_{refr}} \right)^2 + \left(\dfrac{\partial \dot{Q}_{refr}}{\partial h_{refr,in}} U_{h_{refr}} \right)^2 + \left(\dfrac{\partial \dot{Q}_{refr}}{\partial h_{refr}} U_{h_{refr}} \right)^2$	$U_{\dot{Q}_{refr}} = 0.049 \text{ kW}$

REFERENCES

Akers, W., H. Deans and O. Crosser (1958), "Condensing Heat Transfer within Horizontal Tubes," *Chem. Eng. Progr.* Vol. 54.

Baker, O. (1953), "Design of Pipelines for the Simultaneous Flow of Oil and Gas," *Fall Meeting of the Petroleum Branch of AIME*, Society of Petroleum Engineers.

Bandhauer, T. M., A. Agarwal and S. Garimella (2006), "Measurement and Modeling of Condensation Heat Transfer Coefficients in Circular Microchannels," *Journal of Heat Transfer* Vol. 128(10) pp. 1050-1059.

Beecher, D. (1968), "The Effects of Pattern Depth on the Performance of a Typical Air Conditioning Division Fin Tube Heat Exchanger," *Westinghouse Research Lab Report*.

Beecher, D. and T. Fagan (1987). Effects of Fin Pattern on the Air Side Heat Transfer Coefficient in Plate Finned Tube Heat Exchangers. Westinghouse Research and Development Center, Pittsburgh, PA (USA).

Bell, K. and M. Ghaly (1973), "An Approximate Generalized Design Method for Multicomponent/Partial Condenser," *AIChE Symp. Ser*, pp. 72-79.

Biberg, D. (1999), "An Explicit Approximation for the Wetted Angle in Two‑Phase Stratified Pipe Flow," *The Canadian Journal of Chemical Engineering* Vol. 77(6) pp. 1221-1224.

Blasius, H. (1913). Das Ähnlichkeitsgesetz Bei Reibungsvorgängen in Flüssigkeiten. *Mitteilungen Über Forschungsarbeiten Auf Dem Gebiete Des Ingenieurwesens*, Springer pp. 1-41.

Blasius, H. (1950), "The Boundary Layers in Fluids with Little Friction."

Butterworth, D. (1975), "A Comparison of Some Void-Fraction Relationships for Co-Current Gas-Liquid Flow," *International Journal of Multiphase Flow* Vol. 1(6) pp. 845-850.

Cavallini, A., G. Censi, D. Del Col and L. Doretti (2002), "In-Tube Condensation of Halogenated Refrigerants/Discussion," *ASHRAE Transactions* Vol. 108 p. 146.

Cengel, Y. A. and J. M. Cimbala (2006). *Fluid Mechanics*, Tata McGraw-Hill Education.

Chato, J. C. (1960). *Laminar Condensation inside Horizontal and Inclined Tubes*, Massachusetts Institute of Technology.

Chen, Y., K.-S. Yang and C.-C. Wang (2002), "An Empirical Correlation for Two-Phase Frictional Performance in Small Diameter Tubes," *International Journal of Heat and Mass Transfer* Vol. 45(17) pp. 3667-3671.

Chisholm, D. (1967), "A Theoretical Basis for the Lockhart-Martinelli Correlation for Two-Phase Flow," *International Journal of Heat and Mass Transfer* Vol. 10(12) pp. 1767-1778.

Chisholm, D. (1981), "Flow of Compressible Two-Phase Mixtures through Sharp-Edged Orifices," *Journal of Mechanical Engineering Science* Vol. 23(1) pp. 45-48.

Chisholm, D. and A. Laird (1958), "Two-Phase Flow in Rough Tubes," *Trans. ASME* Vol. 80(2) pp. 276-286.

Churchill, S. W. (1977), "Comprehensive Correlating Equations for Heat, Mass and Momentum Transfer in Fully Developed Flow in Smooth Tubes," *Industrial & Engineering Chemistry Fundamentals* Vol. 16(1) pp. 109-116.

Churchill, S. W. and J. Brier (1953). *Convective Heat Transfer from a Gas Stream at High Temperature to a Circular Cylinder Normal to Flow*.

Coleman, J. W. and S. Garimella (2003), "Two-Phase Flow Regimes in Round, Square and Rectangular Tubes During Condensation of Refrigerant R134a," *International Journal of Refrigeration* Vol. 26(1) pp. 117-128.

Del Col, D., A. Cavallini and J. R. Thome (2005), "Condensation of Zeotropic Mixtures in Horizontal Tubes: New Simplified Heat Transfer Model Based on Flow Regimes," *Journal of heat transfer* Vol. 127(3) pp. 221-230.

Delahanty, J. C. (2015), "Desorption of Ammonia-Water Mixtures in Microscale Geometries for Miniaturized Absorption Systems."

Dittus, F. and L. Boelter (1930), "University of California Publications on Engineering," *University of California publications in Engineering* Vol. 2 p. 371.

Dobson, M. and J. Chato (1998), "Condensation in Smooth Horizontal Tubes," *Journal of Heat Transfer* Vol. 120(1) pp. 193-213.

EIA, U. (2016). Annual Energy Outlook 2016 with Projections to 2040. U.S. Energy Information Administration (EIA). Washington, DC, DOE/EIA-0383(2016).

El Hajal, J., J. R. Thome and A. Cavallini (2003), "Condensation in Horizontal Tubes, Part 1: Two-Phase Flow Pattern Map," *International Journal of Heat and Mass Transfer* Vol. 46(18) pp. 3349-3363.

Fernández-Seara, J., J. Sieres, C. Rodríguez and M. Vázquez (2005), "Ammonia–Water Absorption in Vertical Tubular Absorbers," *International journal of thermal Sciences* Vol. 44(3) pp. 277-288.

Ferreira, C. I., C. Keizer and C. Machielsen (1984), "Heat and Mass Transfer in Vertical Tubular Bubble Absorbers for Ammonia-Water Absorption Refrigeration Systems," *International Journal of Refrigeration* Vol. 7(6) pp. 348-357.

Forinash, D. M. (2015), "Novel Air-Coupled Heat Exchangers for Waste Heat-Driven Absorption Heat Pumps."

Frank, M. J., J. A. Kuipers and W. P. van Swaaij (1996), "Diffusion Coefficients and Viscosities of CO2+ H2O, CO2+ CH3OH, NH3+ H2O, and NH3+ CH3OH Liquid Mixtures," *Journal of Chemical & Engineering Data* Vol. 41(2) pp. 297-302.

Friedel, L. (1979), "Improved Friction Pressure Drop Correlations for Horizontal and Vertical Two-Phase Pipe Flow," *European two-phase flow group meeting, Paper E*.

Fronk, B. M. and S. Garimella (2016a), "Condensation of Ammonia and High-Temperature-Glide Ammonia/Water Zeotropic Mixtures in Minichannels–Part I: Measurements," *International Journal of Heat and Mass Transfer* Vol. 101 pp. 1343-1356.

Fronk, B. M. and S. Garimella (2016b), "Condensation of Ammonia and High-Temperature-Glide Zeotropic Ammonia/Water Mixtures in Minichannels–Part Ii: Heat Transfer Models," *International Journal of Heat and Mass Transfer* Vol. 101 pp. 1357-1373.

Gaddis, E. and V. Gnielinski (1985), "Pressure Drop in Cross Flow across Tube Bundles," *Int. Chem. Eng.;(United States)* Vol. 25(1).

Garimella, S. and J. W. Coleman (1998). Design of Cross-Flow Condensers for Ammonia-Water Absorption Heat Pumps. American Society of Heating, Refrigerating and Air-Conditioning Engineers, Inc., Atlanta, GA (United States).

Garimella, S., J. W. Coleman and A. Wicht (1997), "Tube and Fin Geometry Alternatives for the Design of Absorption-Heat-Pump Heat Exchangers," *Journal of Enhanced Heat Transfer* Vol. 4(3).

Garimella, S., C. M. Keinath, J. C. Delahanty, D. C. Hoysall, M. A. Staedter, A. Goyal and M. A. Garrabrant (2016), "Development and Demonstration of a Compact Ammonia–Water Absorption Heat Pump Prototype with Microscale Features for Space-Conditioning Applications," *Applied Thermal Engineering* Vol. 102 pp. 557-564.

Garimella, S. and A. Wicht (1995). Air-Cooled Condensation of Ammonia in Flat-Tube, Multi-Louver Fin Heat Exchangers. American Society of Mechanical Engineers, New York, NY (United States).

Ghiaasiaan, S. M. (2007). *Two-Phase Flow, Boiling, and Condensation: In Conventional and Miniature Systems*, Cambridge University Press.

Gnielinski, V. (1975), "Berechnung Mittlerer Wärme-Und Stoffübergangskoeffizienten an Laminar Und Turbulent Überströmten Einzelkörpern Mit Hilfe Einer Einheitlichen Gleichung," *Forschung im Ingenieurwesen A* Vol. 41(5) pp. 145-153.

Gnielinski, V. (1978), "Gleichungen Zur Berechnung Des Wärme-Und Stoffaustausches in Durchströmten Ruhenden Kugelschüttungen Bei Mittleren Und Großen Pecletzahlen," *Verfahrenstechnik* Vol. 12(6) pp. 363-367.

Gray, D. and R. Webb (1986), "Heat Transfer and Friction Correlations for Plate Finned-Tube Heat Exchangers Having Plain Fins," *Proceedings of the 8th International Heat Transfer Conference*, pp. 2745-2750.

Grimison, E. (1937), "Correlation and Utilization of New Data on Flow Resistance and Heat Transfer for Cross Flow of Gases over Tube Banks," *Trans. ASME* Vol. 59(7) pp. 583-594.

Herold, K., R. Radermacher and S. A. Klein (1996). *Absorption Chillers and Heat Pumps*, CRC press.

Hewitt, G. F. (1990). *Hemisphere Handbook of Heat Exchanger Design*, Hemisphere Publishing Corporation.

Hewitt, G. F., G. L. Shires and T. R. Bott (1994). *Process Heat Transfer*, CRC press Boca Raton, FL.

Hilpert, R. (1933), "Wärmeabgabe Von Geheizten Drähten Und Rohren Im Luftstrom," *Forschung auf dem Gebiet des Ingenieurwesens A* Vol. 4(5) pp. 215-224.

Ibrahim, O. and S. Klein (1993), "Thermodynamic Properties of Ammonia-Water Mixtures," *Transactions-American Society Of Heating Refrigerating And Air Conditioning Engineers* Vol. 99 pp. 1495-1495.

Incropera, F. P., D. P. DeWitt, T. L. Bergman and A. S. Lavine (2011). *Fundamentals of Heat and Mass Transfer*, John Wiley & Sons.

Jacob, M. (1938), "Heat Transfer and Flow Resistance in Cross Flow of Gases over Tube Banks," *Trans. ASME* Vol. 60(38) pp. 384-386.

Jang, J.-Y., M.-C. Wu and W.-J. Chang (1996), "Numerical and Experimental Studies of Threedimensional Plate-Fin and Tube Heat Exchangers," *International Journal of Heat and Mass Transfer* Vol. 39(14) pp. 3057-3066.

Jaster, H. and P. Kosky (1976), "Condensation Heat Transfer in a Mixed Flow Regime," *International Journal of Heat and Mass Transfer* Vol. 19(1) pp. 95-99.

Kang, Y. T., Y. Kunugi and T. Kashiwagi (2000), "Review of Advanced Absorption Cycles: Performance Improvement and Temperature Lift Enhancement," *International Journal of Refrigeration* Vol. 23(5) pp. 388-401. DOI: http://dx.doi.org/10.1016/S0140-7007(99)00064-X.

Kattan, N., J. Thome and D. Favrat (1998a), "Flow Boiling in Horizontal Tubes: Part 1—Development of a Diabatic Two-Phase Flow Pattern Map," *Journal of Heat Transfer* Vol. 120(1) pp. 140-147.

Kattan, N., J. R. Thome and D. Favrat (1998b), "Flow Boiling in Horizontal Tubes: Part 3—Development of a New Heat Transfer Model Based on Flow Pattern," *Journal of Heat Transfer* Vol. 120(1) pp. 156-165.

Kays, W. M. and A. L. London (1984), "Compact Heat Exchangers."

Kim, N.-H., J.-H. Yun and R. Webb (1997), "Heat Transfer and Friction Correlations for Wavy Plate Fin-and-Tube Heat Exchangers," *Journal of heat transfer* Vol. 119(3) pp. 560-567.

Kim, N., B. Youn and R. Webb (1999), "Air-Side Heat Transfer and Friction Correlations for Plain Fin-and-Tube Heat Exchangers with Staggered Tube Arrangements," *Journal of heat transfer* Vol. 121(3) pp. 662-667.

Klein, S. A. (2014). *Engineering Equation Solver*, F-Chart Software.

Lockhart, R. and R. Martinelli (1949), "Proposed Correlation of Data for Isothermal Two-Phase, Two-Component Flow in Pipes," *Chem. Eng. Prog* Vol. 45(1) pp. 39-48.

Mandhane, J., G. Gregory and K. Aziz (1974), "A Flow Pattern Map for Gas—Liquid Flow in Horizontal Pipes," *International Journal of Multiphase Flow* Vol. 1(4) pp. 537-553.

Martin, H. (2002), "The Generalized Lévêque Equation and Its Practical Use for the Prediction of Heat and Mass Transfer Rates from Pressure Drop," *Chemical Engineering Science* Vol. 57(16) pp. 3217-3223.

McAdams, W., W. Woods and L. Heroman (1942), "Vaporization inside Horizontal Tubes-Ii-Benzene-Oil Mixtures," *Trans. ASME* Vol. 64(3) pp. 193-200.

Meacham, J. M. (2002). *An Integrated Experimental and Analytical Study of Ammonia-Water Absorption in Microchannel Geometries*, Iowa State University.

Meacham, J. M. and S. Garimella (2004), "Ammonia-Water Absorption Heat and Mass Transfer in Microchannel Absorbers with Visual Confirmation," *ASHRAE Transactions* Vol. 110(1).

Mills, A. F. (1999). *Basic Heat and Mass Transfer*, Pearson College Div.

Moser, K., R. Webb and B. Na (1998), "A New Equivalent Reynolds Number Model for Condensation in Smooth Tubes," *Journal of Heat Transfer* Vol. 120(2) pp. 410-417.

Müller-Steinhagen, H. and K. Heck (1986), "A Simple Friction Pressure Drop Correlation for Two-Phase Flow in Pipes," *Chemical Engineering and Processing: Process Intensification* Vol. 20(6) pp. 297-308.

Nagavarapu, A. K. (2012). *Binary Fluid Heat and Mass Exchange at the Microscales in Internal and External Ammonia-Water Absorption*, Georgia Institute of Technology.

Nema, G., S. Garimella and B. M. Fronk (2014), "Flow Regime Transitions During Condensation in Microchannels," *International Journal of Refrigeration* Vol. 40 pp. 227-240.

Nusselt, W. (1916), "Die Oberflachenkondesation Des Wasserdamffes the Surface Condensation of Water," *Zetrschr. Ver. Deutch. Ing.* Vol. 60 pp. 541-546.

Pasternak, I. and W. Gauvin (1960), "Turbulent Heat and Mass Transfer from Stationary Particles," *The Canadian Journal of Chemical Engineering* Vol. 38(2) pp. 35-42.

Rattner, A. S. and S. Garimella (2011), "Energy Harvesting, Reuse and Upgrade to Reduce Primary Energy Usage in the USA," *Energy* Vol. 36(10) pp. 6172-6183.

Rouhani, S. Z. and E. Axelsson (1970), "Calculation of Void Volume Fraction in the Subcooled and Quality Boiling Regions," *International Journal of Heat and Mass Transfer* Vol. 13(2) pp. 383-393.

Shah, M. (1979), "A General Correlation for Heat Transfer During Film Condensation inside Pipes," *International Journal of heat and mass transfer* Vol. 22(4) pp. 547-556.

Shah, M. (1981). *Heat Transfer During Film Condensation in Tubes and Annuli: A Review of the Literature*.

Shah, M. M. (2009), "An Improved and Extended General Correlation for Heat Transfer During Condensation in Plain Tubes," *HVAC&R Research* Vol. 15(5) pp. 889-913.

Silver, L. (1947), "Gas Cooling with Aqueous Condensation," *Trans. Inst. Chem. Eng* Vol. 25(3).

Soliman, H. (1982), "On the Annular‑to‑Wavy Flow Pattern Transition During Condensation inside Horizontal Tubes," *The Canadian Journal of Chemical Engineering* Vol. 60(4) pp. 475-481.

Srikhirin, P., S. Aphornratana and S. Chungpaibulpatana (2001), "A Review of Absorption Refrigeration Technologies," *Renewable and sustainable energy reviews* Vol. 5(4) pp. 343-372.

Steiner, D. (1993). *Heat Transfer to Boiling Saturated Liquids*, Verein Deutscher Ingenieure, VDI-Geseelschaft Verfahrenstechnik und Chemieingenieurswesen GCV, Düsseldorf.

Taitel, Y. and A. Dukler (1976), "A Model for Predicting Flow Regime Transitions in Horizontal and near Horizontal Gas‑Liquid Flow," *AIChE Journal* Vol. 22(1) pp. 47-55.

Taylor, B. N. and C. E. Kuyatt (1994), "Nist Technical Note 1297," *Guidelines for evaluating and expressing the uncertainty of NIST measurement results* p. 24.

Thome, J. R., J. El Hajal and A. Cavallini (2003), "Condensation in Horizontal Tubes, Part 2: New Heat Transfer Model Based on Flow Regimes," *International Journal of Heat and Mass Transfer* Vol. 46(18) pp. 3365-3387.

Torikoshi, K. and G. Xi (1995). A Numerical Study of Flow and Thermal Fields in Finned Tube Heat Exchangers (Effect of the Tube Diameter). American Society of Mechanical Engineers, New York, NY (United States).

Wang, C. and K. Chi (1998), "Heat Transfer and Friction Characteristics of Plain fin-and-Tube Heat Exchangers, Part 1: New Experimental," *Int. J. Heat Mass Trans* Vol. 43 pp. 2681-2691.

Wang, C., W. Fu and C. Chang (1997), "Heat Transfer and Friction Characteristics of Typical Wavy Fin-and-Tube Heat Exchangers," *Experimental thermal and fluid science* Vol. 14(2) pp. 174-186.

Webb, R. (1990), "Air-Side Heat Transfer Correlations for Flat and Wavy Plate Fin-and-Tube Geometries," *ASHRAE transactions* Vol. 96(2) pp. 445-449.

Wilke, C. (1950), "A Viscosity Equation for Gas Mixtures," *The journal of chemical physics* Vol. 18(4) pp. 517-519.

Ziegler, F. (1999), "Recent Developments and Future Prospects of Sorption Heat Pump Systems," *International Journal of Thermal Sciences* Vol. 38(3) pp. 191-208. DOI: http://dx.doi.org/10.1016/S1290-0729(99)80083-0.

Ziegler, F. (2002), "State of the Art in Sorption Heat Pumping and Cooling Technologies," *International Journal of Refrigeration* Vol. 25(4) pp. 450-459.

Žukauskas, A. (1972). Heat Transfer from Tubes in Crossflow. *Advances in Heat Transfer*. P. H. James and F. I. Thomas, Elsevier, Vol. Volume 8 pp. 93-160.

Zukauskas, A., V. Makarevicius and A. Slanciauskas (1968), "Heat Transfer in Banks of Tubes in Crossflow of Fluid," *Thermophy* Vol. 1 pp. 47-68.

Zukauskas, A. and R. Ulinskas (1983), "Banks of Plain and Finned Tubes," *Heat exchanger design handbook* Vol. 2 p. 2.2.